Marinho Antunes Lopes

Transições de fase e fenómenos não-lineares em modelos de redes neuronais
Phase transitions and nonlinear phenomena in neuronal network models

Marinho Antunes Lopes

Transições de fase e fenómenos não-lineares em modelos de redes neuronais
Phase transitions and nonlinear phenomena in neuronal network models

Dissertação apresentada à Universidade de Aveiro para cumprimento dos requesitos necessários à obtenção do grau de Doutor em Física (em conjunto com as Universidades do Minho, Aveiro e Porto), realizada sob a orientação científica de Alexander V. Goltsev, Investigador Auxiliar do Departamento de Física da Universidade de Aveiro.

Apoio Financeiro da Fundação para a Ciência e a Tecnologia (SFRH/BD/68743/2010).

QUALIFICAR É CRESCER.

QUADRO DE REFERÊNCIA ESTRATÉGICO NACIONAL PORTUGAL 2007.2013

GOVERNO DA REPÚBLICA PORTUGUESA

UNIÃO EUROPEIA
Fundo Social Europeu

the jury

president

Prof. Dr. Amadeu Mortágua Velho da Maia Soares
Full Professor of Biology of Universidade de Aveiro

Prof. Dr. Miguel Angel Fernández Sanjuán
Full Professor of Physics of Universidad Rey Juan Carlos

Prof. Dr. Jorge Manuel Santos Pacheco
Full Professor of Mathematics of Universidade do Minho

Prof. Dr. José Fernando Ferreira Mendes
Full Professor of Physics of Universidade de Aveiro

Prof. Dr. Iveta Rombeiro do Rego Pimentel
Associate Professor of Physics of Faculdade de Ciências da Universidade de Lisboa

Dr. Sergey Nikolaevich Dorogovtsev
Coordinator Researcher at the Department of Physics of Universidade de Aveiro

Dr. Alfonso Renart
Principal Investigator of Champalimaud Centre for the Unknown

Dr. Alexander Viktotorovich Goltsev
Auxiliary Researcher at the Department of Physics of Universidade de Aveiro

acknowledgements

I thank my supervisor Alexander V. Goltsev for his valuable and supportive guidance.

I also thank KyoungEun Lee, Sooyeon Yoon and Detlef Holstein for interesting discussions related with my research. I also would like to thank all the members of the group I worked with: José F. F. Mendes, Sergey N. Dorogovtsev, António L. C. S. Ferreira, Fernão R. V. de Abreu, Gareth J. Baxter, João G. Oliveira, Rui A. F. da Costa, Fabricio L. Forgerini, Orahcio F. de Sousa, Marta D. A. Santos, Ronan S. Ferreira and Juan M. Hernandez.

I acknowledge FCT for the PhD grant.

I thank my family and friends for their support.

palavras-chave redes neuronais, fenómenos não-lineares, oscilações, transições de fase, ressonância estocástica, epilepsia, plasticidade sináptica.

resumo

A comunicação e a cooperação entre milhares de milhões de neurónios está na base do poder do cérebro. Como é que funções cerebrais complexas emergem da dinâmica celular? Como é que grupos de neurónios se auto-organizam em padrões de atividade? Estas são questões cruciais em neurociências. Para as responder é necessário ter um sólido conhecimento teórico sobre como os neurónios comunicam ao nível microscópico, bem como de que forma ocorre atividade coletiva. Nesta tese pretendemos compreender como é que fenómenos coletivos complexos podem emergir num modelo simples de redes neuronais. Usando um modelo com excitação e inibição balanceadas e uma arquitectura de rede complexa, desenvolvemos métodos analíticos e numéricos para descrever a sua dinâmica neuronal. Estudamos como é que a interação entre neurónios gera vários fenómenos coletivos, tais como o aparecimento espontâneo de oscilações de rede e convulsões epilépticas, assim como também examinamos a forma de antecipar as transições para esses estados.

No nosso modelo mostramos que os vários regimes dinâmicos são separados por transições de fase, e investigamos as correspondentes bifurcações e fenómenos críticos. Isto permite-nos sugerir uma explicação qualitativa do efeito Berger, e investigar fenómenos tais como avalanches, filtro passa-faixa, e ressonância estocástica. O papel da estrutura modular na deteção de sinais fracos é também discutido. Além disso, encontramos excitações não-lineares que podem descrever *spikes* paroxísticos observados em eletroencefalogramas de cérebros epilépticos. Tal permite-nos propor um método para prever convulsões epilépticas.

A memória e a aprendizagem são funções chave no cérebro. Existem evidências de que estes processos resultam de alterações dinâmicas na estrutura cerebral. Ao nível microscópico, as conexões sinápticas são plásticas e são modificadas de acordo com a dinâmica dos neurónios. Por isso, generalizamos o nosso modelo de modo a considerar a plasticidade sináptica e mostramos que o conjunto de regimes dinâmicos se torna mais rico. Em particular, encontramos oscilações de modo misto e um regime de atividade neuronal caótica.

keywords neuronal networks, nonlinear phenomena, oscillations, phase transitions, stochastic resonance, epilepsy, synaptic plasticity.

abstract Communication and cooperation between billions of neurons underlie the power of the brain. How do complex functions of the brain arise from its cellular constituents? How do groups of neurons self-organize into patterns of activity? These are crucial questions in neuroscience. In order to answer them, it is necessary to have solid theoretical understanding of how single neurons communicate at the microscopic level, and how cooperative activity emerges. In this thesis we aim to understand how complex collective phenomena can arise in a simple model of neuronal networks. We use a model with balanced excitation and inhibition and complex network architecture, and we develop analytical and numerical methods for describing its neuronal dynamics. We study how interaction between neurons generates various collective phenomena, such as spontaneous appearance of network oscillations and seizures, and early warnings of these transitions in neuronal networks.

Within our model, we show that phase transitions separate various dynamical regimes, and we investigate the corresponding bifurcations and critical phenomena. It permits us to suggest a qualitative explanation of the Berger effect, and to investigate phenomena such as avalanches, band-pass filter, and stochastic resonance. The role of modular structure in the detection of weak signals is also discussed. Moreover, we find nonlinear excitations that can describe paroxysmal spikes observed in electroencephalograms from epileptic brains. It allows us to propose a method to predict epileptic seizures.

Memory and learning are key functions of the brain. There are evidences that these processes result from dynamical changes in the structure of the brain. At the microscopic level, synaptic connections are plastic and are modified according to the dynamics of neurons. Thus, we generalize our cortical model to take into account synaptic plasticity and we show that the repertoire of dynamical regimes becomes richer. In particular, we find mixed-mode oscillations and a chaotic regime in neuronal network dynamics.

Contents

List of Figures

List of Tables

Chapter 1

Introduction

This chapter is organized in the following way. First, we give a short overview of the present efforts to understand the brain. Second, we consider the History of brain study (mainly according to Ref. [1]). Since this thesis is a theoretical study on neuronal networks, a brief historical review about mathematical models in neuroscience is then presented. Fourth, we succinctly explain how network theory can help us study the brain. In this thesis we focus on a particular set of problems. Here, we briefly review them: brain rhythms, stochastic resonance, band-pass filter, phase transitions and a disease, epilepsy. Finally, we present the outline of this thesis.

1.1 The brain quest

"Solving the brain" has been stated as the main quest in science for the 21st century. This assertion is supported by the recent millionaire investments in Europe (the Human Brain Project directed by Henry Markram) and in USA (the Brain Research through Advancing Innovative Neurotechnologies (BRAIN) Initiative co-chaired by William Newsome and Cornelia Bargmann), whose main goal is to improve our understanding of how the brain works [2]. The brain is the most complex organ, about which the scientists know very little. The pursuit to understand the functioning of the brain promises not only applications in medicine, but also in robotics, computer science, and artificial intelligence. Neuroscientists believe that chronic diseases such as Alzheimer's disease, Parkinson's disease and other neurodegenerative diseases may be cured when we understand them better. Hopefully, all health problems related with brain function might be solvable. For instance, neuroscientists think that in a near future it might be possible to treat traumas by simply localizing them in the brain and then purging them, using drugs or surgery [3]. At the intersection between neuroscience and robotics many other applications may emerge, for example in the way we communicate with computers and machines in general. There are already some video games that implement this idea, and also technologies for disabled people that need help from machines in order to communicate or move (neuroprosthetics, for instance) [4]. One can expect that all these technologies will continue to be perfected as

we study the brain. The intersection between neuroscience, robotics and computer science points out the fact that this is a multidisciplinary field that involves not only clinicians and physicians, but also scientists from mathematics, physics, chemistry, biology, computer science, and other sciences.

1.2 A brief historical review about the understanding of the brain

The History of our understanding of the brain goes back to the Greek physician, surgeon and philosopher Galen, who proposed that the brain controls the motion of our body [5]. This is still correct according to our current knowledge. However, he also proposed that nerves convey a fluid from the brain and spinal cord to the body, a view that held until the late 1800s, when Camillo Golgi developed a way to stain neurons to reveal their structure, and Ramón y Cajal showed that the nervous tissue is not a continuous web but instead a network of discrete neurons. The idea regarding the fluid secreted by the brain was previously questioned by physiological investigations in the eighteenth century by Luigi Galvani, who found electricity in living muscles and nerve tissue. Then, after Cajal revealed the discrete nature of nerve cells, Emil DuBois-Reymond, Johannes Müller and Hermann von Helmholtz discovered that one neuron can use electricity to affect the activity of an adjacent cell in a predictable way.

On the other hand, the brain was (and is) also studied by psychology, the study of human and animal behaviour. Its History also dates back to the classical Greek philosophy, which was only concerned about the human mind. The importance of studying animals as models of human behaviour was only recognized after the contributions of Charles Darwin to the continuity of species in evolution. At the end of the eighteenth century, Franz Joseph Gall made the connection between psychology and neurobiology. This physician and neuroanatomist suggested three radical new ideas. First, he proposed a generalization of Galen's concept: the brain not only controls the body, but it is responsible for all behaviour. Second, he advocated that it was possible to divide the cortex in 35 organs, each controlling a specific behaviour (hope, imitation, generosity, *etc.*, were assigned to a specific region in the brain). Finally, Gall argued that each region could grow with use like a muscle. In the beginning of the nineteenth century, Pierre Flourens subjected the second idea to experimental analysis and concluded that all brain regions participate in every behaviour, in contrast to Gall's ideas (the experiments consisted in removing brain regions from animals, in order to discern the contribution of each one). This is now known as the *aggregate field* view of the brain, which was widely accepted in part as a cultural reaction against the biological reductionism of the human mind (the inexistence of the soul). The belief of Flourens was stated in 1823. About thirty years later, J. Hughlings Jackson was the first to seriously challenging it. He studied epilepsy and showed that sensory and motor functions can be tracked to different regions of the brain. This fact and the *neuron doctrine* of Ramón y Cajal, that identified single neurons as the elementary

signalling units of the nervous system, were brought together into a new view of brain function, the *cellular connectionism*. According to this view, neurons are organized in functional groups and are connected in a precise way. This organizational principle is different from Gall's ideas, because each group of neurons is not responsible for a specific behaviour, but instead it is responsible for a function, such as visual processing, motor control or language. The reason why this principle was not found before is related with what is now known as *parallel distributed processing*. In fact, many cognitive, sensory and motor functions are operated by use of multiple neural pathways, and when one is damaged, others may partially compensate. That is why Flourens was deceived by his experiments. Currently, several neural pathways have been identified and precisely mapped in the brain [1]. Indeed, much of the present research has been devoted to find the human *connectome* [6, 7]. However, knowing the connectome does not imply understanding the brain. The connectome of the worm *Caenorhabditis elegans* is already known, but instead of clarifying how its brain functions, it can only provide a starting point for further studies [8].

Pierre Paul Broca was the first neurologist being able to localize a function in the brain. He had a patient who could understand language but was unable to speak. After the patient died, Broca analysed his brain and found a localized lesion in a region which is now known as *Broca's area* (area in the frontal lobe, left hemisphere). The examination of other cases confirmed the relation between that lesion and the specific deficit. In 1864, Broca announced the famous phrase: "We speak with the left hemisphere!" (This is not entirely correct, because the right hemisphere also plays a role regarding the expression of emotion.) In the next decade, Karl Wernicke studied patients who had an "opposite" deficit to those examined by Broca: they were able to speak but unable to comprehend language. Surprisingly, Wernicke found a lesion in a different region of the brain (*Wernicke's area*). On the basis of this discovery, and generalizing for other functions, he proposed the idea of *distributed processing*, which is nowadays considered central in our understanding of brain function.

At the beginning of the last century, Korbinian Brodmann took a different approach. He distinguished 52 areas in the human cerebral cortex based on the *cytoarchitectonic method*. This method consisted in dividing areas on the basis of variations in nerve cell structures and in the characteristic arrangement of theses cells into layers. Broadmann's scheme of the brain has been continuously updated and is still used today. In fact, Broadmann's anatomical areas of the cortex correspond to different physiological functions. In other words, these areas can be distinguished using independent criteria. Subsequent research has shown that the brain is divided into many more areas and that in each area it is even possible to individualize further functional specialization at the level of single columns of neurons.

In 1958, David H. Hubel and Torsten N. Wiesel made a breakthrough in the understanding of the fundamental organizational principles of the brain [9] (and because of it they won the Nobel Prize in Physiology or Medicine in 1981). They studied the activity of neurons in the primary visual cortex of anesthetized cats. They presented visual stimulus to the animal's eyes and measured the activity of neurons using an electrode inserted into the cat's brain. Surprisingly, the neurons were silent. However, they noticed one day that

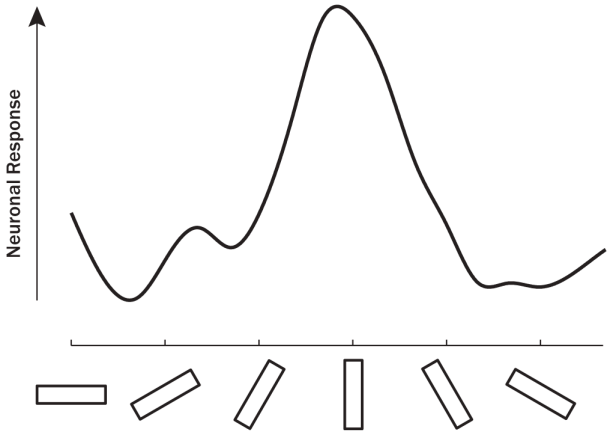

Figure 1.1: Orientation selectivity of neurons in the primary visual cortex. Hubel and Wiesel found that particular neurons respond preferentially to a certain edge orientation of the visual world (in the graph, vertically oriented) [9].

the neuron could fire whenever they changed the presented slide. Then, they realized that the neuron could respond to specific edge orientations in the picture (see Fig. 1.1), instead of patterns of light (or dots at specific locations of the retina, as retinal neurons). From this original finding, these neurophysiologists and others went on to find other neurons that react to other specific attributes, such as the direction of motion, specific colors, and even further specialization as specific objects, hands and faces (in the farthest regions of the cortical tissue, more distant in the neural tract from the sensory receptors). Two fundamental principles emerged: neurons that respond to the same feature are grouped together and there is a hierarchical organization of specialization in the sensory system (i.e., more complex attributes of the sensory input are processed in higher cortical regions, further away from the sensory receptors). Thus, individual brain regions process elementary operations and therefore abilities as thought, memory, perception and movement are the result of the serial and parallel "computing" of many specific brain regions. The most striking example is the fact that even our consciousness is not unitary. Roger Sperry and Michael Gazzaniga found that if the main tract connecting the two hemispheres, the corpus callosum, is removed (as a treatment for epilepsy, for instance), it disrupts consciousness, which is splitted in two. In this case, each hemisphere is able to order a different command to the body at the same time! Indeed, Sperry and Gazzaniga observed a patient who would dress his clothes with one hand, while taking them off with the other [1] (note that the left hemisphere controls the right side of the body, whereas the right hemisphere controls the left).

1.3 Mathematical models in neuroscience

In 1907, Louis Lapicque introduced the integrate-and-fire model [10, 11]. This model captures the essential features of neurons: they sum the signals sent by other neurons and then they fire if the sum is larger than a threshold. Although over a century has passed, the model is still used nowadays in computational neuroscience (usually when the purpose is to simulate large networks of neurons).

Warren McCulloch and Walter Pitts proposed the first model of artificial neurons in 1943 [12]. In this model, the activity of neurons has a binary character (it is either 0 or 1 corresponding to an inactive or an active neuron, respectively). Thus, McCulloch and Pitts were the first to study artificial neural networks.

In 1949, Donald Hebb introduced in his book [13] what is now known as the Hebb's rule: "Cells that fire together, wire together." It is the basis of the Hebbian theory. This theory proposes that during learning processes the synaptic strength between neurons changes depending on their activity. The memory is somehow stored in the synaptic efficacies.

Alan Hodgkin and Andrew Huxley received the Nobel Prize in 1963 for their model of the squid giant axon proposed in 1952 [14]. It provided the first mathematical description of an action potential (for more details see Chapter 2). The Hodgkin-Huxley model continues to be the most complete mathematical model of a neuron and is widely used today in computational neuroscience.

The Hodgkin-Huxley model belongs to the category of micro-scale models in which the dynamical behaviour of individual neurons is well described as well as the interaction between neurons and their local environment. Due to computational limitations, neuronal networks composed of Hodgkin-Huxley neurons are usually small (see for instance the recent papers [15, 16] where a few hundred neurons were considered). A different approach is to model the dynamics of neuronal ensembles rather than the dynamics of individual neurons. These kind of models are called macro-scale models. The idea is to describe the dynamical state of a large population of neurons by use of the distribution function that determines the probabilistic evolution of that population [17]. Wilson and Cowan were pioneers in this framework in the 1970s [18, 19].

All these models illustrate a very important principle in our current understanding of the brain: the remarkable function of the brain is not due to the complexity of its neurons, but instead the complexity of the connections and interactions between its neurons [1].

1.4 Network theory and neuronal networks

A network (graph) is a set of nodes (vertices) connected by links (edges) (see Fig. 1.2). Network theory studies the structural properties of networks [20–22]. In the last two decades many different types of networks have been investigated, including social networks (where nodes are people and links are friendships, for instance), World Wide Web (web pages are connected by hyperlinks), networks of citations between papers, and many others. In particular, neuronal networks have been getting growing attention from scientists.

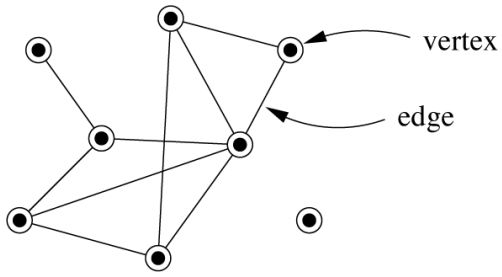

Figure 1.2: A network is a set of vertices connected by edges [22].

Figure 1.3 shows a photo of a neuronal network *in vitro*. In this case, the nodes are the neurons and the links are the synapses. Interestingly, many structural properties of neuronal networks in the brain are similar to properties of other complex networks [6, 7, 23, 24]. Neuronal networks are small-world networks. The small-world properties emerge when the average shortest path between two nodes (characteristic path length) is much shorter in comparison with ordinary lattices. In neuronal networks, it is a consequence of neurons having long axons, which facilitates the interaction between neurons. One can also measure the number of synapses per neuron and construct the degree distribution. This degree distribution follows a power law [23]. In other words, neuronal networks are scale-free (a term that derives from the fact that power-law distributions are scale-invariant). This property makes the network robust against random attacks [20] and conversely vulnerable against targeted attacks on neurons with the highest degrees (hubs). Hubs may play an important role in hyperexcitability stimulated by brain injury [25], providing a mechanism for orchestrating synchrony [26], or integrating multisensory information [27]. Recently, a "rich club" of densely interconnected hub regions was found in the human brain [28, 29] which is similar to "rich clubs" studied in other real complex systems [30, 31]. This rich club is of crucial importance for global brain communication [28, 29].

Another important structural property is that, in the brain, neurons of similar function are grouped together in columns (or modules). This fact is responsible for high clustering coefficients measured in neuronal networks [23]. The columnar organization of the neocortex has been documented in studies of sensory and motor areas in many species [32–34]. For example, rat somatosensory cortex has modular organization where neurons form columns and every column consists of 17000-19000 neurons (each rodent whisker has its own column) [35]. Even the sensory nervous system of the *Caenorhabditis elegans*, which is the smallest nervous system among animals, has modular organization [36].

In the past decade, the growing computational power allowed theoretical neuroscientists to simulate larger and larger networks of neurons. For instance, Izhikevich *et al.* considered neuronal networks composed of a million neurons [38], in order to study spontaneous activity and emergence of brain rhythms. However, it is difficult to obtain insights only from simulation studies about the underlying phenomena without a detailed analytical consideration. Network theory provides a framework to study analytically evolution, dynamics, synchronization, collective phenomena, phase transitions and critical phenomena

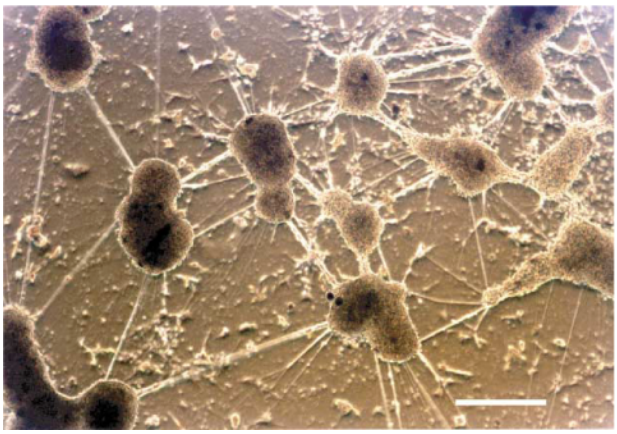

Figure 1.3: Neuronal network *in vitro* with 5×10^6 cells (13100 cells/mm^2), scale bar 500 μm [37]. At high densities (larger than 10000 cells/mm^2), neurons form clusters like *in vivo*.

in networks [39]. All these phenomena are of great importance for the understanding of neuronal networks.

1.5 Brain rhythms

Brain rhythms are a fundamental form of collective activity of neurons resulting from interactions between them. They are ubiquitous in the brain and contribute in every aspect of brain function, from sensory, cognitive processing and memory to motor control (see, for example, [40–44]).

Hans Berger was a pioneer in the study of the brain's electrical activity [41]. He believed that telepathy was possible through an electromagnetic interaction between brains. While trying to prove it, in 1929 he found "large-amplitude" oscillations (around 10 Hz) from the lower rear (occipital) part of the skull when the subject's eyes were close. He called it "alpha" rhythm, because it was the first brain pattern that he observed. When the eyes were open, the amplitude of the alpha rhythm decreased, giving place to faster oscillations, the "beta" rhythm. This is the so-called Berger effect. Regarding telepathy, the hypothesis had to be abandoned, because the electroencephalogram did not record electrical potentials larger than $200\mu V$, which is clearly insufficient to produce electrical currents able to cross air. Berger was not the first to obtain electroencephalographic recordings (EEG). For instance, in 1913 the Russian physiologist Vladimir Pravdich-Neminski recorded the electrical activity from the intact surface of dogs' skulls (he called it "electrocerebrogram"). Berger stands out because of his numerous control experiments, which provided a powerful scientific and clinical method for the study of brain activity.

Since Berger, brain rhythms have been documented in the brains of many mammalian species. Their origin and physiological functions are an open problem in neuroscience. Brain rhythms range from very slow oscillations (periods of minutes) to very fast oscil-

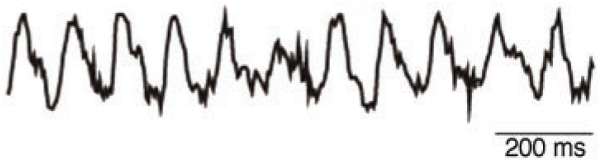

Figure 1.4: Theta waves recorded by EEG from the hippocampus of a rat (adapted from [45]).

lations (600 Hz) [41]. Following Berger's classification, Greek letters were used to label subsequently discovered frequency bands: delta ($0.5 - 4$ Hz), theta ($4 - 8$ Hz), alpha ($8 - 12$ Hz), beta ($12 - 30$ Hz), and gamma ($30 - 80$ Hz) [41]. Frequencies below 0.5 Hz are called slow oscillations, and above 80 Hz are called fast (and ultra fast, for frequencies in the range $200 - 600$ Hz). While slow oscillations can involve many neurons and emerge in large brain regions, fast oscillations are generally local, involving smaller brain areas, mainly because the conduction delays of axons imposes limits in the propagation of fast oscillations [41]. Figure 1.4 displays hippocampal theta oscillations recorded by EEG from a rat.

A useful taxonomy of brain rhythms has not been completed, however, one can mention that slower oscillations (delta, theta and alpha) are usually related with calm and rest states, while faster oscillations (beta and gamma) are associated with alert and high attention states of the mind. For instance, theta oscillations were measured in the hippocampus of anesthetized rabbits, whereas theta-alpha oscillations ($5 - 10$ Hz) were observed in drug-free conditions [41].

1.6 Stochastic resonance and band-pass filter

Brain rhythms are related to unusual phenomena such as stochastic resonance (SR). SR is a phenomenon that describes amplification and optimization of weak signals by noise. Figure 1.5 shows an illustrative example of SR in visual perception. The addition of noise enhances the observer's perception of an image [46]. SR was revealed in many physical systems [47]. In the brain, noise is ubiquitous and strongly influences its function [48, 49]. Thus, SR is recognized as a possible mechanism that allows the brain (and particularly sensory systems) to use noise for its own benefit [48–50]. Indeed, there are experimental evidences that SR can enhance effects of weak intrinsic hippocampal theta or more widespread gamma oscillations within the brain [51]. Apart from brain rhythms, SR was observed experimentally in sensory systems [52–55], in central neurons such as hippocampal CA1 neurons in rat cortex [51, 56, 57], in the human blood pressure regulatory system [58], and the human brain's visual processing area [59, 60]. SR is also considered as a mechanism mediating neuronal synchronization within and between functionally relevant brain areas [61–63]. It has been studied at the single neuron level and as a collective phenomenon at the neuronal network level [50].

One other collective resonance phenomenon was observed in the response of rat hip-

Figure 1.5: Photo of the Big Ben on a 256 gray scale. Noise from a Gaussian distribution was added to the gray scale values in every pixel. Addition of noise enhances the visual perception (see the image in the middle) [59].

---

pocampal neurons to afferent stimulation *in vitro* [64]. Using a functional imaging technique, Sasaki *et al.* revealed that the majority of rat CA1 neurons act collectively like a band-pass filter and fire synchronously in response to a limited range of presynaptic firing rates ($20 - 40$ Hz), although a few neurons exhibited low pass-like or high pass-like characteristics [64].

1.7 Phase transitions in the brain

Beyond brain waves and resonance phenomena, interactions between billions of neurons give rise to phase transitions, self-organization, and critical phenomena in the brain [65, 66]. Phase transitions were observed, for example, in human bimanual coordination [67–72]. In 1981, Kelso asked a subject to move his index fingers antisymmetrically (out-of-phase) and to increase the frequency of the motion. He observed that the subject's fingers shift abruptly to an in-phase symmetrical motion when the frequency was high enough [68] (see Fig. 1.6). Even though the critical frequency was different for different subjects, it was possible to define a dimensionless parameter, which was constant for all subjects. No transitions occur when subjects start in-phase [67]. Similar experimental findings were reported on hand motions around the wrist [68] and ipsilateral hand and foot movements [73]. The coordination dynamics between different cortical areas has also been studied using the relative phase between the two respective neuronal populations [74].

A phase transition was also observed in cultured neural networks when stimulated by an electric field [75]. Despite of the simplicity of these living neural networks, they demonstrate an extremely rich repertoire of activity regimes due to interactions between hundreds to millions of neurons. An external stimulus is able to induce a global activation of these networks, a phenomenon that can be explained on the basis of the concept of percolation without going into details of neuron dynamics [75].

Avalanches is an example of critical collective phenomena that result from the existence of a phase transition (or self-organized criticality) that was observed in the brain [66, 76–78]. A neuronal avalanche is a cascade phenomenon, in which the activation of one neuron

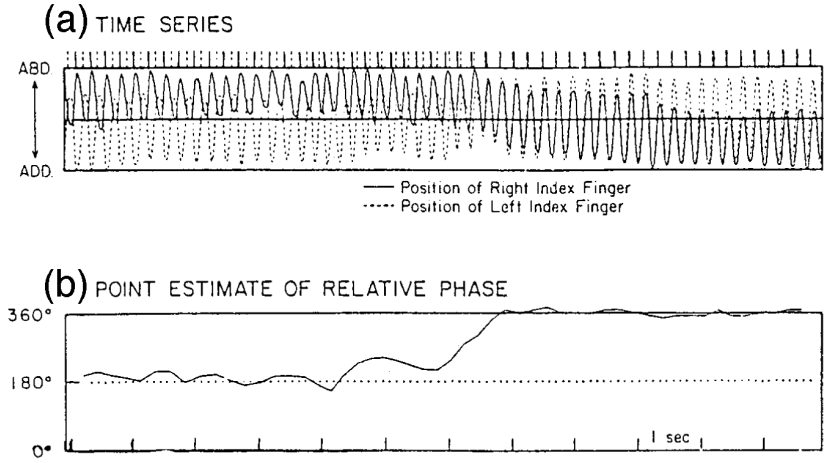

Figure 1.6: Left and right finger positions (a) and relative phase between the fingers (b) as function of time when the subject increases the frequency of motion (adapted from [71]).

---

can cause ultimately the activation of a large cluster of neurons. When the neuronal network state is near a critical point, the avalanche size distribution follows a power law. Power-law distributions of neuronal avalanches were first observed *in vitro* [76] and more recently *in vivo* [78].

Finally, there are also evidences that epileptic seizures, alpha and gamma oscillations, and the ultraslow oscillations of blood-oxygen-level dependent (BOLD) functional magnetic resonance imaging (fMRI) patterns emerge as a result of non-equilibrium phase transitions in the brain. Mean-field approaches for describing these phenomena were discussed in [79].

1.8 Epilepsy

The brain waves described above are associated with healthy behavior, like motor behavior, sensory processing, attention, spatial navigation, learning, memory and sleep [41, 80–85]. Nevertheless, healthy brain activity is usually irregular and uncorrelated, while brain diseases are often characterized by intervals of strongly correlated neuronal activity [86]. Indeed, it is now thought that certain neurological diseases are a consequence of transitions between rhythms [86]. In Alzheimer's disease, the most common neurodegenerative disorder, there is a shift of the power spectrum to lower frequencies and the coherence of fast rhythms decreases [87]. The second most common neurodegenerative disease is the Parkinson's disease, and in this case beta oscillations are abnormally strong [88]. Schizophrenia, sleep disorders and migraine are other examples which have been associated with altered rhythms and abnormal transitions [86, 89–91]. Yet, the most prominent example occurs in epilepsy [92].

Epilepsy is characterized by the recurrent occurrence of seizures. J. H. Jackson was the first to notice that epileptic seizures are represented in the brain by an uncontrolled

and paroxysmal discharge of a large population of neurons [93]. Depending on the type of epilepsy, the abnormal activity can be localized (focal) or generalized [94]. It is widely accepted that the emergence of epileptiform activity is a result of an unbalance between excitation and inhibition toward excitation, and indeed the easiest way to elicit experimental seizures is to block inhibition [95]. This view is also in agreement with the fact that seizures preferentially occur during slow-wave sleep or during the transition from waking to slow-wave sleep, because there is a strengthening in synaptic transmission [95]. Clinicians use EEG to evaluate epilepsy, and they observed three main characteristics: occurrence of a rhythmic pattern during the seizure, which often shows decreasing frequency and increasing amplitude, and the onset and termination of the pattern are unexpected [94, 96]. The last characteristic, the unpredictableness of onset and termination, is one of the main areas of theoretical research in epilepsy (see, for instance, Refs. [97, 98]). Indeed, if we assume that seizures occur due to phase transitions (or bifurcations, as it is more commonly studied in this field [92]), then it might be possible to predict their occurrence in advance by analysing critical phenomena that precede the transition [99, 100].

1.9 Synopsis of the thesis

This thesis is about a research on phase transitions and nonlinear phenomena in neuronal network models done from October 2010 until July 2014, at the Physics Department of Universidade de Aveiro. The present work is the result of a joint collaboration between me, Marinho Lopes, my supervisor, Prof. Alexander V. Goltsev, and Dr. KyoungEun Lee (Post-Doc researcher). Consequently, some of the presented figures in subsequent chapters were obtained by KyoungEun Lee as the result of simulations that she did (in all the cases there is a note in the caption of the figure stating this fact).

In this study, we report analytical and numerical results on an exactly solvable cortical model with stochastic excitatory and inhibitory neurons on a complex network [101, 102]. The analytical and numerical results are compared with simulations of the model and experimental data. We take advantage of the recent developments in network theory, in particular regarding the study of critical phenomena in networks [39], and we apply them to neuronal networks. We consider that neurons are stochastic because that is their nature, which should not be neglected [103, 104]. Neuronal noise is also taken into account, because the brain works as a noisy processor [105], where noise plays an important role [48, 49]. The advantage of our model is that it allows to study both analytically and numerically dynamics of neuronal networks, synchronization and other collective phenomena, non-equilibrium phase transitions between different dynamical states, critical phenomena that precede the transitions, the role of different parameters (which can influence single neuron dynamics or network topology), and even synaptic plasticity, which is related with learning and memory [106–109]. The understanding of these phenomena and mechanisms enables us to explore stochastic resonance in neuronal networks, to give a qualitative explanation of the Berger effect, to observe neuronal avalanches, to describe band-pass filter phenomena, to study the role of modular structure in signal detection, and to investigate

strong nonlinear phenomena similar to paroxysmal activity observed in epileptic brains. It is also important to note that our model has both features of micro-scale and macro-scale models. On one hand, simulations enable us to look into the dynamic behavior of single neurons; on the other hand, rate equations give us the behavior at the neuronal population level (which can also be compared with simulations).

Though this thesis is mainly focused on the analysis of the model proposed and discussed in Refs. [101, 102, 110–114], we also consider other models to study some specific questions. In particular, we compare our model with a similar model where the complex network is substituted by a fully connected network, where each neuron interacts with all other neurons in the network. We also examine dynamical regimes of a neuronal network composed of Izhikevich neurons [115] in order to compare with results obtained within our model. Moreover, we consider a toy model to investigate a subcritical Hopf bifurcation (the model is presented in [116]). The purpose of this last investigation is to uncover if such bifurcation shows critical phenomena preceding the bifurcation, because if it does not, then it is a candidate to describe absence epilepsy (*petit mal* epilepsy), which is a type of epilepsy that has been characterized by its unpredictableness. Indeed, "if warning occurs, the diagnosis of *petit mal* may be questioned" [117].

This thesis is organized in the following way. In Chapter 2, we review some basic concepts in neuroscience. We focus on how single neurons function and we describe the most paradigmatic models that have been developed to describe them. We also summarize the main tools available for neuroscientists to monitor brain activity, because if one wants to compare theoretical results with experimental data, it is necessary to understand what and how it is possible to compare. In Chapter 3, we present our model of neuronal networks. Assumptions and the role of different parameters are discussed. In Chapter 4, the model is analysed. We obtain a phase diagram and we show the different dynamical regimes. In Chapter 5, we find the different phase transitions and respective bifurcations that occur when the system transits from one dynamical state to another. We also discuss the repertoire of critical phenomena that signal the phase transitions. It is shown how these critical phenomena can result in a band-pass filter, and we suggest a qualitative explanation of the Berger effect on the basis of our model. In Chapter 6, we study stochastic resonance in our neuronal network model and we mimic the experiments of Gluckman *et al.* [51]. We further discuss signal detection in sensory systems and we demonstrate that modular structure improves signal processing. In Chapter 7, we propose a nonlinear mechanism based on our model to describe paroxysmal spikes observed in EEG from epileptic brains. Based on this assumption, we reveal early warnings for predicting epileptic seizures. In Chapter 8, we generalize our model to the case in which synapses can be modified over time due to mechanisms of synaptic plasticity. We show the enlarged repertoire of dynamical states that the neuronal network can display. Finally, we sum up conclusions in Chapter 9. Additionally, in Appendix A, we compare patterns of collective activity found in our model with results obtained in a network composed of Izhikevich neurons [115]. In Appendix B, we examine a toy model which has a subcritical Hopf bifurcation. Lastly, in Appendix C, we introduce a new model of neuronal networks similar to the model presented in Chapter 3, but in this case we consider a fully connected network.

Chapter 2

Basics of neuroscience

This chapter is organized in the following way. We start by presenting some general information about the brain. Then, we review how its main component works, the neuron. Subsequently, we examine the Hodgkin-Huxley model which is the most well-succeeded model in neuroscience. Despite its success, the model is not suitable for studying large neuronal networks because it requires massive computational power to be implemented. Next, we briefly present two simple models, the leaky integrate-and-fire model and the Izhikevich model which is used in Chapter 7. For the sake of completeness, we conclude this introductory chapter to neuroscience by mentioning the different experimental tools used to observe brain activity.

2.1 Neuron morphology

The brain is the organ that controls the body. It processes sensory inputs from the environment and orchestrates the behavior of the organism in order to promote its welfare. Perception, cognition, learning, memory, *etc.*, are accomplished by the brain using neurons and synapses (which connect the neurons). A human brain has about 10^{11} neurons and 10^{15} synapses (on average each neuron is connected to ten thousand other neurons). There is one other type of cell in the brain, the glial cells (glia). Per each neuron one can count 10 to 50 glial cells in the central nervous system of vertebrates. Glia is thought to not be involved in information processing [1], instead these cells play a critical role on supporting neurons, by insulating them, by promoting their efficiency in signal transmission, by regulating properties in the synaptic terminals, and by performing other crucial housekeeping tasks.

A neuron is a specialized cell in processing and transmission of electrochemical signals. Although there are at least a thousand different types of neurons, all of them share a similar structure (see Fig. 2.1). Most neurons have three morphologically defined parts: the cell body (soma), dendrites, and the axon. The soma performs the metabolic processes of the cell. It is where the nucleus is located which contains the genes. In turn, the genes orchestrate the synthesis of new proteins which play a central role on the function of the cell. The dendrites form tree-like branches and their purpose is to receive signals from

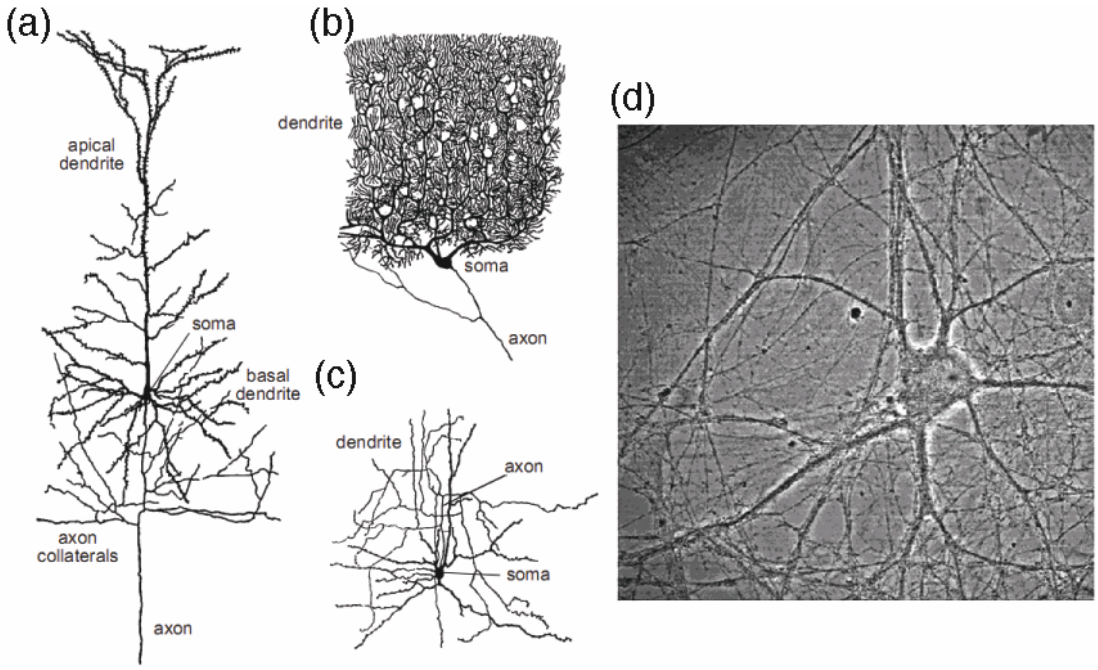

Figure 2.1: Diagrams of (a) a cortical pyramidal cell, (b) a Purkinje cell of the cerebellum, and (c) a stellate cell of the cerebral cortex. These images are magnified about 150 fold [118]. (d) Rat hippocampal neuron *in vitro* [119].

neighbouring neurons. The dendritic trees can gather information from thousands of cells or even from hundreds of thousands, like in the case of the Purkinje cell (see Fig. 2.1(b)) which is one of the biggest neurons found in the human brain. In contrast, the axon transmits the response of the neuron to other cells. While the dendrites are usually short, the axon is one long tube (its length ranges from 0.1 mm to 3 m).

The electrical signals that the axons convey are called *action potentials*. They are fast, transient and all-or-none impulses. They are initiated at the origin of the axon and conducted along the tube to its end without failure or attenuation. Near its terminal, the axon branches out to form connections with other cells. The site of connection is called *synapse* (actually, the neurons are not anatomically connected, there is a space between the cells, the *synaptic cleft*). The axon belongs to the *presynaptic cell*, the cell transmitting the signal, while the neuron receiving the signal is known as *postsynaptic cell*. The neuron receives signals from the *presynaptic terminals* which are located in the neuron's dendrites, or in the cell body, or even, in a few cases, in the axon (either at the beginning or at the end of the axon).

Neurons communicate via action potentials with their postsynaptic neighbours. These signals constitute the "code" by which the brain collects, processes and transmits information. Since all the signals are identical, their shape does not define the information they carry, but instead the pathway the signal travels in the brain codifies the information [1].

2.2 Neuron electrophysiology

In Chapter 1, we mentioned that Ramón y Cajal was the first to identify neurons as the elementary signalling units of the brain, the *neuron doctrine*. Actually, he was also able to understand one other fundamental principle, which is now known as the *principle of dynamic polarization* [1]. Electrical signals are conveyed only in one direction inside a neuron, from the presynaptic terminals to the end of the axon. In fact, it is not one signal, but a sequence of four: an input signal, a trigger signal, a conducting signal and an output signal. The trigger signal is related with the "trigger component" of the neuron that integrates all input signals and determines the conducting signal (and consequently the output signal).

At rest, neurons maintain a difference in the electrical potential between the inside and outside of the cell. A membrane makes the separation. The plasma outside the membrane is arbitrarily set as 0 V. In these conditions, the resting membrane potential is typically -65 mV (it can range from -40 to -90 mV depending on the neuron). The cell is polarized because there is a different distribution of ions on either side of the membrane that may be maintained due to the selective permeability of the membrane to specific ions. Ionic currents sustain and propagate the electrical activity of neurons. Four main species of ions are involved in these transmembrane currents: sodium (Na^+), potassium (K^+), calcium (Ca^{2+}), and chloride (Cl^-). Different concentrations of these ions inside and outside of a neuron result in electrochemical gradients. Transmembrane currents are allowed through ion channels and ion pumps. While ion channels can let specific ions to diffuse rapidly according to the electrical and concentration gradients, ion pumps try to maintain the gradients [120]. For instance, the $Na^+ - K^+$ pump sends out three Na^+ ions for every two K^+ ions pumped in [121]. Since the cell is polarized, positive and negative charges accumulate on both sides of the membrane producing an electric potential across the membrane, the *membrane voltage*. The ion channels can be either closed or open depending on the membrane potential, intracellular agents (second-messengers) and extracellular agents (neurotransmitters and neuromodulators).

Neurons are excitable cells. The membrane potential of these kind of cells can be quickly and significantly altered, and this transient change can be used as a communication mechanism. If the membrane potential is reduced by, for instance, 10 mV (from -65 mV to -55 mV), the membrane becomes more permeable to Na^+ than to K^+. Then, the influx of Na^+ ions makes the inside of the cell less negative relatively to the surrounding bath, and therefore the membrane potential decreases even further. This positive feedback mechanism results in an action potential. It lasts typically about one millisecond and reaches an amplitude of about 100 mV (see Fig. 2.2(a)). Action potentials are originated at the trigger zone, a region in the initial segment of the axon. Subsequently, the signal is conducted down the axon at a rate of $1 - 100$ Hz and as fast as 100 m/s. Action potentials are also commonly called *spikes*.

Depolarization is the process by which the membrane potential decreases. It enhances the probability of the cell to fire a spike and is therefore *excitatory*. *Hyperpolarization* is the opposite process in which the membrane potential increases, it is *inhibitory*. In this

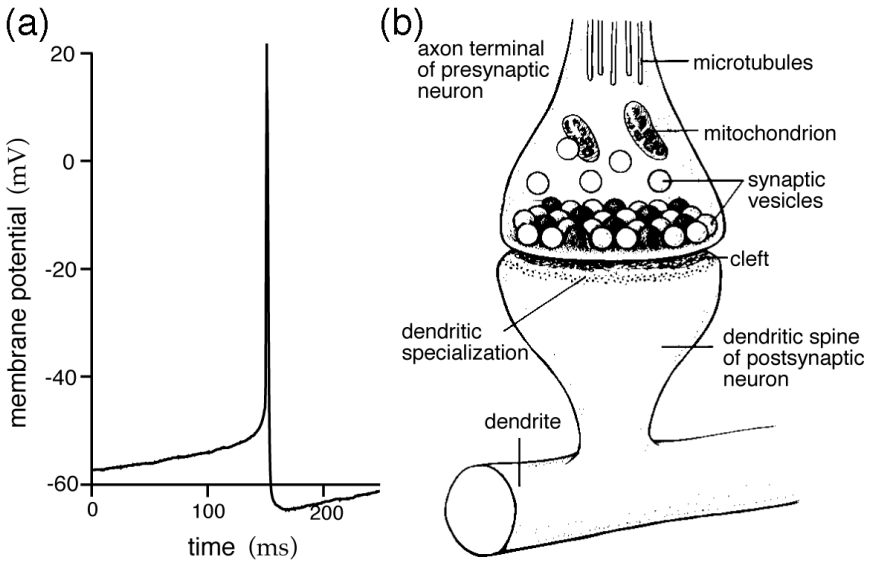

Figure 2.2: (a) An action potential recorded from a rat neocortical pyramidal cell *in vitro*. (b) Diagram of a synapse. The neurons do not touch, there is a "cleft". The axon terminal of the presynaptic neuron appears from the top of the figure, while the dendrite of the postsynaptic neuron is represented below. When an action potential arrives at the axon terminal, it makes the synaptic vesicles to release neurotransmitters into the cleft, which then bind to receptors on the dendritic spine [118].

---

case, the likelihood of firing is reduced. In theoretical neuroscience it is widely assumed that neurons can be either excitatory or inhibitory depending on how they influence their postsynaptic neighbours (either depolarizing or hyperpolarizing them, respectively). It is called the Dale's principle [122]. An example of an excitatory neuron is the pyramidal cell in the cortex (see Fig. 2.1(a)), and the stellate cell (see Fig. 2.1(c)) is an example of an inhibitory neuron. In both cases, a spike fired by a neuron promotes the release of neurotransmitters by the synaptic vesicles into the synaptic cleft (see Fig. 2.2(b)). In turn, the neurotransmitters bind to receptors at the postsynaptic side of the synapse, where it opens ion channels. Inhibition or excitation are not determined by the neurotransmitters, but by its receptors. For instance, the neurotransmitter dopamine can be both involved in depolarization or hyperpolarization depending on the receptor of the postsynaptic neuron.

As mentioned above, action potentials are very important because they are the only way that neurons can communicate over long distances. They are actively regenerated along axon processes without attenuation in contrast with potential fluctuations that are attenuated over distances of about 1mm or less. The positive feedback mechanism that results in a spike is only triggered if the input is larger than a threshold. This threshold depends on the recent activity history of the neuron. After an action potential is fired, there is an absolute refractory time during which the neuron is not able to fire another spike. Then, there is a refractory time, in which the firing probability is low. All these characteristics vary from neuron to neuron, because, for instance, different neurons have

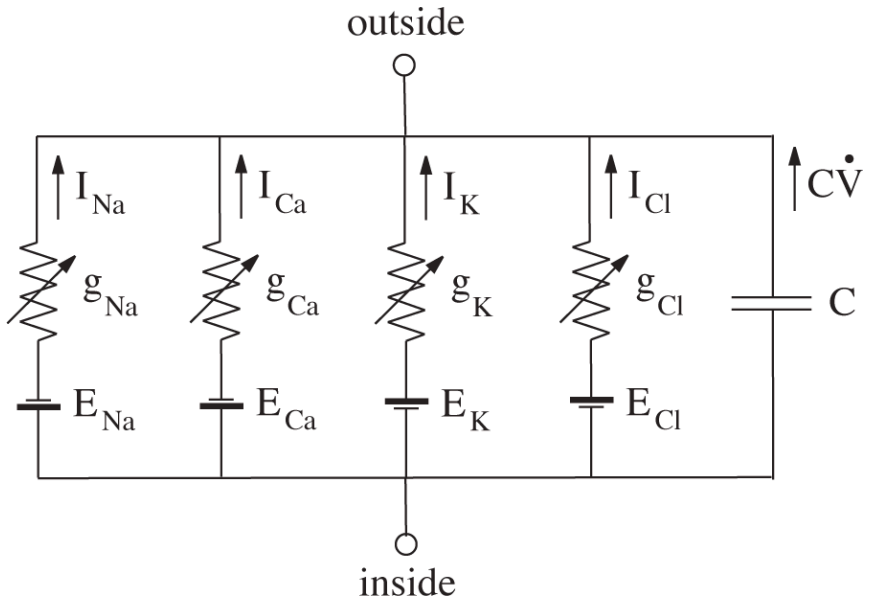

Figure 2.3: Equivalent circuit of a patch of a neuron's membrane [121]. Inside and outside refer to the intracellular and extracellular medium, respectively.

different ion channels. On the other hand, synapses can be modified over time due to synaptic plasticity, which in turn influences on the efficacy of neuronal communication. Synapses change through experience and learning (besides development and regeneration).

Though there are differences among neurons, the general mechanisms of electrical signalling are remarkably similar [1]. If we understand the molecular mechanisms involved in one kind of neuron, then we basically comprehend these mechanisms in most kinds of neurons. That is why the work of Hodgkin and Huxley is so important in neuroscience.

2.3 Hodgkin-Huxley model

Alan Hodgkin and Andrew Huxley introduced a conductance-based model to describe how currents depend on the potential in the squid giant axon. They used the giant axon of a squid because it is a very large axon (up to 1 mm in diameter). The respective neuron is responsible for controlling part of the water jet propulsion system, which is used by the squid when it wants to move fast through the water (to escape from predators, for instance). In their pioneering study in 1952 [14], Hodgkin and Huxley inserted voltage clamp electrodes inside of the axon and they determined that the squid giant axon has three major currents: a voltage-gated persistent K^+ current, a voltage-gated transient Na^+ current, and an Ohmic leak current (which is mainly a Cl^- current).

Besides the currents distinguished by Hodgkin and Huxley, one can also consider a Ca^{2+} current. The electrical properties of the membrane can be represented by an equivalent

circuit as in Fig. 2.3. The Kirchhoff's law dictates the equation,

$$C\dot{V} = I - I_{Na} - I_{Ca} - I_K - I_{Cl}, \tag{2.1}$$

where C is the membrane capacitance ($C \approx 1.0\mu F/cm^2$), V is the membrane potential, I represents additional current sources or sinks (for example, synaptic current or injected current via an electrode), and I_{Na}, I_{Ca}, I_K and I_{Cl} are the ionic currents. $\dot{V}$ denotes the time derivative of the membrane potential. The ionic currents depend on their respective conductances,

$$I_X = g_X(V - E_X). \tag{2.2}$$

Here X is one of the ionic species, g_X is the conductance of ion X, and E_X is the equilibrium potential of this current (Nernst equilibrium potential). For example, when $V = E_{Na}$, the net Na^+ current is zero. Note that inward currents increase the membrane potential (depolarization), whereas outward currents make it more negative (hyperpolarization).

In general, the ionic currents of neurons are not Ohmic, which means that the conductances are not constant (in the particular case of the squid giant axon, there are only two major currents, Na^+ and K^+, and the Cl^- can be considered Ohmic).

Typically, the conductances depend on the membrane potential V and on time. The conductance of an ion is proportional to the number of open ion channels for that ionic specie. The proportion p of open ion channels is

$$p = m^a h^b, \tag{2.3}$$

where m characterizes the activation gates, and h describes the deactivation gates. a and b are the numbers of activation and deactivation gates, respectively. Some ion channels only have activation gates ($b = 0$), which means they do not inactivate, and in this case the ionic current is called persistent (like the K^+ current in the squid giant axon). In contrast, when $b \neq 0$ the channels have inactivation gates and they result in transient currents (as the Na^+ current in the squid giant axon). The dynamics of the activation variable is described by the differential equation

$$\dot{m} = \frac{m_\infty(V) - m}{\tau(V)}, \tag{2.4}$$

where $m_\infty(V)$ is the voltage-sensitive steady-state activation function and $\tau(V)$ is the time constant. These two functions can be measured experimentally. The inactivation variable h can also be described by an equivalent first-order differential equation, with the respective voltage-sensitive steady-state inactivation function and time constant.

In general, all conductance-based models are regarded as Hodgkin-Huxley models. They usually consist of at least four equations and tens of parameters that describe the membrane potential and the ionic currents (and their activation and inactivation variables). These models are important because the parameters are biologically meaningful and measurable, and they allow us to obtain insights about biophysical processes related to single neuron dynamics (synaptic integration, for instance). Unfortunately, the model is very expensive to implement, requiring massive computational power when the purpose is to model the dynamics of hundreds or thousands of neurons [121, 123].

2.4 Simple model of spiking neurons

The leaky integrate-and-fire (I&F) model is the most widely used model in computational neuroscience, because it is the simplest and the cheapest in computational cost [123]. The membrane potential v is described by the first-order differential equation,

$$\dot{v} = I + a - bv, \tag{2.5}$$

where I is the input current, and a and b are parameters. Additionally, when $v \geq v_{th}$, the membrane potential is assumed to fire a spike, and v is reset to a potential c. The threshold value v_{th} and reset value c are also parameters of the model.

The I&F neuron is an integrator. It integrates the input and the likelihood of firing increases as the frequency of the input becomes larger. It also displays tonic spiking, that is, the neuron fires a train of spikes while excited by an input (if the input is a dc current, the neuron fires spikes with constant frequency). Many neurons present this kind of behavior, like the regular spiking (RS) excitatory neurons, and fast spiking (FS) inhibitory neurons in the cortex [124, 125]. Moreover, it is Class 1 excitable (like RS neurons), which means that the frequency of tonic spiking depends on the amplitude of the input. Indeed, Class 1 excitable neurons are good predictors of the strength of the stimulation due to this dependence [123]. In contrast, Class 2 excitable neurons are unable to fire low-frequency spikes. They can either fire trains of spikes with large frequency (say, 40 Hz), or be inactive [123].

This simple model can only describe the three neuro-computational features mentioned above. Izhikevich distinguishes 20 prominent features of biological spiking neurons in [123]. Obviously, the Hodgkin-Huxley model exhibits all properties (at different parameters). In 2003, Izhikevich proposed a simple model of spiking neurons [115] that can also show all these features [121, 123], despite being about one hundred times faster in simulations than the Hodgkin-Huxley model. The downside is that the Izhikevich neuron is not biophysically meaningful as the Hodgkin-Huxley neuron.

The spiking model by Izhikevich [115, 121, 123] consists of two differential equations,

$$\dot{v} = 0.04v^2 + 5v + 140 - u + I, \tag{2.6}$$

and

$$\dot{u} = a(bv - u), \tag{2.7}$$

where v and I are once again the membrane potential and the current, respectively. The values were chosen so that v has mV scale and time has ms scale. u represents a membrane recovery variable, which accounts for the dynamics of the ionic currents that provide negative feedback to v. When the membrane potential reaches 30 mV, v is reset to c and u is reset to $u + d$. a, b, c, and d are the parameters of the model. Note that the value 30 mV is not the threshold for generating a spike, but its apex. The threshold is not fixed, it depends on the history of the membrane potential, like in real neurons.

This simple model of spiking neuron has been used to study large neuronal networks (see, for example, Ref. [38]), in order to investigate collective phenomena and, particularly, brain rhythms. We use this model in Chapter 7.

Figure 2.4: Multiple electrodes are placed on the scalp in order to monitor cerebral activity. The recorded activity is called electroencephalogram [41].

2.5 Monitoring brain activity

On one hand, theoretical neuroscientists model single neurons and populations of neurons; on the other hand experimentalists and clinicians measure activity of real neurons. For a theoretician, it is important to know what are the tools that experimentalists use in order to be able to construct models that can be compared to experimental measurements (or alternatively, the theoretician should know what is the experimental technique that is more similar to his model). Here, we briefly refer some of the most important tools used to monitor brain activity following Ref. [41].

We have already mentioned the electroencephalogram (EEG), which continues to be one of the most used experimental methods to record brain activity (specially among clinicians). It is noninvasive (the electrodes are placed on the scalp, see Fig. 2.4) and it records voltage changes on the scalp due to neuronal activity. The spatial resolution is low and the determination of the specific source of the electrical field is a challenge. Therefore, it is not used to determine the spatial location of neural activity related to a certain thought, for instance. Nevertheless, the technique is good enough to determine whether the brain is alive or dead, or whether it is awake or sleeping. It is also possible to notice a brain seizure in a EEG, as discussed in Chapter 1. On the good side, the temporal resolution is excellent. Thus, EEG is adequate to measure average brain activity at the macro-scale with fine time resolution. (Increasing the number of electrodes on the scalp enhances the spatial resolution only up to a limit, at which nearby electrodes measure approximately the same activity.)

When spatial information is relevant, one uses extracellular electrodes implanted in the brain. This is an invasive procedure, because it requires surgery to implant the electrodes. The electrodes can be used either to measure action potentials of single neurons or to record synaptic events of populations of hundreds or thousands of neurons (local field potential). They can be separated because the time scales are different. Action potentials appear at frequencies above 300 Hz and local field potentials are measured below 300 Hz [126]. These techniques are used, for instance, when it is necessary to localize a precise anatomical structure, which is responsible for a certain abnormality, in order to surgically remove it. Instead of depth electrodes, it is also possible to use subdural grid recordings. In this case, the electrodes are placed on the surface of the brain. It still requires surgery, but it is less invasive, and therefore less risky than the deep wire electrodes. These recordings are called electrocorticograms and they provide a signal with amplitude an order of magnitude larger than the EEG. The spatial resolution is also improved, because the electrodes capture activity from a smaller brain region.

Obviously, invasive procedures are only used in unhealthy people and experimental animals. If one wants to improve spatial resolution while keeping the remarkable temporal resolution of EEG and without using an invasive procedure, one can use a magnetoencephalogram (MEG). In this case, instead of monitoring electric fields, the technique records magnetic fields. The magnitude of the magnetic fields generated by neuronal activity is very small (smaller than 0.5 picotesla), but fortunately it is possible to record these magnetic fields with a SQUID (superconducting quantum interference device). Like with EEG, the MEG also uses many sensors around the head to improve spatial resolution. The advantage of MEG is that no distortion occurs in the skull and scalp allowing a better spatial resolution than EEG. Interestingly, MEG and EEG record different types of activity, because MEG favors the specific currents (with specific directions) that generate the detected magnetic fields.

Functional magnetic resonance imaging (fMRI) also detects magnetic fields, but the method is different from MEG. First, note that fMRI and MRI are different methods. In the case of magnetic resonance imaging, a short pulse of a strong magnetic field aligns the dipoles of hydrogen atoms, which subsequently return to their original alignment by releasing energy that is detected with a "receiver coil" (placed around the head). The technique provides consecutive brain slices, because the electromagnetic field is injected consecutively into single planes. MRI provides much better images of the brain than X-ray and other scanning technologies, but it does not give information about neuronal activity. In contrast, fMRI does. Since neurons consume a lot of energy when they are active, and this process is related with oxygen consumption, then it is possible to assess neuronal activity by measuring local magnetic field inhomogeneities. This method is called blood-oxygenation-level-dependent (BOLD), and it is what gives indirect information about neuronal activity in fMRI. Functional MRI has much better spatial resolution than EEG, however the temporal resolution is much worse.

In contrast with fMRI, which does not give information about what process is consuming energy and therefore it does not provide evidences about the underlying mechanisms of neuronal activity, positron emission tomography (PET) is intrinsically related with the

use and binding of specific neurotransmitters, chemicals, and drugs in the brain. The PET scan depends on a radiolabeled compound which is injected in the subject (or inhaled). The radioactive atoms accumulate in specific locations and decay, releasing positrons. Subsequently, a positron collides with an electron, and two photons result from their annihilation. Finally, the sensor detects the photons and a three-dimensional image is constructed. Unfortunately, the temporal and spatial resolutions of PET are worse than fMRI.

In the last years, optic methods have been developing fast, in particular tools to obtain information about the structure of the brain, like the method CLARITY [127]. Here, we focus on methods used to monitor brain activity. Neuronal activity affects the optical properties of nerve cells, and therefore it is possible to characterize brain activity based on the light reflected and absorbed by the brain tissue. If the camera has sufficiently good temporal resolution, it is possible to observe in real time neurons in action. However, the interpretation of the detected signals is still a challenge. Moreover, it is only appropriate to study the surface of the brain. Temporal and spatial resolution can be improved by using dyes that bind to the membrane of neurons and then act as a transducer of the membrane potential into optical signals (unfortunately, it does not allow to distinguish different neurons, neither separates the input from the output of neurons).

Optic methods can also give information about what is happening inside the brain, in particular using the multiphoton laser scanning microscopy (m-PLSM). This method uses compounds to change the fluorescence of physiological relevant targets to neuronal activity and applies very strong LASER pulses to the brain. Then, a microscope collects the fluorescence photons that are emitted by the targets. (The pulses are very short, 100 femtosecond, otherwise the LASER would fry the brain.) This technique provides high-resolution three-dimensional images. However, there is a trade-off between temporal and spatial resolution, because the scanning beam is a moving point, and so the targets are affected only when the beam moves across them.

Despite the existence of all these techniques, when the goal is to understand the biophysics of single neurons and their collective behavior at the population level, one has to carry out experiments in brain slice preparations *in vitro*. Recordings from individual neurons *in vitro* provide the best spatial resolution available (using, for instance, a microscope and an infrared camera). It allows to characterize pharmacological specificity and even molecular properties of the neurons. There are several techniques to study single neurons [41], for example, the patch-clamp technique allows to investigate single ion channels in the membrane of a neuron. One can also use a microelectrode located in the vicinity of the soma to measure action potentials. In contrast with experiments *in vivo*, in this case the experimentalist can control the extracellular environment to further understand how neurons function. The main drawback is that it compromises the circuits of the brain (and consequently the activity patterns). One should also notice that the neurons will eventually die, thus there is a time limit during which the experiments are possible (usually several hours).

In this chapter, we did not intend to give a full review about neuronal physiology, theoretical models in neuroscience, and experimental tools available to monitor neuronal activity. Instead, we briefly presented the main concepts that are necessary to take into

account to understand the model that is introduced in the next chapter. Indeed, to comprehend collective phenomena between thousands of neurons, it is unnecessary to describe in detail single neuron dynamics [75, 118]. "What makes the brain a remarkable information processing machine is not the complexity of its neurons, but rather its many elements and, in particular, the complexity of connections between them" [1].

Chapter 3

A neuronal network model

3.1 Introduction

In statistical physics, exactly solved models largely help us to understand phase transitions and critical phenomena [128]. Unfortunately, even simple versions of neuronal networks composed of integrate-and-fire neurons are very complex for an analytical consideration [129–136]. According to recent investigations [75, 137, 138], the global activation of living neuronal networks induced by a stimulus can be explained on the basis of the concept of bootstrap percolation [139], a version of a cellular automata [140], without going into details of single neuron dynamics. In this chapter we introduce an exactly solvable cortical model with excitatory and inhibitory neurons on complex networks that allows us to study phase transitions, and critical phenomena accompanying the transitions [101, 102, 114]. In contrast with deterministic models of single neuron dynamics [115, 123], we consider stochastic neurons. The stochastic behavior might be caused by an intrinsic noise within neurons [103], for example, ion channel stochasticity [104]. Moreover, we also take into account neuronal noise, since noise is ubiquitous in the brain and strongly influences its function [48, 49].

3.2 Network structure

We consider neuronal networks composed of stochastic excitatory and inhibitory neurons. We use Dale's principle [122]: excitatory (inhibitory) neurons depolarize (hyperpolarize) their postsynaptic neighbours. Recently, the importance of Dale's principle for dynamics and pairwise correlations in neuronal networks was discussed by Kriener *et al.* [141]. The network has N neurons, $N^{(e)} = g_e N$ neurons are excitatory and $N^{(i)} = g_i N$ neurons are inhibitory ($g_e + g_i = 1$). The neurons are connected by directed edges (synapses). The network is defined by an adjacency matrix a_{nm} where $n, m = 1, 2, \ldots, N$. $a_{nm} = 1$ if there is an edge directed from neuron n to neuron m, otherwise $a_{nm} = 0$. Moreover, the network is weighted. We assume that efficacies (weights) of synaptic connections from excitatory and from inhibitory neurons are uniform and equal to J_e ($J_e > 0$) and J_i ($J_i < 0$),

respectively.

For simplicity, we consider that neurons are connected at random with the probability c/N where c is the mean number of synaptic connections (input and output connections). The probability $B_n(c)$ that a neuron is connected to n presynaptic neurons is given by the binomial distribution,

$$B_n(c) = C_n^N \Big(\frac{c}{N}\Big)^n \Big(1 - \frac{c}{N}\Big)^{N-n}, \tag{3.1}$$

where C_n^N is the binomial coefficient,

$$C_n^N = \frac{N!}{(N-n)!n!}. \tag{3.2}$$

In the infinite size limit, $N \to \infty$, the binomial distribution approaches the Poisson distribution,

$$P_n(c) = \frac{c^n e^{-c}}{n!}. \tag{3.3}$$

This neuronal network has the structure of a directed classical random graph (Erdős-Rényi network), a sparse random uncorrelated directed network. These networks are often considered as a good approximation to real networks [20–22]. This network is locally tree-like and has small-world properties [20–22] similar to those found in brain networks [23]. It is small-world because the mean shortest distance increases as the logarithm of the number of nodes (neurons), in contrast to a three dimensional system where the mean shortest distance increases as the cube root of the size. The advantage of these networks is that they can be studied analytically using mean-field theory, and they can be easily modelled for simulations. Though the mean-field approach is based on the tree-like approximation, it takes into account exactly the heterogeneity of networks and large feedback loops [39]. The drawback is that they do not present high clustering coefficient due to their tree-like structure and do not have degree correlations like real neuronal networks [23, 24]. Both clustering coefficient and degree correlations are zero in the infinite size limit. Nevertheless, in many cases low clustering and weak degree-degree correlations do not qualitatively change the dynamics of the complex network [39]. Understanding the role of clustering and degree correlations on the dynamics of systems with complex network structure is an open problem in the theory of complex networks [39, 142, 143]. Finally, real neuronal networks have a scale-free distribution [23, 24], instead of a Poisson degree distribution. Nevertheless, the model under consideration was also been studied using a scale-free degree distribution [114], and the dynamical properties were similar to the properties presented in the following chapters.

3.3 Single neuron dynamics

Our neurons are tonic, i.e., they fire a train of spikes with constant frequency while a dc input current is presented. As mentioned in Chapter 2, real neurons are either of Class 1 or Class 2. Class 1 excitable neurons show a continuous transition from a silent state to

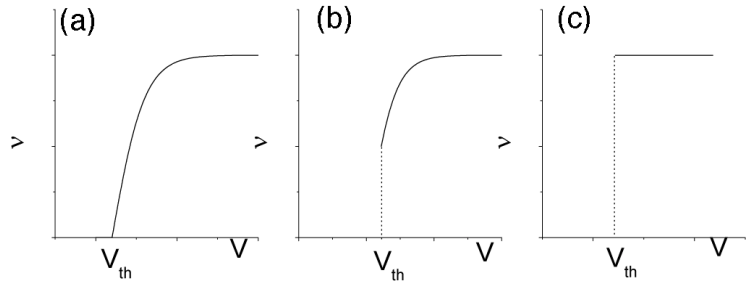

Figure 3.1: Firing rate ν versus input V. (a) Class 1 excitability. (b) Class 2 excitability. (c) Step function approximation that we use in our model (adapted from [101]).

---

an active state with low firing rate when the input V is suprathreshold (see Fig. 3.1(a)), whereas Class 2 excitable neurons present a discontinuous transition (see Fig. 3.1(b)). Instead, we assume that the firing frequency $\nu(V)$ is the Heaviside function,

$$\nu(V) = f\Theta(V - V_{th}), \tag{3.4}$$

where V_{th} is the threshold of the neuron, above which it fires (see Fig. 3.1(c)). The frequency f is the same for both excitatory and inhibitory neurons and it is independent on the input V. We also assume that V_{th} does not depend on prior activity of the neuron, though it does in biological neurons [123].

Since, the neurons can be either regular firing (active) or silent (inactive), we define the binary variable $s_n(t)$. When $s_n(t) = 1$, the neuron n is active at time t. If the neuron n is inactive at time t, $s_n(t) = 0$. In our model, this binary variable plays an auxiliary role (in contrast with the binary McCulloch-Pitts neurons [12]).

Neurons receive delta-like spikes from active presynaptic neighbours. Spikes mediate the interaction among neurons. The total input $V_n(t)$ (post-synaptic potential) of a neuron n at time t is the sum of all spikes sent from its presynaptic neurons,

$$V_n(t) = \tau f \sum_m a_{mn} J_{mn} s_m(t), \tag{3.5}$$

where τ is the integration time during which the neuron integrates the input, $[t - \tau, t]$. The input $V_n(t)$ is a number of spikes, rather than a potential. The equation is self-explanatory: it considers the sum of the outputs of all m presynaptic neighbours of n (a_{mn}), both from the excitatory ($J_{mn} = J_e$) and inhibitory ($J_{mn} = J_i$) population, that are active at the moment ($s_m(t)$). Active excitatory (inhibitory) presynaptic neurons provide positive (negative) inputs to postsynaptic neurons, because $J_e > 0$ ($J_i < 0$). Each neuron contributes with τf spikes during the integration time τ. If $\tau f \ll 1$ and spike emission times of neurons are uncorrelated, then during the time interval $[t - \tau, t]$, each active presynaptic neuron contributes to $V_n(t)$ either one spike with probability τf or none with probability $1 - \tau f$. The results are qualitatively the same either for $\tau f > 1$ or $\tau f < 1$ [101].

Besides spikes from active presynaptic neurons, there is one other contribution for the input $V_n(t)$ from neuronal noise (more details about the noise on the next section). Thus, we can rewrite Eq. (3.5):

$$V_n(t) = kJ_e + lJ_i + nJ_n, \tag{3.6}$$

where k and l are the number of spikes from active presynaptic excitatory and inhibitory neurons, respectively. n is the number of spikes arriving during the time interval $[t-\tau, t]$ from noise and J_n is their amplitude.

We consider stochastic neurons such as those of [144, 145]. It means that the response of a neuron to an input is a stochastic process. Such stochastic behavior might be caused by cellular noise and intensive bombardment by random spikes [103, 104]. Thus, the state $s_n(t)$ of a neuron n is a dynamical variable that obeys to the following rules:

- If the input $V_n(t)$ to an inactive excitatory (inhibitory) neuron n is at least the threshold V_{th}, then this neuron is activated with probability $\mu_e\tau$ ($\mu_i\tau$) and fires spikes.

- An active excitatory (inhibitory) neuron n is inactivated with probability $\mu_e\tau$ ($\mu_i\tau$) if $V_n(t) < V_{th}$.

In this model, the rates μ_e and μ_i are the reciprocal first-spike latencies of excitatory and inhibitory neurons, respectively. (The first-spike latency of a neuron is the time interval from the onset of a stimulus to the time of appearance of the first spike.) For simplicity, we assume that μ_e and μ_i are constant and do not depend on the input. Notice that we consider the probabilities of activation and inactivation equal. In general they could be different, but the results would be qualitatively the same [101]. These rates can be found from statistical analysis of activation and inactivation events in neuronal networks. Alternatively, an experimentalist can stimulate a presynaptic neuron and then measure the probability of activation of a postsynaptic neuron through the analysis of the distribution of first-spike times [101].

3.4 Neuronal noise

Our model takes into account noise, which plays an important role in brain dynamics [48, 49, 146, 147]. Random spikes represented by Dirac delta functions bombard the neurons and produce an input,

$$V(t) = \sum_i J_n \delta(t - t_i), \tag{3.7}$$

where t_i are the arrival times of spikes and J_n is their amplitude. This kind of random input is so-called shot noise. According to Schottky's result [148], in the case of the Poisson distribution of interspike intervals, the power spectral density $S(\omega)$ is proportional to the mean frequency of spikes ω_n:

$$S(\omega) = 2J_n^2\omega_n. \tag{3.8}$$

The flow of random spikes bombarding neurons represents a combined effect of synaptic noise (spontaneous release of neurotransmitters) and stimuli coming from other areas of the brain. For example, neurons in the thalamus and in the cerebral cortex form recurrent loops [149]. The study of the spontaneous activity in neocortical slices provides evidences of both sources of noise [150]. Which one is the most relevant is unimportant for our model. We assume that the probability of a neuron to receive n random spikes during the integration time τ is Gaussian,

$$G(n) = G_0 e^{\frac{-(n-\langle n\rangle)^2}{2\sigma^2}}, \tag{3.9}$$

where G_0 is the normalization constant,

$$G_0 = \Big(\sum_{n=0}^{\infty} e^{\frac{-(n-\langle n\rangle)^2}{2\sigma^2}}\Big)^{-1}, \tag{3.10}$$

$\langle n\rangle = \omega_n \tau$ is the mean number of spikes arriving during the time interval τ, and σ^2 is the variance. We use $\langle n\rangle$ as the control parameter that characterizes the shot noise intensity.

3.5 Rate equations

The behavior of the cortical model is described by the fractions $\rho_e(t)$ and $\rho_i(t)$ of active excitatory and inhibitory neurons, respectively, at time t,

$$\rho_a(t) = \frac{1}{N^{(a)}} \sum_n s_n^{(a)}(t), \tag{3.11}$$

where $a = e, i$ for excitatory and inhibitory neurons, respectively. We call these fractions "activities". Moreover, $\rho_e(t)$ ($\rho_i(t)$) represents the probability to choose at random an active excitatory (inhibitory) neuron at time t from the excitatory (inhibitory) population (in order to simplify equations, from now on we omit the time dependence of the activities, i.e., $\rho_a(t) \to \rho_a$). We also define the probability $\Psi_a(\rho_e, \rho_i)$ that a randomly chosen neuron in population a that has an input equal or larger than the threshold V_{th} at time t.

The stochastic rules presented above allow us to derive rate equations for the activities ρ_e and ρ_i. The rate $\dot{\rho_a} \equiv d\rho_a/dt$ is incremented by

$$(1 - \rho_a)\Psi_a(\rho_e, \rho_i)\mu_a, \tag{3.12}$$

which is the probability of an inactive neuron to have an input larger than the threshold ($\Psi_a(\rho_e, \rho_i)$) that becomes active at the rate μ_a. Similarly, the activity is decreased by those neurons that become inactive:

$$-\rho_a(1 - \Psi_a(\rho_e, \rho_i))\mu_a. \tag{3.13}$$

Thus, summing both contributions,

$$\dot{\rho_a} = (1 - \rho_a)\Psi_a(\rho_e, \rho_i)\mu_a - \rho_a(1 - \Psi_a(\rho_e, \rho_i))\mu_a, \tag{3.14}$$

we obtain a rate equation,

$$\frac{\dot{\rho_a}}{\mu_a} = -\rho_a + \Psi_a(\rho_e, \rho_i). \tag{3.15}$$

Equation (3.15) comprises two rate equations, one for the activity of the excitatory population and another for the activity of the inhibitory population.

In the case $\tau f \ll 1$, as mentioned above, during the integration time τ, a neuron receives only one spike or none from active presynaptic neighbours with probability τf or $1 - \tau f$, respectively. Assuming that there is no phase correlation (which is a common assumption at low activity rates [129]), the probability that during τ a neuron receives m spikes from n uncorrelated tonic spiking presynaptic neurons is

$$C_m^n (\tau f)^m (1 - \tau f)^{n-m}. \tag{3.16}$$

Note that if spikes fired by presynaptic neurons are correlated, Eq. (3.16) is invalid and the spikes can activate a postsynaptic neuron more effectively. Poisson spike trains were found in recordings from neurons *in vivo* and *in vitro* [49]. Since we are considering a classical random graph, we know that the probability of choosing at random an active excitatory or inhibitory neuron follows the Poisson distribution $P_n(g_a \rho_a c)$, where the mean number corresponds to the product of the mean number of neurons (c) of population a (g_a) that are active (ρ_a). Thus, a neuron receives m spikes from n neurons of population a with probability:

$$\sum_{n=m}^{\infty} P_n(g_a \rho_a c) C_m^n (\tau f)^m (1 - \tau f)^{n-m} = P_m(g_a \rho_a c \tau f), \tag{3.17}$$

and we find

$$\begin{aligned} \Psi_e(\rho_e, \rho_i) &= \Psi_i(\rho_e, \rho_i) = \Psi(\rho_e, \rho_i) \\ &= \sum_{k,l,n=0}^{\infty} \Theta(kJ_e + lJ_i + nJ_n - V_{th}) P_k(g_e \rho_e \tilde{c}) P_l(g_i \rho_i \tilde{c}) G(n), \end{aligned} \tag{3.18}$$

where $\tilde{c} = c\tau f$. The Heaviside function $\Theta(x)$ accounts for the condition that the input, Eq. (3.6), must be at least the threshold V_{th}. $P_k(g_e \rho_e \tilde{c})$, $P_l(g_i \rho_i \tilde{c})$, and $G(n)$ are the probabilities that, during the time interval τ, a randomly chosen neuron receives k spikes from excitatory neurons, l spikes from inhibitory neurons, and n spikes from shot noise. The function $\Psi(\rho_e, \rho_i)$ condenses all information regarding network structure, shot noise, and the firing rate versus input relationship of single neurons. Equations (3.15) and (3.18) are valid in the infinite size limit $N \to \infty$, assuming that activities are changed slightly during the integration time τ. These equations are similar to the Wilson-Cowan equations [18, 19], who considered the dynamics of neuronal populations with excitatory and inhibitory interactions. However, there are important differences between the two models. Wilson and Cowan used a deterministic phenomenological model, postulating that a population response function have a sigmoid shape [18, 19]. The mean field approach of Wilson and Cowan neglects spatial heterogeneity and assume that all neurons are subject to the

same average excitation and inhibition from the excitatory and inhibitory populations, respectively. In contrast, we define stochastic rules that govern the behavior of individual neurons and we take into account heterogeneity. The function $\Psi(\rho_e, \rho_i)$ plays the role of the response function in the Wilson Cowan model. It also has sigmoid form (as we show in the next chapter), however it is not an assumption but a consequence of the ingredients considered. Moreover, in our model we can study both single neuron and population dynamics, whereas the Wilson-Cowan model is restricted to population dynamics. Finally, Wilson and Cowan used as relevant variables the fractions of excitatory and inhibitory neurons that become active per unit of time ($g_e\dot{\rho}_e$ and $g_i\dot{\rho}_i$, within our notation), whereas we use the activities ρ_e and ρ_i.

Our activities ρ_e and ρ_i can be roughly compared to measurements of brain activity. Since we consider random neuronal networks, it immediately implies that we are not describing the entire brain which at the macro-scale is clearly not random, as explained in Chapter 1. Instead, we are analysing an intermediate mesoscale at the level of thousands to hundreds of thousands of neurons that constitute columns (or minicolumns) inside brain regions [35]. Therefore, the activities ρ_e and ρ_i are more closely related to measurements of local field potentials. However, one should notice that local field potentials depend on the spatial structure of the nervous tissue, which is absent in our model. Indeed, the translation between local field potentials into neuronal activity similar to our variable ρ_a is an open problem in neuroscience [151].

3.6 Parameters

Throughout this thesis we consider a set of parameters which we assume constant in most of the cases. As mentioned in Chapter 2, the mean degree c in the brain is about 10^4 [1]. Here, we use $c = 1000$ because of computational restrictions (the problem becomes computationally heavier as c is increased). Nevertheless, we expect that the results must be qualitatively the same though c is smaller than in real neuronal networks, an assumption that is supported by results obtained with smaller mean degrees [101]. As we present in the next chapter, the model can be analysed by solving the Eqs. (3.15) and (3.18) and also through simulations. In the case of simulations, the network has finite size, and we consider in most cases a number of neurons $N = 10^4$ or $N = 10^5$ (which are reasonable as we discuss later on, when we compare simulations with numerical results of the model). In the brain, excitatory neurons are usually in majority comparing to inhibitory neurons, ranging from 70% up to 85% [75, 131]. We use $g_e = 0.75$, and consequently $g_i = 0.25$. We introduce a dimensionless activation threshold $\Omega \equiv V_{th}/J_e$. Ω is of the order of $15 - 30$ in living neuronal networks [75, 137, 138] and about $30 - 400$ in the brain. We use the threshold $\Omega = 30$. We consider $1/\mu_e \equiv 1$ as time unit and $J_e \equiv 1$ as input unit. Following [129], we choose $J_i = -3J_e$ (there are physiological reasons for the fact that inhibitory efficacies are usually larger than excitatory efficacies [152]). Note that we have $J_i g_i = J_e g_e$ which means that our network is balanced (provided that $\rho_e = \rho_i$). This is an important feature of cortical networks [153, 154] that results in a high sensitivity of the network to

spike timing and to small fluctuations in the total synaptic input [131, 155, 156].

As mentioned above, $1/\mu_e$ and $1/\mu_i$ are of the order of the first-spike latencies of excitatory and inhibitory neurons that range from 6 to 130 ms in the cortex [157–160]. We define the parameter α,

$$\alpha \equiv \frac{\mu_i}{\mu_e}. \tag{3.19}$$

If $\alpha > 1$, inhibitory neurons respond faster to stimuli than excitatory neurons, i.e., the response time $T_i = 1/\mu_i$ of an inhibitory neuron is smaller than the response time $T_e = 1/\mu_e$ of an excitatory neuron. If excitatory neurons respond faster, i.e., $T_e < T_i$, then $\alpha < 1$. In the cortex, α may be both larger and smaller than 1 [157–160]. In our model, we do not need to define τ and f separately, because only its product τf plays a role. We use $\tau f = 1$. In this case, the neurons are firing regularly, nonetheless, the results are qualitatively the same, when using $\tau f < 1$, or $\tau f > 1$. The membrane time constant τ can range from 1 to 100 ms [152]. If we consider $\tau = 10$ ms, then the firing rate f is 100 Hz. It is a reasonable frequency comparing to the frequencies of Class 1 excitable neurons that lie in the range from 2 to 200 Hz, or even greater, and Class 2 excitable neurons that fire at frequencies larger than 40 Hz [123].

Finally, the amplitude and the variance of shot noise are set to $J_n = J_e$ and $\sigma^2 = 10$. We mainly analyse in the next chapters the dependence of the dynamics of the cortical model on the parameter α and on the shot noise intensity $\langle n \rangle$.

3.7 Other models

Our cortical model based on [101] is similar to the stochastic model of spiking neurons proposed by Benayoun *et al.* [144]. Both models consider networks of stochastic neurons ("input-dependent stochastic switches" in [144]). The difference between the models is in some details about how to describe activation and deactivation processes and external input. Benayoun *et al.* assume that each neuron spikes with a rate dependent on its total synaptic input, while the resulting spiking activity decays at a constant rate independent on the input. In our model, we use a similar activation rule, while spiking activity decays with a certain rate only if the input becomes smaller than a threshold. The rates for activation and decay are different in [144], in contrast to our model where they are the same. Benayoun *et al.* assume that external input to each neuron is fixed, whereas in our model the external input is represented by shot noise. It is not surprising that, despite these differences, these models demonstrate similar dynamics (as we shall see later on in this thesis). The advantage of models with stochastic neurons is that they can be solved explicitly. Benayoun *et al.* [144] and Wallace *et al.* [145] derived explicit rate equations for networks with all-to-all connections while sparse randomly connected networks (classical random graphs) were studied numerically.

Methods of complex network theory [39] allowed us to find explicit rate equations for neuronal networks on classical random graphs [101, 102], as presented above. Rate equations similar to Eqs. (3.15) were derived for disease spreading and contact processes

on complex networks [161–163]. Though we do not study scale-free networks in this thesis, they have been analysed with the same methods in [114]. In Appendix C, we analyse our model in a fully connected network.

The model considered in the previous sections and studied in the next chapters is slightly different from the firstly proposed model by Goltsev *et al.* [101]. In the original work [101], the stochastic model has a spontaneous activation rate (f_a) and a spontaneous inactivation rate (μ_{2a}) that influences the activity of neurons, instead of shot noise. The resulting rate equations are similar to Eqs. (3.15):

$$\dot{\rho_a} = f_a - \nu_a \rho_a + \mu_a \Psi(\rho_e, \rho_i), \tag{3.20}$$

where

$$\Psi(\rho_e, \rho_i) = \sum_{k,l=0}^{\infty} \Theta(J_e k + J_i l - V_{th}) P_k(g_e \rho_e \tilde{c}) P_l(g_i \rho_i \tilde{c}), \tag{3.21}$$

and $\nu_a \equiv f_a + \mu_a + \mu_{2a}$ (all other parameters and variables are the same as the ones presented above). This model is qualitatively similar to the one with shot noise [102]. The reason to make this exchange in the model is because shot noise is a better representation of neuronal noise than spontaneous activation and inactivation rates.

In Ref. [101], it was demonstrated that Eq. (3.20) can accommodate the introduction of pacemakers, a fraction of F_a neurons that permanently fire. In that case, the total activity is

$$\rho_a \equiv F_a + (1 - F_a)\tilde{\rho_a}, \tag{3.22}$$

where only the fraction $1 - F_a$ of neurons have a time dependent activity $\tilde{\rho_a}$ that obey to the stochastic rules of activation and inactivation. Using the same method, one derives

$$\dot{\rho_a} = F_a \nu_a + f_a(1 - F_a) - \nu_a \rho_a + (1 - F_a)\mu_a \Psi(\rho_e, \rho_i), \tag{3.23}$$

which is very similar to Eq. (3.20). Thus, the introduction of pacemakers does not change qualitatively the model. The same is true for the model with shot noise. In Chapter 6 we consider a different approach to introduce a stimulus in the network.

Goltsev *et al.* also show in [101] that it is possible to modify the model in order to take into account synaptic delays. Assuming that there is a time delay T_{ab} for the transmission of a signal from a neuron of population a to a neighbour neuron of population b (where $a, b = e, i$). Then, it is necessary to replace $\Psi(\rho_e, \rho_i)$ in Eq. (3.20) by $\Psi_a(\rho_e(t - T_{ea}), \rho_i(t - T_{ia}))$. There are various sources of delays in the nervous system and their role in the neuronal network dynamics was discussed in Ref. [164]. We consider synaptic delays in Chapter 7, when studying a network composed of Izhikevich neurons [115].

Chapter 4

Steady states and phase diagram of the model

In this chapter we start by explaining the methods employed to analyse the model presented in Chapter 3. Then, we find the fixed points of Eqs. (3.15) and, using the respective eigenvalues, we characterize them concerning their local stability in different regions of parameters. This analysis gives a phase diagram that summarizes the set of dynamical regimes that the model displays. Finally, we discuss how this phase diagram is transformed when parameters are changed. Most of the results presented in this chapter were published in Ref. [102].

4.1 Methods

We studied our model (see Chapter 3) using analytical, numerical and simulation methods. The analytical methods do not require many clarifications. One can mention that in some cases we solved equations graphically. It means that we found the intersection points of two functions numerically defined in an interval $[x_1, x_n]$ by a set of points x_i. If the intersection occurs between the points x_2 and x_3, we consider that the functions behave linearly between the two points, and we take the intersection of the two lines.

Equations (3.15) and (3.18) were solved numerically. Equations (3.15) were solved using Euler's Method:

$$\dot{\rho_a} \approx \frac{\rho_a(t_{n+1}) - \rho_a(t_n)}{\delta t} \tag{4.1}$$

when δt is sufficiently small and where $t_n = n\delta t$ (we used $\delta t = 0.01$). Thus, we obtain

$$\rho_a(t_{n+1}) = \rho_a(t_n) + \delta t \mu_a[-\rho_a(t_n) + \Psi(\rho_e(t_n), \rho_i(t_n))]. \tag{4.2}$$

In most of the calculations we used the initial condition $(\rho_e(0), \rho_i(0)) = (0, 0)$. Equation (3.18) gives $\Psi(\rho_e, \rho_i)$. Numerically, the summation over k, l, and n in Eq. (3.18) is stopped when the terms become sufficiently small. We considered sums up to $n_{max} =$

$\langle n\rangle + 3\sigma^2$, $k_{max} = 3g_e\rho_e\tilde{c}$, and l_{max} determined by the condition of the theta function,

$$l_{max} = \frac{V_{th} - kJ_e - nJ_n}{J_i}. \tag{4.3}$$

One should note that k_{max} is proportional to the activity, and the calculations get heavier when the activity increases. In order to speed up the calculations, we transformed the sums in an integral. The function has an integral representation,

$$\Theta(t) = \frac{1}{2} + \frac{1}{\pi}\int_0^\infty \frac{\sin(tx)}{x}dx \tag{4.4}$$

where $t = kJ_e + lJ_i + nJ_n - V_{th}$ in our case. Equation (3.18) becomes

$$\Psi(\rho_e,\rho_i) = \frac{1}{2} + \sum_{k,l,n=0}^{\infty}\frac{1}{\pi}\int_0^\infty Im\left\{\frac{e^{ix(kJ_e+lJ_i+nJ_n-V_{th})}}{x}\right\}\frac{\zeta_e^k e^{-\zeta_e}}{k!}\frac{\zeta_i^l e^{-\zeta_i}}{l!}G_0 e^{-\frac{(n-\langle n\rangle)^2}{2\sigma^2}}dx, \tag{4.5}$$

where $\zeta_a = g_a\rho_a\tilde{c}$. Then, one uses the normalization condition of the Gaussian distribution, Eq. (3.10), and the normalization condition of the Poisson distribution,

$$\sum_{n=0}^{\infty}\frac{c^n}{n!} = e^c, \tag{4.6}$$

in order to get rid of the sums. Thus, we obtain

$$\Psi(\rho_e,\rho_i) = \frac{1}{2} + \frac{1}{\pi}\int_0^\infty \exp\Big(\zeta_e(\cos(J_e x)-1) + \zeta_i(\cos(J_i x)-1) - \frac{x^2\sigma^2 J_n^2}{2}\Big) \times \sin\Big(\zeta_e\sin(J_e x) + \zeta_i\sin(J_i x) + (J_n\langle n\rangle - V_{th})x\Big)\frac{dx}{x}. \tag{4.7}$$

We used the trapezoidal rule to calculate numerically the integral,

$$\int_a^b \varphi(x)dx \approx \frac{b-a}{2N}\sum_{i=1}^{N}\Big(\varphi(x_i) + \varphi(x_{i+1})\Big), \tag{4.8}$$

where the domain $[a,b]$ was discretized into N equal parts, such that $x_1 = a$ and $x_{N+1} = b$. We computed our integral, Eq. (4.7), using $a = 0$, $b = 1$, and $N = 10^5$.

In our numerical calculations we used both methods, the one with the restricted sum in Eq. (3.18) and the one with the integral representation (Eq. (4.7)), because Eq. (3.18) is computed faster when the activities are small ($\rho_a \leq 0.01$), and Eq. (4.7) is computed faster when the activities are large (at small activities, the interval of integration has to be considered larger than $[0,1]$).

In simulations, we built a directed network, linking neurons with the probability c/N. We divided time into intervals of width $\Delta t = \tau$. At each time step, for each neuron we calculated the input V_n, Eq. (3.6), given that each active presynaptic neuron contributes

a spike with probability τf. The number of random spikes (shot noise) in this input was generated by the Gaussian process $G(n)$, Eq. (3.9). Then, we updated the states of the neurons using the rules formulated in Chapter 3 (parallel update), starting with an inactive network, $(\rho_e(0), \rho_i(0)) = (0, 0)$. Reliable results were obtained when the probabilities $\tau\mu_e$ and $\tau\mu_i$ were about 0.1 or smaller (we used $\tau = 0.1$). As one could expect, different runs and different realizations of the network give slightly different results. With increasing N these differences become smaller and smaller.

The programs were written in Fortran programming language. When using a 3.07 GHz desktop, 1000 time steps of numerical integration of Eqs. (3.15) take from 1 second to 1 minute to run (as mentioned above, our method depends on the activity). 1000 time steps of simulations take about 1 minute and 7 second (considering a network of $N = 10^4$ neurons).

4.2 Steady states and fixed points

The shot noise intensity $\langle n \rangle$ determines the activities ρ_e and ρ_i of excitatory and inhibitory populations at given model parameters. In a steady state,

$$\dot{\rho_a} = 0, \tag{4.9}$$

Eqs. (3.15) gives $\rho_e = \rho_i = \rho$, where ρ is a solution of the steady state equation,

$$\rho = \Psi(\rho, \rho). \tag{4.10}$$

A graphical solution of this equation can be obtained as in Fig. 4.1. If the shot noise intensity $\langle n \rangle$ is either sufficiently small or sufficiently large, then there is only one solution, either point 1 or point 3. These fixed points correspond to steady states with low and high neuronal activities, respectively. In an intermediate range $n_{c1} < \langle n \rangle < n_{c2}$, there are three fixed points (1, 2, and 3, and corresponding activities $\rho^{(1)}$, $\rho^{(2)}$, and $\rho^{(3)}$). The critical point $\langle n \rangle = n_{c1}$ is the point where fixed points 2 and 3 coalesce. Fixed points 1 and 2 coalesce at $\langle n \rangle = n_{c2}$. From Fig. 4.1, one sees that the coalescences occur when

$$\frac{d\Psi(\rho, \rho)}{d\rho} = 1. \tag{4.11}$$

Together with the steady state equation (4.10), the condition (4.11) determines the critical points n_{c1} and n_{c2}.

While the fixed points depend on $\langle n \rangle$, but not on α, their local stability with respect to small perturbations depends on both $\langle n \rangle$ and α. It is determined by the eigenvalues of the Jacobian of Eqs. (3.15) calculated at the fixed points. In order to obtain the Jacobian, one can study the relaxation of the neuronal activities $\rho_a(t)$ to a steady state ρ_a. We consider $\rho_a(t) = \rho_a + \delta\rho_a(t)$, where

$$\frac{\delta\rho_a(t)}{\rho_a} \ll 1. \tag{4.12}$$

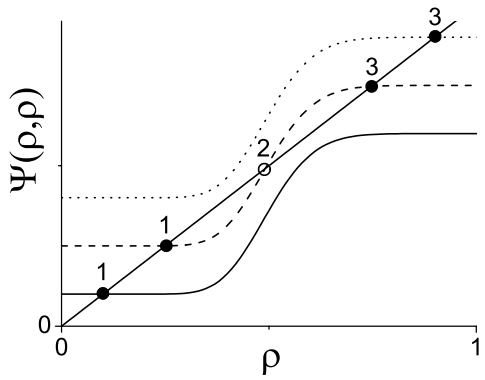

Figure 4.1: Points 1, 2, and 3 represent solutions of the steady state equation, Eq. (4.10), for the cases $\langle n\rangle < n_{c1}$ (solid line), when there is only one solution of low activity (point 1); $n_{c1} < \langle n\rangle < n_{c2}$ (dashed line), that corresponds to three solutions; and $\langle n\rangle > n_{c2}$ (dotted line), where point 3 is the solution which corresponds to high activity.

The linearization of Eqs. (3.15) with respect to $\delta\rho_a(t)$ gives two coupled linear equations:

$$\frac{d\delta\rho_a(t)}{\mu_a dt} = -\delta\rho_a(t) + \frac{\partial\Psi}{\partial\rho_e}\delta\rho_e(t) + \frac{\partial\Psi}{\partial\rho_i}\delta\rho_i(t), \tag{4.13}$$

where $a = e, i$. Equation (4.13) can be rewritten as

$$\dot{\vec{\delta\rho}} = \hat{J}(\rho)\vec{\delta\rho} \tag{4.14}$$

where

$$\vec{\delta\rho} = \begin{pmatrix} \delta\rho_e(t) \\ \delta\rho_i(t) \end{pmatrix} \tag{4.15}$$

and $\hat{J}(\rho)$ is the Jacobian matrix,

$$\hat{J}(\rho) = \begin{pmatrix} -1 + \dfrac{\partial\Psi}{\partial\rho_e} & \dfrac{\partial\Psi}{\partial\rho_i} \\ \\ \alpha\dfrac{\partial\Psi}{\partial\rho_e} & -\alpha + \alpha\dfrac{\partial\Psi}{\partial\rho_i} \end{pmatrix}. \tag{4.16}$$

The eigenvalues λ of the two-dimensional matrix,

$$\begin{pmatrix} J_{11} & J_{12} \\ J_{21} & J_{22} \end{pmatrix}, \tag{4.17}$$

are determined by the condition,

$$\begin{vmatrix} J_{11} - \lambda & J_{12} \\ J_{21} & J_{22} - \lambda \end{vmatrix} = 0, \tag{4.18}$$

that gives

$$\lambda_{\pm} = \frac{1}{2}(J_{11} + J_{22}) \pm \frac{1}{2}\sqrt{(J_{11} - J_{22})^2 + 4J_{12}J_{21}}. \tag{4.19}$$

Thus, the eigenvalues of the Jacobian, Eq. (4.16), are

$$\lambda_{\pm} = \frac{1}{2}(-1 - \alpha + D_e + \alpha D_i) \pm \frac{1}{2}\sqrt{(\alpha - 1 + D_e - \alpha D_i)^2 + 4\alpha D_e D_i}, \tag{4.20}$$

where $D_e = \partial\Psi/\partial\rho_e$ and $D_i = \partial\Psi/\partial\rho_i$. When $\lambda_{\pm} < 0$ at a fixed point, then the point is stable (attractor). If $\lambda_{\pm} > 0$, then the point is unstable. If one of the eigenvalues $\lambda_{\pm}$ is positive and the other is negative, then the point is saddle. When $Re\{\lambda_{\pm}\} < 0$ and $Im\{\lambda_{\pm}\} \neq 0$, the point is a stable spiral. If $Re\{\lambda_{\pm}\} > 0$ and $Im\{\lambda_{\pm}\} \neq 0$, the fixed point is an unstable spiral. The fixed points and their stability determine the phase portraits of Eqs. (3.15).

If the neuronal network is weakly perturbed from an equilibrium state corresponding to a stable fixed point ρ, then the real and imaginary parts of λ_+ at this point determine the relaxation rate γ_r to the state,

$$\gamma_r = -\mathrm{Re}\{\lambda_+(\rho)\}, \tag{4.21}$$

and the angular frequency γ_i of damped oscillations about the fixed point,

$$\gamma_i = \mathrm{Im}\{\lambda_+(\rho)\}. \tag{4.22}$$

4.3 Phase diagram

Analysing the local stability of the fixed points 1, 2, and 3 in the $\langle n\rangle$-α plane (see Table 4.1), we find the phase diagram of the cortical model displayed in Fig. 4.2. According to Table 4.1, in regions Ia-Ie, the network relaxes exponentially to the stable fixed point 1 (provided that a perturbation is small). In regions Ib and IIa, the relaxation to the stable fixed point 3 is exponential while, in regions Ic and IIb, the relaxation occurs in the form of damped oscillations about the fixed point 3. In regions IIIa and IIIb, the fixed point 3 is an unstable point surrounded by a limit cycle. These are the regions with sustained network oscillations about the point 3. The nonlinear equations (3.15) have different phase portraits in the phase regions Ia-IIIb in Fig. 4.2. The phase portraits in the (ρ_e, ρ_i) phase plane can be found by use of the standard methods [116, 165]. They determine the patterns of collective neuronal activity and the response of the network to stimuli. Figures 4.3 and 4.4 show paradigmatic patterns of activity and respective phase planes in each region (from both simulations and numerical calculations).

In regions Ib-Ie, where there are three fixed points, we start with two different initial conditions, $(\rho_e(0), \rho_i(0)) = (0, 0)$ and $(\rho_e(0), \rho_i(0)) = (0.5, 0)$, in order to observe the influence of point 1 and 3 (the role of point 2 is discussed in Chapter 7). In this case, at $\langle n\rangle = 15$, the fixed point 1 corresponds to a very low activity, that is very close to zero in the figure ($\rho^{(1)} \approx 2 \times 10^{-6}$). One sees that when the activity relaxes to a stable

Table 4.1: Local stability of the fixed points 1, 2, and 3 in the regions Ia–IIIb of the phase diagram in Fig. 4.2.

	Ia	Ib	Ic	Id	Ie	IIa	IIb	IIIa	IIIb
1	stable	stable	stable	stable	stable	–	–	–	–
2	–	saddle	saddle	saddle	saddle	–	–	–	–
3	–	stable	stable spiral	unstable spiral	unstable	stable	stable spiral	unstable spiral & limit cycle	unstable & limit cycle

point (regions Ia-Ic and both regions II), the simulations display a noisy activity about the stable point. The fluctuations result from finite-size effects (around the fixed point 1 the fluctuations are too small to be observed). This irregular activity is expected to decrease as N is increased. However, when point 3 is unstable (regions Id, Ie, and both regions III), the nonlinear nature of the dynamics around this point overcomes the finite-size effects and the activities display deterministic shape (this fact is discussed in more detail in the next chapters). Obviously, if N is small enough, the finite-size effects are able to destroy the nonlinear oscillations. Nevertheless, Goltsev *et al.* [101] showed that, even in a small network composed of only 50 neurons (and mean degree $c = 20$), network oscillations can emerge, and in a network of 1000 neurons the simulation result is already in a very good agreement with the mean-field solution. In Fig. 4.4(e), the frequency of sustained oscillations is slightly different between the numerical result and simulations, a difference that can also be attributed to finite-size effects. For instance, the clustering coefficient is zero in the infinite size limit (numerical result), whereas in simulations it is $c/N = 1000/10^4 = 0.1$. As mentioned before, real networks have finite clustering coefficients. For instance, it was found a coefficient $C = 0.53$ in the macaque visual cortex [23, 24]. Thus, the irregular activity observed in real neuronal networks is more similar to the activity in our simulations than to the activity obtained from the numerical integration of the mean field equations (3.15).

Damped oscillations were observed experimentally, for instance in anesthetized rats [166], and in an instance of epilepsy (see, for example, [167]). Note that in simulations (like in real networks), fluctuations give rise to small irregular oscillations (Fig. 4.4(c)). These are similar to spindles, which were observed, for example, in the thalamus [168]. Our model also displays neuronal oscillations similar to brain waves (see Chapter 1, Fig. 1.4). Taking into account that μ_e^{-1} is in the range of $6 - 130$ ms in the cortex [157–160], the network oscillations shown in Fig. 4.4(e) have a frequency of about $1 - 17$ Hz, which is in a biologically reasonable band corresponding to delta, theta, alpha and beta waves [41]. In this work, we choose $\mu_e^{-1} = 20$ ms, a choice that agrees with experimental data according to which the first-spike latency is ranged from 25 to 49 ms for CA3 hippocampal pyramidal (excitatory) neurons [159] and from 20 to 128 ms for inhibitory cerebellar stellate cells

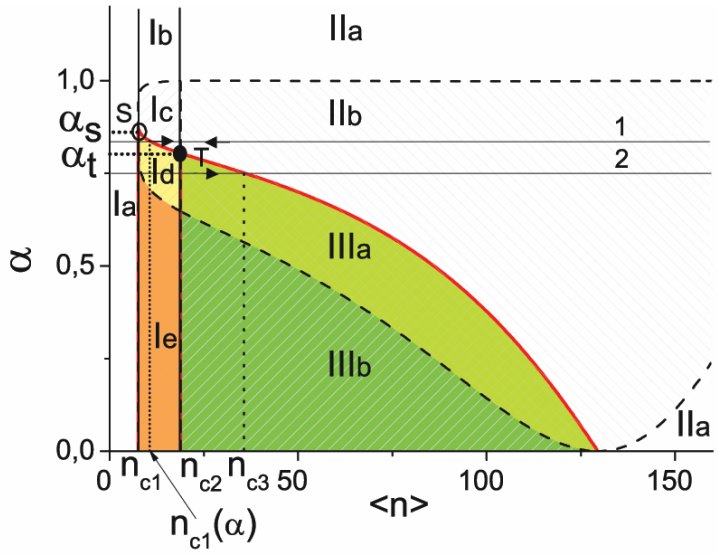

Figure 4.2: $\langle n\rangle$-α plane of the phase diagram of the cortical model. $\langle n\rangle$ is the shot noise intensity, α is the ratio of the response time of excitatory neurons to the response time of inhibitory neurons. The phase regions, the phase boundaries, the points S and T, and the parameters used in numerical calculations are explained in the text. Line 1 and 2 represent two scenarios discussed in the next chapter. Parameters: $\tilde{c} = 1000$, $\Omega = 30$, $g_i = 0.25$, $J_i = -3J_e$, and $\sigma^2 = 10$.

---

[160]. For this choice, the frequency of the oscillations displayed in Fig. 4.4(e) is about 5 Hz, which lies in the range of theta oscillations ($4 - 8$ Hz). The shape of our sustained network oscillations also resembles theta waves measured by EEG in the hippocampus of rats (see Fig. 4 in [169]).

In Fig. 4.5, we show patterns of activity in regions IIa and IIIb, in order to clarify the role of the parameter α. In region IIa, with $\alpha = 1.1$, inhibitory neurons respond faster, and therefore the inhibitory activity goes faster to the steady state (see Fig. 4.5(a)). In region IIIb, where $\alpha < 1$, excitatory neurons are faster, resulting in a time delay between the oscillatory activity of the excitatory and inhibitory populations. The delay gets larger as we decrease α.

In Fig. 4.2, the phase boundaries are represented by the dashed and solid lines. The vertical lines $\langle n\rangle = n_{c1}$ and $\langle n\rangle = n_{c2}$ are determined by the self-consistent solutions of Eqs. (4.10) and (4.11) discussed above. The boundaries between regions IIa and IIb, between regions IIIa and IIIb, and between regions Id and Ie are determined by the condition

$$\gamma_i(\rho^{(3)}) = \mathrm{Im}\{\lambda_+(\rho^{(3)})\} = 0 \tag{4.23}$$

(see the dashed lines in Fig. 4.2). The phase boundaries between regions Ic and Id and between regions IIb and IIIa are determined by the condition

$$\gamma_r(\rho^{(3)}) = -\mathrm{Re}\{\lambda_+(\rho^{(3)})\} = 0 \tag{4.24}$$

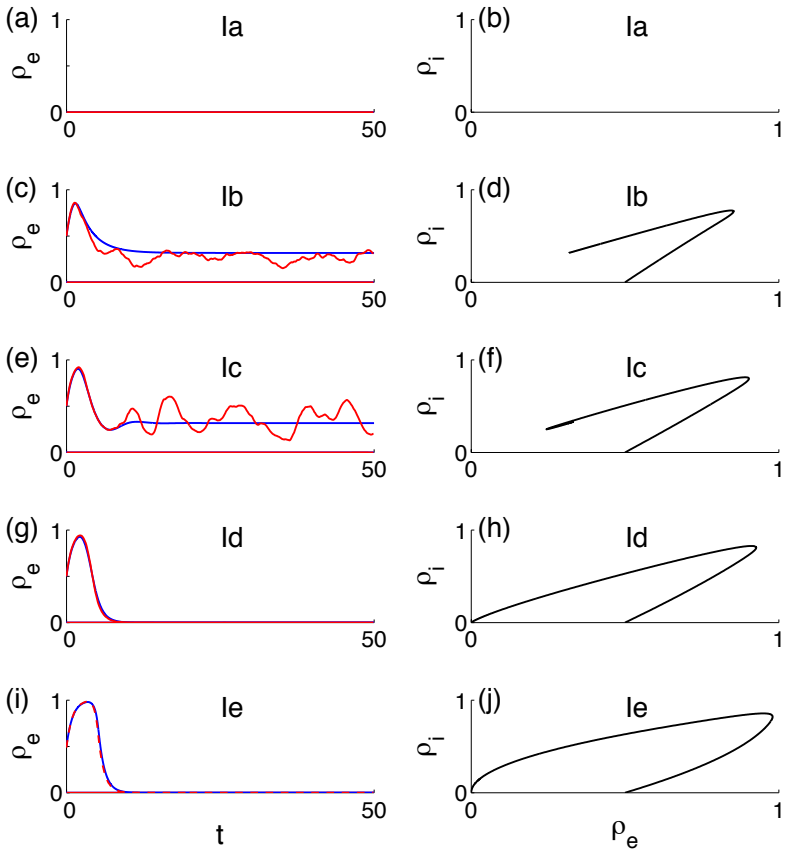

Figure 4.3: In the left column we present patterns of excitatory activity found in regions Ia-Ie, where the blue line corresponds to the numerical solution of Eqs. (3.15), and the red line corresponds to simulations of the model at the same parameters. In the right column we show the respective phase planes (ρ_e, ρ_i) of the numerical results. Activity in region Ia (panels (a) and (b)) relaxes exponentially to a low activity state (almost zero), at $(\langle n \rangle, \alpha) = (5, 0.5)$. In regions Ib-Ie, there are three fixed points (see Table 4.1). We start with two different initial conditions, $(\rho_e(0), \rho_i(0)) = (0, 0)$ and $(\rho_e(0), \rho_i(0)) = (0.5, 0)$. From the inactive state, the activities relax to the steady state $\rho^{(1)}$ in all these regions ($\rho^{(1)} \approx 2 \times 10^{-6}$). When starting with half excitatory population active, in region Ib the activity relaxes exponentially to the fixed point $\rho^{(3)}$ (panels (c) and (d)), whereas in region Ic the activity relaxes to the same fixed point in the form of damped oscillations (panels (e) and (f)). In regions Id (panels (g) and (h)) and Ie (panels (i) and (j)), the fixed point 3 is unstable and it repels the trajectories towards the fixed point 1. The activities of regions Ib-Ie were obtained at the vertical line $\langle n \rangle = 15$, at the points $\alpha = 1.1$ (region Ib), $\alpha = 0.9$ (region Ic), $\alpha = 0.8$ (region Id), and $\alpha = 0.5$ (region Ie). Other parameters are the same as in Fig. 4.2. Additionally, in simulations we used $N = 10^4$, and $\tau = 0.1$. Time t is in units of μ_e^{-1}.

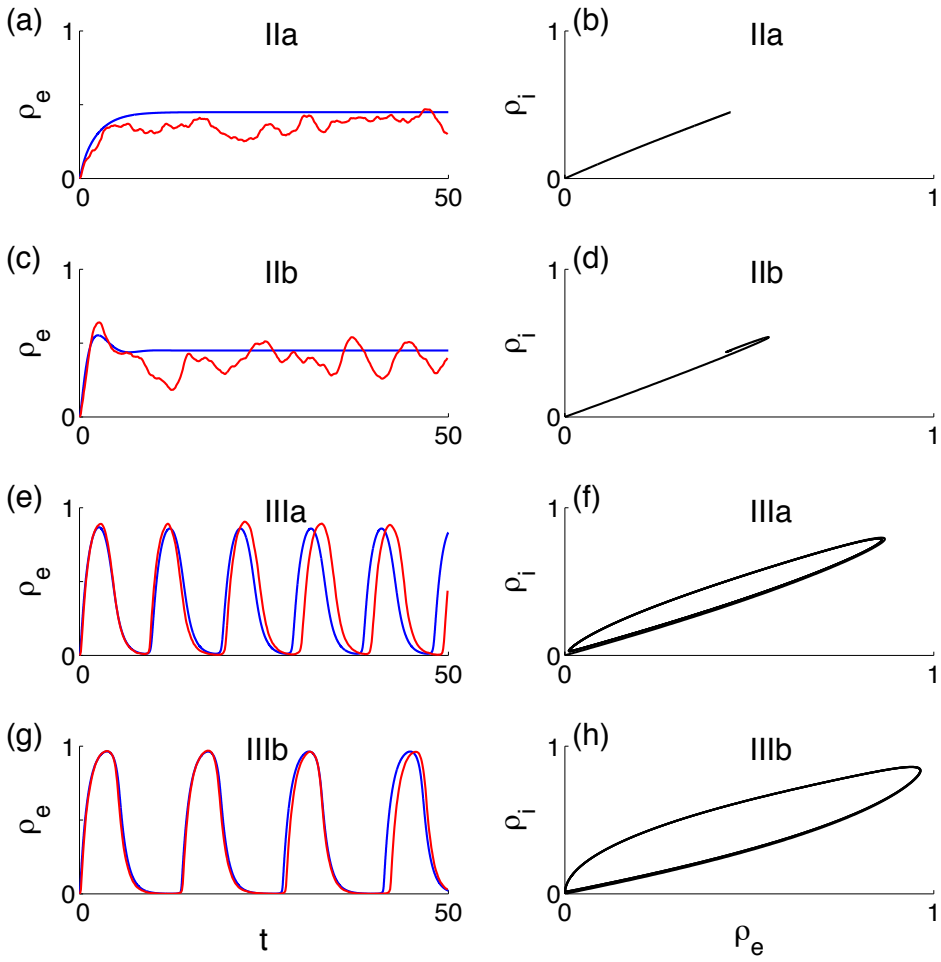

Figure 4.4: In the left column we present patterns of excitatory activity found in regions IIa-IIIb, where the blue line corresponds to the numerical solution of Eqs. (3.15), and the red line corresponds to simulations of the model at the same parameters. In the right column we show the respective phase planes (ρ_e, ρ_i) of the numerical results. In all these regions there is only one fixed point of high activity, $\rho^{(3)}$. This fixed point is stable in region IIa (panels (a) and (b)), and thus the activity relaxes exponentially. In region IIb, the point is a stable spiral, and the activity relaxes in the form of damped oscillations (panels (c) and (d)). In regions IIIa and IIIb, the fixed point 3 is unstable and is responsible for the observed sustained network oscillations (panels (e) and (f) for region IIIa, and panels (g) and (h) for region IIIb). The activities in these regions were obtained at the vertical line $\langle n \rangle = 25$, at the points $\alpha = 1.1$ (region IIa), $\alpha = 0.9$ (region IIb), $\alpha = 0.7$ (region IIIa), and $\alpha = 0.5$ (region IIIb). Other parameters are the same as in Figs. 4.2 and 4.3. Time t is in units of μ_e^{-1}.

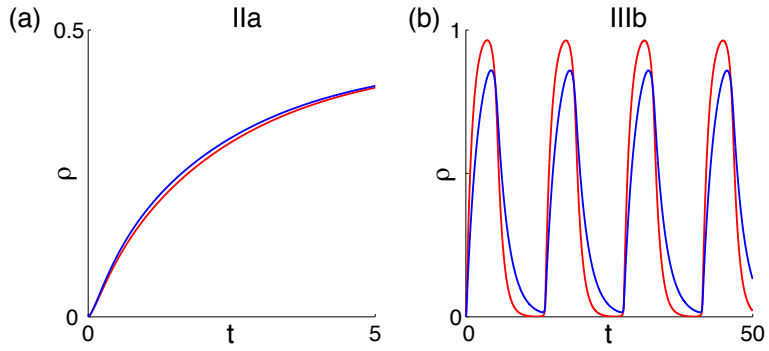

Figure 4.5: Excitatory (red lines) and inhibitory (blue lines) activities at different α. (a) Activities in region IIa at $(\langle n\rangle, \alpha) = (25, 1.1)$. (b) Activities in region IIIb at $(\langle n\rangle, \alpha) = (25, 0.5)$. These results were obtained from numerical integration of Eqs. (3.15). Other parameters are the same as in Fig. 4.2. Time t is in units of μ_e^{-1}.

(see the solid line in Fig. 4.2). According to Eq. (4.24), on the boundary between regions IIb and IIIa, the relaxation rate is zero, i.e., critical slowing down occurs. The point $T = (n_{c2}, \alpha_t)$ in Fig. 4.2 is a tricritical point of coexistence of three phases: the low activity state (regions Ic and Id), the high activity state (region IIb), and the state with sustained network oscillations (region IIIa). According to [116], the fixed point 3 at the tricritical point is called "center". Centers are neutrally stable, because they do not attract, neither repel trajectories, since the real part of their eigenvalues is zero. Simultaneously, points 1 and 2 annihilate each other and form a "ghost" which is responsible for a bottleneck region that slows down trajectories passing nearby (the time Δ spent in this region depends on how close is the system to the critical point, $\Delta \propto (n_{c2} - \langle n\rangle)^{-1/2}$ [116]). At the point T, the line of a first-order phase transition meets the lines of two continuous phase transitions (these phase transitions are discussed in the next chapter). The point $S = (n_{c1}, \alpha_s)$ is the common point of the regions Ia, Ic, and Id. Results from simulations are in agreement with the boundaries displayed in Fig. 4.2. For the parameters indicated in the previous chapter, we find $n_{c1} \approx 7.6$, $n_{c2} \approx 18.8$, $\alpha_s \approx 0.87$, and $\alpha_t \approx 0.80$.

We performed additional investigations of the cortical model with a small imbalance when $g_e J_e \neq -g_i J_i$ in the range $0.23 < g_i < 0.3$ around the balanced state at $g_i = 0.25$ (other model parameters were fixed). We found that the phase diagram is qualitatively the same as in the balanced state in Fig. 4.2. The critical point n_{c2} is almost constant in this range. With increasing g_i from 0.23 to 0.3, the region III with sustained network oscillations is broadening and the critical value α_t increases. At a given α, the critical point n_{c3} that separates region IIb from region IIIa is also monotonously increased as g_i increases from 0.23. Similar results were obtained by changing J_i.

Interestingly, Eq. (4.7) tells us what happens if we consider the threshold V_{th} Gaussian distributed, instead of being a constant. In that case, in Eq. (4.7), V_{th} is replaced by its mean value, and $x^2\sigma^2 J_n^2$ by $x^2(\sigma^2 J_n^2 + \sigma_{th}^2)$, where σ_{th}^2 is the variance of the threshold. It means that the case with a Gaussian distribution of thresholds is completely equivalent to

increasing the variance of the shot noise. We also confirmed that varying the variance of the shot noise σ^2, or its amplitude J_n, does not change qualitatively the phase diagram.

Though here we do not examined how the phase diagram is changed when the mean degree (or $\tilde{c}$) is altered, this was studied within the similar model without shot noise [101]. Goltsev *et al.* [101] showed that the main difference is that when the mean degree is decreased, the region of oscillations also decreases, while the qualitative picture remains unchanged.

Chapter 5

Phase transitions, bifurcations, and critical phenomena

In this chapter, we analyse the phase transitions and respective bifurcation mechanisms that separate the different regions of neuronal dynamics presented in Fig. 4.2. We also show that the different phase transitions are signaled by different critical phenomena. We start with the first-order phase transition that occurs at n_{c2} and $\alpha > \alpha_t$. Then, we consider the two second-order phase transitions that appear at n_{c2} (saddle-node bifurcation) and n_{c3} (supercritical Hopf bifurcation) when $\alpha < \alpha_t$. Most of the results presented in this chapter were published in [102].

5.1 First-order phase transition

In this section, we study critical phenomena accompanying the first-order phase transition. In particular, we examine neuronal bursts and avalanches as precursors of the transition. Although bursts and avalanches have been broadly studied both experimentally and theoretically, understanding of their mechanism in the brain remains elusive [65, 66, 76, 77, 136, 170]. Here, apart from the standard measurements of the distribution function of avalanches over size, we also study critical behavior of the relaxation rate, a dependence of the power spectral density (PSD) of activity fluctuations on the shot noise intensity, and the role of finite-size effects. We find a dramatic increase of the zero-frequency peak of the PSD when the shot noise intensity tends to the critical point n_{c2}, while above the point the relaxation rate is nonzero and there are no critical fluctuations.

The first-order phase transition occurs if $\alpha > \alpha_t$, i.e., when the response time T_i of an inhibitory neuron to stimuli is small enough in comparison with the response time T_e of an excitatory neuron. In simulations and numerical solution of Eqs. (3.15), we increased the noise level $\langle n \rangle$ from zero (region Ia) to a value in region IIa (or IIb) above the critical point n_{c2} and afterwards decreased it again to a value below n_{c1} (see line 1 in Fig. 4.2). When increasing the noise intensity $\langle n \rangle$, the neuronal activity (the order parameter of the transition) undergoes a jump at $\langle n \rangle = n_{c2}$ (as we discuss below). Therefore, the critical

point n_{c2} is the limiting point of the first-order phase transition. This phase transition is caused by a saddle-node bifurcation that corresponds to the coalescence of the stable point 1 and the saddle point 2. Simultaneously, at $\langle n \rangle = n_{c2}$, the eigenvalue $\lambda_+(\rho^{(1)})$ becomes zero while $\lambda_-(\rho^{(1)})$ remains negative. The first-order phase transition was also found in the model of Benayoun *et al.* [144]. The line of the first-order phase transition ends up at the point (n_{c2}, α_t) of the phase diagram (Fig. 4.2). If $\alpha < \alpha_t$, the neuronal network undergoes a second-order phase transition at $\langle n \rangle = n_{c2}$ as we discuss in Section 5.2.

5.1.1 Avalanches

In simulations, at $\langle n \rangle \leq n_{c2}$, we observe bursts of neuronal activity (see the inset of Fig. 5.1(a)). When $\langle n \rangle \to n_{c2}$, the mean interburst interval decreases while the mean burst duration increases. The bursts are caused by avalanches (the activation of a single neuron triggers the activation of a cluster of neurons). These activation processes are stochastic. In our model, in networks of finite size, bursts are generated by finite-size fluctuations. We studied avalanches, analysing spike time series by use of the standard method (see [76] or the recent work [171]). In this method, an avalanche starts when at least one neuron of the network suddenly becomes active and it stops in the time step in which all neurons stopped to fire. The size s of the avalanche is defined as the number of neurons involved in the neuronal activity between those two events. One disadvantage of this method is that it does not take into account the fact that two or more independent avalanches may overlap in time. Nevertheless, it is assumed that this method gives a correct asymptotic behavior of the avalanche size distribution. The avalanche size distribution $P(s)$ is represented in Fig. 5.1(a). Using the maximum likelihood estimate [172], we found that, when $\langle n \rangle$ is close to n_{c2}, the tail of $P(s)$ follows a power law $P(s) \propto s^{-z}$, with the exponent $z \approx 1.50$ and the corresponding p value is $p = 0.88$ (the closeness of p to 1 shows that the fit is good [172]). (We used the software presented in [173]. It gave the log-likelihood $L = -231.4$, and $s_{min} = 1767$ that minimizes the Kolmogorov-Smirnov statistic, $D = 0.069$.) Our estimation is close to the value 1.62 obtained in [144]. Avalanches with the exponent z about 1.5 were also found near a saddle-node bifurcation in networks of leaky integrate-and-fire neurons with short-term synaptic depression [136]. Our estimation also agrees with experimental data [76, 171] and the standard mean-field exponent $z = 3/2$ obtained for other exactly solved models [101, 174–178]. Avalanches may play a very important role in the brain, because they appear to favour information transmission [179].

5.1.2 Hysteresis

At a given $\alpha > \alpha_t$, if $\langle n \rangle$ decreases from a value above n_{c2} to a value below n_{c2}, the network activity remains as high as it was above n_{c2} (see Fig. 5.1(b)). The activity falls to a low value only at the critical intensity $\langle n \rangle = n_{c1}(\alpha)$, where $n_{c1} \leq n_{c1}(\alpha) \leq n_{c2}$. In the general case, $n_{c1}(\alpha)$ depends on α because of the existence of region Id (see Fig. 4.2). If $\alpha > \alpha_s$, where α_s is the α coordinate of the point S on Fig. 4.2, hysteresis occurs in the range $n_{c1} \leq \langle n \rangle \leq n_{c2}$ (the region where points 1 and 3 are stable). If $\alpha_t < \alpha < \alpha_s$,

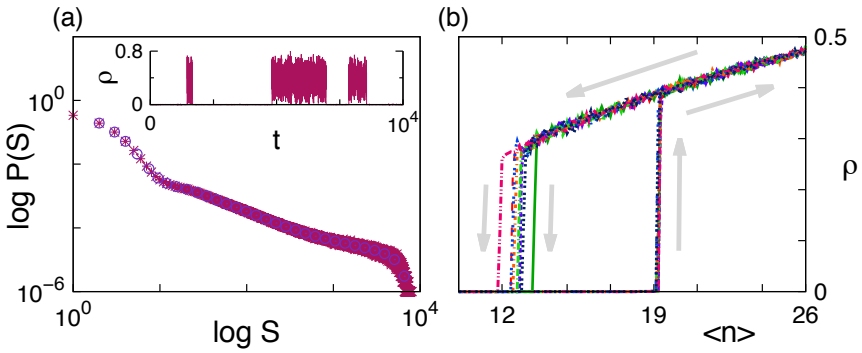

Figure 5.1: (a) Avalanche size distribution $P(s)$ versus the size s at $\langle n\rangle = 18.8$ obtained by use of simulations ($N = 10^4$). Inset: temporal activity of excitatory neurons near the first-order phase transition. Time t is in units of $1/\mu_e$. (b) Hysteresis in neuronal activity for increasing and decreasing noise level $\langle n\rangle$. Parameters: $\tilde{c} = 1000$, $\Omega = 30$, $g_i = 0.25$, $J_i = -3J_e$, $\sigma^2 = 10$, $\tau = 0.1$, and $\alpha = 0.85$. These data and figures were obtained by KyoungEun Lee.

hysteresis occurs in a smaller range of shot noise intensity $n_{c1}(\alpha) < \langle n\rangle < n_{c2}$, where $n_{c1}(\alpha)$ is the $\langle n\rangle$ coordinate of the intersection point of line 1 with the phase boundary between regions Ic and Id ending up at points S and T on the phase diagram in Fig. 4.2. In the interval $n_{c1} < \langle n\rangle < n_{c1}(\alpha)$, the fixed point 3 is unstable, and therefore, after a transient period, the activity falls to the low activity state ($\rho^{(1)}$). The width of the region of hysteresis, i.e., $\Delta = n_{c2} - n_{c1}(\alpha)$, tends to zero when $\alpha \to \alpha_t$. At $\alpha < \alpha_t$, hysteresis is absent because, in regions Id and Ie, the fixed point 3 is unstable and there is only one stable fixed point (point 1). One notes that critical slowing down occurs at both limiting points of the first-order phase transition, i.e., at $\langle n\rangle = n_{c2}$ in the low activity state ($\rho^{(1)}$) and at $\langle n\rangle = n_{c1}$ in the high activity state ($\rho^{(3)}$). In simulations, $\rho^{(1)}$ and $\rho^{(3)}$ can be found by measuring the neuronal activity $\rho_e(t)$ and averaging it over a sufficiently large observation time. Hysteresis was observed, for example, in living neural networks [180] and in simulations of thalamocortical systems [38].

5.1.3 Neuronal activity near the critical point n_{c2}

Let us find the activity $\rho^{(1)}(\langle n\rangle)$ in the low activity state near the critical point $\langle n\rangle = n_{c2}$ of the saddle-node bifurcation, i.e., at $0 < n_{c2} - \langle n\rangle \ll n_{c2}$. In Eq. (4.10), we use the Taylor expansion of the function $\Psi(\rho, \rho)$ over $\varepsilon \equiv \langle n\rangle - n_{c2}$ and $\delta\rho \equiv \rho^{(1)}(\langle n\rangle) - \rho^{(1)}(n_{c2})$ up to the second order in $\delta\rho$. Then, Eq. (4.10) takes the form

$$\delta\rho = \frac{\partial\Psi}{\partial\langle n\rangle}\varepsilon + \frac{d\Psi}{d\rho}\delta\rho + \frac{1}{2}\frac{d^2\Psi}{d\rho^2}\delta\rho^2 + \ldots, \tag{5.1}$$

where the function Ψ and its derivatives are calculated at $\langle n\rangle = n_{c2}$. Using Eqs. (4.10) and (4.11), we find a solution

$$\delta\rho = \rho^{(1)}(\langle n\rangle) - \rho^{(1)}(n_{c2}) \approx -K\sqrt{n_{c2} - \langle n\rangle}, \tag{5.2}$$

where

$$K = \left|2\frac{\partial\Psi}{\partial\langle n\rangle}\Big/\frac{d^2\Psi}{d\rho^2}\right|^{1/2}. \tag{5.3}$$

The singular behavior (5.2) is a general attribute of hybrid and first-order phase transitions [176–178]. Note that $\rho^{(2)}(\langle n\rangle)$ near the fixed point 2 is

$$\rho^{(2)}(\langle n\rangle) - \rho^{(1)}(n_{c2}) \approx K\sqrt{n_{c2} - \langle n\rangle}, \tag{5.4}$$

because, at $\langle n\rangle = n_{c2}$, the points 1 and 2 coalesce and $\rho^{(1)}(n_{c2}) = \rho^{(2)}(n_{c2})$.

5.1.4 Critical slowing down of neuronal dynamics

For deeper understanding of the first-order phase transition, we now find analytically the relaxation rate to the low activity state. Writing Eq. (4.11) in the form

$$\frac{\partial\Psi}{\partial\rho_e} + \frac{\partial\Psi}{\partial\rho_i} = 1 \tag{5.5}$$

and substituting it into Eq. (4.20), we find that, at $\langle n\rangle = n_{c2}$, the eigenvalue $\lambda_+(\rho^{(1)})$ is zero at the fixed point 1. Therefore, the relaxation rate (Eq. (4.21)) to the low activity state is also zero:

$$\gamma_r = -\lambda_+(\rho^{(1)}) = 0. \tag{5.6}$$

This phenomenon is the so-called critical slowing down. Note that it takes place on the line $\langle n\rangle = n_{c2}$ at all α, both above and below α_t (see Fig. 4.2).

We now find the dependence of the relaxation rate γ_r on $\langle n\rangle$ at $0 < n_{c2} - \langle n\rangle \ll n_{c2}$. We use the Taylor expansion of λ_+ over small $\delta\rho \equiv \rho^{(1)}(n_{c2}) - \rho^{(1)} \ll \rho^{(1)}(n_{c2})$ in Eq. (4.20) and we obtain

$$\lambda_+(\rho) = \lambda_+[\rho^{(1)}(n_{c2})] + \frac{d\lambda_+(\rho)}{d\rho}\delta\rho + \dots. \tag{5.7}$$

The first term is zero. Using Eq. (5.2) for $\delta\rho$, in the leading order, we obtain

$$\gamma_r = -\lambda_+(\rho) \propto \sqrt{n_{c2} - \langle n\rangle}. \tag{5.8}$$

This behavior occurs both at $\alpha > \alpha_t$ and $\alpha < \alpha_t$.

If a neuronal network has a finite but large size $N \gg 1$, then according to the scaling law hypothesis, the relaxation rate γ_r is described by the general scaling law

$$\gamma_r(\langle n\rangle, N) = (\langle n\rangle - n_c)^\sigma X[(\langle n\rangle - n_c)N^{1/\nu}] \tag{5.9}$$

with a scaling function $X(x)$ and exponents σ and ν which can be found by use of renormalization group techniques [181–183]. One assumes that the scaling law also is valid near the limiting point n_{c2} of the first-order phase transition [175]:

$$\begin{aligned} \gamma_r(\langle n\rangle, N) &\propto \left(\frac{\langle n\rangle}{n_c} - 1\right)^{\sigma}, \qquad \text{if} \qquad N^{-1/\nu} \ll \frac{\langle n\rangle}{n_c} - 1 \ll 1 \\ &\propto N^{-\sigma/\nu}, \qquad \text{if} \qquad \frac{\langle n\rangle}{n_c} - 1 \ll N^{-1/\nu} \end{aligned} \tag{5.10}$$

where $\sigma = 1/2$. Thus, at a finite but large size $N \gg 1$, the relaxation rate γ_r is nonzero at any $\langle n\rangle$ due to finite-size effects that smear the critical singularity. This agrees with results of our simulations presented below.

5.1.5 Power spectral density near the 1st-order phase transition

We now find the power spectral density (PSD) of activity fluctuations in the low activity state when $\langle n\rangle$ is close to n_{c2}. The PSD of fluctuations of neuronal activity encodes rich information about critical phenomena. According to the Wiener-Khintchine theorem, the power spectral density $S(\omega)$ of activity fluctuations of the excitatory population is the Fourier transform of the autocorrelation function $C_{ee}(t)$:

$$S(\omega) = \frac{1}{2\pi}\int_{-\infty}^{\infty} e^{-i\omega t} C_{ee}(t) dt. \tag{5.11}$$

The autocorrelation function

$$C_{ab} \equiv \frac{1}{T}\int_0^T \delta\rho_a(t_1)\delta\rho_b(t_1 + t) dt_1, \tag{5.12}$$

where $\delta\rho_a(t) = \rho_a(t) - \rho$, describes the fluctuations of activity $\rho_a(t)$ of population $a, b = e, i$, around the averaged value ρ. $C_{ab}(t)$ is a measure of the correlations between values of $\delta\rho_a(t_1)$ and $\delta\rho_b(t_1 + t)$ at two different instants separated by a lag t and averaged over a large time window T (according to, for instance, [184]). Additionally, the PSD is also defined as

$$S(\omega) \equiv \langle \delta\tilde{\rho}_e(\omega)\delta\tilde{\rho}_e(-\omega)\rangle. \tag{5.13}$$

In order to calculate the PSD, we assume that activity fluctuations are driven by weak white-noise forces $F_a(t)$ that mimic forces caused by finite-size effects,

$$\langle F_a(t)F_b(t')\rangle = F_0^2\delta_{a,b}\delta(t - t'), \tag{5.14}$$

where $F_0 \propto 1/\sqrt{N}$. These forces act on excitatory and inhibitory neurons that are inactive at time t. Thus, Eqs. (3.15) become

$$\begin{aligned} \dot{\rho_e}(t) &= F_e(t)[1 - \rho_e(t)] - \mu_e\rho_e(t) + \mu_e\Psi(\rho_e(t), \rho_i(t)), \\ \dot{\rho_i}(t) &= F_i(t)[1 - \rho_i(t)] - \mu_i\rho_i(t) + \mu_i\Psi(\rho_e(t), \rho_i(t)). \end{aligned} \tag{5.15}$$

This method was also used in [130]. In this case, one can use the linear response theory to find $\delta\rho_a(t) = \rho_a(t) - \rho$ from the linearized system. Equation (4.14) has now a new term:

$$\dot{\vec{\delta\rho}} = (1-\rho)\vec{F} + \hat{J}(\rho)\vec{\delta\rho} \tag{5.16}$$

where $\vec{F} = [F_e(t), F_i(t)]$. Making the Fourier transformation

$$\delta\tilde{\rho}_a(\omega) = \frac{1}{2\pi}\int_{-\infty}^{\infty} e^{-i\omega t}\delta\rho_a(t)dt, \tag{5.17}$$

we find the linear response

$$\begin{aligned}
\delta\tilde{\rho}_e(\omega) &= \frac{(1-\rho)[(i\omega - J_{22})\tilde{F}_e(\omega) + J_{12}\tilde{F}_i(\omega)]}{(i\omega+\lambda_+)(i\omega+\lambda_-)}, \\
\delta\tilde{\rho}_i(\omega) &= \frac{(1-\rho)[(i\omega - J_{11})\tilde{F}_i(\omega) + J_{21}\tilde{F}_e(\omega)]}{(i\omega+\lambda_+)(i\omega+\lambda_-)},
\end{aligned} \tag{5.18}$$

where J_{ij} are the entries of the Jacobian, Eq. (4.16), and $\lambda_\pm$ are the eigenvalues, Eq. (4.20). Substituting this result into Eq. (5.12), we find the PSD for excitatory neurons

$$S(\omega) = \frac{F_0^2(1-\rho)^2}{2\pi}\frac{J_{12}^2 + J_{22}^2 + \omega^2}{(\lambda_+^2+\omega^2)(\lambda_-^2+\omega^2)}. \tag{5.19}$$

The PSD of inhibitory neurons is obtained from this equation after the replacements $J_{12} \to J_{21}$ and $J_{22} \to J_{11}$.

In the low activity state (fixed point 1), in regions Ib and Ic in Fig. 4.2, the eigenvalues λ_+ and λ_- are real. When the noise intensity $\langle n\rangle$ tends to the critical point n_{c2} of the first-order phase transition, the eigenvalue λ_+ tends to zero according to Eq. (5.8) while the eigenvalue λ_- remains finite. Therefore, at small ω, Eq. (5.19) takes the form

$$S(\omega) \approx \frac{F_0^2(1-\rho)^2(J_{12}^2 + J_{22}^2)}{2\pi\lambda_-^2\gamma_r^2}\frac{1}{(\omega/\gamma_r)^2+1}. \tag{5.20}$$

It means that the power spectral density has a sharp zero frequency peak described by the following shape function:

$$\frac{S(\omega)}{S_{max}} \approx \frac{1}{(\omega/\gamma_r)^2+1}, \tag{5.21}$$

where the peak maximum is $S_{max} \propto 1/\gamma_r^2$. Figure 5.2(a) displays the PSD $S(\omega)$ measured in our simulations in the low activity state in region Ic. In Fig. 5.2(b), we compare simulations with the theoretical prediction. One sees that Eq. (5.21) describes well the measured frequency dependence of the PSD. According to Eq. (5.8), at $\langle n\rangle \to n_{c2}$, the peak maximum increases as

$$S_{max} \propto \frac{1}{n_{c2} - \langle n\rangle}. \tag{5.22}$$

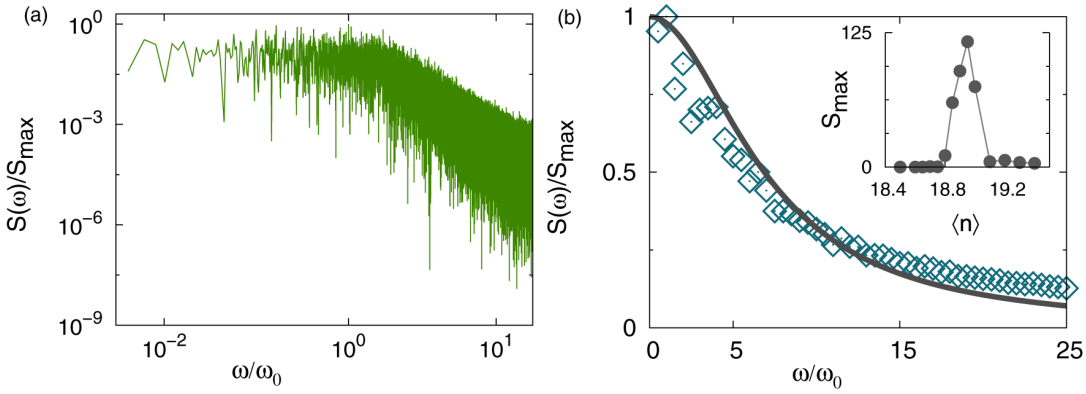

Figure 5.2: (a) Power spectral density $S(\omega)$ of activity fluctuations versus frequency ω in the low activity state of the cortical model (results of simulations at $(\langle n\rangle, \alpha) = (18.7, 0.85)$. (b) Averaged frequency dependence of $S(\omega)$ at small frequencies. Open diamonds show results of simulations. The solid line represents Eq. (5.21) with $\gamma_r = 6.9(2)$ and $\omega_0 \equiv \sqrt{\gamma_i^2 + \gamma_r^2} = 0.03$. Frequencies are in units of μ_e. Inset: zero-frequency peak $S_{max} = S(\omega = 0)$ versus the shot noise intensity $\langle n\rangle$ when increasing $\langle n\rangle$. The observation time was $10000\mu_e^{-1}$. Other parameters are the same as in Fig. 5.1. These data and figures were obtained by KyoungEun Lee.

Our simulations support the predicted increase of the zero-frequency peak S_{max} (see the inset in Fig. 5.2(b)). When $\langle n\rangle$ is close to n_{c2}, finite-size effects (Eqs. (5.10)) become important and γ_r remains nonzero even at the critical point, although very small. Consequently, S_{max} has a maximum at $\langle n\rangle = n_{c2}$ instead of divergency. The numerical results also confirm the linear decrease of $1/S_{max}$, $1/S_{max} \propto n_{c2} - \langle n\rangle$, predicted by Eq. (5.22) when $\langle n\rangle \to n_{c2}$. In contrast, S_{max} has no maximum at n_{c2} when $\langle n\rangle$ tends to n_{c2} from the high activity state (this is a manifestation of hysteresis).

The Lorentzian behavior of the PSD of synaptic currents has been observed in cat cortex during wakefulness [185]. In Ref. [185], it was suggested that this behavior may be driven by a white-noise process. During slow-wave sleep, the PSD deviates from the Lorentzian [185]. This deviation suggests that, in general, stochastic forces may be statistically different from white noise.

Thus, the cortical model shows that bursts and avalanches appear near the limiting point of metastable states of the first-order phase transition caused by a saddle-node bifurcation in agreement with other network models [136, 144, 174, 175]. Critical phenomena (power-law statistics for avalanches and sharp zero-frequency peak of the PSD) due to critical slowing down in the low activity state (when approaching the critical point from below), the absence of critical phenomena above the point (because, in the high activity state, the relaxation rate is nonzero at the critical point) and hysteresis are the characteristic properties of the first-order phase transition, which can be experimentally tested. Note that here we did not focus on what happens near n_{c1}, in the high activity state (fixed point

3), when decreasing the shot noise intensity $\langle n \rangle$. In this case, similar critical phenomena can be observed. In particular, instead of having avalanches that activate clusters of neurons, we have avalanches of inactivation, where the sudden inactivation of one neuron in a given cluster can lead to the inactivation of the complete cluster.

Another mechanism of avalanches based on ideas of self-organized criticality (SOC) by Per Bak [186] was discussed in [65, 66]. From our point of view, at the present time, there is no direct experimental evidence that supports one approach over the other. One important difference between the two mechanisms is that the critical phenomena appear symmetrically in respect to a critical point in SOC, whereas in a first-order phase transition it can only be measured when approaching the critical point from one side, as shown above. This difference may help to distinguish the two mechanisms in experiments. Further experimental and theoretical investigations of these two approaches are necessary to understand the origin of avalanches in the brain.

5.2 Second-order nonequilibrium phase transitions

We now consider the case $\alpha < \alpha_t$, i.e., when excitatory neurons respond sufficiently faster to stimuli compared to inhibitory neurons. We show that, when increasing the shot noise intensity, the cortical model undergoes successively two second-order phase transitions. We find that sustained network oscillations emerge at a saddle-node bifurcation and disappear at a Hopf bifurcation. We study properties of the phase transitions, critical phenomena, patterns of spontaneous activity, and sustained network oscillations near the critical intensities of shot noise. Note that the emergence of network oscillations implies the symmetry breaking of these two second-order phase transitions. The ordered phase must have a lower symmetry in comparison to the symmetry of the disordered phase [181]. In our model, in the state with damped oscillations or exponential relaxation, the behavior of the neuronal network, at large times, does not depend on initial conditions because relaxation time is finite. In contrast, in the state with sustained oscillations, the phase of oscillations at every moment is determined by the initial conditions. Therefore, it is the time homogeneity that is broken in the state of sustained network oscillations.

5.2.1 Saddle-node bifurcation

At a given $\alpha < \alpha_t$, we increase the shot noise intensity $\langle n \rangle$ from $\langle n \rangle = 0$ (see line 2 in Fig. 4.2). The neuronal network goes from region Ia with the single fixed point 1 into region Id or region Ie where the dynamics is determined by three fixed points: the stable point 1, the saddle point 2, and the unstable point 3 (see Table 4.1). At $\langle n \rangle = n_{c2}$, the points 1 and 2 coalesce and the network undergoes a second-order phase transition due to a saddle-node bifurcation from a state with a low activity and short-range temporal correlations between neurons into a state with regular sustained network oscillations and strong correlations (region IIIa or IIIb). In regions IIIa and IIIb, the dynamics of neuronal networks is determined by the unstable fixed point 3 surrounded by a limit cycle. At

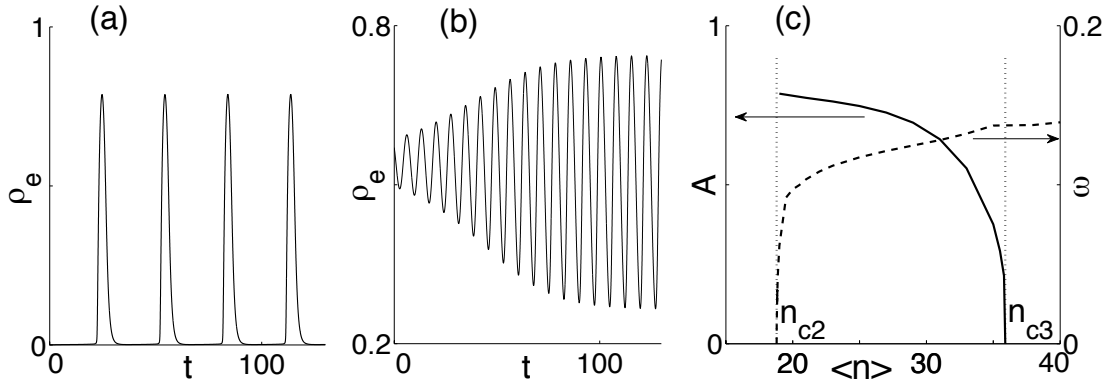

Figure 5.3: Network oscillations near (a) the saddle-node ($\langle n\rangle = 18.805, n_{c2} = 18.8$) and (b) supercritical Hopf ($\langle n\rangle = 34, n_{c3} = 36$) bifurcations. (c) Amplitude (solid line) and frequency (dashed line) of network oscillations versus $\langle n\rangle$. At $\langle n\rangle > n_{c3}(\alpha)$, the oscillations are damped. These results were obtained from numerical integration of Eqs. (3.15). Time t is in units of μ^{-1}, and $\alpha = 0.75$. Other parameters are the same as in Fig. 5.1.

$\langle n\rangle > n_{c2}$, the network oscillations emerge with a large amplitude (see Fig. 5.3(a)) and their frequency increases from zero as $\omega \propto \sqrt{\langle n\rangle - n_{c2}}$ (see Fig. 5.3(c)). This frequency dependence is a general feature of oscillations in nonlinear dynamic systems close to a saddle-node bifurcation [116, 187, 188]. Note, however, that in our model we deal with a phase transition, i.e., a collective phenomenon in neuronal networks. We suggest that for this kind of continuous phase transition the frequency is the order parameter.

In simulations, at $\langle n\rangle$ below n_{c2}, we observe irregular almost identical sharp spikes of neuronal activity (see Fig. 5.4). These "spikes" are collective events of neuronal activity, obviously different from the spikes, action potentials, that neurons fire. This term is used, for instance, to designate some forms of epileptiform activity (see, for example, Ref. [94]), and it stresses the similarity with action potentials: both are strong single events. The sharp spikes are described by trajectories topologically equivalent to a heteroclinic orbit that connects points 2 to 1, and goes around the unstable point 3 in the $(\rho_e, \rho_i)-$phase plane (more details in Chapter 7). In our model, the mean frequency of the spikes is very small and increases when the shot noise intensity tends to the critical point n_{c2} while the spike duration is almost constant and much larger than the period $(1/f)$ of oscillations generated by a single neuron. This kind of activity differs sharply from bursts found near the first-order phase transition (compare the inset of Fig. 5.1(a) with the spikes in Fig. 5.4). The sharp spikes emerge from a low background activity with a rapid onset (Fig. 5.4(b)), reaching a large amplitude that involves in synchronized activity about 90% of neurons, and end up with an abrupt return to lower activity. In Fig. 5.4, the spike duration is about 90 ms and the mean interspike interval is about 34 s at $\mu_e^{-1} = 20$ ms.

In order to understand the mechanism of generation of sharp spikes, we performed the numerical integration of Eq. (5.15) with nonzero stochastic forces F_e and F_i representing finite-size effects at the same parameters as in simulations. The numerical integration also

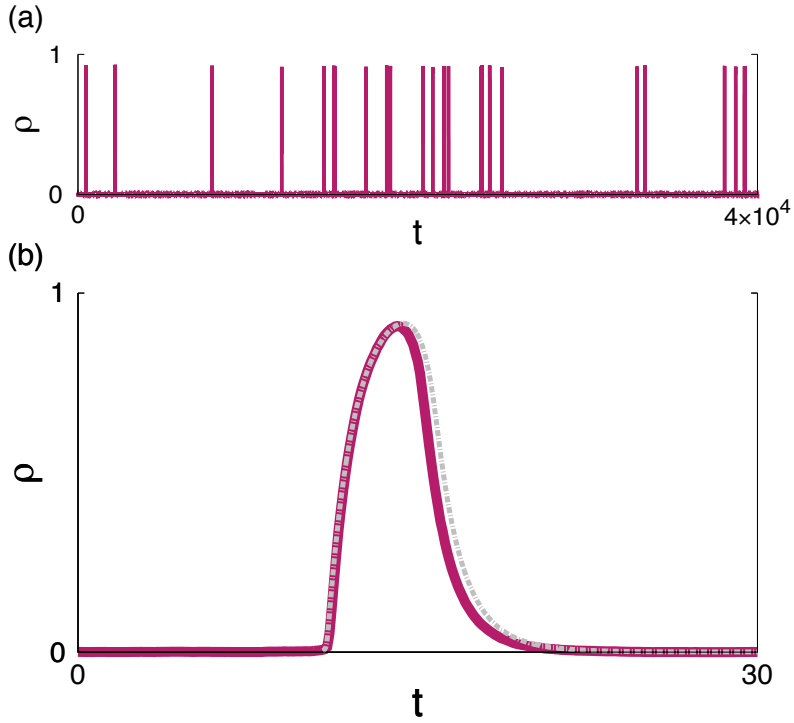

Figure 5.4: (a) Series of sharp spikes of neuronal activity near the saddle-node bifurcation. (b) All spikes of the time series at the same phase. Solid and dashed lines represent spikes found in simulations and numerical integration of Eqs. (5.15), respectively. Parameters: shot noise intensity $\langle n \rangle = 18.76$ and $\alpha = 0.55$. Other parameters are the same as in Fig. 5.1. Time t is in units of μ_e^{-1}. The data from simulations and figures were obtained by KyoungEun Lee.

---

reveals sharp spikes that are identical to those observed in simulations (Fig. 5.4(b)). Our analysis of the phase portrait of Eqs. (3.15) in regions Id and Ie shows that the sharp spikes are strongly nonlinear events in neuronal activity that can be generated by fluctuations (as we approach the critical point n_{c2}, it becomes easier to generate sharp spikes, because points 1 and 2 become closer). In the (ρ_e, ρ_i)-phase plane, the trajectories (Fig. 4.3 panels (h) and (j)) are topologically equivalent to the heteroclinic orbits found in the Morris-Lecar model (see Fig. 7.4 in Ref. [187]).

The analysis of the properties of the sharp spikes, such as emergence conditions, course of events, their shape, amplitude, duration, and frequency, leads us to propose that this kind of spontaneous neuronal activity is similar to epileptiform activity as the paroxysmal spikes observed in EEG [95, 189]. Based on this similarity we suggest that the paroxysmal spikes and other seizure-like events, such as slow-wave oscillations [95] or sharp waves in hippocampus [41, 190], are strongly nonlinear waves appearing in neuronal networks near a saddle-node bifurcation. Of course, in order to describe in detail the events, a realistic network structure and realistic single neuron dynamics must be taken into account. We

discuss this in more detail in Chapter 7.

At $\langle n \rangle$ below n_{c2}, the relaxation rate γ_r is $\gamma_r \propto \sqrt{n_{c2} - \langle n \rangle}$, as shown before. This result is in contrast to the standard mean-field theory (the Landau theory) that predicts $\gamma_r \propto |n_{c2} - \langle n \rangle|$ for a second-order phase transition. The non-standard scaling behavior and emergence of paroxysmal-like spikes near the saddle-node bifurcation show an unusual character of the phase transition. Our simulations and numerical integration also reveal an almost constant nonzero time lag Δt_l between excitatory and inhibitory activities at $\langle n \rangle$ around n_{c2}. For the spike in Fig. 5.4, the inhibitory activity reaches a maximum 11 ms after the excitatory activity.

In the context of stochastic resonance, several nonlinear dynamical systems [191–193] and single neuron models [56, 57, 193, 194], which have excitable dynamics of the same kind as the Morris-Lecar model and our cortical model, have been analysed (we discuss stochastic resonance in the next chapter). Phase transitions triggered by a saddle-node bifurcation were also found in complex physical and chemical systems such as the system of limit-cycle oscillators with all-to-all coupling [195] and CO oxidation on the Pt(110) surface [196]. However, critical phenomena and single nonlinear oscillations preceding the transition were not studied. Also, as far as we know, paroxysmal-like spikes as collective nonlinear objects were not studied within a neuronal network model. The nature and mechanism of generation of the paroxysmal-like spikes are discussed in Chapter 7.

5.2.2 Supercritical Hopf bifurcation

We now study the second-order phase transition due to the supercritical Hopf bifurcation. For this purpose, we perform simulations of the cortical model, numerical integration, and analytical analysis of Eqs. (3.15). We find critical behavior and demonstrate the difference in the critical properties between the saddle-node bifurcation and the supercritical Hopf bifurcations.

When increasing the shot noise intensity $\langle n \rangle$ above n_{c2}, the frequency of sustained oscillations increases while their amplitude decreases (see Fig. 5.3(c)). The oscillations disappear at the critical noise intensity $\langle n \rangle = n_{c3}$ which depends on α (see the line 2 in Fig. 4.2). At $\langle n \rangle = n_{c3}$, the network undergoes a phase transition from a state with the unstable point 3 surrounded by a limit cycle (region IIIa) into a state in which the fixed point 3 is a stable spiral (region IIb). From the stability analysis presented in Chapter 4, it follows that this transition is due to a supercritical Hopf bifurcation, because the eigenvalues of the fixed point 3 cross the imaginary axis, i.e., the real part of the eigenvalues changes sign. Above n_{c3}, the network enters region IIb with damped network oscillations about the fixed point 3. Note also that network oscillations taking place near the saddle-node and supercritical Hopf bifurcations have different shapes (compare Fig. 5.3(a) with Fig. 5.3(b)). Oscillations emerging due to a Hopf bifurcation were also found in a stochastic rate model [145].

Neuronal activity below the Hopf bifurcation

First, we study analytically sustained network oscillations and relaxation dynamics near the Hopf bifurcation in a shot noise intensity range $0 < |n_{c3} - \langle n \rangle| \ll n_{c3}$ (a range around the boundary between regions IIIa and IIb in Fig. 4.2). In this range, the oscillations have a small amplitude that allows us to use the Taylor expansion over $\delta\rho_a(t) = \rho_a(t) - \rho^{(3)}$ in Eqs. (3.15). Taking into account terms up to the third order in $\delta\rho_a(t)$, we obtain two coupled nonlinear equations

$$\begin{aligned}\frac{d\delta\rho_a(t)}{\mu_a dt} =& -\delta\rho_a(t) + D^{(1,0)}\delta\rho_e(t) + D^{(0,1)}\delta\rho_i(t) \\ &+ \frac{1}{2}\big(D^{(2,0)}\delta\rho_e(t)^2 + 2D^{(1,1)}\delta\rho_e(t)\delta\rho_i(t) + D^{(0,2)}\delta\rho_i(t)^2\big) \\ &+ \frac{1}{6}\big(D^{(3,0)}\delta\rho_e(t)^3 + 3D^{(2,1)}\delta\rho_e(t)^2\delta\rho_i(t) \\ &+ 3D^{(1,2)}\delta\rho_e(t)\delta\rho_i(t)^2 + D^{(0,3)}\delta\rho_i(t)^3\big),\end{aligned} \tag{5.23}$$

where $a = e, i$, and

$$D^{(n,m)} \equiv \frac{\partial^{n+m}\Psi}{\partial\rho_e^n \partial\rho_i^m}. \tag{5.24}$$

In Fig. 5.5(a), we compare results of numerical integration of the reduced equations (5.23) with the exact equations (3.15). In the numerical integration, we studied the relaxation of the system to a state with sustained oscillations (see Fig. 5.5(a)) from an initial point $\rho_e = \rho_i = \rho^{(3)}$. One sees that the frequency of the oscillations described by the reduced equations (5.23) is very close to the frequency of oscillations from the exact equations (3.15), though the amplitude of the sustained oscillations from Eqs. (5.23) is a little bit larger. These results evidence that the reduced equations (5.23) are a good approximation to the exact equations (3.15) (near the Hopf bifurcation). A similar analysis based on a reduced equation was used in [130, 131] to study analytically oscillations near the Hopf bifurcation in networks of integrate-and-fire neurons. Now, we can use the reduced equations to study the critical behavior of the amplitude of sustained oscillations, the relaxation rate to the state of oscillations, and the phase lag between the activities of excitatory and inhibitory populations.

It is convenient to rewrite Eqs. (5.23) in a vector form

$$\dot{\vec{\delta\rho}} = \hat{J}\vec{\delta\rho} + \hat{M}(\delta\rho_e, \delta\rho_i)\vec{\delta\rho}, \tag{5.25}$$

where $\hat{J}$ is the Jacobian (Eq. (4.16)), and $\hat{M}(\delta\rho_e, \delta\rho_i)$ is a matrix which contains the

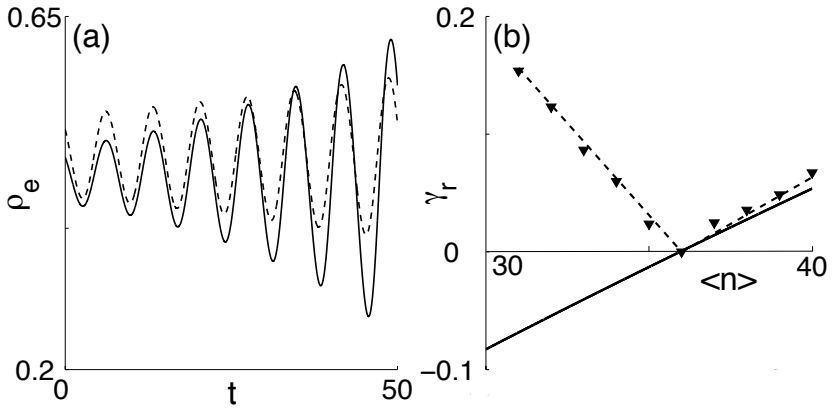

Figure 5.5: (a) Relaxation of the activity of excitatory neurons from an initial state (the fixed point 3) to a state with sustained network oscillations at $\langle n\rangle < n_{c3}$: the solid line represents the numerical integration of the approximate equations (5.23), and the dashed line is the solution of the exact equations (3.15). (b) The parameter γ_r (Eq. (4.21)) versus $\langle n\rangle$ from a numerical solution of Eq. (4.10) at the fixed point 3 (solid line). The relaxation rate γ_r^* is obtained from the numerical integration of equations (3.15) (triangles). Time t is in units of μ_e^{-1}. Parameters: $(\langle n\rangle, \alpha) = (36, 0.75)$. Other parameters are the same as in Fig. 5.1.

---

nonlinear terms

$$
\begin{aligned}
M_{11} &= \frac{1}{2}D^{(2,0)}\delta\rho_e + \frac{1}{6}D^{(3,0)}\delta\rho_e^2,\\
M_{12} &= \frac{1}{2}D^{(0,2)}\delta\rho_i + \frac{1}{6}D^{(0,3)}\delta\rho_i^2 + D^{(1,1)}\delta\rho_e + \frac{1}{2}D^{(2,1)}\delta\rho_e^2 + \frac{1}{2}D^{(1,2)}\delta\rho_e\delta\rho_i,\\
M_{21} &= \frac{\alpha}{2}D^{(2,0)}\delta\rho_e + \frac{\alpha}{6}D^{(3,0)}\delta\rho_e^2 + \alpha D^{(1,1)}\delta\rho_i + \frac{\alpha}{2}D^{(1,2)}\delta\rho_i^2 + \frac{\alpha}{2}D^{(2,1)}\delta\rho_e\delta\rho_i,\\
M_{22} &= \frac{\alpha}{2}D^{(0,2)}\delta\rho_i + \frac{\alpha}{6}D^{(0,3)}\delta\rho_i^2.
\end{aligned}
\tag{5.26}
$$

The Jacobian (Eq. (4.16)) can be represented in a form

$$\hat{J} = -\gamma_r\hat{I} + \vec{a}\hat{\vec{\sigma}}, \tag{5.27}$$

where $\hat{I}$ is the identity matrix. The parameter γ_r is determined by Eqs. (4.21) and (4.20) at the fixed point 3, $\rho^{(3)}$. In regions IIb and IIIa, Eq. (4.19) gives

$$\gamma_r = \frac{J_{11} + J_{22}}{2}. \tag{5.28}$$

Furthermore, $\vec{a}$ is a complex vector

$$\vec{a} = \frac{1}{2}\begin{pmatrix} J_{12} + J_{21} \\ iJ_{12} - iJ_{21} \\ J_{11} - J_{22} \end{pmatrix} \tag{5.29}$$

with the property $\vec{a}^2 = -\gamma_i^2$. We also use $\hat{\vec{\sigma}} = (\hat{\sigma_1}, \hat{\sigma_2}, \hat{\sigma_3})$ where $\hat{\sigma_1}$, $\hat{\sigma_2}$, and $\hat{\sigma_3}$ are the Pauli matrices. Taking into account only linear terms in $\delta\rho_a$, the solution of Eq. (5.25) can be written in a form

$$\delta\vec{\rho} = e^{-\gamma_r t + \vec{a}\hat{\vec{\sigma}}t}\vec{A} = e^{-\gamma_r t}\Big(\cos(\gamma_i t) + \frac{\sin(\gamma_i t)}{\gamma_i}\vec{a}\hat{\vec{\sigma}}\Big)\vec{A}, \tag{5.30}$$

where the vector $\vec{A} = (A_e, A_i)$ is determined by an initial condition $\vec{\rho}(t=0) = \vec{\rho_0}$.

The dependence of the parameter γ_r on $\langle n\rangle$ near the critical point n_{c3} can be found by use of the Taylor expansion of $Re\{\lambda_+(\rho^{(3)})\}$ in Eq. (4.21) over $\delta\rho = \rho^{(3)} - \rho^{(3)}(n_{c3})$:

$$\gamma_r(\rho^{(3)}) = -\mathrm{Re}\{\lambda_+[\rho^{(3)}(n_{c3})]\} - \frac{d\mathrm{Re}\{\lambda_+\}}{d\rho}\delta\rho + \ldots. \tag{5.31}$$

The neuronal activity $\rho = \rho^{(3)}(\langle n\rangle)$ near the Hopf bifurcation can also be found using the Taylor expansion (Eq. (5.1)) with $\varepsilon \equiv \langle n\rangle - n_{c3}$ and $\delta\rho \equiv \rho - \rho^{(3)}(n_{c3})$ (at $0 < \langle n\rangle - n_{c3} \ll n_{c3}$), where the function Ψ and its derivatives are calculated at $\langle n\rangle = n_{c3}$. In this case, the linear terms give the leading contribution to a solution

$$\rho^{(3)}(\langle n\rangle) - \rho^{(3)}(n_{c3}) \approx \frac{\partial\Psi}{\partial\langle n\rangle}\frac{\langle n\rangle - n_{c3}}{1 - d\Psi/d\rho}, \tag{5.32}$$

in contrast to the square root dependence in Eq. (5.2). Therefore, taking into account the critical slowing down, Eq. (4.24), and Eq. (5.32), we obtain

$$\gamma_r \approx \Gamma(\langle n\rangle - n_{c3}), \tag{5.33}$$

where the coefficient Γ is positive according to our numerical estimations. At $\langle n\rangle > n_{c3}$, γ_r is positive and neuronal activity weakly perturbed from the the stable fixed point 3 relaxes exponentially to the steady state with the relaxation rate γ_r (see Eq. (5.30)). At $\langle n\rangle < n_{c3}$, γ_r is negative and describes the process of runaway from the fixed point 3 (see Figs. 5.3(b) and 5.5(a)). In order to find a correct solution of Eq. (5.25) and the relaxation rate in the state with sustained network oscillations, we must take into account the nonlinear terms. We look for a solution in the following form:

$$\delta\vec{\rho} = e^{\vec{a}\hat{\vec{\sigma}}t}\vec{A}(t). \tag{5.34}$$

Then, Eq. (5.25) takes the form

$$\dot{\vec{A}} = -\gamma_r\vec{A} + e^{-\vec{a}\hat{\vec{\sigma}}t}\hat{M}(\delta\rho_e, \delta\rho_i)e^{\vec{a}\hat{\vec{\sigma}}t}\vec{A}. \tag{5.35}$$

In the leading order in $\varepsilon = n_{c3} - \langle n\rangle$, in the limit $t \to \infty$, the oscillation amplitude $\vec{A}(t)$ tends to a stationary value that can be found by use of the averaging theory [116]. We integrate Eq. (5.35) over the period $T = 2\pi/\gamma_i$ of oscillations,

$$0 = \int_0^T \{-\gamma_r\vec{A} + e^{-\vec{a}\hat{\vec{\sigma}}t}\hat{M}[\delta\rho_e(t), \delta\rho_i(t)]e^{\vec{a}\hat{\vec{\sigma}}t}\vec{A}\}dt, \tag{5.36}$$

and obtain two coupled equations for A_e and A_i:

$$\begin{aligned} 0 &= -\gamma_r A_e + a_1^{(e)} A_e^3 + a_2^{(e)} A_e^2 A_i + a_3^{(e)} A_e A_i^2 + a_4^{(e)} A_i^3, \\ 0 &= -\gamma_r A_i + a_1^{(i)} A_i^3 + a_2^{(i)} A_i^2 A_e + a_3^{(i)} A_i A_e^2 + a_4^{(i)} A_e^3, \end{aligned} \tag{5.37}$$

where $a_n^{(a)}$ are coefficients. A simple analysis of these equations shows that, at $|\gamma_r| \ll 1$, a solution for the complex amplitudes A_e and A_i has a form

$$\vec{A} = \sqrt{|\gamma_r|}\vec{B} \propto \sqrt{n_{c3} - \langle n \rangle}\vec{B}, \tag{5.38}$$

where $\vec{B} = (e^{i\varphi_e} b_e, e^{i\varphi_i} b_i)$ is a complex vector and $\Delta\varphi = \varphi_e - \varphi_i$ is a phase lag between excitatory and inhibitory activities. The square root dependence in Eq. (5.38) agrees with the numerical solution of Eqs. (3.15) for the supercritical Hopf bifurcation (see Fig. 5.5(c)). This dependence is a general property of the supercritical Hopf bifurcation (which distinguishes this bifurcation from the subcritical type) [116].

Equation (5.35) also allows us to find the relaxation rate of perturbed neuronal activity in the region IIIa of sustained network oscillations. We denote the relaxation rate as γ_r^* in order to distinguish it from the parameter γ_r (that describes the runaway from the fixed point 3, rather than the relaxation to the oscillations with constant amplitude). We look for a solution of Eq. (5.35) in a form

$$\vec{A}(t) = \vec{A} + e^{-\gamma_r^* t}\delta\vec{A}, \tag{5.39}$$

where $\delta\vec{A}$ is a small perturbation and $\gamma_r^* \ll \gamma_i$ is assumed. A linear perturbation analysis with respect to $\delta\vec{A}$ gives

$$\gamma_r^* \approx G(n_{c3} - \langle n \rangle), \tag{5.40}$$

where G is a positive coefficient. γ_r^* tends to zero when $\langle n \rangle \to n_{c3}$. Results of our numerical calculations displayed in Fig. 5.5(b) agree with this result. In the numerical integration of Eqs. (3.15), we choose the fixed point 3 as the initial condition, i.e., $\rho_e(t = 0) = \rho_i(0) = \rho^{(3)}$. Since the point 3 is unstable, at first the amplitude of network oscillations exponentially increases in time with the rate $-\gamma_r$ (see Fig. 5.5(a)). At large t, the amplitude tends exponentially (with the relaxation rate γ_r^*) to a steady value.

Solving Eqs. (5.37), we find the phases φ_e and φ_i. The lag $\Delta\varphi = \varphi_e - \varphi_i$ is proportional to $|\gamma_r|$, i.e.,

$$\Delta\varphi \approx \phi^*(n_{c3} - \langle n \rangle), \tag{5.41}$$

where ϕ^* is a positive coefficient. At $\langle n \rangle \geq n_{c3}$, in the state with damped oscillations, the phase lag $\Delta\varphi$ is determined by Eq. (5.47) (which we find in the next section) and (5.33) that give

$$\Delta\varphi \approx \phi(\langle n \rangle - n_{c3}), \tag{5.42}$$

where the positive coefficient ϕ differs from ϕ^*. Thus, the phase lag $\Delta\varphi$ is zero at the critical point and increases with increasing distance $|\langle n \rangle - n_{c3}|$ from the critical point. $\Delta\varphi$ determines the time lag $\Delta t_l = \Delta\varphi/\gamma_i$ between maximums of excitatory and inhibitory

activities. At $\langle n \rangle = n_{c3}$, $\Delta\varphi$ and Δt_l are zero which means a strict synchronization between excitatory and inhibitory activities. This is in contrast to the always-finite time lag in the case of the saddle-node bifurcation.

Thus, Eqs. (5.38), (5.40), and (5.41) show that, when the shot noise intensity $\langle n \rangle$ tends to the critical point n_{c3} of the supercritical Hopf bifurcation, the phase transition is signaled by a decrease of the oscillations amplitude $\vec{A}$, the relaxation rate γ_r^*, and the time lag Δt_l. At $\langle n \rangle = n_{c3}$, γ_r^* is zero which manifests critical slowing down. The amplitude $\vec{A}$ is the order parameter of the phase transition. These phenomena are general features of the supercritical Hopf bifurcation. Comparing Eq. (5.40) with Eq. (5.8) and the behavior of the time lag Δt_l at $\langle n \rangle = n_{c2}$ and at $\langle n \rangle = n_{c3}$, we conclude that the continuos phase transitions corresponding to the saddle-node and supercritical Hopf bifurcations have different critical behaviors and, therefore, belong to different classes of universality.

Neuronal activity above the Hopf bifurcation

As mentioned in the previous chapter, our simulations show that, above n_{c3}, spontaneous activity has a form of spindle oscillations (see the inset in Fig. 5.6). If $\langle n \rangle$ tends to n_{c3} from above, then the amplitude of spindle oscillations increases while the relaxation rate γ_r tends to zero as $\gamma_r \propto \langle n \rangle - n_{c3}$ according to Eq. (5.33). It results in an increase of the peak of the power spectral density of activity fluctuations at the frequency of damped oscillations (see Fig. 5.6). Moreover the phase lag $\Delta\varphi$ between synchronized activities of excitatory and inhibitory populations also tends to zero as $\Delta\varphi \propto \langle n \rangle - n_{c3}$ according to Eq. (5.42). These critical phenomena signal an approach to the Hopf bifurcation. In order to understand the phenomena, we use simulations and analytical calculations.

In the high activity state (fixed point 3) at $\langle n \rangle > n_{c3}$ (region IIb in Fig. 4.2), the eigenvalues $\lambda_\pm$ are complex. Their real and imaginary parts determine the relaxation rate γ_r and the frequency γ_i of damped oscillations, respectively (see Eqs. (4.21) and (4.22)). In this case, Eq. (5.19) can be written in a form

$$S(\omega) = \frac{F_0^2(1-\rho)^2}{2\pi\omega_0^4} \frac{J_{12}^2 + J_{22}^2 + \omega_0^2 x^2}{(x^2-1)^2 + 4\zeta^2 x^2}, \tag{5.43}$$

where $x \equiv \omega/\omega_0$, $\omega_0 \equiv \sqrt{\gamma_i^2 + \gamma_r^2}$, and $\zeta \equiv \gamma_r/\omega_0$. ζ is the damping ratio of the damped oscillations.

In the case when the shot noise intensity $\langle n \rangle$ tends from above to the critical point n_{c3}, the relaxation rate γ_r tends to zero (see Eq. (5.33)). If $\zeta \ll 1$, then the PSD has a sharp peak at the resonance frequency $\omega = \omega_r \equiv \omega_0\sqrt{1-2\zeta^2}$. The peak maximum is

$$S_{max} \equiv S(\omega_r) = \frac{F_0^2(1-\rho)^2}{2\pi\omega_0^4} \frac{J_{12}^2 + J_{22}^2 + \omega_0^2(1-2\zeta^2)}{4\zeta^2(1-\zeta^2)}. \tag{5.44}$$

Near the resonance frequency $|\omega - \omega_r| \ll \omega_0$, $S(\omega)$ is described by a shape function $F(x,\zeta)$:

$$\frac{S(\omega)}{S_{max}} \approx F(x,\zeta) \equiv \frac{4\zeta^2(1-\zeta^2)}{(1-x^2)^2 + 4\zeta^2 x^2}. \tag{5.45}$$

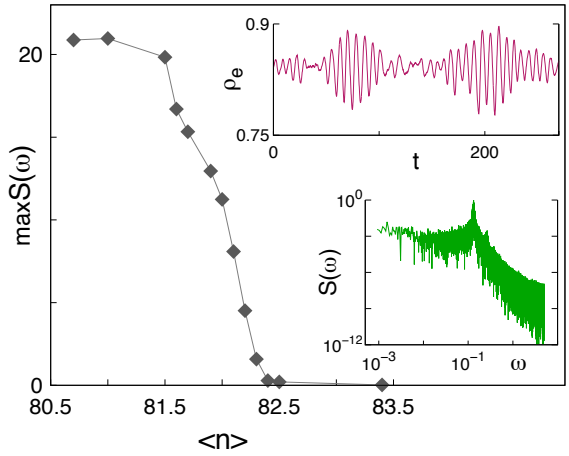

Figure 5.6: The peak maximum S_{max} of the power spectral density (PSD) of fluctuations versus $\langle n \rangle$ above the supercritical Hopf bifurcation (in simulations, $\langle n \rangle > n_{c3} \approx 80.5$ and $\alpha = 0.55$). Inset: temporal neuronal activity in the form of spindles (upper panel) and the PSD $S(\omega)$ versus the frequency ω at $\langle n \rangle = 82.5$. Other parameters are the same as in Fig. 5.1. Time t is in units of μ_e^{-1}. These data and figures were obtained by KyoungEun Lee.

Substituting Eqs. (5.18) into Eq. (5.12), we find that the autocorrelation function $C_{ee}(t)$ has a form

$$C_{ee}(t) = A_e e^{-\gamma_r t} \cos(\gamma_i t + \varphi_e). \tag{5.46}$$

The amplitude A_e and the phase φ_e behave as $A_e \propto 1/\gamma_r$ and $\varphi_e \propto \gamma_r/\gamma_i$ at $\gamma_r \ll \gamma_i$. Thus, as $\langle n \rangle$ approaches the critical point n_{c3} from above, the amplitude of the damped oscillations increases. For inhibitory neurons, we obtain a similar behavior with A_i and φ_i. There is a phase lag between the maximums of excitatory and inhibitory activities,

$$\Delta\varphi = \varphi_e - \varphi_i \propto \frac{\gamma_r}{\gamma_i}, \tag{5.47}$$

which, again, is related with the time lag $\Delta t_l = \Delta\varphi/\gamma_i$. Interestingly, from data analysis of the time dependence of the autocorrelation function (Eq. (5.12) and Eq. (5.46)), one can find the relaxation rate γ_r that determines the time decay of the damped oscillations, and also the dimensionless parameter ζ, which is an important characteristic of the closeness of the network to the critical point n_{c3}. The smaller is ζ, the closer is the network to the critical point. In the infinite-size limit, ζ is zero at $\langle n \rangle = n_{c3}$. A similar resonance peak of the PSD was found within the integrate-and-fire model in [131–133].

We confirmed the prediction of Eq. (5.46) using simulations. We analysed time series $\delta\rho_e(t_i)$ for $i = 1, \ldots, N_T$, and calculated the autocorrelation function $C_{ee}(t)$ using the discrete representation of Eq. (5.12),

$$C_{ee}(t) = \frac{1}{N_T} \sum_{i=1}^{N_T} \delta\rho_e(t_i)\delta\rho_e(t_i + t). \tag{5.48}$$

The number of points N_T in the time interval T was 7000. Figure 5.7(d) shows the autocorrelation function C_{ee}(t) of the excitatory activity. One can see that $C_{ee}(t)$ has a form of damped oscillations as predicted by Eq. (5.46). When decreasing the noise level from $\langle n \rangle = 85$ to $\langle n \rangle = 82.5$, approaching the supercritical Hopf bifurcation, the amplitude of spindle oscillations increase (compare Fig. 5.7(a)-(c)), and the amplitude of the damped oscillations of the autocorrelation function also increases (see Fig. 5.7(d)), showing the enhancement of critical fluctuations preceding the transition. Damped oscillations of the autocorrelation function similar to the ones in Fig. 5.7(d) were also observed, for example, in spontaneous alpha activity in EEG recordings of a healthy man [197], and in EEG recordings of human epileptic seizures [167].

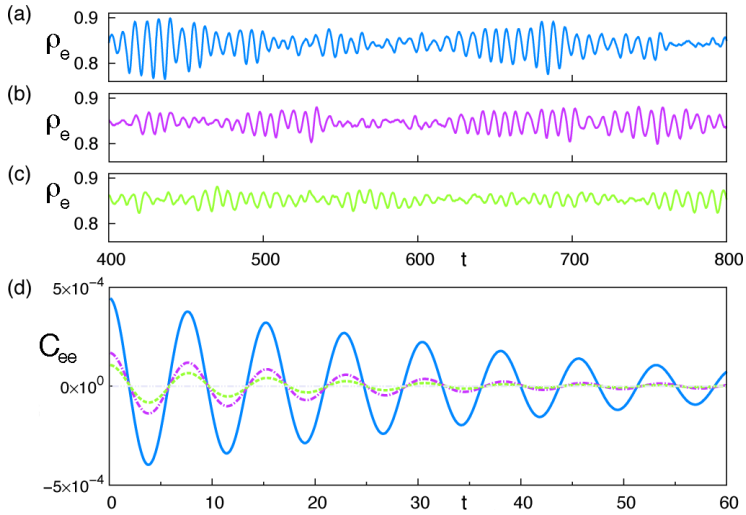

Figure 5.7: Panels (a), (b) and (c) display time series of activity of excitatory populations in the region of damped oscillations at shot noise levels $\langle n \rangle = 82.5$, $\langle n \rangle = 83.4$, and $\langle n \rangle = 85$, respectively (near $n_{c3} = 80.5$). (d) Autocorrelation function $C_{ee}(t)$, Eq. (5.48), versus time for the time series in panel (a) (solid blue line), panel (b) (dashed purple line), and panel (c) (dotted green line). Time is in units of μ_e^{-1}. The results were obtained from simulations of the cortical model with the following parameters: $\alpha = 0.55$, and $N = 10^5$. Other parameters are the same as in Fig. 5.1. These data and figures were obtained by KyoungEun Lee.

In Fig. 5.8, we present the PSD of activity fluctuations measured in simulations. In agreement with the theoretical prediction, the measured PSD, $S(\omega)$, reveals a sharp maximum at the frequency of damped oscillations. Figure 5.6 shows that, when $\langle n \rangle \to n_{c3}$, the maximum value S_{max} first strongly increases and then saturates at a certain value due to finite-size effects (Eqs. (5.10)). Figure 5.8 shows that the shape of this maximum is well described by the shape function (5.45).

The critical behavior of the cortical model near the supercritical Hopf bifurcation helps to understand the attenuation of alpha rhythms by visual or auditory stimuli (the Berger effect) [198, 199]. Recall that the Berger effect manifests itself in the activation of alpha

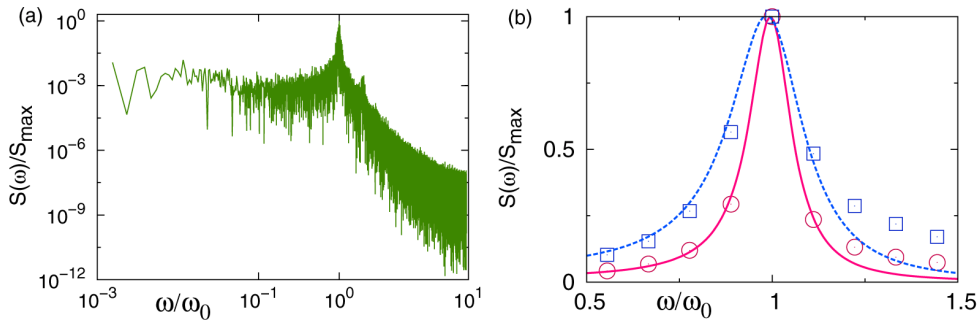

Figure 5.8: (a) Power spectral density $S(\omega)$ of activity fluctuations above the supercritical Hopf bifurcation at $\langle n \rangle = 82.5$ (from simulations). (b) Averaged frequency dependence of $S(\omega)$ around the peak at $\omega_0 = 0.15$: the PSD at $\langle n \rangle = 85$ (blue open rectangles); the analytical calculation from Eq. (5.45) with $\gamma_r = 0.12(1)$ (blue dashed line); the PSD at $\langle n \rangle = 82.5$ (pink open circles); the analytical calculation from Eq. (5.45) with $\gamma_r = 0.069(4)$ (pink solid line). In both figures $\alpha = 0.55$, and $n_{c3} \approx 80.5$. Other parameters are the same as in Fig. 5.1. Frequencies are in units of μ_e. These data and figures were obtained by KyoungEun Lee.

waves on the electroencephalogram when the eyes are closed and diminution of alpha waves when they are opened (see, for example, the review [198]). Based on our cortical model, we suggest that opening eyes may result in an increase of the flow of spikes bombarding neurons in the area of the cortex that is responsible for the alpha waves. As a result, the neuronal network goes away from the Hopf bifurcation and the amplitude of damped oscillations decreases. A similar phenomenon was also observed in the auditory cortex where the tau rhythm (this rhythm belongs to the family of alpha rhythms) was transiently suppressed by auditory stimuli [199].

Band-pass filter behavior

Above the supercritical Hopf bifurcation, in region IIb, the activities ρ_e and ρ_i relax to the stable fixed point 3 in the form of damped oscillations. Indeed, if we take the time derivative of the two coupled equations (5.15), we find in the linear-response regime that the neuronal network behaves as a damped oscillator driven by $\Phi_e(t)$,

$$\frac{d^2\delta\rho_e(t)}{dt^2} + 2\zeta\omega_0\frac{d\delta\rho_e(t)}{dt} + \omega_0^2\delta\rho_e(t) = \Phi_e(t), \tag{5.49}$$

where $\delta\rho_e(t) \equiv \rho_e(t) - \rho^{(3)}$, and

$$\Phi_e(t) = (1 - \rho^{(3)})\Big(\frac{dF_e(t)}{dt} - J_{22}F_e(t)\Big), \tag{5.50}$$

when $F_i(t) = 0$ (J_{22} is given by Eq. (4.16)). The damping ratio ζ determines the behavior of the neuronal network. The oscillator is overdamped if $\zeta > 1$ and underdamped if $\zeta < 1$.

Taking into account its definition, $\zeta = \gamma_r/\sqrt{\gamma_r^2 + \gamma_i^2}$, the network always behaves as an underdamped oscillator. Consistently, the angular frequency of the underdamped oscillator is in general

$$\omega = \omega_0\sqrt{1-\zeta^2}, \tag{5.51}$$

substituting the undamped frequency $\omega_0 = \sqrt{\gamma_r^2 + \gamma_i^2}$ and the damping ratio $\zeta = \gamma_r/\omega_0$, we obtain $\omega = \gamma_i$, as expected.

We can also determine the linear response function $\chi_{ab}(t-t')$,

$$\delta\rho_a(t) = \sum_{b=e,i}\int_{-\infty}^{t}\chi_{ab}(t-t')F_b(t')dt'. \tag{5.52}$$

Taking into account Eq. (5.49), we obtain

$$\chi_{ee}(t-t') = X_e e^{-\gamma_r(t-t')}\sin\Big(\gamma_i(t-t') - \theta_e\Big), \tag{5.53}$$

where

$$X_e = (1-\rho^{(3)})\sqrt{1 + \frac{(J_{22}+\gamma_r)^2}{\gamma_i^2}}, \tag{5.54}$$

and

$$\theta_e = \tan^{-1}\Big(\frac{\gamma_i}{J_{22}+\gamma_r}\Big). \tag{5.55}$$

If $\gamma_r > 0$, then Eq. (5.53) shows loss of memory in the neuronal network with increasing the time interval $t-t'$. When $\gamma_r \to 0$, the memory becomes long-range. The Fourier transform $\widetilde{\chi}_{ee}(\omega)$ of the linear response function in Eq. (5.53) is

$$\widetilde{\chi}_{ee}(\omega) = \frac{(1-\rho^{(3)})(i\omega - J_{22})}{\omega_0^2 - \omega^2 + 2i\zeta\omega_0\omega}. \tag{5.56}$$

The function $||\widetilde{\chi}_{ee}(\omega)||$ has a maximum at the resonance frequency ω_r, $||\max\widetilde{\chi}_{ee}(\omega)|| = ||\widetilde{\chi}_{ee}(\omega_r)||$ ($\omega_r = \omega_0\sqrt{1-2\zeta^2}$). At the critical point n_{c3}, ζ is zero and $||\widetilde{\chi}_{ee}(\omega_r)||$ diverges. The divergency of the response function is a characteristic feature of a second-order phase transition. One should also remind that the response function is related to the power spectral density,

$$S(\omega) = F_0^2||\widetilde{\chi}_{ee}(\omega)||^2, \tag{5.57}$$

because the autocorrelation function of fluctuations is

$$C_{ee}(t) = 2\pi F_0^2\int_{-\infty}^{\infty} e^{i\omega t}||\widetilde{\chi}_{ee}(\omega)||^2 d\omega, \tag{5.58}$$

and the PSD is equal to the Fourier transform of the autocorrelation function, according to the Wiener-Khintchine theorem, Eq. (5.11). Thus, the behavior of the response function near the supercritical Hopf bifurcation is equivalent to the behavior of the PSD studied above. Equation (5.56) shows that if the damping ratio $\zeta < 1/\sqrt{2}$, the neuronal network

acts as a band-pass filter. It passes frequencies within a range of the order of $\zeta\omega_0$ around the resonance frequency ω_r, while frequencies outside that range are attenuated. Moreover, at $\zeta \ll 1$, frequencies around the resonance frequency ω_r are strongly enhanced, because the $||\widetilde{\chi}_{ee}(\omega_r)||$ diverges as $1/\zeta$ when $\zeta \to 0$ ($\langle n \rangle \to n_{c3}$). The function $\widetilde{\chi}_{ii}(\omega)$ for inhibitory neurons has a similar behavior.

In physics and engineering, the dimensionless quality factor (Q factor) determines the qualitative behavior of simple damped oscillators or resonators and characterizes a resonator's bandwidth Δf relative to its center frequency f_c, i.e.,

$$Q = \frac{f_c}{\Delta f}. \tag{5.59}$$

For a damped oscillator [200], we have

$$Q = \frac{1}{2\zeta}, \tag{5.60}$$

$f_c = \omega_0$, and $\Delta f = \omega_0/Q$. Thus, in our neuronal network, the Q factor is

$$Q = \frac{\omega_0}{2\gamma_r} = \frac{\sqrt{\gamma_i^2 + \gamma_r^2}}{2\gamma_r}. \tag{5.61}$$

A higher Q implies a lower attenuation, i.e., the network oscillations die out more slowly. Accordingly, when approaching the critical point $\gamma_r \to 0$, the Q factor increases as

$$Q \approx \frac{\gamma_i}{2\gamma_r}. \tag{5.62}$$

One can, for instance, estimate the Q factors of the activities presented in the time series displayed in Fig. 5.7. At $\langle n \rangle = 82.5$, $\gamma_i \approx 0.82$ and $\gamma_r \approx 0.022$, we find $Q = 19$; at $\langle n \rangle = 83.4$, $\gamma_i \approx 0.85$, and $\gamma_r \approx 0.034$, $Q = 12$; and at $\langle n \rangle = 85$, $\gamma_i \approx 0.83$, and $\gamma_r \approx 0.037$, $Q = 11$. The Q factor increases as we approach the critical point, as expected. Thus, in experiments, the Q factor can be used to estimate the distance of the neuronal network to the supercritical Hopf bifurcation.

In order to confirm the band-pass filter behavior in region IIb, we carried out simulations of the cortical model with $N = 10^4$ neurons. We studied the case when a periodic stimulus $f(t) = f_0(1+\sin(\omega t))$ with amplitude $f_0 = 5$ modulates the activation threshold of neurons, $\Omega(t) = \Omega - f(t)$ (remember that $V_{th} = \Omega/J_e$ in Eqs. (3.15), and $\Omega = 30$). Figure 5.9 displays our results at three frequencies ω of periodic stimulation: (a) $\omega < \gamma_i$; (b) $\omega \approx \gamma_i$ (resonance); and (c) $\omega > \gamma_i$. One can see that a weak periodic stimulation results in synchronized neuronal activity when the frequency is close to the intrinsic frequency of damped oscillations γ_i. Stimuli with frequencies above and below γ_i affect weakly the neuronal activity.

The band-pass filter behavior described by Eq. (5.56) seems to be supported by measurements of the response of rat CA1 neurons to afferent stimulation *in vitro* [64]. These

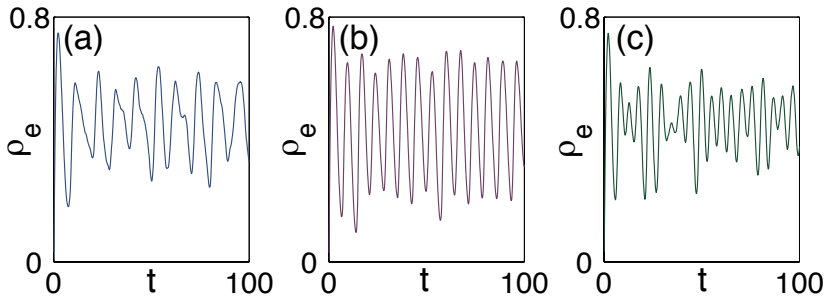

Figure 5.9: Band-pass filter behavior. Temporal activity of excitatory populations stimulated by a sinusoidal stimulus (amplitude $f_0 = 5$) with frequency ω: (a) $\omega = 0.61 < \gamma_i$; (b) $\omega = 0.87 \approx \gamma_i$ (resonance); and (c) $\omega = 1.2 > \gamma_i$. Time t is in units of μ_e^{-1}. Parameters in simulations: $(\langle n \rangle, \alpha) = (20.4, 0.82)$, and $N = 10^4$. Other parameters are the same as in Fig. 5.1. These data were obtained by KyoungEun Lee.

measurements revealed that the majority of rat CA1 neurons act collectively like a band-pass filter and fire synchronously in response to a limited range of presynaptic firing rates ($20 - 40$ Hz) that are in the range of gamma oscillations in the rat hippocampus [201]. One can also note that, a long time ago, a number of characteristics of a band-pass filter behavior and a resonance response to a sinusoidal wave were observed in EEG recordings of alpha waves [197]. Based on the results obtained above, we suggest that the band-pass filter behaviors observed in [64] and [197] are a manifestation of the damped oscillator behavior that occurs when the neuronal network is close to a supercritical Hopf bifurcation.

5.3 Similarity between our model and the Morris-Lecar model

In Chapter 4, we discussed the local stability of the fixed points and, in this chapter, the bifurcations of the nonlinear equations (3.15) in dependence on the shot noise intensity and the parameter α. Figure 5.10 displays the bifurcation diagram of our model at $\alpha < \alpha_t$. A similar bifurcation diagram was found within the Morris-Lecar model stimulated by an applied current in the case when the $I - V$ relation is N shaped [187]. The Morris-Lecar model is a two-dimensional simplified version of the Hodgkin-Huxley model to describe single neuron dynamics. Within this model, a system of two nonlinear equations describes a relationship between the membrane potential and the activation of K^+ ion channels within the membrane. Moreover, one can build phase portraits of Eqs. (3.15). In the case $\alpha < \alpha_t$, the phase portraits in regions Id, Ie, IIIa, and IIIb are topologically equivalent (in other words, homeomorphic) to the phase portraits found in the Morris-Lecar model [187]. It is well known that the topological equivalence of phase portraits of two dynamical systems results in similar dynamics and similar responses to stimuli [165]. Therefore, the dynamic behavior of our cortical model stimulated by shot noise is similar in some respects to the

dynamic behavior of the Morris-Lecar model stimulated by an applied current. Thus, we can apply results obtained for the well-studied Morris-Lecar model to our cortical model. Izhikevich [188] showed that the Morris-Lecar neuron acts as an "integrator", when it is close to the saddle-node bifurcation, and as a "resonator", when it is close to the Hopf bifurcation. Based on the topological equivalence, we can conclude that the cortical model acts in a similar way near the bifurcations. Indeed, in Subsection 5.2.1, we showed that if the mean frequency of incoming random spikes is a little bit larger than the critical frequency corresponding to the saddle-node bifurcation, then a neuronal network oscillates with an arbitrary low frequency. The higher the mean frequency of incoming random spikes, the higher the frequency of sustained network oscillations. Thus, we can say that the network acts as an integrator. In contrast, when the network is in the rest state near the supercritical Hopf bifurcation, it acts as a resonator because it responds preferentially to a certain (resonant) frequency of input (see Subsection 5.2.2). Furthermore, in Subsection 5.2.1, the topological equivalence helped us to understand the nature of paroxysmal-like spikes observed near the saddle-node bifurcation because similar nonlinear spikes were found in the Morris-Lecar model [187]. In agreement with this similarity between single neuron and network dynamics, in experiments with neuronal cultures, it has been observed that neurons form clusters that behave as "super-neurons", i.e., with excitable properties similar to single neurons [180].

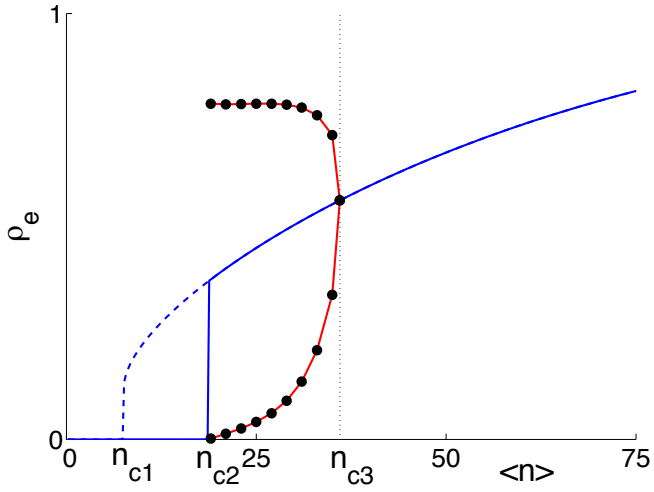

Figure 5.10: Bifurcation diagram that shows the dependence of the activity ρ_e on the shot noise intensity $\langle n \rangle$ at $\alpha < \alpha_t$. The blue line is the numerical solution of Eq. (4.10). In the interval $n_{c1} < \langle n \rangle < n_{c2}$, there are three fixed points: the fixed point 1 is of low activity (indistinguishable from zero in this figure); the fixed point 2, which is not represented; and the fixed point 3 (dashed line), which is unstable. (Note that Eq. (4.10) does not depend on α, therefore the blue line also represents the hysteresis at $\alpha > \alpha_t$.) In the interval $n_{c2} < \langle n \rangle < n_{c3}$, the fixed point 3 is unstable which results in a limit cycle. The maximums and minimums of the limit cycle are represented by the red line (the black dots are the maximums and minimums of sustained network oscillations obtained from numerical integration of Eqs. (3.15) at different levels of shot noise). The limit cycle emerges with large amplitude at the saddle-node bifurcation ($\langle n \rangle = n_{c2}$) and disappears with zero amplitude at the supercritical Hopf bifurcation $\langle n \rangle = n_{c3}$. α equals 0.75, smaller than $\alpha_t \approx 0.80$. Other parameters are the same as in Fig. 5.1.

Chapter 6

Stochastic resonance and modular structure in signal detection

6.1 Introduction

As stated in previous chapters, noise is ubiquitous in the brain, in particular, in sensory systems and strongly affects their function [48, 49]. Understanding how sensory systems compensate, counter or account for noise in order to detect and process sensory information remains elusive. Stochastic resonance (SR) is recognized as a possible mechanism that allows sensory systems to use noise for their own benefit [48–50]. As explained in Section 1.6, SR is a phenomenon that manifests itself in an amplification and an optimization of weak signals by noise. It was revealed in many physical systems [47]. Namely in the brain, SR was observed experimentally in sensory systems [52–55], and other areas [51, 56–58, 60]. SR is also considered a mechanism that may mediate neuronal synchronization within and between functionally relevant brain areas [61–63].

Most of the theoretical works on SR, including the seminal paper [202], and experimental realizations of SR refer to systems based on the motion of a particle subjected to a weak periodic signal in a bistable potential [47]. Another mechanism of SR was revealed in a class of dynamical systems based on excitable dynamics [191, 193]. A key ingredient of these systems is that if the system is kicked by a stimulus from its "rest state" above an activation threshold, then it returns to the state deterministically, within a certain refractory time [191–193]. Based on these ideas, several single neuron models have been proposed to explain SR observed in the brain [53, 56, 57, 193, 194].

SR was also observed at the level of an entire sensory system, i.e., as a collective phenomenon. Gluckman *et al.* [51] revealed a resonance in the response of a neuronal network from mammalian brain on a weak periodic electric stimulus with a certain magnitude of the stochastic component. Since no manifestation of SR at the single cell level was clearly seen in these experiments, one can assume that the observed SR has another nature. Until now, no theoretical explanation of these experiments was proposed. There are some studies of SR in arrays of neurons [203, 204] and summing networks [205], but they did not study

the role of interactions between neurons. Pacemaker-driven SR [15, 206] was observed in complex networks of interacting excitable units modeled by Rulkov's discrete map. Also, evidences for SR were found in simulations of small networks of interacting Hodgkin-Huxley neurons [207, 208] and in hippocampal CA3-CA1 networks [209]. Actually, small networks (at most 300 neurons in these papers) do not allow to study collective phenomena due to finite-size effects that manifest themselves in strong irregular fluctuations destroying synchronized activity of neurons. Their impact on critical fluctuations of neuronal activity was recently analyzed in [102]. The breaking of collective phenomena by finite-size effects is a well known phenomenon in physical systems [39, 183], but these effects are still poorly understood in the dynamics of neuronal networks.

In previous chapters we have shown that due to interactions among neurons, neuronal networks in the brain are nonlinear dynamical systems in which critical transitions from one to another dynamical state have bifurcation nature [116]. The influence of a bifurcation is not restricted by a region near the critical point in a space of network parameters. Actually, a bifurcation can expand their influence in a broad region of parameters sufficiently far from the critical point [102] (see Chapter 5). In particular, it can affect the excitability of neuronal networks and their sensitivity to weak stimuli. These dynamical properties determine the performance of signal detection in sensory systems. In the context of signal detection, the role of bifurcation mechanisms was only studied within single neuron models [53, 56, 57, 193, 194].

The experimental observations and theoretical investigations of SR both at the level of single neurons and at the level of neuronal populations revealed that, in the regime of SR, the response of nervous systems to weak signals still has a large stochastic component due to noise. It means that the detection of a signal is unreliable because a part of the input signal may be lost. Therefore, the starting question remains: what does the system need in order to detect reliably a sensory signal? At the present time it is well-recognized that network structure plays an important role in the function of nervous systems [24]. An important structural property is that, in the brain, neurons of similar function are grouped together in columns (or modules). The columnar organization of the neocortex has been documented in studies of sensory and motor areas in many species [32–34]. As mentioned in Section 1.4, rat somatosensory cortex has modular organization where neurons form columns and every column consists of $17000 - 19000$ neurons (each rodent whisker has its own column) [35]. Even the sensory nervous system of the *Caenorhabditis elegans*, which is the smallest nervous system among animals, has modular organization [36]. At the present time, it is unclear what advantage, if any, is given by a modular organization. The evolutionary origin of this structure was discussed by Kashtan and Alon [210]. They suggested that modularly varying goals leads to the spontaneous evolution of modular structure. However, modular organization can have other advantages since it allows to perform parallel processing and subsequent summation and averaging of information. Indeed, these are key principles used by sensory systems [49]. These ideas have been discussed in cognitive science within the connectionist models [211]. There are electrophysiological studies in monkeys which show that signals are averaged across neuronal modules and over time in the formation of a behavioral decision [212]. If we assume that every module can work in the regime of SR,

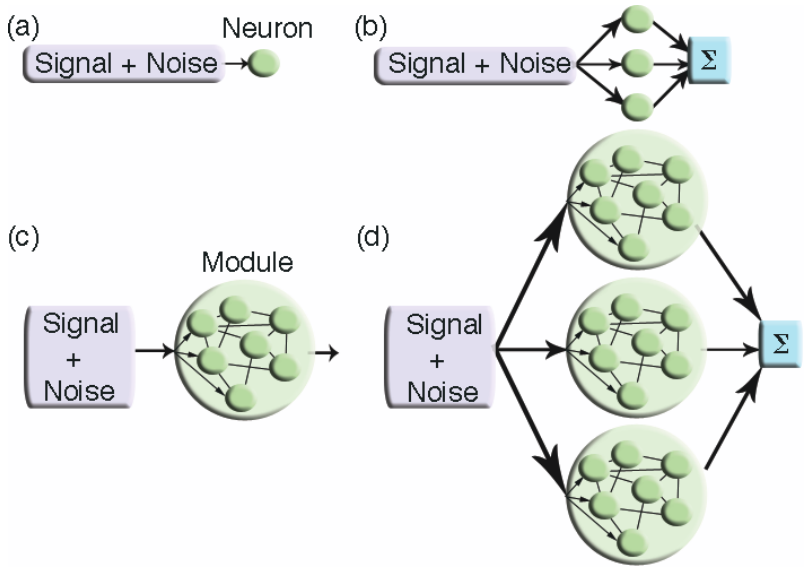

Figure 6.1: Different strategies of signal processing using (a) a single neuron, (b) an array of non-interacting single neurons, (c) a neuronal network, and (d) a neuronal network with modular organization.

---

then this structure can easily overcome the limited reliability of SR in signal detection discussed above. Thus, nature may find in the modular organization a way to introduce redundancy in order to increase reliability of signal detection. One can speculate that this kind of modular organization may have appeared due to the process of evolution that resulted in the selection of such sensory systems that have higher reliability of signal detection. Sensory systems may have evolved from the processing of information by a single cell in Fig. 6.1(a) to arrays of cells in Fig. 6.1(b) and from a neuronal network with a single module in Fig. 6.1(c)) to a modular organized neuronal network in Fig. 6.1(d).

In this chapter, at first we show that sensory noise delivered together with a weak periodic signal can not only enhance the nonlinear response of neuronal networks, but can also improve synchronization between the response and the signal. We find this nonlinear phenomenon in neuronal networks that are in a dynamical state near the saddle-node bifurcation corresponding to the appearance of sustained network oscillations (described in the previous chapter, $\alpha < \alpha_t$). We reveal that, when noise is applied, subthreshold sensory signals can evoke the activity of a large fraction of neurons (the sharp spikes presented in Chapter 5), which is synchronized with some degree of correlation with the signal. The response of neuronal activity to sensory signals and the signal-to-noise ratio reach a maximum at an optimum level of sensory noise. It manifests stochastic resonance at the population level. We mimic the experiments of Gluckman *et al.* [51] and we find qualitative agreement with the data. Second, we discuss the role of modular organization in the detection of weak signals. For this purpose, we study networks where neurons are grouped in modules and every module works in the regime of SR. We demonstrate that, in this case, the reliability of signal detection by the system is strongly enhanced in

comparison with the case when modular organization is absent. The results presented in this chapter were accepted for publication [213].

6.2 Stochastic resonance in the cortical model

In this section, we demonstrate SR in neuronal networks described by the cortical model. In particular, we show that the model allows us to explain SR observed in mammalian brain [51]. In the experiments [51], hippocampal slices of rat's brain were stimulated by a time-varying electric field. The field had two components, a stochastic one representing noise and the other representing a signal. As the magnitude of the stochastic component was increased, a resonance was observed in the response of the neuronal network to the weak periodic signal.

In order to explain these experiments, let us study the response of a neuronal network described by the cortical model to a weak periodic stimuli in the case when shot noise intensity is in the range $n_{c1} < \langle n \rangle < n_{c2}$, and $\alpha < \alpha_t$ (regions Id and Ie in Fig. 4.2). We remind that in this region there are three fixed points: point 1 is stable, point 2 is saddle, and point 3 is unstable. When the activity overcomes point 2, this point repels the trajectory towards larger activities, which then unavoidably gives rise to a deterministic sharp spike (we study in detail these sharp spikes in Chapter 7). As the intensity of noise approaches the critical point n_{c2}, points 1 and 2 become closer. Consequently, it is easier to generate sharp spikes (a smaller fluctuation above the stable fixed point 1 is able to produce a spike). In other words, the activation threshold of a sharp oscillation depends on model parameters, and it tends to zero when the network approaches the critical point n_{c2}. For example, in a network of 10^4 neurons (7500 excitatory and 2500 inhibitory neurons), at $\langle n \rangle = 16$, the simultaneous activation of 75 excitatory neurons chosen at random among 7500 excitatory neurons (i.e., about 1% of excitatory neurons), while the other neurons are inactive at that moment, generates a single sharp oscillation formed by the synchronized activity of about 9000 neurons [102]. As we will show below, this phenomenon opens the possibility to enhance weak stimuli and observe SR in neuronal networks. When noise is applied, the neuronal network fires sharp oscillations with some degree of correlation with subthreshold sensory signals.

We remind that we assume the first-spike latencies $1/\mu_e$ and $1/\mu_i$ of excitatory and inhibitory neurons equal to 20 ms and 28.6 ms, respectively. For the chosen parameters, the cyclic frequency of sustained network oscillations in the cortical model is about 5.2 Hz (when the noise intensity is $\langle n \rangle = 25$ above $n_{c2} \approx 18.8$ and below $n_{c3} \approx 49.9$, at $\alpha = 0.7$). The frequency lies in the range of frequencies $4 - 12$ Hz of theta waves observed in the brain [169]. The burst frequency observed by Gluckman *et al.* was also within the range $4-12$ Hz. The observed bursts (synchronous population events) typically lasted for $10-30$ ms. In our model, the single sharp spikes last for about 74 ms at $\alpha = 0.7$.

6.2.1 Numerical integration

First, we discuss results of the numerical integration of Eqs. (3.15). We stimulate the neuronal network with a sensory stimulus $x(t)$ that contains both noise $\xi(t)$ and a periodic signal $S(t)$,

$$x(t) = \xi(t) + S(t). \tag{6.1}$$

We assume that the sensory stimulus is delivered by $N_s = g_s N_e = g_s g_e N$ sensory neurons, where g_s is a model parameter. These additional sensory neurons are connected at random with the probability c/N only to excitatory neurons. Therefore, each excitatory neuron receives in average an input from $g_s g_e c$ sensory neurons. This method of stimulation assumes that excitatory neurons receive the same signal+noise inputs Eq. (6.1). It is similar to the experimental method in [51] where all neurons were stimulated by the same electric field.

One can show that the introduction of these sensory neurons leads to a simple modification of Eqs. (3.15). Namely, in Eqs. (3.15), we must substitute the function $\Psi(\rho_e, \rho_i)$ by $\Psi(\rho_e + A_e(t), \rho_i)$ where

$$A_e(t) = x(t) g_s/(f\tau). \tag{6.2}$$

We also introduce an additional stochastic force $F(t)$ acting on neurons and representing other sources of noise different from shot and sensory noise (for example, the force can represent irregular fluctuations caused by finite-size effects [102]). Equations (3.15) takes the form

$$\frac{\dot{\rho_a}}{\mu_a} = (1 - \rho_a)F(t) - \rho_a + \Psi(\rho_e + A_e(t), \rho_i). \tag{6.3}$$

We consider the sensory noise $\xi(t)$ generated by the Gaussian process with the mean number $\langle \xi(t) \rangle = 4 \times 10^{-2}$ of random spikes per the integration time τ and the variance $\sigma_{sn}^2 = 7.3 \times 10^{-4}$ (we only use the positive part of this Gaussian process and the effective mean amplitude of noise, A_ξ, is 4.3×10^{-2}) (see Fig. 6.2(c)). The sensory signal is sinusoidal,

$$S(t) = A_s[\sin(2\pi f_s t) + 1]/2, \tag{6.4}$$

with the amplitude $A_s = 4.5 \times 10^{-3}$ and the frequency $f_s = 1.25$ Hz. The stochastic force $F(t)$ representing finite-size effects is a random variable uniformly distributed in the interval $[0, 0.009]$.

Analyzing the dynamics of the cortical model by use of Eqs. (6.3), we find that, in the absence of a periodic signal, the sensory noise produces occasionally sharp oscillations. Adding a sinusoidal subthreshold sensory signal, which alone can not generate network oscillations (see Fig. 6.2(b)), we find that sharp spikes appear preferentially near the maximums of the signal (see Fig. 6.2(d)).

Following the analysis of Gluckman *et al.*, we find the burst probability density (BPD) defined as the probability to observe a burst (a sharp spike in our case) of network activity when the sinusoidal signal $S(t)$ has a phase ϕ (the signal maximums take place at $\phi = \pi(2n + 1)/2$, where $n = 0, 1, \dots$). Figure 6.3 displays the BPD of the neuronal network at different levels of sensory noise. One can see that the BPD correlates with the sensory

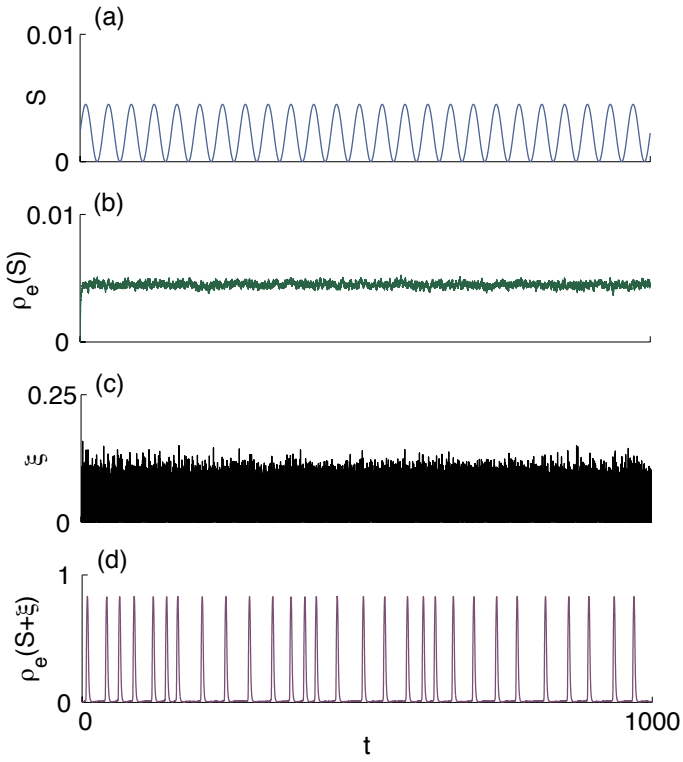

Figure 6.2: In the absence of sensory noise, a periodic sensory signal (S) with the amplitude $A_s = 4.5 \times 10^{-3}$ (see panel (a)) generates a weak perturbation of the excitatory population activity ρ_e that can hardly be identified in panel (b). However, the addition of sensory noise ξ with the mean amplitude $A_\xi = 4.3 \times 10^{-2}$ (see panel (c)), which is about 10 times larger than the signal's amplitude A_s, results in neuronal activity with single sharp oscillations shown in panel (d). The single sharp oscillations appear preferentially near the peaks of the sensory signal. Time t is in units $1/\mu_e$. Parameters: $\tilde{c} = 1000$, $\Omega = 30$, $g_i = 0.25$, $J_i = -3J_e$, $\sigma^2 = 10$, $\langle n \rangle = 10$, $\alpha = 0.7$, $g_s = 0.1$, and $f_s = 1.25$ Hz.

signal (see Fig. 6.3(c)) around an optimal level of sensory noise, while no correlations were observed at weaker and stronger levels of sensory noise (see Figs. 6.3(b) and 6.3(d), respectively). These results agree with the results in [51].

Finally, we define the signal-to-noise ratio (SNR) as follows:

$$SNR = \frac{a}{b}, \tag{6.5}$$

where a is the amplitude of the peak of the power spectral density (PSD) of neuronal activity at the signal's frequency f_s and b is the average value of the background PSD excluding the peak (Gluckman *et al.* used a similar method). This method is the same as the one in [51]. The only difference is that in [51] the SNR was defined as $SNR = (a-b)/b$.

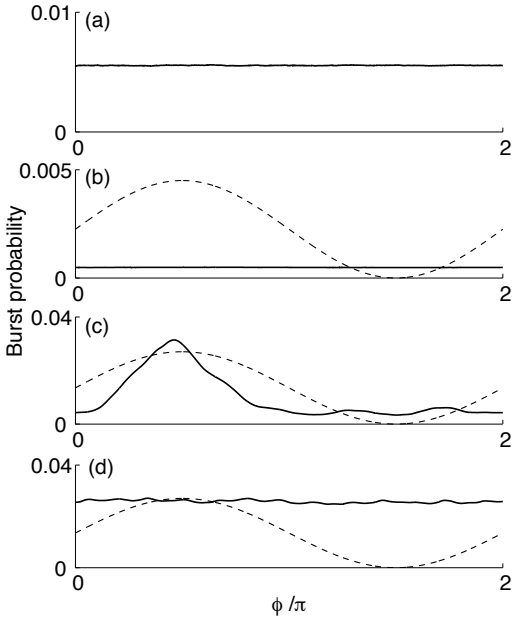

Figure 6.3: Burst probability density (BPD) versus the phase ϕ of the sinusoidal sensory signal from the numerical integration of Eqs. (6.3). (a) The BPD does not correlate with ϕ in the presence of sensory noise with the mean amplitude $A_\xi = 4.3 \times 10^{-2}$ if the signal is very weak ($A_s \ll A_\xi$). (b) BPD versus ϕ at weak sensory noise, $A_\xi = 2.4 \times 10^{-2}$. (c) BPD at the optimal level of sensory noise, $A_\xi = 4.3 \times 10^{-2}$. (d) BPD at strong sensory noise, $A_\xi = 7.0 \times 10^{-2}$. The signal's amplitude $A_s = 4.5 \times 10^{-3}$ is the same for panels (b), (c), and (d). The data were obtained by averaging over 2500 periods of the signal. The dashed lines represent the signal versus ϕ. Other parameters are the same as in Fig. 6.2.

We apply the periodic sinusoidal signal plus noise to the network as discussed above and then analyze the PSD of the neuronal activity. Results of numerical integration of Eqs. (6.3) and estimation of the SNR for different levels of mean sensory noise are displayed in Fig. 6.4. The error bars represent the statistics: for each level of noise, we repeated 10 times the measurements of the response of the neuronal network. The maximum of the SNR at a nonzero level of noise in Fig. 6.4 is a fingerprint of stochastic resonance.

6.2.2 Simulations

In our simulations we considered a different stimulation method. The sensory noise and the sinusoidal signal (Eqs. (6.1) and (6.4)) were delivered directly to a fraction g_s of $g_e N$ excitatory neurons chosen at random. Sensory noise ξ was represented by random spikes with the mean number $\langle \xi \rangle$ of spikes per the integration time τ and the variance σ_{sn}^2. The amplitude A_s of the sinusoidal signal $S(t)$ was fixed while the level $\langle \xi \rangle$ of sensory noise was gradually increased. Note that there is a simple approximate relationship between $\langle \xi \rangle$ and

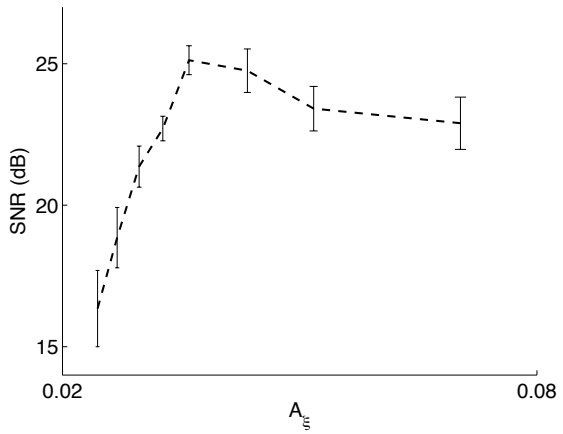

Figure 6.4: Signal-to-noise ratio (SNR) versus the mean amplitude A_ξ of the sensory noise in the cortical model from numerical integration of Eqs. (6.3). SNR is in decibel $[10\log_{10}(SNR)]$. The inverted U-shape is characteristic of stochastic resonance. Error bars were estimated from rms distribution of 10 measurements. The bar length is equal to twice the standard deviation, and the middle point of the bar corresponds to the mean value of SNR. Parameters are the same as those in Fig. 6.2.

---

the noise amplitude A_ξ used in Section 6.2.1, $\langle\xi\rangle \propto cA_\xi$. We used the amplitude of the sinusoidal signal $A_s = 4.5$ as in the numerical integration. Other model parameters were the same as those in Section 6.2.1, except $\langle\xi\rangle$ and the variance ($\sigma^2_{sn} = 5$).

Results of our simulations for $N = 10^4$ are represented in Figs. 6.5 and 6.6. At a small level $\langle\xi\rangle$ of sensory noise ($\langle\xi\rangle \leq 5$), the response of the neuronal network to the sinusoidal sensory signal is weak since the probability of generation of sharp oscillations by the signal is small (see Fig. 6.5(a)). When the level $\langle\xi\rangle$ of sensory noise is increased, sharp oscillations are generated with a larger probability. Note also that the degree of correlation of the sharp oscillations with the sensory signal also increases. At the optimum level of sensory noise ($\langle\xi\rangle \approx 7$), the network response (Fig. 6.5(d)) is well synchronized with the sensory signal (Fig. 6.5(e)). This synchronization is remarkable since only 10% of excitatory neurons receive the signal+noise input and the level of sensory noise is larger than the signal's amplitude. With increasing $\langle\xi\rangle$ above the optimum level, the correlation between the signal and the network response becomes worse (see Fig. 6.5(f)).

In order to characterize the network response, we also measured the power spectral density of activity fluctuations and calculated the SNR from Eq. (6.5). Figures 6.6(a) and 6.6(b) show the PSD of the neuronal activity displayed in Fig. 6.5(d). One sees that the PSD has a strong peak at the frequency of the sinusoidal signal $S(t)$ (other peaks correspond to the respective harmonics). The amplitude of this peak characterizes the network response. With increasing the level $\langle\xi\rangle$ of sensory noise, the peak increases in comparison with the background amplitude of the PSD, and consequently the SNR increases (see Fig. 6.6(c)). The SNR reaches a maximum at the optimal noise and then

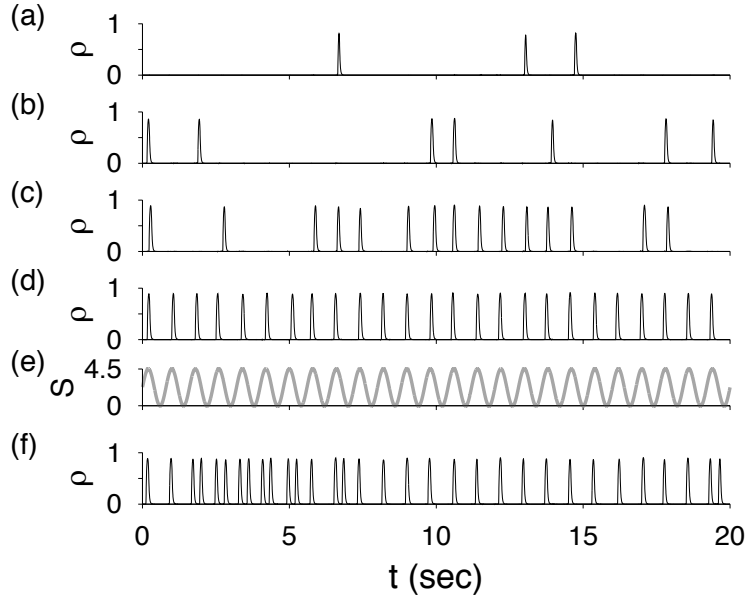

Figure 6.5: Response of the neuronal network to the sinusoidal sensory signal $S(t)$ at different levels $\langle\xi\rangle$ of sensory noise: (a) $\langle\xi\rangle = 5.0$; (b) $\langle\xi\rangle = 5.5$; (c) $\langle\xi\rangle = 6.0$; (d) $\langle\xi\rangle = 7.0$; (e) sinusoidal signal $S(t)$; (f) $\langle\xi\rangle = 7.5$. Parameters: $N = 10^4$, $\tau = 0.1$, $A_s = 4.5$ and $\sigma^2_{sn} = 5$. Other parameters in simulations are the same as in Fig. 6.2. These data and figures were obtained by KyoungEun Lee.

---

decreases. Again, the inverted-U shape of the SNR is a hallmark of stochastic resonance.

Comparing Figs. 6.4 and 6.6(c), one sees that the different methods of stimulation of neurons by signal+noise inputs, which were used in our numerical integration and simulations, give a similar behavior of the SNR. A quantitative comparison of the optimum noise levels in these two different methods is not simple since in numerical calculations we stimulated all excitatory neurons by a signal+noise input from a small group of sensory neurons while in simulations we delivered the signal+noise directly to a small fraction of excitatory neurons. Another reason for this difference is due to strong activity fluctuations caused by finite-size effects. This kind of fluctuations plays a role of an additional noise that affects collective phenomena in interacting systems [183]. We discuss finite-size effects in Section 6.3.2.

The proposed mechanism of SR in neuronal networks is similar to the mechanism of SR discussed previously within single neuron models [53, 56, 57, 193, 194]. The important difference is that, in our model, SR is a collective phenomenon due to interaction between neurons, rather than just due to excitable dynamics of single neurons as in single neuron models [53, 56, 57, 193, 194]. Therefore, breaking of cooperation between neurons results in suppression of this mechanism. Indeed, in Section 6.3, we observe suppression of signal detection by finite-size effects. However, these effects play no role for single neuron dynamics. As mentioned in the previous chapter, when $\langle n\rangle$ is close to n_{c2}, fluctuations of neuronal activity caused by finite-size effects can also generate sharp oscillations. This fact

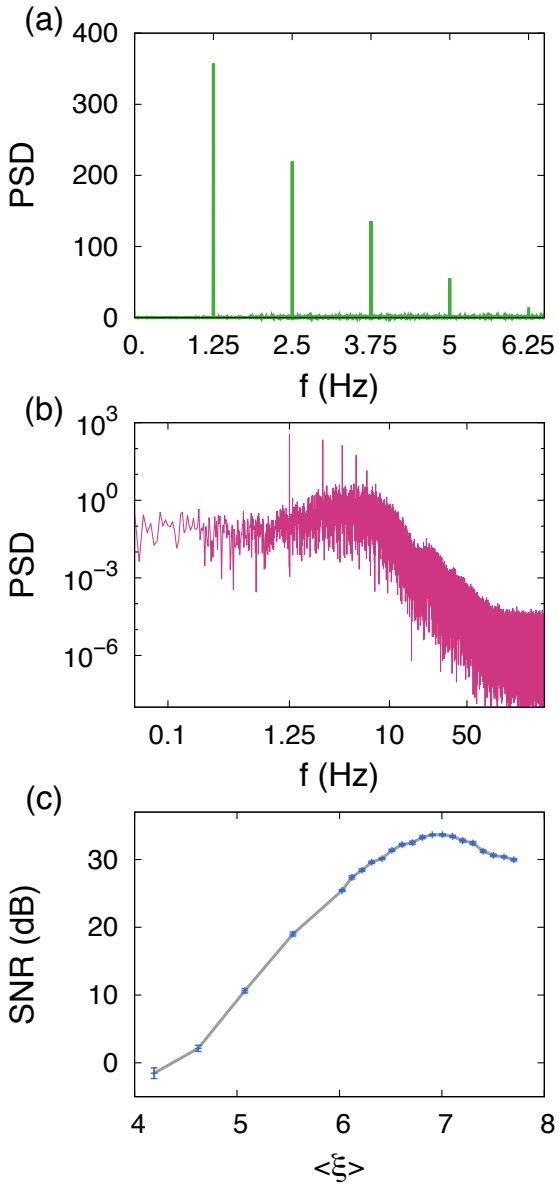

Figure 6.6: Power spectral density (PSD) of the cortical model in which a small fraction ($g_s = 0.1$) of excitatory neurons is stimulated by a sinusoidal signal (Eq. (6.4)) with frequency $f_s = 1.25$ Hz in the presence of sensory noise with $\langle \xi \rangle = 7.0$. (a) PSD versus the frequency f, linear scale; (b) PSD versus f, log-log scale. (c) Signal-to-noise (SNR) ratio versus $\langle \xi \rangle$. SNR is in decibel $[10 \log_{10}(SNR)]$. Parameters in simulations are the same as in Fig. 6.2 and 6.5. These data and figures were obtained by KyoungEun Lee.

can mask the useful response of the network to weak sensory signals. This effect restricts the region where SR may be observed in neuronal networks. We suggest that this kind of network response represented by a strongly synchronized activity of a large fraction of neurons may also play an important role in various mechanisms of signal processing in the brain. The fact that the sharp oscillations have a deterministic form and can be evoked by a small group of neurons may be of crucial importance not only for signal detection, but also for information transmission and communication between different areas of the brain. Moreover, the mechanism under consideration also enables a small group of neurons to control a large neuronal network.

Based on the proposed approach, we mimicked the experiments of Gluckman *et al.* [51] who observed SR in hippocampal slices from mammalian brain. Our results support the suggestion given by Gluckman *et al.* that SR may enhance effects of weak hippocampal theta or more widespread gamma oscillations within the brain. In our model, SR occurs if a neuronal network is in a dynamical state in the range of parameters below the critical point of a saddle-node bifurcation. Above the critical point, sustained network oscillations with frequency in the range of theta waves (or higher frequencies, depending on parameters) emerge. Here, we have focused on the theta range in order to compare with Gluckman experiments. However, similar results can be obtained with frequencies in the gamma range which are related with the function of sensory systems [214].

We would like to note that the considered fluctuation and response phenomena are universal for the saddle-node bifurcation and do not qualitatively depend on the underlying model. We suggest that SR at the single neuron and population levels can coexist and cooperate in order to improve the performance of signal detection in sensory systems. At a first stage, a sensory signal can activate a group of neurons working in the regime of SR as it was proposed in [53, 56, 57, 193, 194]. Then, at the second stage, the activated neurons can stimulate a synchronized activity of a finite fraction of the neuronal network in the form of nonlinear sharp oscillations.

One can note the following important properties of our model: (1) the amplification of subthreshold signals can be regulated by a flow of spikes from other brain areas; (2) a sensory signal can be delivered to a small fraction (we used 10%) of neurons without a loss in the output signal; and (3) neurons in our network use for its own benefit not only sensory noise but also internal synaptic noise.

6.3 Signal detection in a modular neuronal network

In the brain, neurons of similar function are grouped together in columns (or modules). This kind of organization assumes that synaptic connections are arranged denser within columns and sparser between columns. The columnar organization of the neocortex has been documented in studies of sensory and motor areas in many species [32–34]. Cortical columns are formed by the binding of many minicolumns (their number varies between 50 and 80) by common input and short range horizontal connections [34]. Understanding the role of modular organization (community structure, clustered networks) is an open

problem in neuroscience [215, 216].

In this section we show by use of numerical integration and simulations that the signal recognition in the regime with SR may be remarkably improved if a neuronal network has a modular organization similar to the partition of columns into minicolumns. We consider a neuronal network in which N neurons are grouped in n modules of size N/n. These modules are described by our cortical model and act in the regime of SR. A modular system is shown schematically in Figs. 6.1(d) and 6.7(a). All modules receive signal+noise inputs. Signals are represented by trains of pulses instead of periodic signals. Then the responses of the modules are summed up and averaged.

6.3.1 Detection of pulsed signals in numerical integration

The sinusoidal signal in Fig. 6.2(a) carries no information. Let us consider a case when a sensory signal contains information. We choose the message "ola" ("hello" in Portuguese) expressed in Morse code as the digital code, 11101110111000101110101000 10111. In order to represent this message as a sensory signal, we consider rectangular pulses separated by a time interval equal to 235 ms (the period of the sustained network oscillations corresponding to 5.2 Hz). The duration of these pulses was chosen about 30 ms, which is about eight times smaller than the period of network oscillations. The number of these pulses equals the number of bits in our message. Finally, we remove pulses corresponding to zeros. As a result we obtain a sensory signal representing our message "ola" (see Fig. 6.7). Despite the pulse amplitude being chosen sufficiently small, every pulse can generate with a certain probability a single sharp oscillation in a module. Figure 6.7(b) shows that the response of the modules to this message is stochastic even at the optimal level of sensory noise. On one hand, the module does not detect some pulses. On the other hand, it may elicit "false" responses. For given network parameters, sensory noise level, and signal's amplitude, we measured the probability p that a pulse in the signal is detected in a module, i.e., the pulse generates a single sharp oscillation. For the parameters chosen in our model and the signal's amplitude $A_s = 0.0135$, numerical integration of Eqs. (3.15) gives $p \approx 5/7$. Alternatively, one can say that two pulses of seven may be missed or may be "false". In our numerical integration of Eqs. (3.15) we assume that all modules receive the same signal+noise input (note that apart from the sensory noise there is also intrinsic synaptic noise in every module). This method is similar to the stimulation of neuronal networks by an electric field as in [51]. Then, responses of the modules to the sensory signal are combined and we obtain an averaged response shown in Fig. 6.7(b). For every pulse in the message "ola", the probability that at least one of the modules detects it is

$$\Pi(n) = 1 - \prod_{m=1}^{n} (1 - p_m), \tag{6.6}$$

where p_m is the probability that the module with index $m = 1, ..., n$ detects a pulse. If the modules have the same probability $p_m = p$, then $\Pi(n)$ increases with increasing the number of modules n as $\Pi(n) \approx np$ at $p \ll 1$. In turn, the probability of an error, $1 - \Pi(n)$,

decreases exponentially with increasing n as $1 - \Pi(n) = \exp[-n|\ln(1-p)|]$. If we want to detect every pulse of the message with probability of, say, 99%, then the necessary number n of modules can be found from the condition $\Pi(n) = 0.99$ (see, for example, Ref. [217]). For the obtained $p \approx 5/7$, Eq. (6.6) gives $n = 4$. The response to the message "ola" averaged over four neuronal modules is shown in Fig. 6.7(b). This result illustrates that modular structure improves remarkably the detection of weak signals.

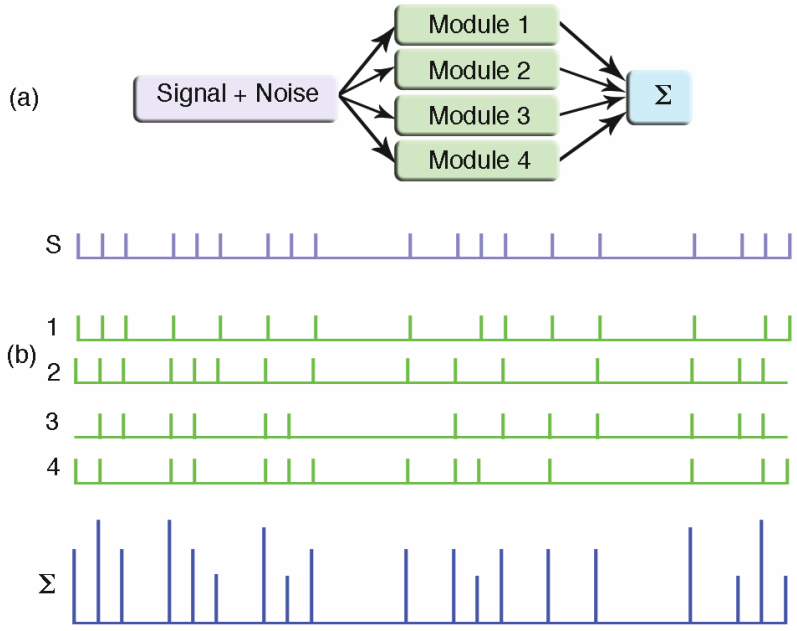

Figure 6.7: Signal detection in neuronal networks with modular structure from numerical integration of Eqs. (3.15). (a) A signal together with noise is delivered to four modules 1, 2, 3, and 4. Responses of these modules are averaged in a module denoted as Σ. (b) S represents the signal "ola" sent to these four modules. This signal with noise generates output signals 1, 2, 3, and 4 from the respective modules. The signal Σ represents the average over the output signals. Parameters are the same as those in Fig. 6.2, except the signal's amplitude $A_s = 0.0135$.

6.3.2 Simulations of modular networks

In our simulations of modular networks, $N = 50400$ neurons were grouped in n modules of size $N_m = N/n$, $n = 1, 2, \ldots, 50$. The modules are bound together by a common input but there are no connections between modules. The modules have the same structure as the random networks considered in the previous sections. We used a train of random pulses obtained from a periodic pulse train by the removal of pulses with probability 40%. The pulse duration was $W = 0.2$ s, the amplitude $A_s = 4.5$, and the pulse rate $f = 0.75$ Hz. The pulsed signal was delivered to the modules together with sensory noise (normally distributed random spikes with the mean number $\langle\xi\rangle = 5.7$ of spikes per integration time,

and the variance $\sigma_s^2 = 5$). We used two stimulation methods. In both methods, we chose at random a small fraction, $g_s = 10\%$, of excitatory neurons in each module. In the first method, every chosen neuron received independent sensory noise together with the pulsed signal. In the second method, the pulsed signal was delivered with the same noise to all chosen neurons. While the first method takes into account the synaptic noise in sensory systems, the second method mimics the stimulation of neuronal networks by an electric field that acts simultaneously on many neurons as in [51]. Analyzing dynamics of the network during a large observation time (80 s), we found the probability p_m that a signal's pulse is detected by a module with index $m = 1, \ldots, n$ of size N/n (a pulse is detected if it evokes a sharp large-amplitude network oscillation during a time interval equal to twice of the pulse duration after the signal's pulse begins). Averaging p_m over 10 network realizations, we found the average probability $p(n)$ shown in Fig. 6.8(a) for the two stimulation methods. Using the first stimulation method (uncorrelated sensory noise), we observed that $p(n)$ first increases, meaning that the excitability of the modules increases. After reaching a maximum, $p(n)$ decreases. Using the second stimulation method (correlated sensory noise), we observed a monotonic decrease of $p(n)$ with decreasing the module size. Since, except the module size, all model parameters were fixed in our simulations for uncorrelated and correlated noise, we believe that the observed decrease of $p(n)$ at large n is mainly due to finite-size effects. Finite-size fluctuations are expected to increase as n increases and disrupt collective oscillations in the neuronal networks.

We also suggest that the peak of the function $p(n)$ observed at $n = 10$ in the case of uncorrelated noise may be caused by competition between the increase of module excitability and suppression of collective oscillations as n increases. The large values of $p(n)$ observed in the case of correlated noise (see Fig. 6.8(a)) may be due to the fact that the correlated noise results in correlations between neuronal activities of modules. As one can expect, these correlations increase $p(n)$ in comparison to the case of uncorrelated noise. However, it is unclear how these correlations together with finite-size effects are responsible for the observed monotonic decrease of $p(n)$ as n increases in the case of correlated noise, in contrast to the non-monotonic behavior of $p(n)$ observed in the case of uncorrelated noise.

Figure 6.9 shows that when the module size decreases, sharp network oscillations evoked by signal's pulses lose their deterministic shape and strongly vary in amplitude. Unfortunately, the mechanism of this effect is unknown. It may be due to an increase of the clustering coefficient when size N_m of the modules decreases. Neglecting the directness of connections between neurons, we can estimate the clustering coefficient characterizing the occurrence of triangles in the network structure. The clustering coefficient is c/N_m, where c is the mean degree (size dependence of structural properties of complex networks and the role of triangles in network dynamics are discussed in the review [39]). Appearance of numerous triangles may destroy the balance between excitation and inhibition. Note that standard statistical analysis shows that the scale of stochastic activity fluctuations in a network of size N_m is $O(1/N_m^{1/2})$ (see, for example, [184]).

Finally, we found the probability $\Pi(n)$ using Eq. (6.6) and averaging over the observation time. As one can see in Fig. 6.8(b), $\Pi(n)$ increases with increasing the number

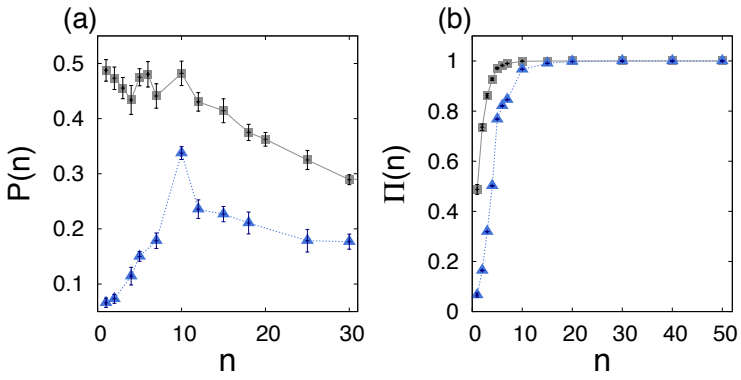

Figure 6.8: (a) Probability $p(n)$ that a signal's pulse is detected by a module of size N/n versus n ($N = 50400$ in our simulations). (b) Probability $\Pi(n)$ of signal detection in a network with n modules. In panels (a) and (b), the symbols represent results using two stimulation methods: (1) each neuron in every module receives independent sensory noise but the same pulsed signal (triangles); (2) neurons in the modules receive the same sensory noise and the same pulsed signal (squares). Parameters of the signal: random pulsed signal with 40% removal of pulses, pulse duration $W = 0.2$ s, amplitude $A_s = 4.5$, and pulse rate $f = 0.75$ Hz. Parameters of the noise: $\langle \xi \rangle = 5.7$, and $\sigma_s^2 = 5$. Other parameters are the same as in Figs. 6.2 and 6.5. These data and figures were obtained by KyoungEun Lee.

---

of modules n for both stimulation methods. Interestingly, at large n, even though $p(n)$ decreases, $\Pi(n)$ remains large, meaning that the large number of modules compensates the decrease of $p(n)$. These results show that the fragmentation of the neuronal system into several modules increases the reliability of signal detection.

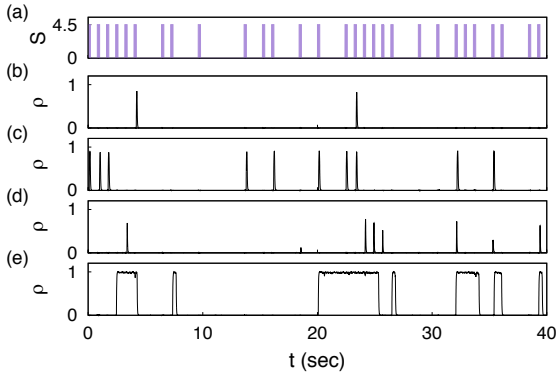

Figure 6.9: (a) A train of random rectangular pulses as a sensory signal. Panels (b)-(e) show stimulated neuronal activity of one of n modules of size $N_m = N/n$ for $N = 50400$: (b) $n = 2$ ($N_m = 25200$); (c) $n = 10$ ($N_m = 5040$); (d) $n = 30$ ($N_m = 1680$); (e) $n = 40$ ($N_m = 1260$). Neurons receive independent sensory noise but the same signal. Other parameters are the same as in Fig. 6.8. These data and figures were obtained by KyoungEun Lee.

Chapter 7

Paroxysmal-like spikes

7.1 Introduction

In this chapter, we discuss the paroxysmal-like spikes that emerge in regions Id and Ie of the phase diagram of our model (see Fig. 4.2). These spikes are very strong nonlinear events that involve in synchronized activity about 90% of the neurons in the network. They resemble freak waves, which are very large ocean surface waves that occur far out at sea. Freak waves are also known as rogue waves, monster waves, extreme waves, killer waves, and abnormal waves. Some of these names stress their destructive power, whereas others state their rarity. One can distinguish a set of properties of these freak waves: (1) they are nonlinear objects; (2) they occur as single events; (3) they have a very rapid and very steep onset; (4) they reach very large amplitudes; and (5) they appear from "nowhere" [218]. According to a theoretical study of Dyachenko and Zakharov [218], it is possible to discriminate two more features: there is an activation threshold, above which a freak wave emerges, and the characteristic time of this nonlinear event is about 10 "normal" wave periods. We found all of these properties in our spikes. However, there are two important differences: our spikes are not "waves" in the sense that they do not propagate in space; and freak waves are described by homoclinic solutions [219], whereas the paroxysmal-like spikes are topologically equivalent to a heteroclinic orbit (they become topologically equivalent to a homoclinic orbit only at the critical point).

As in the case of freak waves, the importance of understanding our spikes is that these large macroscopic objects may be dangerous for the system. Indeed, as mentioned in previous chapters, such strong synchronized activity can represent paroxysmal activity, which is the hallmark of epilepsy. In Fig. 7.1 we show the remarkable resemblance between these three nonlinear oscillations. Here we propose that our sharp oscillations (Fig. 7.1(c)) can model paroxysmal spikes observed in the epileptic brain (Fig. 7.1(b)).

Epilepsy is considered as a dynamical disease [92, 220], and it has been proposed that seizures may result from a bifurcation [92]. What kind of bifurcation is unknown. Here, we propose the saddle-node bifurcation as the candidate, because our paroxysmal-like spikes emerge near this type of bifurcation. There are some important features regarding

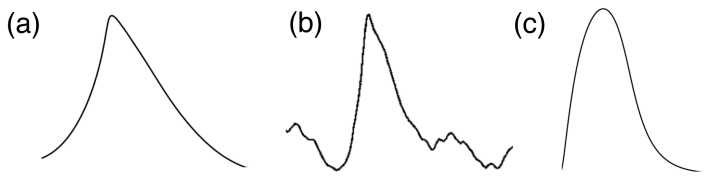

Figure 7.1: Nonlinear phenomena with similar form and properties. (a) A freak wave [218]; (b) an EEG recording of a paroxysmal spike (adapted from [189]); and (c) a sharp oscillation in our model.

the dynamics of epileptic activity, that one can find in our model if we take some simple assumptions. When measuring the neuronal activity with EEG, one distinguishes an "ictal" pattern corresponding to the seizure and an "interictal" epileptiform activity, when the patient is apparently "normal". The ictal pattern is generally rhythmic and it usually shows increasing amplitude and decreasing frequency of the activity [94, 96]. One can find such evolution of activity inside of our region of oscillations, when the network tends to the critical point of the saddle-node bifurcation from above, i.e., from the region of large noise intensities (see Fig. 5.3(c)). On the other hand, interictal patterns are composed of spikes, sharp waves, multiple spike wave complexes, *etc.*, which are generally transients that are clearly distinguishable from the background activity [94]. This type of pattern is the one that we match with our nonlinear excitations (see Figs. 7.1(c) and 5.4(a)). Thus, our model can mimic epileptic activity if we assume that the transition from interictal to ictal activity is due to an increase of noise intensity, and the reverse transition is due to either a decrease of the shot noise intensity or a change in another control parameter (for example, one characterizing dynamics of neurons or synapses). This assumption allows us to propose a measurement to forecast epileptic seizures.

7.2 Properties of the paroxysmal-like spikes

As we demonstrated in Chapter 5, in the considered model, paroxysmal-like spikes (see Fig. 5.4) appear in regions Id and Ie (see the phase diagram in Fig. 4.2). In order to understand their nature, we study their phase trajectories in the plane $\rho_e - \rho_i$ (see Fig. 7.2(a)). In these regions, as mentioned in previous chapters, there are three fixed points, whose stability has been analysed (see Table 4.1). In this case, we have a stable fixed point of low activity, a saddle point at an intermediate activity, and an unstable point (unstable spiral in region Id and unstable point in region Ie). Here, following the nomenclature of Rinzel and Ermentrout [187], we call the stable point as the rest state (R), the saddle point as the threshold (T), and the unstable point (U) keeps the same name. There are two heteroclinic orbits connecting points T and R, one that follows a direct path that corresponds to exponential relaxation to the rest state, and another that goes around the unstable point, reaching high activity, and then relaxing to the rest point. The second

path is the one that is responsible for the paroxysmal-like spikes.

Given a certain initial condition, which path does the trajectory follow? In order to answer this question, we must find the nullclines,

$$\begin{aligned} \dot{\rho_e} =& 0 \Leftrightarrow \rho_e = \Psi(\rho_e, \rho_i), \\ \dot{\rho_i} =& 0 \Leftrightarrow \rho_i = \Psi(\rho_e, \rho_i). \end{aligned} \tag{7.1}$$

These equations can be solved graphically, similarly to Eq. (4.10) (see Fig. 4.1). The difference is that ρ_i plays the role of parameter for the ρ_e-nullcline ($\dot{\rho_e} = 0$), and ρ_e is a parameter for the ρ_i-nullcline. We get the ρ_e-nullcline (ρ_i-nullcline) by solving the equation above repeatedly at different constant values of ρ_i (ρ_e). The nullclines are displayed in Fig. 7.2. Note that Fig. 7.2(b) provides a schematic representation of the nullclines, in order to be easier to understand the solution of Eqs. (7.1) shown in Fig. 7.2(c) (Fig. 7.2(d) and Fig. 7.2(e) are zooms of Fig. 7.2(c) near the rest and threshold points, respectively). The nullclines intersect each other at the fixed points, because a common solution of Eqs. (7.1) coincides with a solution of Eq. (4.10). When a trajectory crosses the ρ_e-nullcline (ρ_i-nullcline), it means that the excitatory (inhibitory) activity reached a maximum or a minimum. In our case, below the respective nullcline, the activity of the population a increases,

$$\dot{\rho_a} > 0, \tag{7.2}$$

whereas above the nullcline it decreases. It implies that the direction of motion on the trajectory presented in Fig. 7.2(a) is counterclockwise. Thus, any perturbation of neuronal activity that pushes a trajectory from the rest state into a point below the nullclines will result in a sharp spike, whose trajectory is similar to the one displayed in Fig. 7.2(a) (note that the nullclines are almost coincidental in a large range of ρ_e and ρ_i). At the critical point n_{c2}, the points R and T merge, and there is a homoclinic orbit around the unstable point, connecting the saddle point to itself.

One can define an activation threshold $A_{th}(\langle n \rangle)$ of spikes as the distance from the rest state to the threshold (or to the ρ_e-nullcline, or alternatively as the distance from the rest state to the stable manifold for the saddle point, which is almost coincidental with the ρ_e-nullcline). Note that above T, a trajectory can start above the ρ_i-nullcline, but below the ρ_e-nullcline. In this case, the trajectory is immediately pushed into the region of $\dot{\rho_i} > 0$, below the ρ_i-nullcline. When the dynamical system approaches the critical point n_{c2}, the activation threshold $A_{th}(\langle n \rangle)$ decreases, because the stable and saddle points get closer to each other. The dependence of $A_{th}(\langle n \rangle)$ on the distance to the critical point was obtained in Subsection 5.1.3, Eq. (5.4),

$$A_{th}(\langle n \rangle) \propto \sqrt{n_{c2} - \langle n \rangle}. \tag{7.3}$$

Thus, in a finite network, finite-size effects are able to elicit activity fluctuations above the activation threshold that generate paroxysmal-like spikes, provided that the network is close enough to the critical point n_{c2} (see Fig. 7.3(a)). Figures 7.3(c) and 7.3(d) show that all spikes share the same shape, because all trajectories follow a path topologically

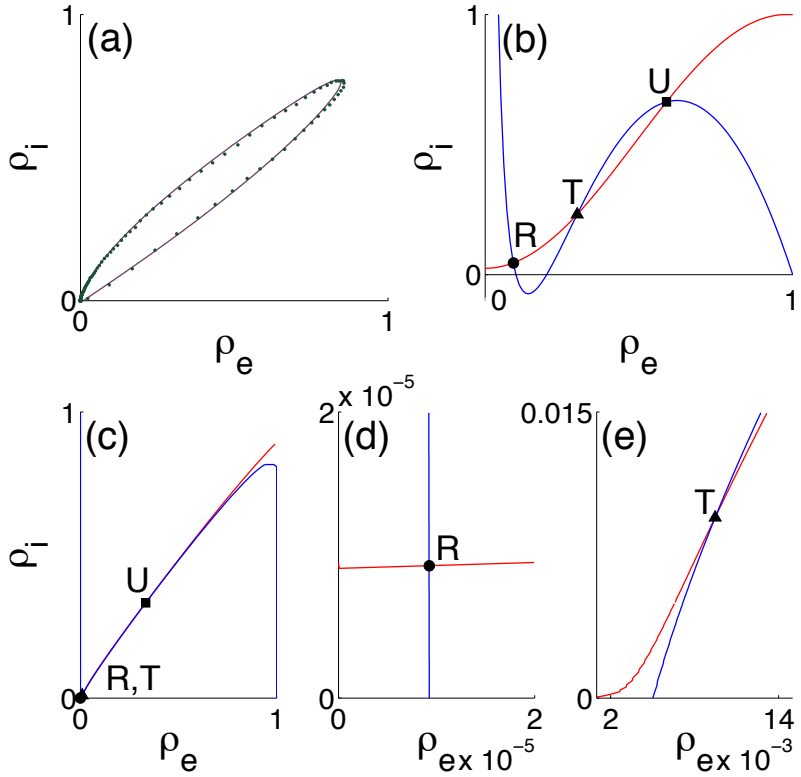

Figure 7.2: (a) Trajectory in the $(\rho_e, \rho_i)-$phase plane. The trajectory starts from the initial condition $(\rho_e, \rho_i) = (0.02, 0.01)$ and it follows a path equivalent to the heteroclinic orbit that goes around the unstable fixed point. The trajectory was obtained from the numerical integration of Eqs. (3.15) (solid line) and simulations (dotted line). (b) Representation of the nullclines in the $(\rho_e, \rho_i)-$phase plane that are topologically equivalent to the ones in our model. The red line corresponds to ρ_i-nullcline and the blue line to ρ_e-nullcline (the same is valid for panels (c), (d) and (e)). The intersection of the nullclines gives the fixed points: the stable fixed point or rest state (R), the saddle (or threshold) point (T), and the unstable point (U). (c) Nullclines in the $(\rho_e, \rho_i)-$phase plane (solution of Eqs. (7.1)). (d) Zoom of panel (c) at the stable point. (e) Zoom of panel (c) at the saddle point. Parameters: $\tilde{c} = 1000$, $\Omega = 30$, $g_i = 0.25$, $J_i = -3J_e$, $\sigma^2 = 10$, $\langle n \rangle = 16$, and $\alpha = 0.7$.

---

equivalent to the heteroclinic orbit that goes around the unstable point. Noteworthy, these strongly nonlinear objects, which involve in synchronized activity a large majority of the neuronal network (about 90%), can be triggered by the activation of a small fraction of neurons. In the brain, it means that a small number of neurons is able to activate a large network, if the network is in a dynamical state near a saddle-node bifurcation like the one that we describe here. Note also that the network may be almost inactive, in the rest state, characterized by an average activity as small as $\langle \rho \rangle \approx 10^{-6}$ (in a network with 10^6 neurons,

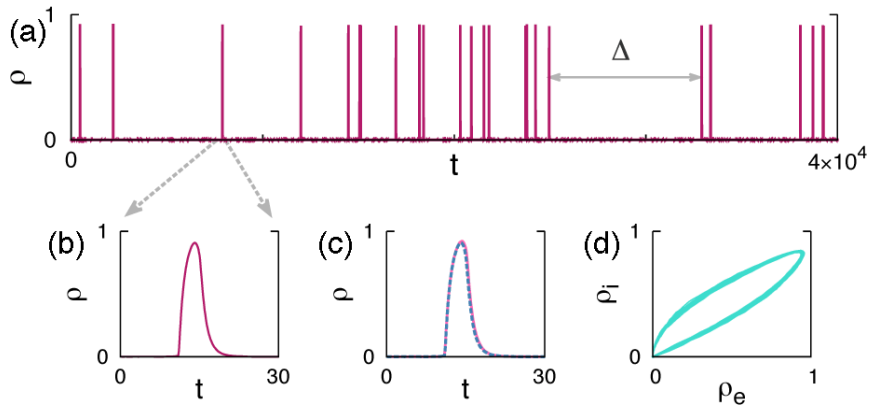

Figure 7.3: (a) Series of paroxysmal-like spikes that are generated at random close to n_{c2} due to finite-size effects. (b) Zoom of a spike from panel (a). (c) All spikes presented in panel (a) at the same phase. (d) The series of spikes shown in panel (a) in the (ρ_e, ρ_i)-phase plane. All spikes share the same shape. Parameters in simulations are the same as in Fig. 7.2, except $(\langle n \rangle, \alpha) = (18.76, 0.55)$, $\tau = 0.1$, and $N = 10^4$. These data and figures were obtained by KyoungEun Lee.

---

it means that on average there is only one neuron active). We found that, at $\langle n \rangle = 16$ (it corresponds to a dimensionless distance to the critical point $(n_{c2} - \langle n \rangle)/n_{c2} \approx 0.15$), the activation of only 1% of excitatory neurons is enough to elicit a spike. Thus, the spikes can appear from "nowhere" (like freak waves in a calm sea [218]). Moreover, the spikes occur as single events. In order to elicit two spikes, it is necessary to apply two pulses. Finally, as one can see in Fig. 7.3, these nonlinear excitations have a very rapid onset (like paroxysmal activity, see Fig. 7.1(b)).

7.3 Forecasting the transition to low-frequency oscillations

One can expect that since the activation threshold decreases as the system approaches the critical point, Eq. (7.3), the rate of spikes generated by finite-size effects increases. However, in order to understand the statistics of spikes, it is necessary to take into account a repulsion between spikes that is related to the fact that as the stable point gets closer to the saddle point, the system spends a larger time D near these points,

$$D \propto (n_{c2} - \langle n \rangle)^{-1/2}. \tag{7.4}$$

This equation describes a general attribute of a saddle-node bifurcation [116]. Figure 7.4(a) shows that indeed D increases near the critical point. The figure was obtained from a numerical study of Eqs. (3.15). We applied a delta-like field having amplitude F (in simulations, its duration equals the time step), as in Eqs. (5.15), in order to generate a spike. At each noise intensity $\langle n \rangle$ in Fig. 7.4, we found the minimum F that was able to

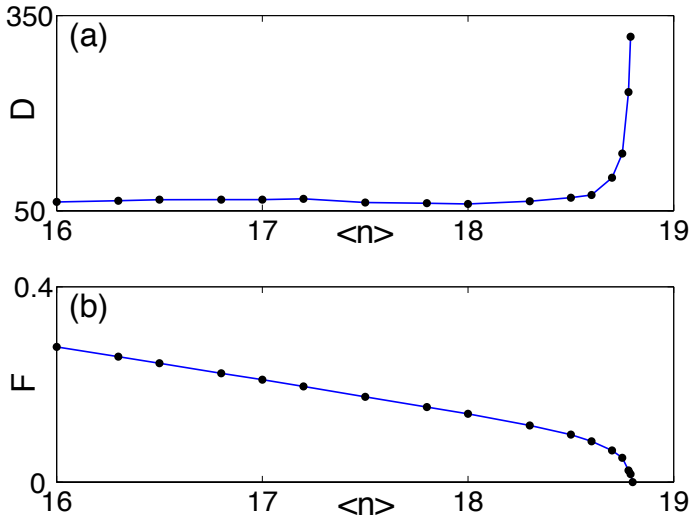

Figure 7.4: (a) Minimum interval of time D between paroxysmal-like spikes as function of the level of noise $\langle n \rangle$. (b) Minimum amplitude of a delta-like stimulation F that is able to elicit a spike as function of the noise intensity $\langle n \rangle$. Parameters in the numerical integration of the rate equations (3.15) are the same as in Fig. 7.2.

---

elicit a spike. As expected, the minimum amplitude F tends to zero near the critical point, because it is equal to the activation threshold,

$$F_{min} \propto \sqrt{n_{c2} - \langle n \rangle}, \tag{7.5}$$

as presented in Fig. 7.4(b). In this calculations, D was estimated as the minimum time necessary to wait until a similar delta-like stimulation with the amplitude F_{min} was capable of eliciting a second spike. At the critical point, F is zero, and $D \to \infty$, meaning that network oscillations emerge with zero frequency, which corresponds to the homoclinic orbit mentioned above.

Since the saddle-node bifurcation is the mechanism of a continuous phase transition, one can expect critical phenomena that signal the transition. In particular, one can look for a susceptibility-like parameter that should diverge at the critical point [181]. In this case, as mentioned in Subsection 5.2.1, we assume that the order parameter is the frequency. Consequently, we expect that the variance of the frequency should diverge (it is our susceptibility). At $n_{c1} < \langle n \rangle < n_{c2}$, the frequency is the rate of randomly generated paroxysmal-like spikes, i.e., the reciprocal of the time interval Δ between spikes (see Fig. 7.3(a)). Its variance is

$$\mathrm{var}(\Delta^{-1}) = \langle (\Delta^{-1} - \langle \Delta^{-1} \rangle)^2 \rangle, \tag{7.6}$$

where $\langle x \rangle$ is the mean of x. Figure 7.5 displays the dependence of this variance on the intensity of noise. As predicted, the variance has a maximum at the critical point (the

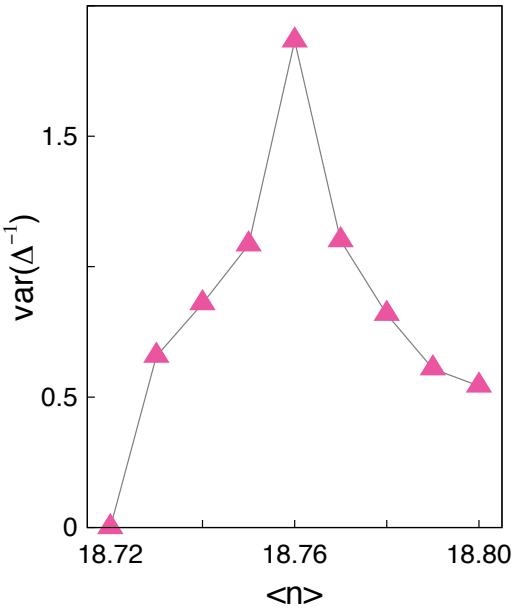

Figure 7.5: Variance of the recriprocal of the time interval Δ between spikes (represented in Fig. 7.3(a)) as function of the noise intensity $\langle n \rangle$. Parameters in simulations are the same as in Fig. 7.3. These data and figure were obtained by KyoungEun Lee.

divergency is smoothed by the finite-size effects, as explained in Chapter 5). It means that we can use this measurement to assess how close is the system to the critical point, and to predict the transition in advance.

7.4 Discussion

In the introduction of this chapter we compared our sharp oscillations with freak waves, which are known for their destructive power. Such comparison may also remind us of the most re-published science fiction story, "A Sound of Thunder" by Ray Bradbury. In this story, a time traveller crushes a butterfly and, as a result, the world history is changed. This story is inspired by the butterfly effect, a phenomenon that describes the sensitivity of a chaotic system to the initial conditions. The name was coined by Edward Lorenz when studying a model of hurricane's formation. According to Lorenz, if a butterfly would flap its wings, then, as a consequence, after several weeks a hurricane could emerge.

Our spikes tell a different story. In our model, when the butterfly flaps its wings, if the perturbation is larger than an activation threshold (which can be very small and tends to zero near a critical point), the air perturbation will immediately start to grow following well-defined mathematical rules and it will unavoidably turn into a tornado. Similarly, the story can also be about a butterfly flying above the water in the ocean. The delicate and small wings of the butterfly can produce a small wave that grows and becomes a giant

(freak) wave. The important difference between this story and the one told by Edward Lorenz is that, in our story, the perturbation created by the butterfly wings turns quickly and unavoidably into a tornado, in contrast to the perturbation produced by Lorenz's butterfly which has only a small probability to turn into a tornado. The consequences following the flap of the wings of our butterfly are predictable and deterministic. Obviously, in our model, the butterfly represents the mechanism that induces a small perturbation in neuronal activity, and the tornado (or freak wave) is the paroxysmal-like spike.

Our paroxysmal-like spikes are generated at random due to fluctuations of network activity in regions Id and Ie (see the phase diagram, Fig. 4.2). This activity is similar to interictal activity in epilepsy [94]. During a seizure, the pattern of collective activity changes and becomes rhythmic; it is called ictal activity [94]. As mentioned above, the ictal activity is often characterized by a particular evolution. The amplitude of the oscillations increases over time, while the frequency decreases [94, 96]. Then, the seizure and the corresponding ictal activity suddenly stop, returning to interictal activity. In our model we can observe a similar evolution of collective activity if we control adequately the noise intensity. At $\alpha < \alpha_t$ and $n_{c1} < \langle n \rangle < n_{c2}$, we find random spikes (interictal state). If the noise intensity exceeds n_{c2}, the neuronal activity is rhythmic, like ictal activity. Finally, by decreasing $\langle n \rangle$, the amplitude of network oscillations increases, while the frequency decreases (see Fig. 5.3). Thus, not only the shape of our network activity is similar to paroxysmal activity, but it also represents well the time evolution of epileptic activity. The transition from interictal to ictal activity is due to an increase of the level of noise in our model (or other kind of "excitatory" stimulation). This is in agreement with photosensitive epilepsy, in which a seizure can be provoked by means of intermittent photic stimulation [98]. Note that in our model the shot noise also accounts for spikes arriving from neighboring brain areas, meaning that these areas can be responsible for the generation of epileptiform activity at a certain region. Likewise, one can identify the neighboring areas that inhibit the epileptic focus, and stimulate them in order for them to abort the seizures. Indeed, such procedure is used within electrical brain stimulation [221].

If we assume that our model gives a good description of epileptiform activity, then one can ask how this knowledge may help clinicians. There are two fundamental open questions related to epilepsy: how to avoid seizures in an epileptic brain, and how to predict the occurrence of seizures [222]. Regarding the first question, our model tells us that "excitatory" stimulation is the key ingredient to generate ictal activity. Thus, if possible, excitation should be avoided (as it is in the case of photosensitive epilepsy). This is in agreement with the methods employed to treat epilepsy using brain stimulation. Indeed, neurostimulation is designed to supress neuronal activity in the seizure focus [221]. More importantly, we believe that our model may be especially relevant to address the second question.

Based on our model, we propose two methods to forecast epileptic seizures. First, Fig. 7.4(b) indicates that a paroxysmal spike becomes easier to be provoked by external stimulation as the system approaches the critical point, i.e., the transition to the ictal state. In this context, "easier" means that smaller amplitude is required from the stimulation to elicit paroxysmal spikes. In the case of photosensitive epilepsy, one can use intermittent

photic stimulation. In other epilepsies it may be necessary to use implanted electrodes to electrically stimulate the brain, like it was proposed by Lopes da Silva *et al.* [98]. Thus, for a given patient, and after many trials, it may be possible to associate the minimum stimulation necessary to elicit a paroxysmal spike with the distance to the ictal state. Evidently, this method has the risk of inducing seizures, if the stimulation is too strong.

The second method does not require stimulation, instead it uses the analysis of ongoing recordings of EEG (it is common to record neuronal activity continuously for hours or even days in patients with epilepsy [94]). In our model, the transition from interictal to ictal activity is due to a continuous phase transition. Therefore, one can look for critical phenomena that signal the transition. In our model we identified the variance of the rate of randomly generated paroxysmal-like spikes as a good predictor, since it diverges at the critical point. Thus, we propose to the clinicians to measure the variance of the paroxysmal spikes during the interictal regime. Obviously, one measurement of the variance does not give any information. It is necessary to measure continuously the variance of the ongoing activity during a certain time window. The adequate size of the time window depends on how fast is the control parameter changing. Unfortunately the control parameter in the epileptic brain is unknown (in our model is the noise intensity). Moreover, finite-size fluctuations smooth the divergency, and therefore the transition is signaled by a maximum of this variance. In order to apply this method, first it would be necessary to examine what is the "normal" magnitude of the variance. Second, it would be required to find how much time in advance to the seizure the variance starts to increase above the "normal" values. If our prediction is not verified, it can either imply that the internal control parameter varies too abruptly, or our model does not model correctly the transition from interictal to ictal activity. It is possible that the internal control parameter may vary differently in different kinds of epilepsy, as suggested by Lopes da Silva *et al.* [92]. Consequently, the method proposed here may only be suitable for certain types of epilepsy. If this method works, it may be used within responsive neurostimulation, in which it is critical to predict the onset of seizures in order to apply in advance electrical stimulation to avoid their occurrence [221].

Phase transitions and critical phenomena are universal, meaning that one should be able to find the same collective behavior independently of the details of single unit dynamics [223]. In other words, we expect that the results presented in this chapter must occur in other models, provided that the topology and the mechanism of interaction between single units are the same. Thus, in Appendix A, we analysed the dynamics of a random network composed of Izhikevich neurons [115, 123]. We could find some similarities between the dynamics of the two models. Particularly, at small intensities of noise, the network composed of Izhikevich neurons also presents low activity, and above a certain intensity of noise we found low frequency oscillations as in our model. However, the shape of the oscillations is strikingly different between the two models (compare Figs. 5.3(a) and A.4(a)). Also, we could not find paroxysmal-like spikes in the low activity state. We attribute the differences between the two models to a lack of variability in the network composed of Izhikevich neurons. Furthermore, the single neuron dynamics may be fundamentally different between the two models.

In contrast with the idea explored in this chapter, that the epileptic transition is a second-order phase transition accompanied by critical phenomena, Lopes da Silva *et al.* proposed that absence epilepsy may be characterized by a paroxysmal attractor very close to the normal state, such that transitions between these states can be induced by random fluctuations of some variables [92]. In this case, it would be impossible to predict the onset of a seizure, as it is believed to be the case in absence epilepsy [92, 117]. In Appendix B, we studied a possible alternative mechanism that can explain why absence seizures may be unpredictable, based on the type of bifurcation, rather than on the distance between the different attractors. We suggest that the transition to the ictal state may be due to a subcritical Hopf bifurcation, which unlike the supercritical case, it is a transition "much more dramatic, and potentially dangerous" to the system [116], because the bifurcation forces the trajectories to jump to a distant attractor. This bifurcation presents hysteresis, and no scaling law governs the amplitude or period of the limit cycle near the bifurcation point [116]. Since in our neuronal network model we do not have a subcritical Hopf bifurcation, in this appendix we studied a toy model that presents the bifurcation, in order to test the idea that it may be an alternative to the suggestion of Lopes da Silva *et al.* to model absence epilepsy. Our simple analysis of the toy model showed that the transitions from one attractor to the other occur at random, meaning that the transition occurs without any early warnings, as a first-order phase transition. Thus, we suggest that a subcritical Hopf bifurcation may underlie the epileptic transition in absence epilepsy.

Chapter 8

Synaptic plasticity

8.1 Introduction

In previous chapters, we considered synapses characterized by constant synaptic efficacies, and homogeneous in each neuronal population (J_e for all excitatory neurons, and J_i for all inhibitory neurons). Both assumptions are not realistic. The synaptic strength varies from neuron to neuron, and changes over time. This is a very important process, since there are strong experimental evidences that memory is the result of synaptic dynamics (see for example Ref. [109]).

There are two mechanisms responsible for changing synaptic efficacies J_{nm}: facilitation and depression. Facilitation is responsible for an increase of synaptic efficacies while depression leads to decreasing efficacies. In 1997, Abbott *et al.* [224] proposed a phenomenological model to describe short-term synaptic plasticity. The model can be expressed by the following equations [109, 225]:

$$\dot{x} = \frac{1-x}{\tau_D} - ux\delta(t-t_{sp}) \tag{8.1}$$

for depression (the variable x) and

$$\dot{u} = \frac{U-u}{\tau_F} + U(1-u)\delta(t-t_{sp}) \tag{8.2}$$

for facilitation (the variable u). The variable x is interpreted as the amount of available resources, and u is the utilization parameter that determines the amount of resources used by one spike. In these equations, δ is the Dirac delta function, τ_D, τ_F and U are parameters. The depression variable x is decreased by a value ux when a spike arrives at time t_{sp} at the synapse, whereas the facilitation variable u is increased by a value $U(1-u)$. Consequently, spikes coming from presynaptic neurons can either decrease the probability of the postsynaptic neuron to fire (depression), or increase it (facilitation). In the absence of spikes, the depression and the facilitation variables relax exponentially to 1 and U, respectively. $J_{nm}(t)$ is given by the product, $J_0x(t)u(t)$, where J_0 is a constant, and

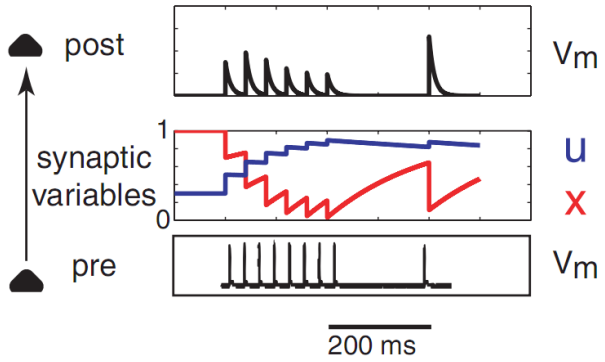

Figure 8.1: Postsynaptic response (above) to a train spike (below), and in the middle the corresponding synaptic dynamics. During the train spike, the facilitation parameter u increases (and facilitates spike generation in the postsynaptic neuron), and the depression parameter x decreases (decreasing the probability of the neuron to fire). The product ux modulates the synaptic efficacy. V_m is the membrane potential [109].

$x(t)u(t)$ is the amount of the available resources at the synapse that are used to produce the postsynaptic current (that is why x is reduced by this quantity). These mechanisms are represented in Fig. 8.1. Note that there are also long-term synaptic mechanisms (long-term potentiation and long-term depression), but we do not consider them here, because they take place during hours [226, 227], a time scale in which we are not interested.

Equations (8.1) and (8.2) together with Eqs. (3.15) and (3.18) permit us to study how synaptic plasticity influences on the dynamics of neuronal networks. These equations also open a way to study working memory in the brain [109]. Part of the results presented in this chapter are similar to the results we published in [111], where we used a slightly different model.

8.2 Short-term synaptic depression in neuronal networks

For simplicity, we assume that only excitatory-excitatory synapses are dynamical, and they are only affected by synaptic depression. Equation (8.1) takes the form

$$\dot{x}_{ij} = \frac{1 - x_{ij}}{\tau_R} - P_d x_{ij} \delta(t - t_{sp}), \tag{8.3}$$

where τ_R is the recovery time of the synapse, and P_d controls the strength of the depression mechanism. The index i and j denote the presynaptic and postsynaptic excitatory neurons. The synaptic efficacy between the excitatory neurons is now $J_{ij}(t) = J_0 x_{ij}(t)$. In all the results presented here, we use $J_0 = J_e = 1$.

As mentioned above, in the phenomenological model, the quantity ux (now $P_d x_{ij}$) is used to generate the postsynaptic current. However, in our model, the synaptic current is

not defined. Consequently, we assume that the amount of resources $P_d x_{ij}$ is used to elicit a spike in the postsynaptic neuron. Thus, Eq. (8.3) can be easily introduced in simulations of our model:

$$\begin{aligned} \dot{x}_{ij}(t) &= \frac{1 - x_{ij}(t)}{\tau_R} - P_d x_{ij}(t), \qquad \text{if} \qquad p \leq \nu\tau s_i(t) s_j(t) \\ \dot{x}_{ij}(t) &= \frac{1 - x_{ij}(t)}{\tau_R}, \qquad \text{if} \qquad p > \nu\tau s_i(t) s_j(t) \end{aligned} \tag{8.4}$$

where p is a random number generated at each time step from the uniform distribution in the interval $[0, 1]$, $\nu\tau$ is the probability that the neuron has fired during the integration time τ, and $s_i(t)$ is the activity state of neuron i at time t (as explained in Section 3.3). Instead of using the Delta function to detect presynaptic spikes, we use the activity state of both presynaptic and postsynaptic neurons within a time step to make sure that the amount of resources $P_d x_{ij}(t)$ is used.

In our mean field equations (3.15), we can not introduce heterogeneous synaptic efficacies as in simulations. We could, instead, consider a time dependent distribution of synaptic efficacies, but unfortunately it is not clear how to generalize the previous equations to obtain such distribution. Thus, we consider that all synapses (excitatory-excitatory) are changed together and are described by a mean field variable $J_{ee}(t)$,

$$J_{ee}(t) = \frac{\sum_{i,j} x_{ij}(t) a_{ij}^{(ee)}}{2N^{(ee)}}, \tag{8.5}$$

where $a_{ij}^{(ee)}$ is the adjacency matrix for excitatory-excitatory connections, and $N^{(ee)}$ is the number of excitatory-excitatory synapses. In our mean field equations we have assumed that neurons with the same degree behave in a similar way. Here, we assume that the efficacy does not depend on the degree of the neuron. This is a good approximation because for a classical random graph the standard mean deviation of the degree distribution is $\sqrt{c}$, which is small for $c = 1000$ ($\sqrt{c} \approx 32$). Therefore, we take Eq. (8.4) and we sum over the synapses and integrate over the time interval $\Delta = n\tau$, where τ is the integration time,

$$\int_{J_{ee}(0)}^{J_{ee}(\Delta)} dJ_{ee} = \sum_{j=1}^{N^{(ee)}} \int_0^{\Delta} \Big(\frac{1 - x_j}{\tau_R} - P_d x_j a_{ij}^{(ee)} s_j(t) s_i(t) \Big) dt. \tag{8.6}$$

We make the following mean field assumption:

$$\sum_{j=1}^{N^{(ee)}} \int_0^{\Delta} x_j a_{ij}^{(ee)} s_j(t) s_i(t) dt \approx J_{ee}(t) \nu \rho_e(t) \rho_e(t) \Delta, \tag{8.7}$$

where ν is the firing rate, and we obtain

$$\dot{J_{ee}}(t) = \frac{1 - J_{ee}(t)}{\tau_R} - P_d J_{ee}(t) \nu \rho_e(t) \rho_e(t). \tag{8.8}$$

Note that it was assumed that $J_{ee}(t)$ is almost constant in the time interval Δ, i.e., $\tau_R \gg \Delta$. Now, $J_{ee}(t) \neq J_{ei}$, and consequently $\Psi_e(\rho_e, \rho_i) \neq \Psi_i(\rho_e, \rho_i)$ (see Eq. (3.18)). In this case, in Eq. (3.15) we should consider $\Psi_a(\rho_e, \rho_i)$ defined as follows:

$$\Psi_a(\rho_e, \rho_i) = \sum_{k,l,n=0}^{\infty} \Theta(kJ_{ea}(t) + lJ_{ia} + nJ_n - V_{th}) P_k(g_e \rho_e \tilde{c}) P_l(g_i \rho_i \tilde{c}) G(n), \qquad (8.9)$$

where $J_{ee}(t)$ is given by Eq. (8.8), $J_{ei}(t) = J_e = 1$, and $J_{ie} = J_{ii} = J_i = -3J_e$.

We first discuss simulation results, and then we compare some of these simulation results with the mean field calculations.

Figure 8.2(a) displays the phase diagram of our model without synaptic plasticity, i.e., in the case when synaptic efficacies are constant. Note that it seems to differ from the previous phase diagram that we presented in Chapter 4, Fig. 4.2, that was obtained analytically. In simulations it is very difficult to distinguish all regions displayed in Fig. 4.2. In this case, the "inactive state" corresponds to a low activity state (the steady state $\rho^{(1)}$), in other words, it corresponds to regions Ia-Ie in Fig. 4.2. The "active state" corresponds to regions IIa and IIb. In both these regions, the activity relaxes to the high activity steady state $\rho^{(3)}$ (in simulations it is difficult to distinguish accurately the two regions). Finally, "oscillations" corresponds to regions IIIa and IIIb in Fig. 4.2. One can also note that the region of oscillations in Fig. 8.2(a) is smaller than regions IIIa and IIIb in Fig. 4.2. It is due to the fact that we are using $\nu\tau = 0.3$ here, in contrast with $\nu\tau = 1$ in Fig. 4.2, consequently the "effective" mean degree $\tilde{c} = c\nu\tau$ is smaller now. As explained at the end of Chapter 4, a smaller mean degree leads to a smaller region of oscillations.

In this phase diagram, Fig. 8.2(a), we choose three paradigmatic points to study the role of synaptic depression, one inside of the active state, another in the oscillations state, and one more near the boundary between the two regions (in other words, near the supercritical Hopf bifurcation). We do not present here results in the inactive state, because it is clear that synaptic depression does not change qualitatively this state: the neuronal network remains in the inactive state, despite the choice of parameters τ_R and P_d. Thus, at the chosen points we have a corresponding phase diagram in the τ_R-P_d plane when synaptic depression is turn on. In all of these phase diagrams, when τ_R and P_d are sufficiently large, the neuronal activity relaxes to a "suppressed state" of low activity (see Figs. 8.3(e) and 8.3(f), Figs. 8.4(e) and 8.4(f), and Figs. 8.5(g) and 8.5(h)). This fact can be easily understood from the mean-field equation (8.8). At a steady state, $\dot{J_{ee}}(\infty) = 0$, we obtain

$$J_{ee}(\infty) = \frac{1}{P_d \tau_R \nu \rho_e(\infty)^2 + 1}, \qquad (8.10)$$

where $\rho_e(\infty)$ is the steady state of the excitatory activity. Thus, increasing P_d and τ_R decreases $J_{ee}(\infty)$, i.e., it increases depression, and therefore the neuronal network is unable to present large activities. Note that we are only changing excitatory-excitatory connections, which means that we are applying depression to the excitatory mechanisms of the neuronal network. If excitatory neurons are no longer able to excite other excitatory neurons, then it leads to an effective decrease of the number of active excitatory neurons, and

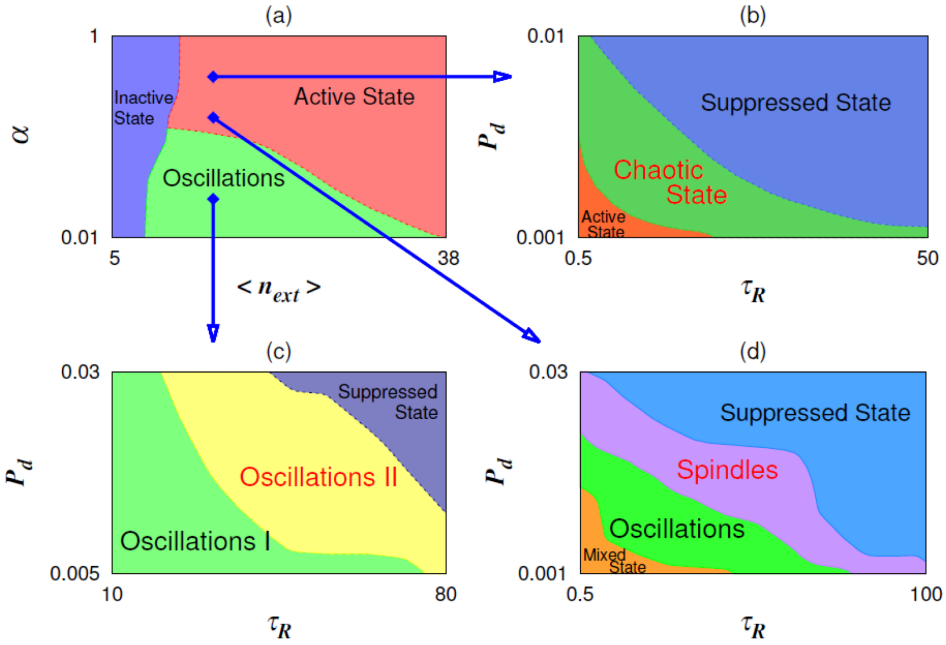

Figure 8.2: (a) $\langle n \rangle$-α plane of the phase diagram without synaptic dynamics. This is a simplified phase diagram (in comparison with Fig. 4.2), where "inactive state" corresponds to a region of parameters at which almost all neurons in the network are inactive; in the "active state" almost all neurons are active; and in the "oscillations" regime, there are network oscillations. At $\langle n \rangle = 15$, three points are distinguished corresponding to $\alpha = 0.2$, $\alpha = 0.6$, and $\alpha = 0.8$. Panels (b), (c), and (d) are τ_R-P_d planes of the phase diagram at each of these points, when synaptic depression between excitatory neurons is turned on. All the new states are discussed in the text. The phase diagrams presented here were obtained from simulations of the model. Parameters: $N = 10^4$, $c = 1000$, $g_i = 0.25$, $\Omega = 30$, $J_e = J_0 = 1$, $J_i = -3$, $\nu = 3$, $\tau = 0.1$, and $\sigma^2 = 10$. These data and figures were obtained by KyoungEun Lee.

---

consequently also inhibitory neurons. In contrast, at sufficiently small values of P_d and τ_R, synaptic depression does not play a role, because $J_{ee}(t)$ remains approximately constant ($J_{ee}(t) \approx J_e = 1$). Phase diagram (d), Fig. 8.2(d), may appear to be an exception, because it displays a "mixed state" in this region. Actually, it is not an exception, because we can also find this mixed state without synaptic depression near the boundary between the active state and oscillations, though it is not represented in Fig. 8.2(a). This mixed state results from finite-size effects rather than synaptic depression, and it is characterized by transient shifts from the oscillatory regime to the active state and *vice versa* (see Fig. 8.5(a)).

In all the cases, at intermediate parameters τ_R and P_d, we find new interesting regions of neuronal activity. First, in phase diagram (b), Fig. 8.2(b), there is a chaotic state (see Fig. 8.3(c)). In order to confirm that it is indeed a chaotic state, we performed the $0-1$

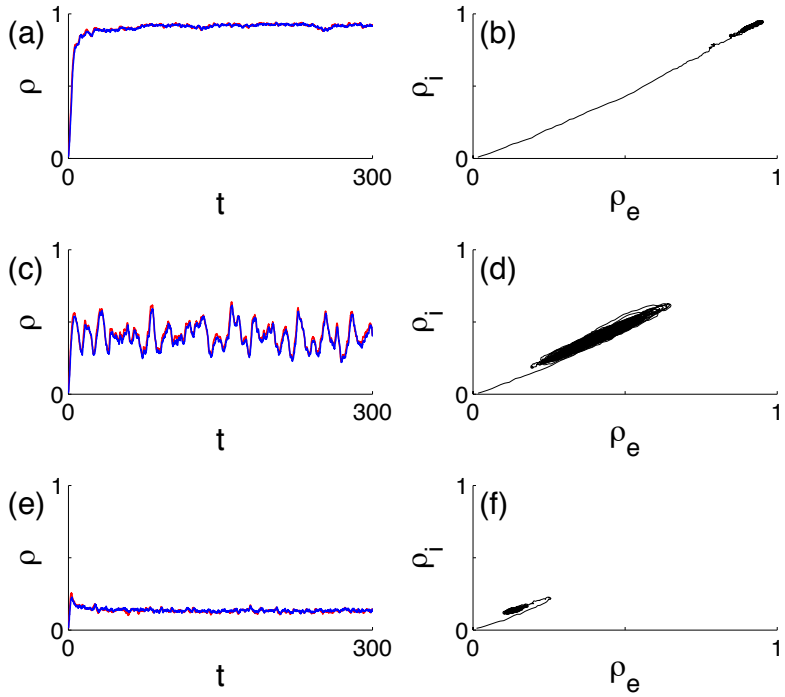

Figure 8.3: Representative activities (left column) of phase diagram (b), in Fig. 8.2(b), and respective (ρ_e, ρ_i)-phase-planes (right column), at $(\langle n \rangle, \alpha) = (15, 0.8)$. Panels (a) and (b) represent the active state at $(\tau_R, P_d) = (0.5, 0.001)$; panels (c) and (d) show the chaotic state at $(\tau_R, P_d) = (2.5, 0.004)$; and panels (e) and (f) display the suppressed state at $(\tau_R, P_d) = (50, 0.02)$. Other parameters are the same as in Fig. 8.2. The red lines correspond to excitatory activities, and the blue lines correspond to inhibitory activities (the activities almost coincide). Time t is in units of μ_e^{-1}. These data were obtained by KyoungEun Lee.

---

test for chaos, recently introduced by Gottwald and Melbourne [228, 229]. The method is based on the calculation of a K value. If $K \approx 1$, then the "observation" is chaotic (in our case the observation is the time series of the activity), whereas $K \approx 0$ indicates regular dynamics. For the activity displayed in Fig. 8.3(c), we obtained $K \approx 0.97$. Thus, we can affirm that this activity is chaotic. In the brain, chaotic neuronal activity has been observed in EEG signals [230]. Unfortunately, we did not find this regime in our numerical calculations, though it could emerge, since the dynamical system is described by three dynamical equations, Eqs. (3.15) and Eq. (8.8) (chaos can only emerge in a three- or higher-dimensional system [116]).

Second, in phase diagram (c), Fig. 8.2(c), the system displays a new kind of oscillations (see Fig. 8.4(c)): large amplitude oscillations periodically give place to small amplitude oscillations. As the parameters τ_R and P_d are increased, the neuronal activity shows more

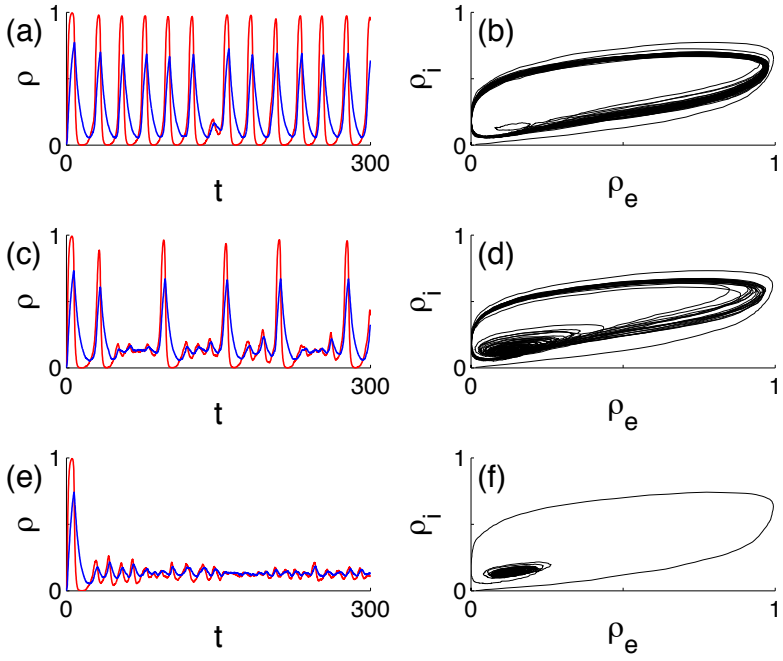

Figure 8.4: Representative activities (left column) of phase diagram (c), in Fig. 8.2(c), and respective (ρ_e, ρ_i)-phase-planes (right column), at $(\langle n \rangle, \alpha) = (15, 0.2)$. Panels (a) and (b) represent the state oscillations I at $(\tau_R, P_d) = (35, 0.01)$; panels (c) and (d) show the state oscillations II at $(\tau_R, P_d) = (67, 0.01)$; and panels (e) and (f) display the suppressed state at $(\tau_R, P_d) = (200, 0.01)$. Other parameters are the same as in Fig. 8.2. The red lines correspond to excitatory activities, and the blue lines correspond to inhibitory activities. Time t is in units of μ_e^{-1}. These data were obtained by KyoungEun Lee.

---

and more small amplitude oscillations (i.e., the rate of large amplitude oscillations decreases). In numerical calculations of Eqs. (3.15) and (8.8), we find the same behavior (a more detailed comparison is presented below). As the depression parameters are increased, the neuronal activity transits from oscillations I (ordinary sustained oscillations like those found without synaptic plasticity, see Fig. 8.4(a)) to "doubling", a state characterized by large oscillations intercalated by small oscillations, such that the period of large oscillations is twice the one presented in the "pure" oscillatory regime (which has only large amplitude oscillations). Further increase of τ_R and/ or P_d leads to "triplication" of the period, "quadruplication" and so on, until eventually one can only observe small amplitude oscillations. Each type of oscillations appears in a very narrow range of parameters (we combine all of these oscillations in the same region of the phase diagram corresponding to oscillations II). These oscillations (II) can also be called "mixed-mode oscillations". Mixed-mode oscillations correspond to an oscillatory regime that possesses two or more characteristic periods, where the ratio of the periods is an integer. This kind of oscillations has been observed

in the networks that generate the respiratory rhythm in mammals [231]. Interestingly, in Ref. [231], by increasing the neuronal excitability the authors observed a sequence of states: first oscillations, then mixed-mode oscillations, and finally an asynchronous state. In our model we find the same sequence of states in phase diagram (c), Fig. 8.2(c), when increasing the intensity of shot noise. Although it is out of the scope of this chapter to analyze in detail the phase transitions that take place when the neuronal network transits from one state to another, one should note that, based on the fact that second-order phase transitions are always accompanied by symmetry breaking and, in contrast, first-order phase transitions can occur without symmetry breaking [181, 232], one can find the order of the transitions. As mentioned in Sec. 5.2, in our model, it is the time homogeneity that is broken. Taking into account that both oscillations I and oscillations II have qualitatively the same long-term time correlations (they both correspond to an ordered state), we expect that the transition between these states is a first-order phase transition.

Third, in phase diagram (d), Fig. 8.2(d), between mixed and suppressed states, we find oscillations (see Fig. 8.5(c)), and spindles (see Fig. 8.5(e)). One can interpret that first synaptic depression prevents the system of staying in the active state (as it occurs transiently in the mixed state), and because of it the mixed state transits to a state of "pure" oscillations. Then, the depression mechanism becomes strong enough to disrupt the large oscillations and, as consequence, spindle oscillations emerge. Note that this spindle oscillations are slightly different from the ones we find without synaptic depression (see the inset in Fig. 5.6), because in this case the amplitude of the fluctuations is larger while the mean neuronal activity is smaller than in the case of the spindles without synaptic depression. In this case, the ratio between the leading and the mean modulation frequencies, f_L/f_M, is about 11.

Figure 8.6 shows the power spectral density (PSD) of the most interesting activities discussed above that appear at intermediate values of P_d and τ_R (obviously, the PSD was calculated with much larger time series than the ones we displayed in the previous figures). The PSD of panel (a) has several maximums, that correspond to the different frequencies present in Fig. 8.4(c). In the case of spindle oscillations, panel (b), the PSD has one distinct peak at the leading frequency of the oscillations in Fig. 8.5(e). The PSD of the chaotic activity displayed in Fig. 8.3(c), does not show any prominent peak (see Fig. 8.6(c)), meaning that the neuronal network does not oscillate with any preferred frequency.

In our numerical calculations (integration of Eqs. (3.15) and (8.8)), we could not find some of the dynamical regimes presented in Fig. 8.2, meaning that the mean-field approximation introduced in Eq. (8.7) impoverishes the system. Also, one should keep in mind that finite-size effects can play an important role in neuronal network dynamics. Since we could not find analytically a phase diagram when the system has synaptic depression, we used the same "brute-force" method as in simulations to study the system point-by-point. As mentioned for simulations, when the parameters τ_R and P_d are sufficiently small, the depression does not play any role, whereas when they are sufficiently large, the neuronal activity is "suppressed". In contrast with simulations, in numerical calculations anything "special" seems to occur near the boundary between oscillations and the active state, i.e., we could not find all the phases shown in the phase diagram (d), Fig. 8.2(d). In this case,

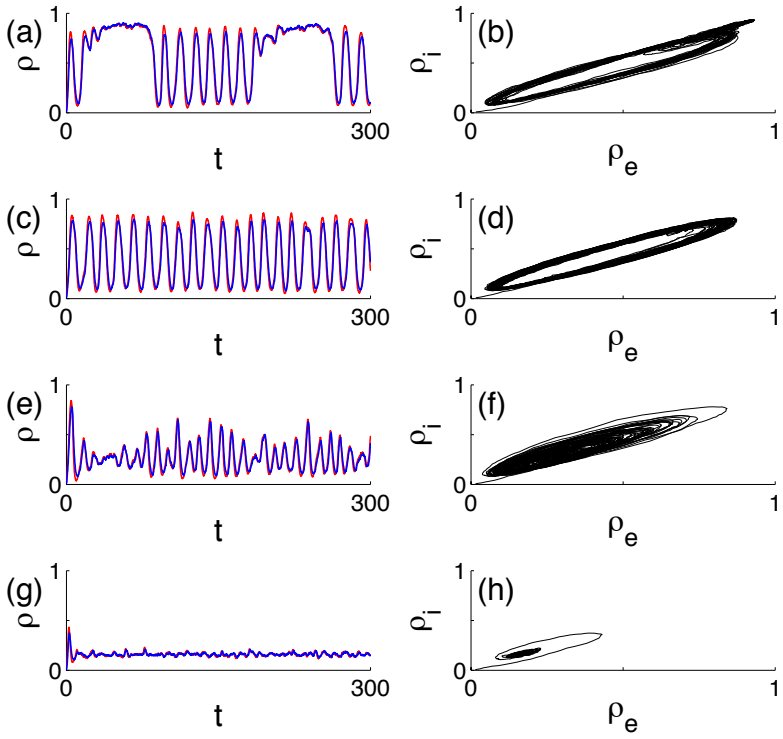

Figure 8.5: Representative activities (left column) of phase diagram (d), in Fig. 8.2(d), and respective (ρ_e, ρ_i)-phase-planes (right column), at $(\langle n \rangle, \alpha) = (15, 0.6)$. Panels (a) and (b) represent the mixed state at $(\tau_R, P_d) = (0.8, 0.005)$; panels (c) and (d) show the oscillatory state at $(\tau_R, P_d) = (4, 0.002)$; panels (e) and (f) display the spindles state at $(\tau_R, P_d) = (9, 0.008)$; and panels (g) and (h) present the suppressed state at $(\tau_R, P_d) = (10, 0.03)$. Other parameters are the same as in Fig. 8.2. The red lines correspond to excitatory activities, and the blue lines correspond to inhibitory activities (the activities almost coincide). Time t is in units of μ_e^{-1}. These data were obtained by KyoungEun Lee.

---

the boundary is well-defined, and we can either study the system in one side or the other (i.e., in the oscillatory state, or in the active state). The qualitative behavior inside a region does not seem to depend on how close the system is to the boundary. As mentioned above, we could not find the chaotic state of Fig. 8.2(b), but we observed the oscillations II of Fig. 8.2(c). In Fig. 8.7 we compare the simulation results with the numerical calculations. Once again, there is a small difference in the frequency of oscillations, that can be attributed to finite-size effects, as discussed in Chapter 4. Moreover, the different shapes of oscillations take place at slightly different parameters (see the caption of Fig. 8.7). Nevertheless, in this case, the numerical calculations are in fair agreement with the simulations. The

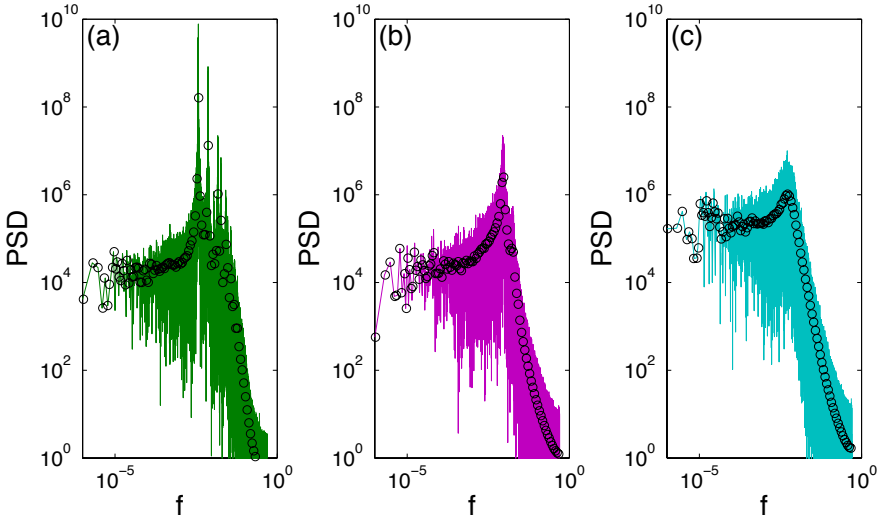

Figure 8.6: Power spectral density (PSD) as function of the frequency f for (a) the oscillatory state II, corresponding to the activity represented in Fig. 8.4(c); (b) for spindles, corresponding to the activity displayed in Fig. 8.5(e); and (c) for the chaotic state, corresponding to the activity presented in Fig. 8.3(c). The circles correspond to logarithmic binning. The parameters are mentioned in the respective figure of each activity. These data were obtained by KyoungEun Lee.

---

transition from one type of oscillations to another may be due to a Shil'nikov bifurcation [165], however it is necessary a more detailed analytical analysis to prove it. In regard to Fig. 8.2(b), in numerical calculations the depression mechanism seems to push the system to the inactive state (in other words, it is similar to a decrease of the intensity of noise $\langle n \rangle$, though the suppressed state presents larger activity than the inactive state, as mentioned before). Interestingly, the three points chosen in the phase diagram (a), Fig. 8.2(a), do not capture all possible qualitative outcomes of introducing synaptic depression. Figure 8.8 shows the consequences of turning on synaptic depression in the case when the system has damped oscillations (see Fig. 8.8(a)), near the supercritical Hopf bifurcation, but far from the saddle-node bifurcation. Once again, synaptic depression plays a role similar to a decrease in $\langle n \rangle$, and oscillations emerge (see Fig. 8.8(c)). However, depending on the recovery variable τ_R, $J_{ee}(t)$ may recover quicker (see Fig. 8.8(d)), or slower (see Figs. 8.8(f) and 8.8(h)), which in turn is responsible for transient periods of small amplitude oscillations. Remarkably, the large amplitude oscillations appear in pairs, a feature that was absent in the state oscillations II (see Fig. 8.7). Thus, we can not guarantee that we have presented the complete repertoire of dynamical regimes.

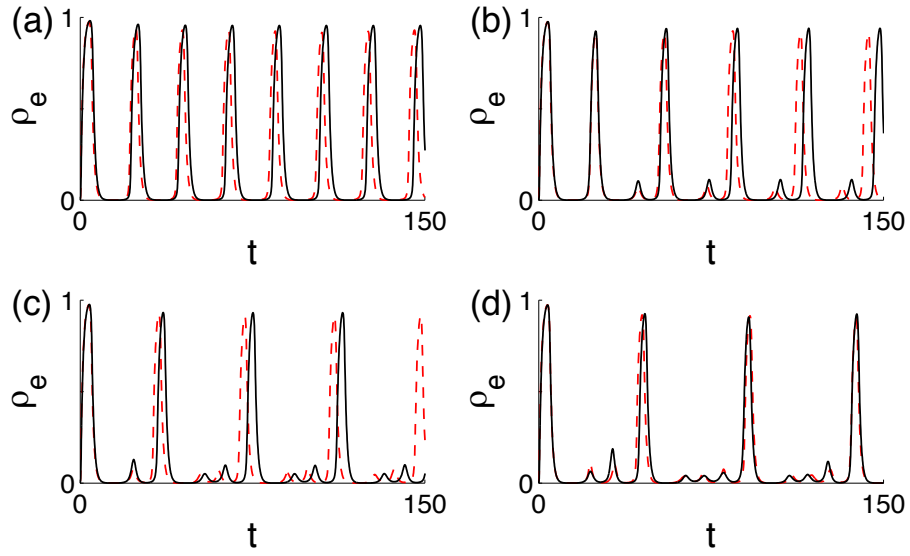

Figure 8.7: Comparison between excitatory activities obtained by simulations and by numerical calculations. Red dashed lines correspond to simulation results, and black lines correspond to numerical integration of Eqs. (3.15) and (8.8). The parameters of synaptic depression of simulations (numerical calculations) for each panel are the following: (a) $P_d = 0.03$ (0.03) , and $\tau_R = 25$ (25); (b) $P_d = 0.03$ (0.04) , and $\tau_R = 36$ (40); (c) $P_d = 0.03$ (0.04) , and $\tau_R = 46$ (55); and (d) $P_d = 0.03$ (0.045) , and $\tau_R = 56$ (67). These activities appear in phase diagram (c), in Fig. 8.2(c), i.e., $(\langle n \rangle, \alpha) = (15, 0.2)$. Other parameters are the same as in Fig. 8.2. Time t is in units of μ_e^{-1}. The data from simulations were obtained by KyoungEun Lee.

8.3 Facilitation and depression

We now turn to facilitation and depression mechanisms together. Note that in the case of depression there were many other possibilities to investigate, in particular, one could consider synaptic depression not only on excitatory-excitatory connections, but also between other neurons. In general, one can play with a set of four pairs of parameters τ_R and P_d for all types of connections (J_{ee}, J_{ei}, J_{ie}, and J_{ii}). One can mention, for example, that if the depression mechanism on J_{ie} is strong enough, then it leads to a complete active network, because inhibitory neurons are unable to suppress excitatory activity.

In this section, we present some preliminary numerical results. We take Eqs. (8.1) and (8.2), and we apply the mean field approximation used above, Eq. (8.7), and we obtain

$$\begin{aligned} \dot{x_{ab}}(t) &= \frac{1 - x_{ab}(t)}{\tau_D} - u_{ab} x_{ab}(t) \nu \rho_a(t) \rho_b(t), \\ \dot{u_{ab}}(t) &= \frac{U - u_{ab}(t)}{\tau_F} + U(1 - u_{ab}(t)) \nu \rho_a(t) \rho_b(t), \end{aligned} \tag{8.11}$$

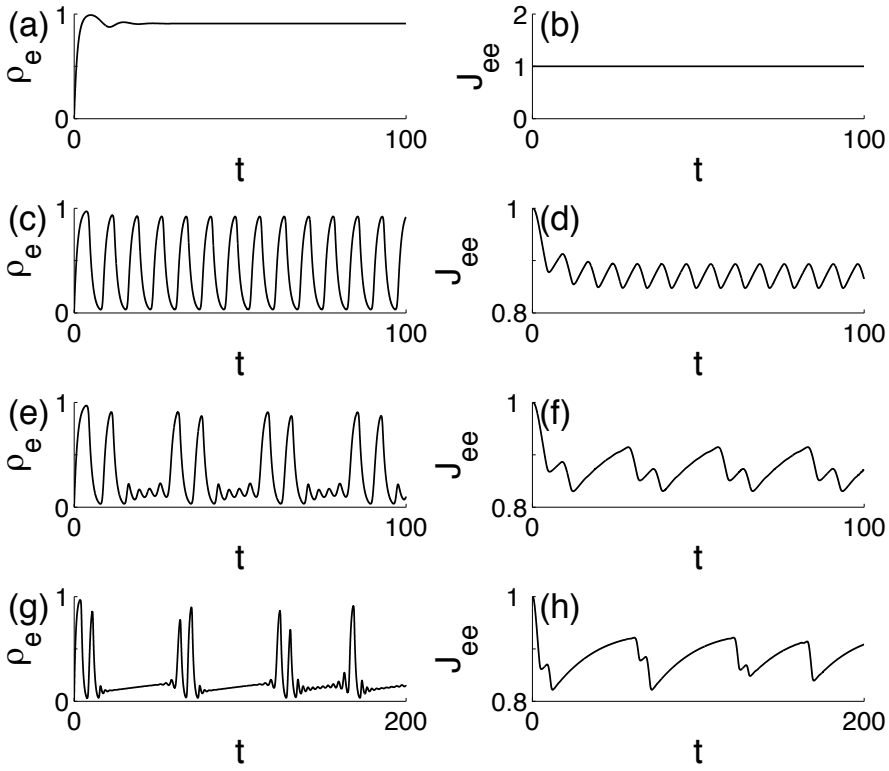

Figure 8.8: At noise intensities above the supercritical Hopf bifurcation ($\langle n \rangle > n_{c3}$), the network activity relaxes in the form of damped oscillations to a high activity state (panel (a)), when synaptic depression is turn off (panel (b) presents the synaptic depression variable $J_{ee}(t)$, as well as the other panels on the right column show the variables $J_{ee}(t)$ that correspond to the activities on the left column). When synaptic depression is turn on ($P_d = 0.005$), the activity can either display network oscillations (panel (c)), if the recovery variable of synaptic depression is fast enough (panel (d), $\tau_R = 10$); or complex oscillations (panels (e) and (g)), whose frequency depends on the synaptic dynamics, i.e., on τ_R (panels (f) and (h), to which correspond $\tau_R = 20$ and $\tau_R = 40$, respectively). Note that in the figure it is only represented the excitatory activity, because the inhibitory activity has a similar behavior. These are numerical results obtained from the integration of Eqs. (3.15) and (8.8). Parameters: $\alpha = 0.5$, $\langle n \rangle = 100$, $\nu = 10$, and $\tau = 0.1$. Other parameters are the same as in Fig. 8.2. Time t is in units of μ_e^{-1}.

---

where $a, b = e, i$. Parameters τ_D and τ_F are the recovery times of synaptic depression and facilitation, respectively. The parameter U determines the rest state of variable u. In order to simplify, we consider again the mechanism only applied on excitatory-excitatory

connections. Thus, we have

$$J_{ee}(t) = J_0 x_{ee}(t) u_{ee}(t), \tag{8.12}$$

where $J_0 = J_e = 1$. The steady states of Eqs. (8.11) are obtained from the conditions $\dot{x_{ee}}(\infty) = 0$ and $\dot{u_{ee}}(\infty) = 0$, and we find

$$\begin{aligned} x_{ee}(\infty) &= \frac{1}{1 + u_{ee}(\infty)\nu\rho(\infty)^2\tau_D}, \\ u_{ee}(\infty) &= \frac{U(1 + \nu\rho(\infty)^2\tau_F)}{1 + U\nu\rho(\infty)^2\tau_F}. \end{aligned} \tag{8.13}$$

If the steady state activity $\rho(\infty)$ is sufficiently small, then $u_{ee}(\infty) \approx U$, and $x_{ee}(\infty) \approx 1$. In this case, if U is smaller than one, depression is the dominant mechanism, whereas if $U > 1$, facilitation is the dominant one. Thus, in Figs. 8.9(a)-(d), we show that when $U < 1$, synaptic plasticity plays the role of depression, and because of it the oscillations that would occur without synaptic plasticity (at $(\langle n \rangle, \alpha) = (25, 0.2)$) give place to oscillations of type II (Fig. 8.9(a)), similar to the ones displayed in Fig. 8.7(b). If U is small enough, the neuronal activity transits to the suppressed state (Fig. 8.9(c)), as in the previous section. In contrast, when $U > 1$, the inactive state (at $(\langle n \rangle, \alpha) = (18, 0.2)$) can be "activated" by facilitation. Increasing U is similar to an increase of the noise intensity $\langle n \rangle$, because as one can see in Figs. 8.9(e)-(h), network oscillations emerge, and the frequency becomes larger as we increase U. Further investigations are necessary to understand how τ_D and τ_F can influence neuronal networks dynamics. These investigations are motivated by the fact that, for example, diseases may change these parameters and consequently neuronal dynamics may also be affected.

Finally, motivated by the fact that synaptic plasticity is believed to be the mechanism responsible for memory in the brain [109], we study how synaptic plasticity can influence on the response of a network to a signal. As in Chapter 6, we introduce a signal in the neuronal network through a number $g_s g_e N$ of sensory neurons that are connected at random to the excitatory neurons. As an example, we stimulated the neuronal network at an inactive state, $(\langle n \rangle, \alpha) = (18, 0.2)$, with a sinusoidal signal $S(t)$,

$$S(t) = \frac{A}{2}(\sin(2\pi t/T) + 1), \tag{8.14}$$

(recall that the signal is introduced in A_e, see Eqs. (6.2) and (6.3)). Figure 8.10(a) displays the signal, which is only four periods long. The idea was to observe if the neuronal network would shift its dynamical state to a different state due to the transient presence of the signal. In other words, the neuronal network was at a certain state (1), then the signal would affect this state, and consequently, after the transient stimulation, the neuronal network would stay at a state (2) different from state (1). It would mean that the system was affected by the signal and had a memory of it. Without synaptic plasticity it is clear that when an input signal is turn off, the neuronal network returns to its original state. Can we have a different scenario when synaptic plasticity is present? Unfortunately, we could not find such scenario. As Figs. 8.10(b) and 8.10(c) show, when the signal is turn off, the neuronal

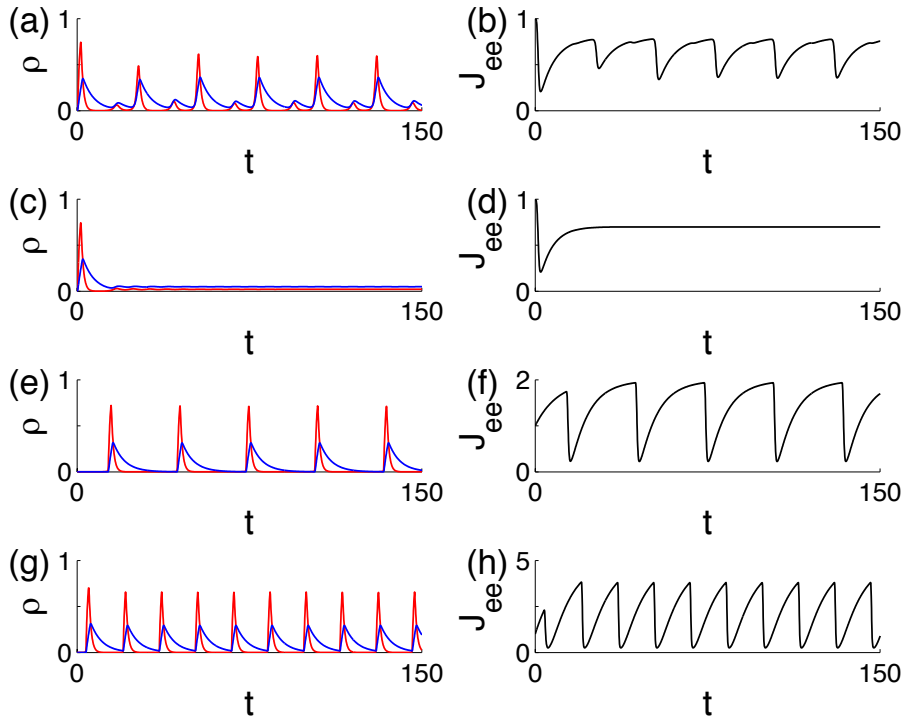

Figure 8.9: Activities (left column) and respective synaptic plasticity variables $J_{ee}(t)$ (right column), when both facilitation and depression mechanisms are present. The red lines correspond to excitatory activities, and blue lines correspond to inhibitory activities. The figures were obtained solving numerically Eqs. (3.15) and (8.11) at the following parameters: (a) and (b) at $(\tau_R, U, \tau_F) = (8, 0.8, 10)$ and $(\langle n \rangle, \alpha) = (25, 0.2)$; (c) and (d) at $(\tau_R, U, \tau_F) = (8, 0.7, 10)$ and $(\langle n \rangle, \alpha) = (25, 0.2)$; (e) and (f) at $(\tau_R, U, \tau_F) = (5, 2, 10)$ and $(\langle n \rangle, \alpha) = (18, 0.2)$. (g) and (h) at $(\tau_R, U, \tau_F) = (5, 5, 10)$ and $(\langle n \rangle, \alpha) = (18, 0.2)$. Other parameters are the same as in Fig. 8.2. Time t is in units of μ_e^{-1}.

network dynamics returns to the previous state. We have tried other parameters, but the results were equally disappointing. Obviously, these very naive attempts do not imply that the idea is infeasible.

We conclude by reminding that this chapter presented preliminary results about the role of synaptic plasticity on neuronal networks dynamics. As we showed, even synaptic depression alone on excitatory-excitatory connections largely enriches the repertoire of dynamical states. Certainly, synaptic plasticity on all types of connections can open many other possibilities. The problem is that it is too difficult to analyse the system point-by-point. Besides, without an analytical approach, it is unclear how to systematize the obtained knowledge.

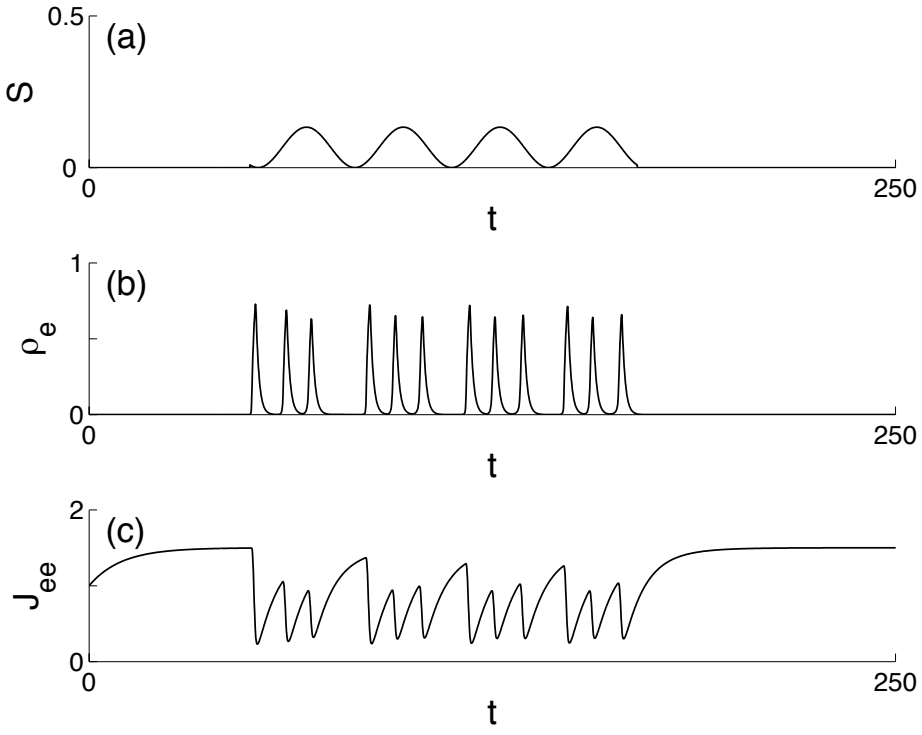

Figure 8.10: Response of a neuronal network with synaptic plasticity to a signal. (a) Sinusoidal signal sent to 13% of excitatory neurons (amplitude $A = 1$, and period $T = 30\mu_e^{-1}$). (b) Response of the neuronal network (excitatory activity) to the signal. (c) Corresponding response of the synaptic plasticity variable $J_{ee}(t)$. These are numerical results obtained from the integration of Eqs. (6.3) and (8.11). With exception to U ($U = 1.5$), all parameters are the same as in Fig. 8.9(e). In Eqs. (6.3), $F(t) = 0$. Time t is in units of μ_e^{-1}.

Chapter 9

Conclusion

This thesis presented a research performed from October 2010 to July 2014, at the Physics Department of Universidade de Aveiro. The subject under consideration was dynamics, phase transitions and nonlinear phenomena in neuronal network models. These investigations were done in collaboration with my supervisor, Prof. Alexander V. Goltsev, and Dr. KyoungEun Lee (Post-Doc researcher).

We started this manuscript by stating the current motivation and effort to study the brain, followed by a brief historical review concerning its understanding. In particular, we presented the most successful mathematical models in neuroscience. Then, we introduced network theory, and we explained how it can help to study features of neuronal networks, and certain dynamical phenomena. Since these phenomena are the main topic of investigation in this thesis, we completed Chapter 1 with a brief introduction of each one: brain rhythms, band-pass filter, stochastic resonance, phase transitions in the brain, and epilepsy.

In Chapter 2, we examined some basic concepts in neuroscience. We gave a brief review about the morphology and electrophysiology of neurons, in order to present a simplified overview about how the neurons function. Then, we introduced some paradigmatic models in theoretical neuroscience, namely, the Hodgkin-Huxley model [14], the integrate-and-fire model [10], and the more recent Izhikevich model [115]. Finally, we provided a summary of the main experimental tools to monitor brain activity.

Chapter 3 presents our model of neuronal networks, and in Chapter 4 the model is analysed. It also contains a description of the methods employed to study the model. We have obtained the fixed points of the model rate equations, and by studying the local stability of the points we got a phase diagram that condenses the different dynamical regimes that occur at different parameters. In Chapter 5, we have shown the different phase transitions and respective bifurcations. Moreover, we discussed the critical phenomena that accompany the phase transitions. These results allowed us to suggest a qualitative explanation of the Berger effect, and to describe a band-pass filter phenomenon. Most of these results were published in Ref. [102].

Stochastic resonance is one other nonlinear phenomenon that occurs in our neuronal network as a consequence of a phase transition. In Chapter 6, we have studied this phe-

nomenon and we mimicked the experiments of Gluckman *et al.* [51]. Taking into account that stochastic resonance is not a reliable mechanism for signal detection, we have also discussed the role of modular structure in sensory systems, showing how it can improve signal processing. These results are accepted for publication [213].

In Chapter 7, we proposed that paroxysmal spikes observed in EEG from epileptic brains can be described by a nonlinear object found in our model. Our paroxysmal-like spikes appear near a second-order phase transition. Consequently, it allowed us to suggest a measurement to predict epileptic seizures. In this chapter we also discussed the results presented in Appendices A and B, regarding a comparison of network dynamics between our model and a network composed of Izhikevich neurons, and an analysis of metastability near a subcritical Hopf bifurcation in a toy model. Part of these results is being prepared to submit to a journal.

Synaptic plasticity is a mechanism that modifies the strength of synapses over time. We studied this mechanism in neuronal networks in Chapter 8. The phase diagram of the model became richer with new dynamical states. In particular, we found a range of parameters at which the network is in a chaotic state. Some of these results were published in Ref. [111].

Finally, Appendix C presents models of neuronal networks on complete graphs. The dynamics of single neurons were considered similar to the model presented in Chapter 3. We have shown that topology plays a very important role in network dynamics. These results are also being prepared to submit to a journal.

Throughout the thesis we have discussed several results within our model that can be compared with experiments, or that can provide a theoretical explanation to understand experimental observations. Here, we give a summary of the most interesting results among those:

- We have found neuronal avalanches near the limiting point of the metastable states of a first-order phase transition, whose distribution over sizes is a power-law with the mean-field exponent $\alpha = -1.5$. Similar avalanches have been found in neuronal cultures [76] and also in neuronal networks *in vivo* [78].

- Within our model, the first-order phase transition is characterized by hysteresis. This is in agreement with experiments, where a similar phenomenon has been observed by measuring the activity of neurons *in vitro* when subjected to an electrical field [180]. It means that our model gives a qualitative explanation for both the jump from low activity to high activity [138], and for the reverse jump from high activity to low activity that occurs at lower intensity of the stimulation [180].

- The Berger effect is characterized by a decrease of alpha rhythm's amplitude when the eyes are open [41]. Qualitatively, opening the eyes results in an increase of stimulation to the occipital area of the brain. In our model, we also find a decrease of the amplitude of neuronal network oscillations when increasing noise (or any other kind of "excitatory" stimulation) near the supercritical Hopf bifurcation. (Recall that the Berger effect can also occur in the case of auditory stimuli [198, 199].)

- We found that the supercritical Hopf bifurcation is responsible for a band-pass filter phenomenon. One can compare it with the experiments of Sasaki *et al.* that showed that the majority of rat CA1 neurons can act collectively like a band-pass filter and fire synchronously [64].

- If inhibitory neurons respond slower than excitatory neurons ($\alpha < \alpha_t$), when increasing the noise intensity from zero, our neuronal network undergoes first a saddle-node bifurcation and then a Hopf bifurcation. The Morris-Lecar neuron experiences the same sequence of bifurcations when increasing the input current (at a certain set of parameters) [187]. Additionally, the phase portraits of our neuronal network model are topologically equivalent to the ones in the Morris-Lecar model. Consequently, these models have similar excitable dynamics. Interestingly, it has been found in neuronal cultures that neurons form clusters ("super-neurons") that present excitable features similar to single neurons [180].

- We demonstrated that stochastic resonance takes place in a region that precedes a saddle-node bifurcation. Stochastic resonance has also been studied experimentally in neuronal cultures. Here, we have mimicked the experiments of Gluckman *et al.* [51], and our model provides a qualitative explanation of these experiments.

- Near the saddle-node bifurcation we have found nonlinear excitations similar to paroxysmal spikes. These sharp spikes that we found are strong nonlinear objects that appear from a very low neuronal activity and quickly reach very high amplitudes, combining in synchronized activity about 90% of the neurons in the network, similar to epileptic activity, particularly interictal activity. Moreover, it is well-known that during a seizure the ictal pattern is generally rhythmic, and the rhythm usually displays increasing amplitude and decreasing frequency [94, 96]. The same dynamical evolution of collective activity occurs in our model if we assume that the neuronal network is in the regime of network oscillations, near the saddle-node bifurcation, and the intensity of noise is gradually decreasing. Thus, based on our model we propose that the transition from interictal to ictal activity is due to a saddle-node bifurcation, where the interictal activity corresponds to our nonlinear excitations, and the ictal activity matches the network oscillations. Increasing stimulation leads to the transition from interictal to ictal activity (like in photosensitive epilepsy [98]), while decreasing the stimulation drives the reverse transition.

- Based on our investigations of neuronal networks with synaptic plasticity we propose that mixed-mode oscillations appear due to the mechanism of synaptic depression. This kind of oscillations has been observed in the networks that generate the respiratory rhythm in mammals [231]. Moreover, at certain parameters, when increasing the intensity of shot noise, first we find oscillations, then mixed-mode oscillations, and finally an asynchronous state. Interestingly, the same sequence of states was observed in the respiratory network of neonatal rodents and human infants *in vivo* [231] when increasing neuronal excitability.

Our investigations also led to some predictions that may be confirmed experimentally. Here, we review the most promising:

- As mentioned above, our model can provide a qualitative explanation of the Berger effect. In order to confirm, one can further study the phenomenon starting from the assumption that it is related with a second-order phase transition (as our model suggests). The control parameter may be the intensity of light that the eyes receive. Thus, by changing the intensity of light gradually, one can measure neuronal activity fluctuations. As the system approaches the critical point, the theory predicts that the autocorrelation function of activity fluctuations should increase. Moreover, based on our model, we further suggest that it may be possible to observe a decrease in the phase lag between excitatory and inhibitory activities due to the supercritical Hopf bifurcation.

- We showed that power spectral density (PSD) analysis can be a very powerful tool to qualify phase transitions and bifurcations in a neuronal network. We demonstrated that critical slowing down occurs at the critical points of the saddle-node and Hopf bifurcations. This critical phenomenon can be observed as an increase of the zero frequency peak of the PSD when approaching the saddle-node bifurcation. When the network approaches the Hopf bifurcation, critical fluctuations increase due to the critical slowing down, which results in a divergence of the PSD at the frequency of the damped oscillations. We showed that finite-size effects smear these peaks in the PSD. We propose to experimentalists to use PSD analysis to describe critical phenomena that may occur in real neuronal networks.

- We have demonstrated that modular structure can improve the reliability of signal detection, in particular, if we consider that each module is working in the regime of stochastic resonance. It is an experimental fact that the nervous system has columnar organization [233], and at least some sensory systems are organized in modules, each one responsible for the processing of a particular feature of the input signal (for instance, different frequencies are processed by different groups of neurons in the auditory system [1]). Furthermore, cortical columns are formed by many minicolumns, which are bound by a common input and short range horizontal connections [34]. In our model, the considered modules match those cortical minicolumns, because all our modules receive the same signal. They process it independently, and then their response is combined in an averaging module. Our proposal does not reject the well-studied stochastic resonance at the level of single neurons. Instead, we suggest that single neurons may be working in a regime of stochastic resonance as a single component that helps a module to respond to an input signal.

- Based on the assumption that the transition from interictal to ictal activity is well-modelled by the saddle-node bifurcation, we propose two methods to forecast epileptic seizures. Within our model, as the neuronal network approaches the critical point from the interictal state, the paroxysmal-like spikes become easier to be stimulated.

Consequently, one can assume that it may be possible to estimate how close is an epileptic brain from a seizure state by repeatedly measuring the minimum amplitude of stimulation required to elicit a paroxysmal spike. Additionally, since the saddle-node bifurcation is the mechanism of a second-order phase transition, we expect a divergency of a susceptibility-like variable in the system at the critical point. Accordingly, we suggest that the variance of the rate of paroxysmal spikes should increase as the system gets closer to the transition point from interictal to ictal activity. In order to test these predictions, we have started a collaboration with physicians from Coimbra University Hospitals.

Note that these results should not be mere features of our model. Our confidence is based on the concept of universality in statistical physics [234]. The discussed phenomena are related with phase transitions, and phase transitions are universal [234]. It means that the emergent collective behavior is independent on the details of single unit dynamics [223]. On the other hand, it is important to realize that such emergent collective phenomena can not be understood from a simple extrapolation of the properties of a few interacting neurons. As P.W. Anderson stated in his seminal paper [235], "more is different", i.e., in the limit of large systems, new properties and complexity arise, which could not be predicted from a reductionist analysis of the system. Indeed, for instance, one could not predict the emergence of paroxysmal-like spikes only taking into account how single neurons function.

The investigations presented in this thesis can serve as starting point for other projects. In general, one can add new ingredients to our neuronal network model to make it more realistic and to study the role of the new "elements". In the brain, neurons are not as simple as in a model, and they do not function "alone". Proteins and gene networks play a crucial role on the dynamics of neuronal networks, though they are frequently neglected. Moreover, glial cells provide essential support to neurons, and their role may not be as passive as it was thought and assumed [236]. One can also consider space in our model. In this case, we could study the propagation of neuronal oscillations as waves. Alternatively, we can consider simultaneously several interacting neuronal networks in different dynamical regimes. It could be used to model the interaction between different areas in the brain. On other hand, brain diseases often offer a framework to study specific collective phenomena in neuronal networks under specific conditions in comparison with the healthy case. In this thesis we have focused on epilepsy, and further work is necessary to verify our predictions. Our model could also qualitatively describe the decrease of the frequency of brain waves due to Alzheimer's disease [114]. Holstein *et al.* [114] studied the impact of damage on the collective dynamics of neuronal networks, a damage that can be compared to neurodegenerative processes in this disease. Additional research can be designed to further study Alzheimer's disease. Other diseases may also be examined, for instance Parkinson's disease and the role of deep brain stimulation in the control of symptoms of the disease [237]. Finally, in this thesis we presented a preliminary investigation about the role of synaptic plasticity on neuronal network dynamics. The next step is to try to model the most simple mechanisms of memory formation, like habituation and sensitization [1], using these mechanisms of synaptic plasticity.

Appendix A

Network of Izhikevich neurons

In this appendix we aim to investigate the dynamics of a random network composed of Izhikevich neurons [115, 123]. Particularly, we study different approaches in order to compare the dynamics of this network with the neuronal network dynamics studied in Chapters 4, 5 and 7. These investigations were motivated by the fact that phase transitions and related phenomena (such as critical phenomena) are believed to be universal, independent on details of single unit dynamics [223]. We were specially interested about the possibility of finding paroxysmal-like spikes (see Chapter 7) in a different model.

A.1 Single neurons

The Izhikevich model of a single neuron was already presented in this thesis, in Section 2.4. The membrane potential v of the Izhikevich neuron obeys to the differential equation [115],

$$\dot{v} = 0.04v^2 + 5v + 140 - u + I, \tag{A.1}$$

where I is the input current, and u represents a membrane recovery variable, which is also time dependent,

$$\dot{u} = a(bv - u). \tag{A.2}$$

The variable u accounts for the activation of K^+ ionic currents and also for the inactivation of Na^+ ionic currents, providing negative feedback to the membrane potential. The parameter a characterizes the time scale of u (larger values of a result in a faster recovery). The parameter b tunes the sensitivity of u to v. When v reaches its apex ($v = 30$), it is reset to c, the after-spike reset value of the membrane potential, and, simultaneously, u is reset to $u + d$, where d is the after-spike reset of the recovery variable. All variables (v and u) and parameters (a, b, c, and d) are dimensionless. The membrane potential v has mV scale and the time t has ms scale. As Izhikevich, we use Euler's Method to solve numerically the differential equations.

We start by looking for candidates to replace our excitatory and inhibitory neurons. In the cortex, excitatory neurons are usually regular spiking (RS) neurons, whereas inhibitory neurons can be fast spiking (FS) neurons [124]. In his paper [115], Izhikevich

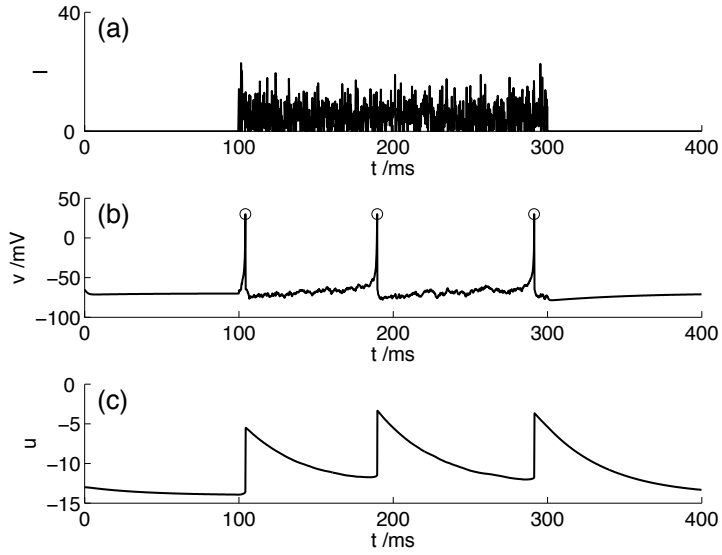

Figure A.1: Response of a regular spiking neuron to a noisy current. (a) The input current I is active in the time interval $[100, 300]$ ms. The amplitude of the current is generated by a Gaussian process, whose mean amplitude is $\mu = 5$, and standard deviation $\sigma = 5$. (b) Membrane potential v of the neuron when subjected to the current displayed in panel (a). The circles signal the apex of the action potential and consequent reset. Panel (c) displays the corresponding dynamics of the recovery variable u. Parameters: $(a, b, c, d) = (0.02, 0.2, -65, 8)$, and time step $dt = 0.2$.

provides the appropriate parameters for these neurons. RS neurons are characterized by $(a, b, c, d) = (0.02, 0.2, -65, 8)$, and FS neurons have $(a, b, c, d) = (0.1, 0.2, -65, 2)$. Note that FS neurons have larger a than RS neurons, which means that the u variable recovers quickly after a spike, allowing them to present larger firing rates (that is why they are called "fast" spiking neurons). Figures A.1 and A.2 show the response of a RS and a FS neuron to a noisy input current (this current was active in the time interval $[100, 300]$ ms, and it was generated by a Gaussian process characterized by $(\mu, \sigma) = (5, 5)$). These figures show that the u variable has much slower dynamics than the membrane potential, and that the firing rate is mainly controled by u. As expected, the FS neuron has a larger firing rate than the RS neuron, though the noisy current was equivalent in the two cases.

In our model, excitatory and inhibitory neurons have the same firing rate. Therefore, and to simplify, in the network composed of Izhikevich neurons we consider only regular spiking neurons. Figure A.3 shows the firing rate of a regular spiking neuron as function of the input current. At a given dc current, the firing rate was calculated as the number of spikes the neuron fired during 0.5 s, divided by the time interval. (The apparent discontinuities in the firing rate become smaller and smaller as the time step is reduced, and the time interval is increased.) This neuron fires if the input current is larger than $I_{th} \approx 3$,

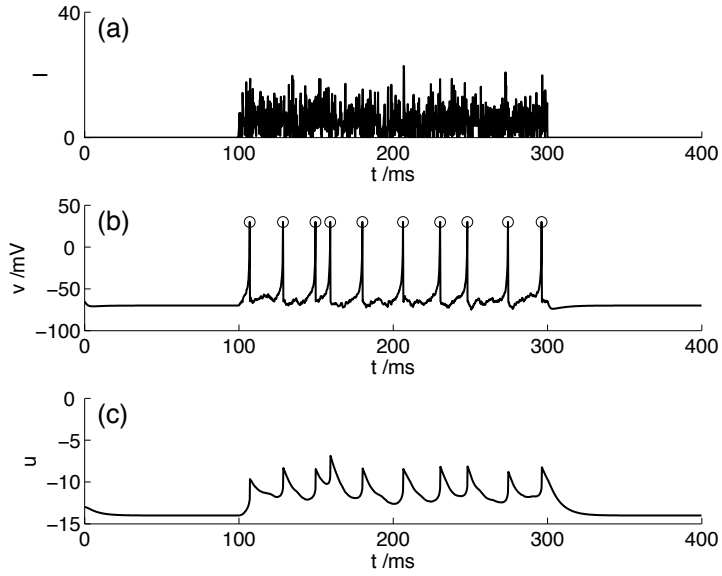

Figure A.2: Response of a fast spiking neuron to a noisy current. As in Fig. A.1, the current in panel (a) is active in the time interval $[100, 300]$ ms, and it generated by a Gaussian process, $\mu = \sigma = 5$. Panels (b) and (c) show the corresponding response of the membrane potential v and recovery variable u to the current. Parameters: $(a, b, c, d) = (0.1, 0.2, -65, 2)$, and time step $dt = 0.2$.

---

and, at large currents, the firing rate grows approximately linearly with the current. One should recall that, in contrast, the firing rate of our neurons is a step function of the input current (see Fig. 3.1(c)).

This brief analysis of Izhikevich neurons was meant to obtain a rough insight about how one can compare our neuronal network dynamics with the dynamics of a network composed of Izhikevich neurons. In particular, there are two crucial ingredients that one should be able to compare, in order to study both neuronal networks in a similar dynamical regime: the noise intensity and the ratio of the time responses of excitatory and inhibitory neurons (α). Obviously, the Gaussian noise can be introduced in the current I, and it should be related with the threshold of single neurons (V_{th} in our model). Thus, we assume the following relation:

$$I_n = \langle n \rangle \frac{X}{V_{th}}, \tag{A.3}$$

where I_n is the mean noise current in the Izhikevich network that corresponds to the noise intensity $\langle n \rangle$ in our neuronal network model. X is a threshold-like value for the Izhikevich neuron. We remind that this model does not have a well-defined threshold for single neurons to fire, instead the internal threshold depends on the previous activity of the neuron. We choose $X = 5$ (larger than the value $I_{th} \approx 3$ identified in Fig. A.3, because the neuron is only able to fire at such small input current if it has been silent for a sufficiently

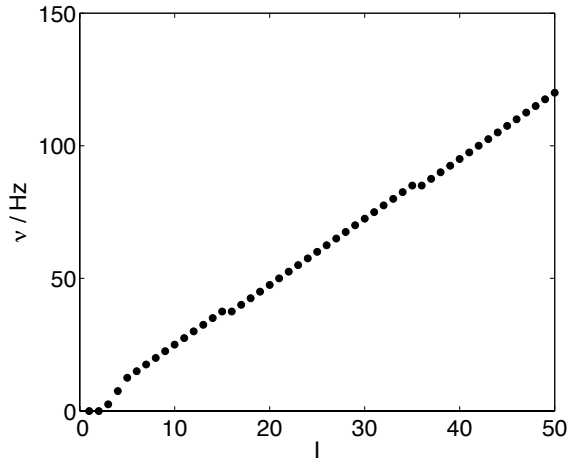

Figure A.3: Firing rate of a regular spiking neuron as function of the input current I. The neuron fires if the input current is larger than $I_{th} \approx 3$. Parameters: $(a, b, c, d) = (0.02, 0.2, -65, 8)$, and time step $dt = 0.1$.

---

long time, due to the recovery of u, a condition that might be unreasonable in an active network). Similarly, we define

$$I_\sigma = \sigma \frac{X}{V_{th}}, \tag{A.4}$$

where I_σ is the standard deviation of the noise introduced in the Izhikevich network (σ is the corresponding standard deviation in our model). A justification for this choice is given in Appendix C.3.

It is more difficult to define the α parameter within the Izhikevich neuron model. Unfortunately, in this model there is no parameter that controls directly the response time of a neuron. When the membrane potential goes above an internal threshold, i.e., when v crosses the parabola of the v-nullcline, $\dot{v} = 0$ (see Eq. (A.1)), the membrane potential continues to increase until it reaches its apex, at which it is reset to c. Therefore, the response time is related with $\dot{v}$: it depends on how quickly the spike reaches its apex. A solution would be to change the constants in Eq. (A.1), however the model could lose its plausibility. For instance, an alteration to these values would change the position of the v-nullcline, and consequently the internal threshold. It would be necessary to study a complete set of new parameters, including a, b, c, and d, in order to maintain realistic single neuron dynamics. Since we want to use Izhikevich model, and not some modified (and questionable) model, we look for other possible solutions in the next section.

A.2 Simulations of network dynamics

We consider a network completely equivalent to the one we study in our model: N neurons connected at random with probability c/N. There are two populations of neurons,

$N^{(e)}$ excitatory neurons, and $N^{(i)}$ inhibitory neurons ($N^{(a)} = g_a N$, and $g_e + g_i = 1$). The connections are weighted: J_e (J_i) are the weights for incoming links from excitatory (inhibitory) neurons. We also consider the same parameters as for our model: $N = 10^4$, $c = 1000$, $g_e = 0.75$, $J_e = 1$, and $J_i = -3$. The difference is that at each node of the network we substitute our neurons by Izhikevich neurons. Each neuron has its own membrane potential variable v_j and recovery variable u_j ($j = 1, \ldots, N$). The interaction between neurons is only due to spikes, and it is introduced in the current I_j,

$$I_j(t + dt) = \sum_{i=1}^{N} a_{ij} J_{ij} f_i(t) + \xi(t), \tag{A.5}$$

where a_{ij} is the adjacency matrix; J_{ij} is the synaptic efficacy (it is J_e if neuron i is excitatory, and J_i if neuron i is inhibitory); $f_i(t)$ is a variable that indicates if neuron i fired a spike in the previous time step ($f_i(t) = 1$) or did not fire ($f_i(t) = 0$); and $\xi(t)$ is the noise. Izhikevich used a similar method in [115]. In this case, we define the activity $\rho_a(t)$ of population a as

$$\rho_a(t) = \frac{\sum_{j=1}^{N^{(a)}} f_j^{(a)}(t)}{N^{(a)}}, \tag{A.6}$$

i.e., the fraction of neurons in population a that fired at time t. It goes without saying that no analytic treatment is known for this network, consequently we present here only simulation results.

Recall that we are interested in finding paroxysmal-like spikes in this model. Thus, according to our model, it is necessary that excitatory neurons respond faster than inhibitory neurons (at $\alpha = 1$, for instance, instead of nonlinear excitations in region $n_{c1} < \langle n \rangle < n_{c2}$, we have irregular bursts of neuronal activity). As mentioned above, there is no clear way how to define α within Izhikevich model. Therefore, we present some possibilities that we have tried.

The simplest choice is to define α in the following way:

$$\alpha_1 = \frac{a^{(i)}}{a^{(e)}}, \tag{A.7}$$

where $a^{(i)}$ and $a^{(e)}$ are the parameters a in Eq. (A.2) of the recovery variable for inhibitory and excitatory neurons, respectively. If $\alpha_1 < 1$, it means that $a^{(i)} < a^{(e)}$, and the variable u of excitatory neurons recovers faster than the one of inhibitory neurons (note that we are considering all other parameters the same for both excitatory and inhibitory neurons). Unfortunately, it also means that excitatory neurons have larger firing rates than inhibitory neurons (when stimulated with the same input). In Fig. A.4(a), we present the network activity at $\alpha_1 = 0.5$ and $\langle n \rangle = 35$ (that corresponds to $I_n \approx 5.8$, taking into account Eq. (A.3)). The Izhikevich network displays network oscillations (like in our model at these parameters, see the phase diagram, Fig. 4.2). Figures A.4(b) and A.4(c) show the mean membrane potential (v_{net}) and the mean value of the recovery variable (u_{net}) for excitatory and inhibitory neurons (note that v_{net} reaches quite high values, because in the

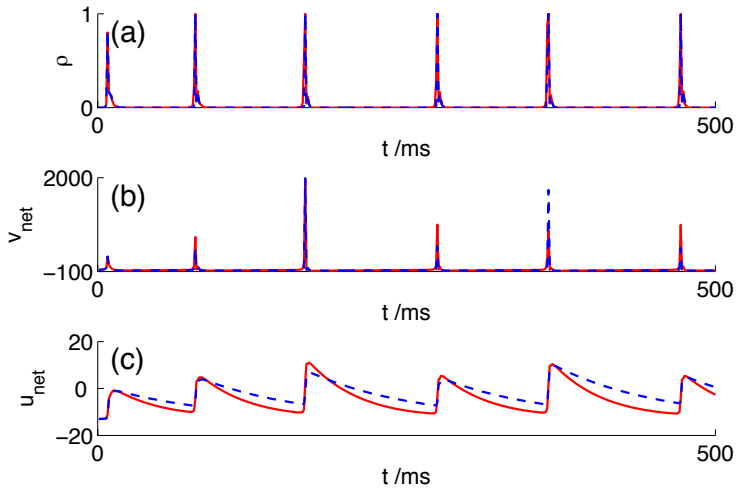

Figure A.4: Activity ρ in a network composed of Izhikevich neurons (panel (a)), and corresponding mean membrane potential v_{net} (panel (b)) and mean recovery variable u_{net} (panel (c)). The red lines correspond to variables of the excitatory population, and blue dashed lines correspond to variables of the inhibitory population. Parameters of single neurons: $(b, c, d) = (0.2, -65, 8)$, $a^{(e)} = 0.02$ and $\alpha_1 = 0.5$. Time step $dt = 0.5$. Noise parameters: $\langle n \rangle = 35$, $X = 5$, $V_{th} = 30$, and $\sigma^2 = 10$ (Eqs. (A.3) and (A.4)). Network parameters: $N = 10^4$, $c = 1000$, $g_e = 0.75$, $J_e = 1$, and $J_i = -3$.

---

program the membrane potential v was only compared with the condition $v \leq 30$ at each two time steps, like in [115]). This delta-like activity means that the activity of all neurons is very strongly correlated, and consequently v_{net} and u_{net} are similar to the membrane potential v and recovery variable u of a single neuron (compare with Fig. A.1). The activity ρ is very similar to the mean membrane potential, because the membrane potential is either fluctuating around the rest state (that corresponds to silent activity), or it quickly rises as an action potential (see Fig. A.1). The oscillations of the mean recovery variable are more similar to our oscillations. Nevertheless, there is a crucial difference between the two models: in our model, if the excitatory activity is large ($\rho_e \approx 1$), but the inhibitory activity is sufficiently small, then most excitatory neurons remain active (because in average their input is larger than the threshold); whereas in Izhikevich network, if a large fraction of neurons fires at a certain time, then in the next time step they are reset, and immediately the input becomes insufficient to maintain high activity (and high firing rates).

Figure A.5 displays network activity at the same parameters as in Fig. A.4, except the noise intensity $\langle n \rangle$. At $\langle n \rangle < 19$, the network is silent, while above it presents network oscillations, whose frequency increases with increasing noise (it is interesting that the value is close to the n_{c2} of our neuronal network, although it is not surprisingly, taking into account Eq. (A.3), where X could be chosen in order to achieve such similarity). The dependence of the frequency on the noise intensity is a direct consequence of the fact

that the firing rate of single neurons increase with the current (see Fig. A.3). Thus, the oscillations emerge with increasing frequency and large amplitude, like in our model. At large $\langle n \rangle$, the activity becomes more irregular, but the activity remains highly correlated (see Fig. A.5(e)).

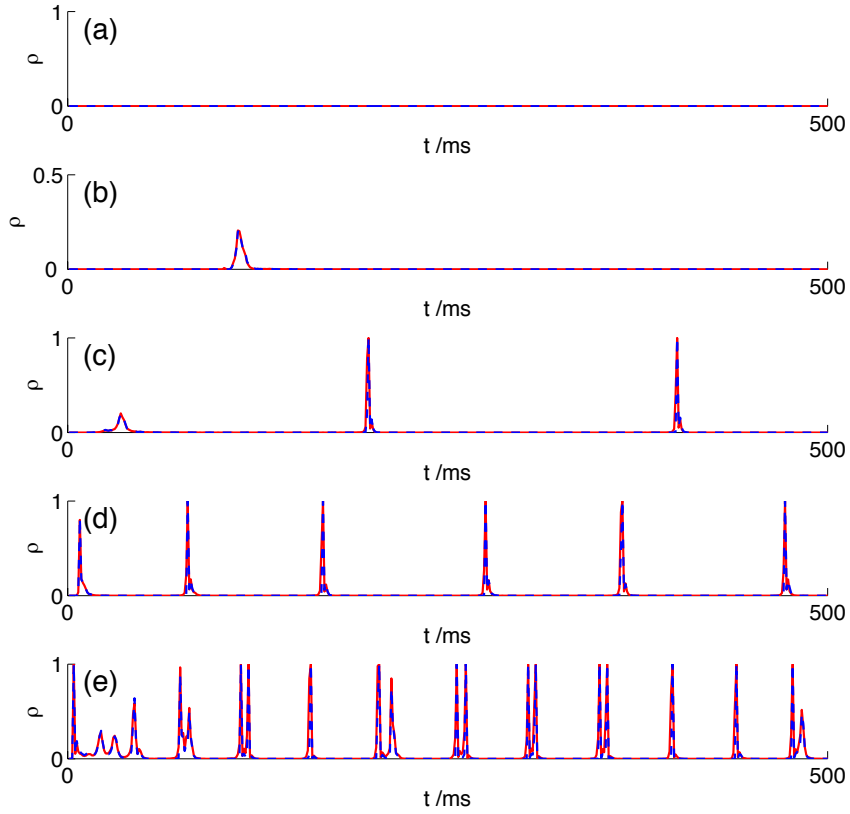

Figure A.5: Network activity at different levels of noise. Panels (a) and (b) at $\langle n \rangle = 15$, and panels (c), (d) and (e) at $\langle n \rangle = \{20, 35, 150\}$, respectively. In panel (b), 10% of excitatory neurons received a delta-like pulse of amplitude $I_p = 20$. As a consequence, about 20% of the neurons in the network became active. Red lines correspond to excitatory activity, and blue dashed lines correspond to inhibitory activity. Other parameters are the same as in Fig. A.4.

In the inactive state, we delivered a stimulation to 10% of excitatory neurons as a delta-like pulse (duration equal to one time step, and an amplitude sufficient to active these neurons). As a response, about 20% of the neurons in the network became active (see Fig. A.5(b)). It is different from our paroxysmal-like spikes, because at least the amplitude of this response should be similar to the amplitude of network oscillations at $\langle n \rangle = 20$, and it is not. Also, other stimulations elicited different responses, meaning that

the response's shape is not deterministic, and, unlike our network model, the trajectory should not be equivalent to a heteroclinic orbit around an unstable point.

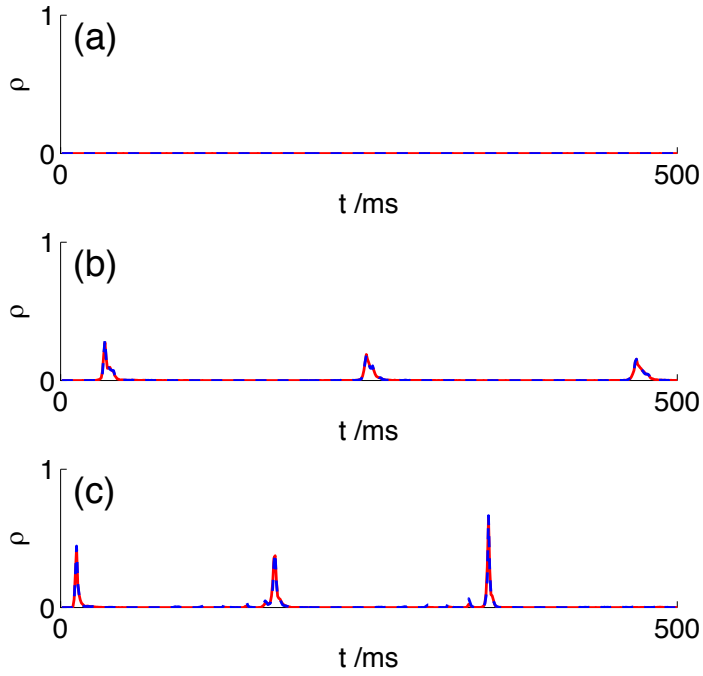

Figure A.6: Network activity at $\alpha_1 = 1.5$, i.e., $a^{(i)} = 1.5a^{(e)}$. The noise intensity $\langle n \rangle$ is 18 in panel (a), 19 in panel (b), and 25 in panel (c). Red lines correspond to excitatory activities, and blue dashed lines correspond to inhibitory activities. Other parameters are the same as in Fig. A.4.

Figure A.6 displays network activity at $\alpha_1 = 1.5$. It means that in this case the recovery variable u of inhibitory neurons is faster than the one of excitatory neurons. In this case, the transition from the inactive state to oscillations occurs at more less the same noise intensity as in the case with $\alpha_1 = 0.5$, and additionally we found a similar result at different values of α_1, in the range $[0, 1.2]$. It means that there is one vertical line in the phase diagram, similar to n_{c2} in our model. Note also that the amplitude of the oscillations is smaller than before, at $\alpha_1 = 0.5$. Indeed, we found that at $\alpha_1 > 1$, the amplitude of the oscillations appears always smaller than at $\alpha_1 < 1$. It is a consequence of a quicker recover of the inhibitory neurons, that allows them to fire first, preventing excitatory neurons to fire, which in turn blocks further activation of the network of both excitatory and inhibitory neurons.

A.3 Neuronal variability and stochasticity

The most clear difference between the network activity just presented using Izhikevich neurons and the activity in our model is the shape of the oscillations. Obviously, delta-like oscillations can not be found in real neuronal networks. Thus, we now consider different approaches to prevent neurons to become so strongly synchronized.

First, we present the case studied by Izhikevich in [115]. The author introduced heterogeneity in the network by assigning different parameters to each neuron, in order to have different neurons with different dynamics. In his network, excitatory neurons have the parameters $(a_j^{(e)}, b_j^{(e)}) = (0.02, 0.2)$ and $(c_j^{(e)}, d_j^{(e)}) = (-65, 8) + (15, -6)r_j^2$, where r_j is a random variable uniformly distributed in the interval $[0, 1]$, and j is the neuron index. The case $r_j = 0$ corresponds to regular spiking neurons (as we used above), whereas $r = 1$ corresponds to chattering cells [115]. The square is meant to bias the distribution towards the RS cells. Inhibitory neurons have the parameters $(a_j^{(i)}, b_j^{(i)}) = (0.02, 0.25) + (0.08, -0.05)r_j$ and $(c_j^{(i)}, d_j^{(i)}) = (-65, 2)$. In this case, $r_j = 0$ corresponds to low-threshold spiking neurons, and $r_j = 1$ corresponds to fast spiking cells [115]. Figure A.7 displays network activity at noise intensity $\langle n \rangle = 25$ (panel (a)), and at $\langle n \rangle = 45$ (panel (b)). Excitatory neurons have smaller activity than inhibitory neurons, because inhibitory neurons have larger firing rates. Inhibitory neurons seem to oscillate mainly independently of excitatory neurons, which means that these oscillations are noise driven, except when excitatory activity is larger enough to influence their dynamics. In this case, after a combined activation of excitatory and inhibitory neurons, there is a transient time of smaller activity, which is a consequence of a relatively large fraction of inhibitory neurons being activate in the previous time steps. Larger noise results in larger activities, larger firing rates, and also in larger variability.

Second, we introduce a different kind of variability. Izhikevich neurons are deterministic, whereas our neurons are stochastic switches. Therefore, we insert stochasticity in the recovery variable u of the Izhikevich neurons,

$$\dot{u} = a(bv - u) + \zeta(t), \tag{A.8}$$

where $\zeta(t)$ is a random variable that follows a Gaussian distribution (whose mean is zero). Schneidman *et al.* [104] studied channel stochasticity in the Hodgkin-Huxley model, and they distinguished three experimentally observed phenomena in their model: a neuron can fire spontaneously when the input current is subthreshold, and it may "miss" spikes when the current is suprathreshold. Additionally, the neuron presents subthreshold oscillations in the membrane potential as a response to a subthreshold dc current. Similarly, the introduction of $\zeta(t)$ in the recovery variable u of the Izhikevich neuron can lead to these phenomena. Naturally, it is necessary to tune appropriately the standard deviation of $\zeta(t)$. Using the parameters for a regular spiking cell, we found that with the standard deviation $\sigma_\zeta = 0.5$, the dynamics of a single neuron is not affected by $\zeta(t)$, whereas with $\sigma_\zeta = 1$, all features referred above are present. If σ_ζ is too large ($\sigma_\zeta > 2$), the noise is too strong, and the response of the neuron is uncorrelated with the input current. Thus,

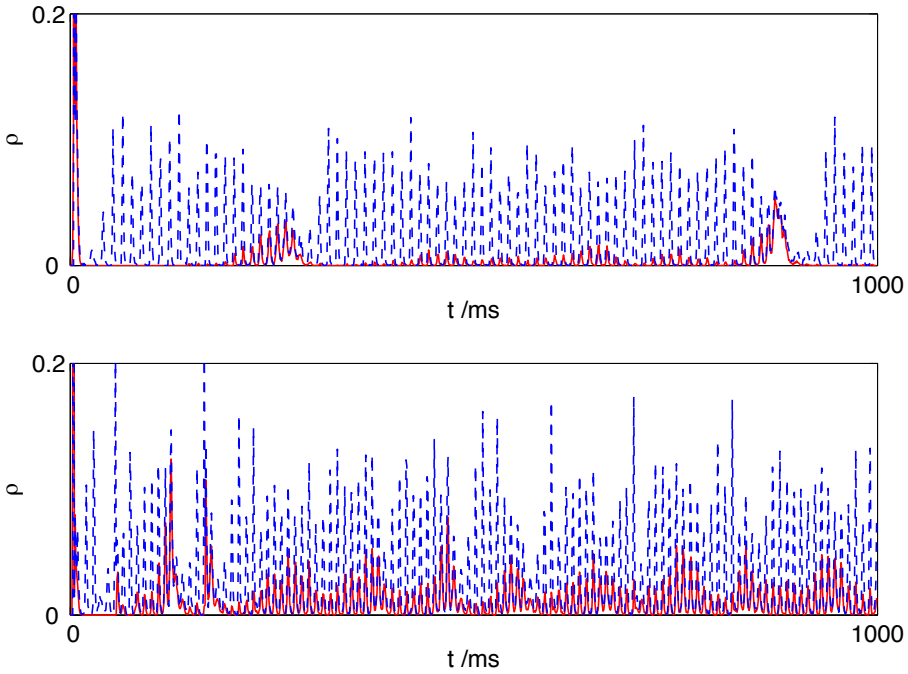

Figure A.7: Network activity in a heterogeneous neuronal network. (a) Activity at the noise intensity $\langle n \rangle = 25$. (b) Activity at the noise intensity $\langle n \rangle = 45$. Red lines correspond to excitatory activity, and blue dashed lines correspond to inhibitory activity. Parameters of excitatory neurons: $(a_j^{(e)}, b_j^{(e)}) = (0.02, 0.2)$ and $(c_j^{(e)}, d_j^{(e)}) = (-65, 8)+(15, -6)r_j^2$. Parameters of inhibitory neurons: $(a_j^{(i)}, b_j^{(i)}) = (0.02, 0.25) + (0.08, -0.05)r_j$ and $(c_j^{(i)}, d_j^{(i)}) = (-65, 2)$. r_j is a random variable uniformly distributed in the interval $[0, 1]$. Other parameters are the same as in Fig. A.4.

---

we simulated a neuronal network similar to the one in Fig. A.4 ($\alpha_1 = 0.5$), but now with the noise $\zeta(t)$. If the standard deviation is small enough, ($\sigma_\zeta \approx 0.5$), the neuronal activity remains unchanged. However, larger standard deviations ($\sigma_\zeta \approx 1$) destroy completely the oscillations. Figure A.8 displays the mean firing rate of the neuronal populations at $\sigma_\zeta = 1$. This mean firing rate is the average activity during a time window T,

$$\nu_a(t) = \frac{1}{Tdt} \sum_{k=t-T}^{t} \rho_a(k), \tag{A.9}$$

where dt is the time step. In this case, we used $dt = 0.1$ ms and $T = 10$. Obviously, the larger the value T, the smoother will the activity look like. As one can see, after a transient period, the neurons are no longer able to fire synchronously. We tried to find an intermediate value σ_ζ at which the neurons present oscillations, though not delta-like oscillations like in Fig. A.4, but we failed. Decreasing σ_ζ from 1 (the case presented in

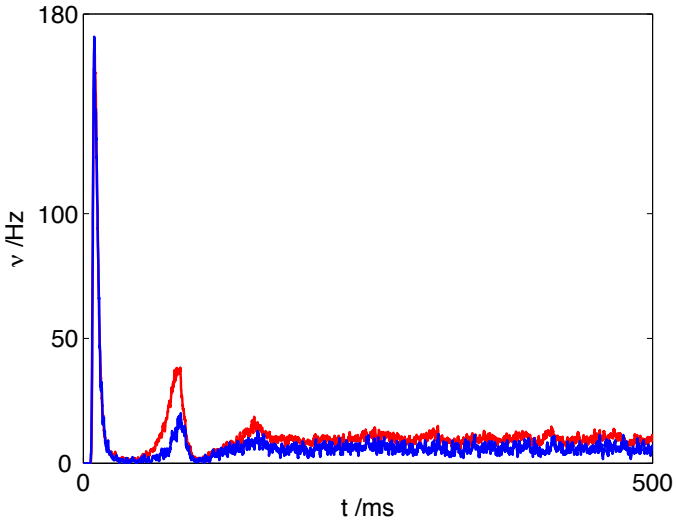

Figure A.8: Mean firing rate ν, Eq. (A.9), of excitatory (red line) and inhibitory neurons (blue line) as function of time. The recovery variable u of each neuron is affected by the noise term $\zeta(t)$, Eq. (A.8), which is a Gaussian process characterized by $(\mu, \sigma) = (0, 1)$. The noise intensity is $\langle n \rangle = 25$. Time step $dt = 0.1$. Other parameters are the same as in Fig. A.4.

---

the Fig. A.8) appears to lead to an increase of the transient period, until the delta-like oscillations are recovered.

Third, we introduce an alternative definition of α based on synaptic delays:

$$\alpha_2 = \frac{D^{(e)}}{D^{(i)}}, \tag{A.10}$$

where $D^{(e)}$ and $D^{(i)}$ are the synaptic delays of excitatory and inhibitory neurons, respectively. These delays are incorporated in the input current I of the neurons. It means that neurons of population a receive at time t the current $I(t - D^{(a)})$. It is a realistic assumption, because action potentials travel at a finite velocity in the axons (see Chapter 2). For simplicity, we assume that excitatory and inhibitory neurons are both regular spiking neurons. Figure A.9 displays the network activities and the mean firing rates of both neuronal populations when $D^{(e)} = 1$ ms, and $\alpha_2 = 1/4$ (which are reasonable parameters according to [131] and [159]). Excitatory and inhibitory activities oscillate together apart from the time shift, combining in synchronized activity about 5% of the neurons in the network. Interestingly, the amplitude of the oscillations seems to be modulated by a signal with twice the period of the oscillations. At larger delays and at smaller α_2, the oscillations amplitude increase, though the parameters are no longer biologically plausible.

We have tried other possibilities, but the results were similar to the ones presented here. For instance, defining α as the ratio b^i/b^e results in similar dynamics as the one presented above for α_1. We also substituted RS cells that present Class 1 excitability, by

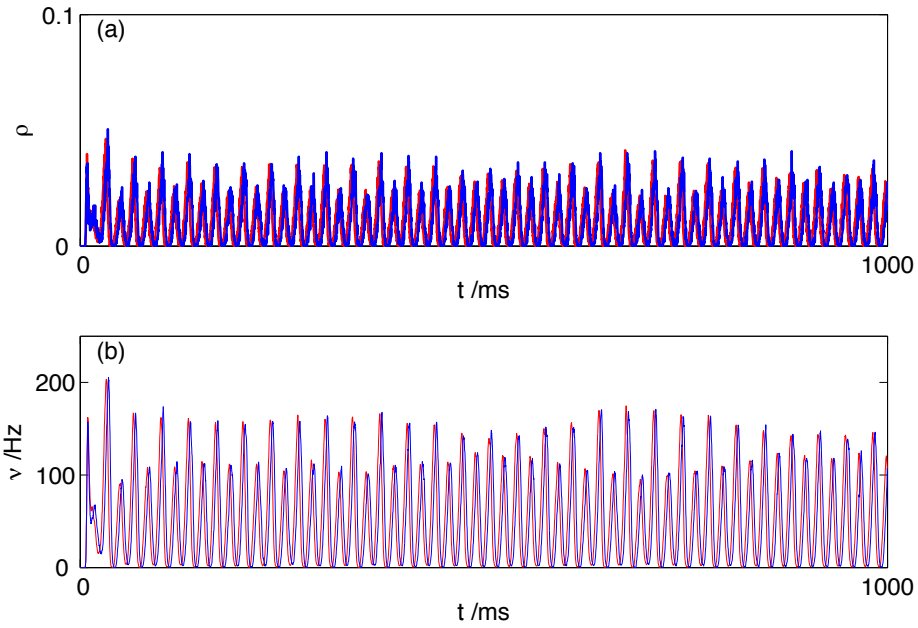

Figure A.9: Network activities and mean firing rate in a network with synaptic delays. Activities and mean firing rates of excitatory (red lines) and inhibitory neurons (blue lines) are represented in panels (a) and (b) respectively. The synaptic delays are $D^{(e)} = 1$ ms, and $D^{(i)} = 4$ ms, i.e., $\alpha_2 = 1/4$. Time step $dt = 0.1$. Other parameters are the same as in Fig. A.4.

Class 2 excitable neurons, because they seem more similar to our neurons (see Fig. 3.1). Finally, we introduced variability on the condition $v = 30$ mV (apex of a spike), but it had apparently no effect on the neuronal network dynamics.

In this appendix we studied the dynamics of random networks composed of Izhikevich neurons. First, we analyzed single neuron dynamics in order to understand how one could define interaction between neurons, and introduce neuronal noise. Then, since our goal was to compare this model with the one we studied in Chapters 4, 5 and 7, we identified an important difference between the two models: there is no clear way to introduce the parameter α (the ratio of excitatory and inhibitory response times) in the network composed of Izhikevich neurons. Consequently, we presented representative patterns of neuronal activity using different methods of introducing alternatives to the parameter α. Interestingly, it appears to exist a critical noise intensity above which neuronal oscillations emerge (similar to n_{c2} in the model with stochastic neurons, Chapter 5). We were interested about the possibility of finding paroxysmal-like spikes in this model, similar to those analyzed in Chapter 7. Unfortunately, we could not find those nonlinear objects. Indeed, even network oscillations are too different between the two models. Here, we found delta-like oscillations, which are unlikely to be found in real neuronal networks. We suggest that the differences between the two models are attributable to fundamental differences between the dynamics

of single neurons in these models. Moreover, the network composed of Izhikevich neurons manifested a lack of variability, resulting in those delta-like oscillations. Our attempts to introduce variability proved to be either insufficient to counter the strong correlations between neurons, or too strong, destroying completely the collective patterns of neuronal activity. Further investigations are necessary to find an appropriate way of introducing a parameter that plays the role of α, and also a suitable variability for this model.

Appendix B

Metastable states near a subcritical Hopf bifurcation in a toy model

Lopes da Silva *et al.* proposed that absence epilepsy may be characterized by a paroxysmal attractor very close to the normal state, such that transitions can be induced by random fluctuations of some variables [92]. In this case, it would be impossible to predict the onset of a seizure, as it is believed to be the case in absence epilepsy [92, 117]. Here, we study a possible alternative, based on the type of bifurcation, rather than on the distance between the different attractors. We propose that the transition to the ictal state may be due to a subcritical Hopf bifurcation, which unlike the supercritical case, it is a transition "much more dramatic, and potentially dangerous" to the system [116], because the bifurcation forces the trajectories to jump to a distant attractor. This bifurcation presents hysteresis, and no scaling law governs the amplitude or period of the limit cycle near the bifurcation point [116]. In this appendix we study a toy model that presents a subcritical Hopf bifurcation, in order to test the idea that it may be an alternative to the suggestion of Lopes da Silva *et al.* to model absence epilepsy.

The toy model under consideration is an oscillator [116]:

$$\dot{r} = \mu r + a_1 r^3 + a_2 r^5, \tag{B.1}$$

and

$$\dot{\theta} = \omega + b r^2, \tag{B.2}$$

where r is the amplitude, θ is the angular position, μ is a parameter that controls the stability of the fixed point at the origin ($r = 0$), ω is a parameter that defines the frequency of infinitesimal oscillations (when $r \to 0$), and b determines the dependence of the frequency on the amplitude for large amplitude oscillations. We use the parameters a_1 and a_2 to control the type of Hopf bifurcation that can occur in the system. Below, we compare the supercritical case ($a_1 = -1$ and $a_2 = 0$) with the subcritical case ($a_1 = 1$ and $a_2 = -1$).

First, we find the Jacobian, which is the same in both cases. In order to simplify, we

analyse the system in Cartesian coordinates,

$$\begin{aligned} x =& r\cos\theta, \\ y =& r\sin\theta. \end{aligned} \tag{B.3}$$

Their derivatives are

$$\begin{aligned} \dot{x} =& \dot{r}\cos\theta - \dot{\theta}r\sin\theta, \\ \dot{y} =& \dot{r}\sin\theta + \dot{\theta}r\cos\theta, \end{aligned} \tag{B.4}$$

and using Eqs. (B.1) and (B.2), we obtain

$$\begin{aligned} \dot{x} =& \mu x - \omega y + \text{higher order terms}, \\ \dot{y} =& \mu y + \omega x + \text{higher order terms}, \end{aligned} \tag{B.5}$$

Thus, the linearized system is

$$\dot{\vec{v}} = \hat{J}\vec{v}, \tag{B.6}$$

where

$$\vec{v} = \begin{pmatrix} x \\ y \end{pmatrix} \tag{B.7}$$

and $\hat{J}$ is the Jacobian matrix,

$$\hat{J} = \begin{pmatrix} \mu & -\omega \\ \omega & \mu \end{pmatrix}. \tag{B.8}$$

Taking into account Eq. (4.19), the eigenvalues are

$$\lambda_{\pm} = \mu \pm \omega i \tag{B.9}$$

The Hopf bifurcation occurs at $\mu = 0$, when the real part of the eigenvalues changes sign.

In the case of the supercritical Hopf bifurcation (i.e., $a_1 = -1$ and $a_2 = 0$ in Eq. (B.1)),

$$\dot{r} = 0 \Leftrightarrow r(\mu - r^2) = 0 \Leftrightarrow r = 0 \vee r = \sqrt{\mu}, \tag{B.10}$$

at $\mu < 0$, the origin is a stable spiral, and the oscillator presents damped oscillations (see Fig. B.1(a)). At $\mu > 0$, the origin is an unstable spiral, and the system has a limit cycle (see Fig. B.1(b)), whose amplitude is $r = \sqrt{\mu}$, and the frequency is

$$\dot{\theta} = \omega + b\mu. \tag{B.11}$$

In the case of the subcritical Hopf bifurcation, the positive term r^3 is destabilizing and drives trajectories away from the origin, even at $\mu < 0$:

$$\dot{r} = 0 \Leftrightarrow r(\mu + r^2 - r^4) = 0 \Leftrightarrow r = 0 \vee r_{\pm} = \sqrt{\frac{1}{2}\left(1 \pm \sqrt{1 + 4\mu}\right)}. \tag{B.12}$$

At $\mu < -1/4$, there is only one solution, the fixed point at the origin, which is a stable spiral, like in the supercritical case. However, when $-1/4 < \mu < 0$, there are two limit cycles, besides the stable spiral at the origin. We analysed the stability of each one (by studying trajectories in the phase plane), and we concluded that the exterior limit cycle (r_+) is stable, and the interior limit cycle (r_-) is unstable. It means that oscillations that go inside of the unstable limit cycle ($r < r_-$) relax to the origin ($r = 0$), while oscillations that go outside of the unstable limit cycle ($r > r_-$) are attracted by the exterior stable limit cycle (r_+). Figure B.1(c) shows two trajectories, one that starts outside of the unstable limit cycle (solid line) and stays in the stable limit cycle, and another that starts inside of the unstable limit cycle (dashed line) and because of it relaxes in the form of damped oscillations to the origin. At $\mu = -1/4$, the limit cycles collide and annihilate each other, whereas at $\mu = 0$ the unstable limit cycle engulfs the origin. It means that when increasing μ in the interval $-1/4 < \mu < 0$, the unstable limit cycle shrinks, and so does the stable region that attracts trajectories towards the origin. At $\mu > 0$, the origin is unstable, and therefore there is only one stable limit cycle, r_+ (see Fig. B.1(d)).

Figure B.2 displays the dependence of the amplitude r_∞ and the frequency ω_∞ of the stable limit cycle on μ for both Hopf bifurcations. Note that the frequency of the limit cycle is given by Eq. (B.2),

$$\omega_\infty = \omega + b r_\infty^2, \tag{B.13}$$

i.e., it is defined by the amplitude of the limit cycle (at fixed parameters ω and b). In the supercritical Hopf bifurcation, the amplitude of the limit cycle obeys the scaling law, Eq. (B.10). Thus, the size of the limit cycle grows continuously from zero and proportional to $\sqrt{\mu - \mu_c}$, as expected for a supercritical Hopf bifurcation [116]. In the subcritical Hopf bifurcation, the limit cycle emerges at $\mu = -1/4$ with nonzero amplitude. Moreover, in this case there is hysteresis, because when increasing μ from, say -1, and by keeping the oscillator at the origin, it only jumps to the stable limit cycle at $\mu = 0$, when the origin loses its stability (see the dashed line in Fig. B.2(c)). Then, by decreasing μ, the oscillator stays in the stable limit cycle until it disappears at $\mu = -1/4$ (see the solid line in Fig. B.2(c)).

If we assume that Eqs. (B.1) and (B.2) represent the dynamics of a many-body system, then the bifurcation is the mechanism of a phase transition. In the case of the subcritical Hopf bifurcation, since it presents jump phenomena and hysteresis, we expect that it describes a first-order phase transition [181]. In a real system there is always noise, so we introduce it in the model:

$$\dot{r} = \mu r + r^3 - r^5 + \xi(t), \tag{B.14}$$

where $\xi(t)$ is a Gaussian variable (mean value $\langle \xi \rangle = 0$).

In order to look for an early warning of the transition from the origin to the stable limit cycle, we analyse the time D the system spends in this limit cycle near $\mu = -1/4$. In this case, the unstable limit cycle is very close to the stable limit cycle. The distance Δ between the limit cycles is

$$\Delta = r_+ - r_- = \sqrt{\frac{1}{2}\left(1 + \sqrt{1 + 4\mu}\right)} - \sqrt{\frac{1}{2}\left(1 - \sqrt{1 + 4\mu}\right)} \approx \sqrt{\frac{1 + 4\mu}{2}}. \tag{B.15}$$

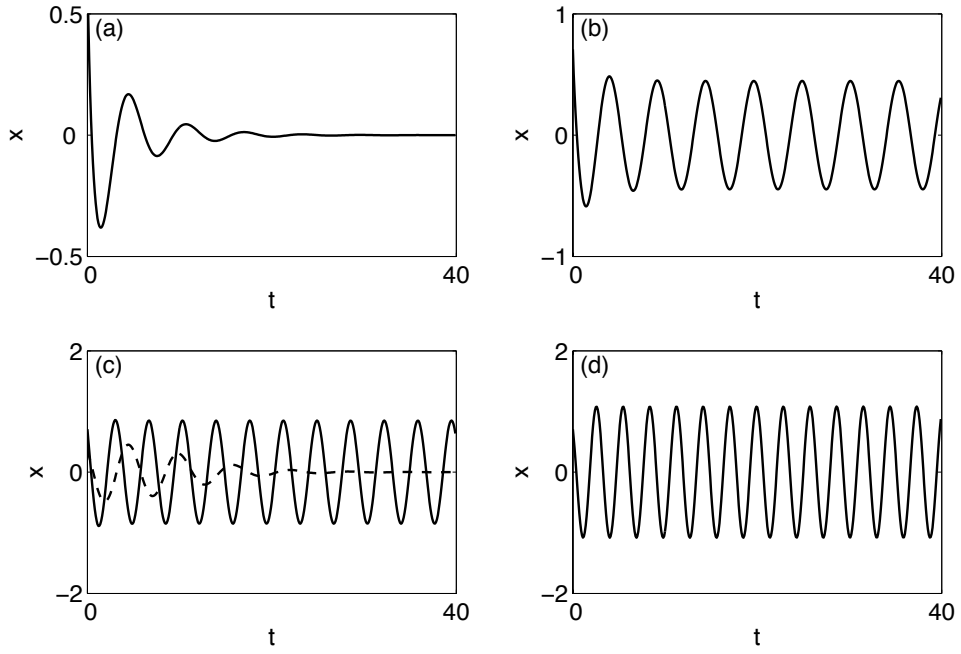

Figure B.1: Oscillations below and above the supercritical and subcritical Hopf bifurcations. Panels (a) and (b) refer to the supercritical case ($a_1 = -1$ and $a_2 = 0$ in Eq. (B.1)), and panels (c) and (d) to the subcritical case ($a_1 = 1$ and $a_2 = -1$ in Eq. (B.1)). At $\mu = -0.2$, below the supercritical Hopf bifurcation (panel (a)), the system relaxes in the form of decaying oscillations to the origin. At $\mu = 0.2$, above the supercritical Hopf bifurcation (panel (b)), the oscillator has a limit cycle. At $\mu = -0.2$, below the subcritical Hopf bifurcation (panel (c)), depending on the initial condition, the oscillator either stays in a limit cycle (solid line), or it presents damped oscillations towards the origin. At $\mu = 0.2$, above the subcritical Hopf bifurcation (panel (d)), the oscillator has a limit cycle. The presented numerical result was obtained by solving Eqs. (B.1), (B.2), and (B.3) using Euler's Method. The initial conditions were in all cases $(r(t=0), \theta(t=0)) = (1, \pi/4)$, except for the dashed line in panel (c), $(r(t=0), \theta(t=0)) = (1/2, \pi/4)$. Parameters: $\omega = 1$, $b = 1$, and time step $dt = 0.1$.

It is much easier to jump from the stable limit cycle to the origin, than the opposite, because $\Delta \ll r_-$ near $\mu = -1/4$. Therefore, when the variance of ξ is small, the system spends much more time at the origin, than at the stable limit cycle (if the variance is large, the system is constantly jumping from one state to the other, and it is completely governed by the noise). Indeed, studying how much time the system stays in the stable limit cycle when the variance of the noise is sufficiently small, makes the problem similar to considering the unstable limit cycle as an absorbing boundary, i.e., when $\xi(t) < -\Delta$ the oscillator is unavoidably "absorbed" into the origin (and stays there for a long time). In other words, it makes the distribution of D equivalent to the first passage time distribution

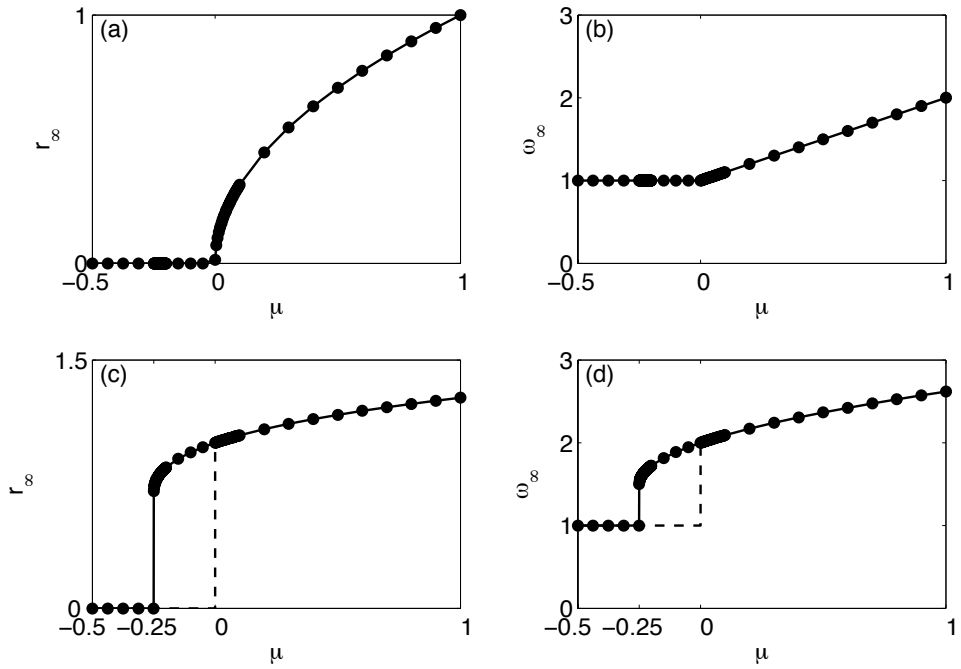

Figure B.2: Panels (a) and (b) show the dependence of the amplitude r_∞ and frequency ω_∞ on μ, respectively, for the supercritical Hopf bifurcation. Panels (c) and (d) present the same dependencies for the subcritical Hopf bifurcation. We solved numerically Eqs. (B.1) and (B.2), and at each μ we obtained the steady state, represented as a dot in the figures. The line in panel (a) corresponds to the analytic solution of Eq. (B.10); in panel (c) it corresponds to Eq. (B.12); and in panels (b) and (d) it is the solution of Eq. (B.13), using the respective r_∞. In panels (c) and (d), the dashed line represents the case when the initial condition is inside of the unstable limit cycle, and the trajectory relaxes to the origin; at $\mu = 0$ the origin becomes unstable, and the oscillator jumps to the stable limit cycle. Parameters: $\omega = 1$, $b = 1$, and time step $dt = 0.1$.

---

at the point $r - \Delta$. Figure B.3(a) shows the distribution of the time D that the system stays at the stable limit cycle before it falls to the origin. The distribution has exponential decay (see panel (b)) as expected for a Poisson-like process. As the system approaches the critical point $\mu_c = -1/4$, the distribution gets thinner, because Δ is smaller, and therefore it is easier (and quicker) to cross the unstable limit cycle. Interestingly, the peak point of the distribution does not seem to depend on the distance to the critical point, while the slope of the curves presented in panel (b) depends linearly on the distance $\mu - \mu_c$ (see panel (c)).

Near $\mu = 0$, the scenario is similar, the difference is that the stable limit cycle exchanges roles with the stable fixed point at the origin. Now, the distance Δ is

$$\Delta = r_- - 0 \approx \sqrt{-\mu}, \tag{B.16}$$

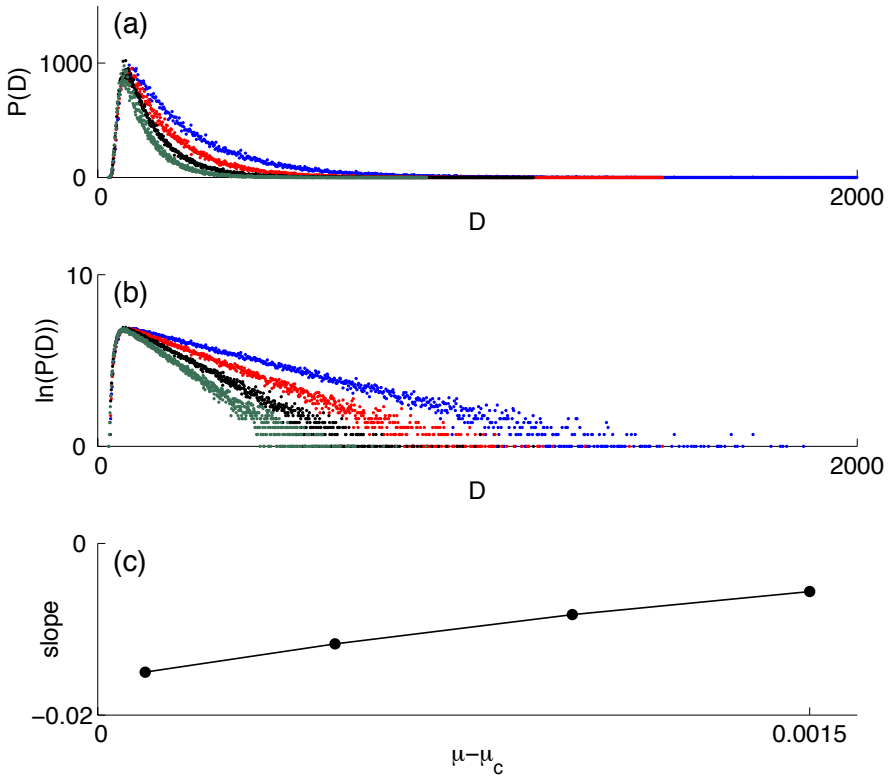

Figure B.3: (a) Distribution of time intervals $P(D)$ at the stable limit cycle near $\mu_c = -1/4$. (b) Logarithm of $P(D)$ versus D. In both panels (a) and (b), the blue, red, black and green dots correspond respectively to $\mu = \{-0.2485, -0.249, -0.2495, -0.2499\}$. (c) Slope of the curves presented in panel (b) as function of the distance to the critical point. The results were obtained by solving numerically Eq. (B.14). We use the variance of ξ equal to 9×10^{-4}. Parameters: $\omega = 1$, $b = 1$, and time step $dt = 0.1$.

(note that μ is negative, because when it becomes positive, the origin is unstable); and $P(D)$ is the distribution of time intervals at the origin.

Thus, the subcritical Hopf bifurcation seems to meet the conditions to model absence epilepsy, in alternative to the idea proposed by Lopes da Silva *et al.* [92]. Our simple analysis of the toy model indicates that the transitions from one attractor to the other occur at random, even near the critical point. It means that the transition can occur without giving any early warnings, like a first-order phase transition. Consequently, if absence seizures occur due to a subcritical Hopf bifurcation, then they are indeed unpredictable, like Lennox postulated [117].

Appendix C

Fully connected neuronal network

C.1 Introduction

In this appendix we study a model similar to the one presented in Chapter 3. The difference is that we now consider a complete graph, i.e., all neurons are connected to all other neurons. In this case, the interaction between neurons is much more effective than in a sparse random network, because all neurons influence all other neurons. The advantage of using such network is that it allows us to obtain analytic results, whereas its disadvantage is that it is not biologically plausible. This study aims a comparison between the two models, in order to understand how important is the role of network structure in the qualitative dynamical behavior of the neuronal network.

We start this appendix by presenting and analysing a model that we call "F-model". It corresponds to the model introduced in Ref. [101], that we mentioned in Section 3.7, Eq. (3.20), on a complete graph. Then, we introduce some modifications, in order to find neuronal oscillations. Finally, we show results for the "$\langle n \rangle$-model", i.e., a model equivalent to the one in Chapter 3, Eq. (3.15), on a fully connected network.

C.2 F-model

In Section 3.7, it was referred that the model discussed in Chapter 3, and subsequent chapters, published in [102], was derived from the original model published in [101]. The main difference between the two models is that in the original one the noise $\langle n \rangle$ is absent. Instead there is a parameter f_a that is the probability of an inactive neuron of population a being activated spontaneously. We recall the rate equations of the activities ρ_a, Eqs. (3.20):

$$\dot{\rho_a} = f_a - \nu_a \rho_a + \mu_a \Psi(\rho_e, \rho_i), \tag{C.1}$$

where, once again, $\nu_a \equiv f_a + \mu_a$ (here, we consider $\mu_{2a} = 0$, see Section 3.7). One can rewrite these equations as follows,

$$\frac{\dot{\rho_a}}{\nu_a} = F_a - \rho_a + (1 - F_a)\Psi(\rho_e, \rho_i), \tag{C.2}$$

where $F_a = f_a/\nu_a$, and it determines the relative strength of the stimulation [101]. These rate equations do not depend on the structure of the network, which is encoded in the function $\Psi(\rho_e, \rho_i)$ (the probability of a randomly chosen neuron to have an input larger than the threshold V_{th}). In other words, in order to solve these equations on a complete graph, all we have to do is to find the function $\Psi(\rho_e, \rho_i)$ that corresponds to this network structure. We remind that in the case of a random network,

$$\Psi(\rho_e, \rho_i) = \sum_{k,l=0}^{\infty} \Theta(J_e k + J_i l - V_{th}) P_k(g_e \rho_e \tilde{c}) P_l(g_i \rho_i \tilde{c}). \tag{C.3}$$

In the case of a fully connected network, the number of spikes coming from active excitatory neurons (k) and from active inhibitory neurons (l) are known:

$$\begin{aligned} k &= N g_e \rho_e, \\ l &= N g_i \rho_i. \end{aligned} \tag{C.4}$$

It corresponds to the total number of active neurons of the respective population. Note that we are considering that neurons send in average one spike per integration time, otherwise it would be necessary to multiply k and l by $\tau\nu$ (it would not change qualitatively the results, as explained in Chapter 3). Thus, we get

$$\Psi(\rho_e, \rho_i) = \Theta(J_e^* N g_e \rho_e + J_i^* N g_i \rho_i - N V_{th}^*), \tag{C.5}$$

where the input of all neurons is compared to the sum of all thresholds, NV_{th}^*. We redefine J_a^* in a mean-field fashion, since we want to study the thermodynamic limit $N \to \infty$,

$$J_a^* = \frac{J_a}{N}. \tag{C.6}$$

Similarly, the threshold $V_{th}^* = V_{th}/N$ (obviously, this is the same as to divide the argument of the theta function by N). (In this appendix, we use $V_{th} = 0.03$. Note that the argument of the theta function is no longer function of the number of spikes, but rather a function of the fractions ρ_e and ρ_i. It means that the previous $V_{th} = 30$ does not make sense here. Instead, and for the sake of comparison with results shown in Chapter 4, we assume $V_{th} = 30/c$, where c is the mean degree of the random network that we considered before, i.e., $c = 1000$, and so $V_{th} = 0.03$.) Thus, we get the rate equations for the complete graph:

$$\frac{\dot{\rho_a}}{\nu_a} = F_a - \rho_a + (1 - F_a)\Theta(J_e g_e \rho_e + J_i g_i \rho_i - V_{th}). \tag{C.7}$$

These rate equations can be solved analytically. Given a certain initial condition, we check the theta function. If $X \equiv J_e g_e \rho_e(0) + J_i g_i \rho_i(0) - V_{th}$ is smaller than zero, then $\Theta(X) = 0$, and we have to solve

$$\frac{\dot{\rho_a}}{\nu_a} = F_a - \rho_a, \tag{C.8}$$

otherwise, $\Theta(X) = 1$, and we have

$$\frac{\dot{\rho_a}}{\nu_a} = F_a - \rho_a + (1 - F_a) = 1 - \rho_a. \tag{C.9}$$

Thus, depending on $\Theta(X)$, the activities either relax to F_a, or to 1. It is what one could expect in a complete graph, since all neurons receive the same input. In the first case, a fraction $\rho_a = F_a$ will become active (by definition of F_a), whereas in the second case, all neurons will become active (after a transient period of exponential relaxation).

If we consider that the network is balanced, $J_e g_e = -J_i g_i = z$, then we have $X = \rho_e - \rho_i - V_{th}/z$. In this case, starting from an inactive network, $(\rho_e(0), \rho_i(0)) = (0, 0)$, the activities will increase exponentially towards F_a:

$$\begin{aligned} \rho_e(t) &= F_e(1 - e^{-t}), \\ \rho_i(t) &= F_i(1 - e^{-\alpha t}), \end{aligned} \tag{C.10}$$

where $\alpha = \nu_i/\nu_e$. If $\alpha = 1$ and $F_e = F_i = F$, the activities are equal, consequently $X = -V_{th}/z < 0$, and the activities relax to F. When $\alpha > 1$, i.e., when the inhibitory activity is faster than the excitatory activity, and therefore $\rho_i(t) \geq \rho_e(t)$, and $X < 0$. Thus, in this case, both activities also relax to F. At $\alpha < 1$, the excitatory activity grows quicker towards F ($\rho_e(t) > \rho_i(t)$, before reaching the steady state), and it is possible to meet the condition $X > 0$. The instant t^* at which the rate equations change is given by

$$\rho_e(t^*) - \rho_i(t^*) = \frac{V_{th}}{z} \Leftrightarrow -e^{-t^*} + e^{-\alpha t^*} = \frac{V_{th}}{Fz}. \tag{C.11}$$

Note that $\alpha < 1$ is a necessary condition, but not sufficient. Equation (C.11) gives the maximum α at which it is possible to find the regime $X > 0$. Subsequently, at $t > t^*$, solving Eqs. (C.9), the activities grow as

$$\begin{aligned} \rho_e(t) &= (\rho_e(t^*) + e^{t-t^*} - 1)e^{-(t-t^*)}, \\ \rho_i(t) &= (\rho_i(t^*) + e^{\alpha(t-t^*)} - 1)e^{-\alpha(t-t^*)}. \end{aligned} \tag{C.12}$$

The excitatory activity continues to increase quicker than the inhibitory activity, which means that the excitatory population will become completely active ($\rho_e = 1$). Then, the inhibitory activity will catch up, and before all inhibitory neurons become active ($\rho_i = 1$), the condition $X < 0$ will occur at time t^{**}, given by

$$(\rho_e(t^*) + e^{t^{**}-t^*} - 1)e^{-(t^{**}-t^*)} - (\rho_i(t^*) + e^{\alpha(t^{**}-t^*)} - 1)e^{-\alpha(t^{**}-t^*)} = \frac{V_{th}}{z}. \tag{C.13}$$

Consequently, at $t > t^{**}$ both activities relax to F,

$$\begin{aligned} \rho_e(t) &= (\rho_e(t^{**}) + F[e^{t-t^{**}} - 1])e^{-(t-t^{**})}, \\ \rho_i(t) &= (\rho_i(t^{**}) + F[e^{\alpha(t-t^{**})} - 1])e^{-\alpha(t-t^{**})}. \end{aligned} \tag{C.14}$$

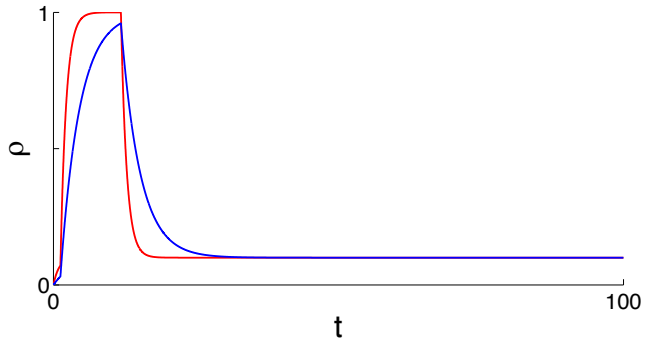

Figure C.1: Excitatory (red line) and inhibitory (blue line) activities in the F-model. The activities were obtained solving numerically Eqs. (C.7), using Euler's Method (the curves coincide with the analytical solution of Eqs. (C.10), (C.12), and (C.14)). Parameters: $F_e = F_i = F = 0.1$, $\alpha = 0.3$, $g_e = 0.75$, $\nu\tau = 1$, $V_{th} = 0.03$, $J_e = 1$, $J_i = -3$, and time step $dt = 0.01$. Time t is in units of μ_e^{-1}.

Although Eqs. (C.10) can be obtained from Eqs. (C.14) (substituting $\rho_a(t^{**}) = 0$ and $t^{**} = 0$), there is one important difference between the two scenarios. In this case, $\rho_a(t^{**}) > F$, and it means that the excitatory activity decreases faster towards F, than the inhibitory activity, implying that it is impossible to meet again the condition $X > 0$. The excitatory activity relaxes exponentially to F, followed by the inhibitory activity. This scenario is represented in Fig. C.1. Therefore, in this model, at these parameters ($F_e = F_i$ and $J_e g_e = -J_i g_i$), there are no oscillations. The activity either relaxes immediately to F, or there is a single large oscillation before it goes also to the steady state $\rho_a = F$.

However, if $F_e \neq F_i$, one can choose these parameters in order to have $X > 0$, i.e., $J_e g_e F_e + J_i g_i F_i - V_{th} > 0$. Now oscillations are unavoidable, because when the neuronal network tries to relax to $\rho_a = F_a$, it meets the condition $X > 0$, and then the activities increase and tend to $\rho_a = 1$, but in that case X becomes smaller than zero, and again the activities try to relax to F_a. This unavoidable loop is independent on α, though the amplitude and period of the oscillations does depend on α, because this parameter determines how quickly the activities meet the conditions $X > 0$ and $X < 0$. At intermediate values of $\alpha < 1$, one can find large amplitude oscillations, as displayed in Fig. C.2.

It is interesting to note that in this F-model, oscillations can only appear when $F_e \neq F_i$, in contrast to the model studied in Chapter 4, where the level of noise $\langle n \rangle$ was the same for both excitatory and inhibitory neurons. One can suppose that this difference is a consequence of the singular behavior of the theta function. Therefore, we study the case when the theta function $\Theta(X)$ is replaced by a function $A(X)$,

$$A(X) = \frac{1}{1 + e^{-\beta X}}, \tag{C.15}$$

where β controls the slope of the function at the origin. Thus, when $\beta \to \infty$, $A(X) \to$

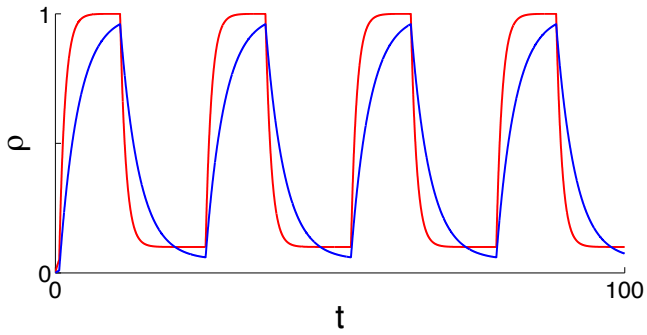

Figure C.2: Excitatory (red line) and inhibitory (blue line) activities in the F-model. The activities were obtained solving numerically Eqs. (C.7), using Euler's Method (the curves coincide with the analytical solution of Eqs. (C.10), (C.12), and (C.14), where F is substituted by F_a). The parameters are the same as in Fig. C.1, except $F_e = 0.1$ and $F_i = 0.05$. Time t is in units of μ_e^{-1}.

$\Theta(X)$. One can obtain the fixed points when $\dot{\rho_a} = 0$,

$$\rho_a = F_a + (1 - F_a)A(X). \tag{C.16}$$

Once again, the stability of the fixed point depends on the Jacobian $\hat{J}$. Using the same methods employed in Chapter 4, we find

$$\hat{J} = \begin{pmatrix} -1 + (1 - F_e)\dfrac{\partial A}{\partial \rho_e} & (1 - F_e)\dfrac{\partial A}{\partial \rho_i} \\ \\ \alpha(1 - F_i)\dfrac{\partial A}{\partial \rho_e} & -\alpha + \alpha(1 - F_i)\dfrac{\partial A}{\partial \rho_i} \end{pmatrix}, \tag{C.17}$$

whose eigenvalues of $\hat{J}$, $\lambda_\pm$, are given by Eq. (4.19). In order to obtain a phase diagram, we use $F_e = F_i = F$, and we must solve a set of two equations

$$\begin{aligned} \mathrm{Re}\{\lambda_\pm\} &= 0, \\ \mathrm{Im}\{\lambda_\pm\} &= 0. \end{aligned} \tag{C.18}$$

These equations determine the boundaries of the different dynamical regimes in the phase diagram. Figure C.3 shows F-α planes at different fractions of excitatory neurons g_e (we call this model β-model in the caption of the figure, to distinguish from the case with the theta function). Interestingly, we find regions of oscillations (colored regions in the figure). Recall that above, using the theta function, when $F_e = F_i$, it was impossible to find oscillations. Indeed, we find that as β increases, the region of oscillations decreases (it is not represented in Fig. C.3). It is a consequence of the fact that the Jacobian depends on the derivatives of the function under consideration. If it is the theta function, its derivative is the Dirac delta function, which implies that $\mathrm{Re}\{\lambda_\pm\} < 0$ independently

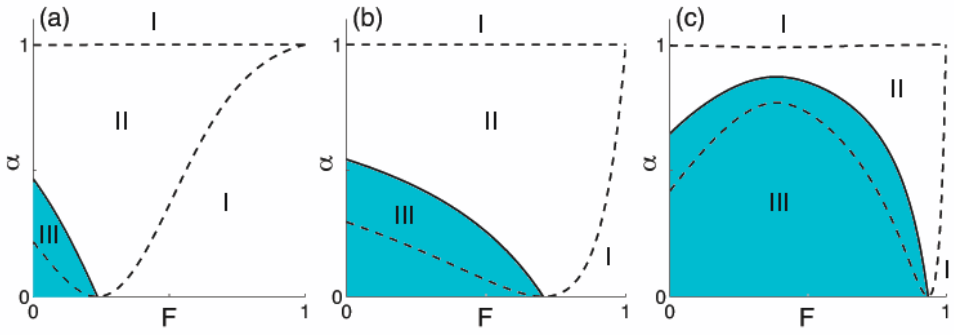

Figure C.3: F-α planes of the phase diagram at different fractions of excitatory neurons g_e of the β-model. Panels (a), (b), and (c) correspond to $g_e = \{0.74, 0.75, 0.76\}$, respectively. In regions I, the activity relaxes exponentially to the steady state, whereas in regions II, it relaxes in the form of damped oscillations. In regions III, there are network oscillations. The solid lines correspond to $\mathrm{Re}\{\lambda_\pm\} = 0$, and the dashed lines correspond to $\mathrm{Im}\{\lambda_\pm\} = 0$. The parameters are the same as in Fig. C.1. Additionally, $\beta = 100$.

on the parameters. One should also note that in this case the boundary to the oscillatory regime corresponds to a Hopf bifurcation, because the unique fixed point becomes unstable. Using the argument of symmetry breaking of time homogeneity as used in Chapter 8, we expect that this Hopf bifurcation corresponds to a second-order phase transition [181, 232].

Figure C.3 also shows that the larger g_e, the larger is the region of oscillations. This is the opposite of what we found when the network was random as discussed in Chapter 4. One other striking difference between the models is the absence of a saddle-node bifurcation in the case of the complete graph. Moreover, oscillations can emerge at $F \ll 1$ (provided that α is sufficiently small), whereas in the case of the shot noise model, oscillations could only appear at $\langle n \rangle > n_{c2}$ (we remind that the phase diagram in Fig. 4.2 is similar to the one found in the model with the stimulation F [101]). In contrast, and not surprisingly, both models demand $\alpha < 1$ in order to observe neuronal network oscillations.

C.3 $\langle n \rangle$-model

We now turn to the main model studied in this thesis (presented in Chapter 3), but when the network is a complete graph. In other words, instead of using F as input stimulation to the network as in the previous section, we use the shot noise $\langle n \rangle$. In this case, the rate equations are

$$\frac{\dot{\rho}_a}{\mu_a} = -\rho_a + \sum_{n=0}^{\infty} \Theta(J_e g_e \rho_e + J_i g_i \rho_i + \frac{n}{c} - V_{th}) G(n), \tag{C.19}$$

where $G(n)$ is the Gaussian distribution, Eq. (3.9). Note that we replace n by n/c, where c is the mean degree of the random network ($c = 1000$). Let us simplify the second term

on the right-hand side of Eq. (C.19),

$$\Psi(X^*) = \sum_{n=0}^{\infty} \Theta(X^*) G(n), \tag{C.20}$$

where $X^* = J_e g_e \rho_e + J_i g_i \rho_i + \frac{n}{c} - V_{th}$. Using Eq. (4.4) and the same method as in Eq. (4.5), we obtain

$$\Psi(X) = \frac{1}{2} + \frac{1}{\pi} \int_0^{\infty} \frac{\sin(Xy)}{y} e^{-y^2\sigma^2/(2c^2)} dy. \tag{C.21}$$

where $X = J_e g_e \rho_e + J_i g_i \rho_i + \frac{\langle n \rangle}{c} - V_{th}$. It is interesting to note that dividing n by c led to $\langle n \rangle / c$ and σ / c (it justifies the choice of the variance of the input current in Appendix A). One can rewrite Eq. (C.21) using the special function Gauss error function $\mathrm{erf}(x)$ [238]:

$$\Psi(X) = \frac{1}{2}(1 + \mathrm{erf}\Big[\frac{Xc}{\sqrt{2}\sigma}\Big]), \tag{C.22}$$

or the cumulative distribution function $\Phi(x)$ of the standard normal distribution [238]:

$$\Psi(X) = \Phi(Xc/\sigma). \tag{C.23}$$

This result is also easily derived from Eq. (C.19) by approximating the sum over n by an integral, and applying the condition within the theta function to the limits of the integral.

As in the previous section, the Jacobian is given by Eq. (C.17), where $F_a = 0$, and the function A is substituted by $\Phi(Xc/\sigma)$. Thus, by solving the derivatives, we obtain the Jacobian

$$\hat{J} = \begin{pmatrix} -1 + J_e g_e G(X) & J_i g_i G(X) \\ \alpha J_e g_e G(X) & -\alpha + \alpha J_i g_i G(X) \end{pmatrix}, \tag{C.24}$$

where $G(X)$ is the Gaussian distribution, whose mean value is zero, and standard deviation is σ/c,

$$G(X) = \frac{c}{\sqrt{2\pi\sigma^2}} e^{-\frac{(Xc)^2}{2\sigma^2}}. \tag{C.25}$$

The eigenvalues of the Jacobian are obtained using Eq. (4.19), and consequently the boundaries of the phase diagram that separate different dynamical regimes are given by Eqs. (C.18). Figure C.4 presents the fixed points as function of the intensity of noise $\langle n \rangle$ and $\langle n \rangle$-α planes of the phase diagram at different fractions of excitatory neurons g_e. First, one can note that increasing g_e makes the fixed point to grow quicker from low to high activity (see panels (a) and (c)), until a jump appears (panel (e)) and with it there is a region of small noise in which the neuronal network dynamics has three fixed points (the points of low and high activity are stable, and the intermediate one is saddle). In Fig. C.3, we do not show the steady states at each g_e since, in all cases, there is only a monotonically increasing single solution. Consistently with all models analysed, ρ grows quicker with F when g_e is larger, as one could expect, since larger fractions of excitatory neurons result in larger excitation and consequently larger neuronal activity. Additionally, we also found

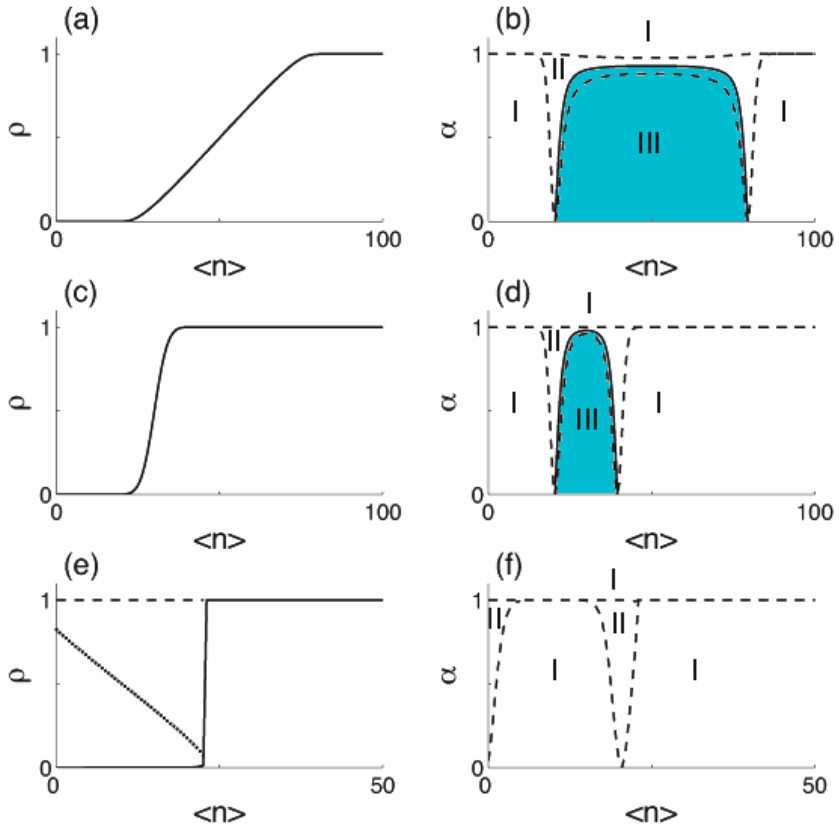

Figure C.4: Fixed points as function of the intensity of noise $\langle n \rangle$ (left column), and $\langle n \rangle$-α planes of the phase diagram (right column) of the $\langle n \rangle$-model at different fractions of excitatory neurons g_e. Panels (a)-(b), (c)-(d), and (e)-(f) correspond to $g_e = \{0.74, 0.75, 0.76\}$, respectively. In panel (e), at small $\langle n \rangle$, there are three fixed points. Besides the stable point of low activity (solid line), there is also a saddle point of intermediate activity (dotted line), and another stable point of high activity (dashed line). (Note that at large $\langle n \rangle$, the high activity fixed point is represented by a solid line, though it is the same point that is represented as a dashed line in the region at which there are three fixed points.) In the $\langle n \rangle$-α planes, in regions I, the activity relaxes exponentially to the steady state, whereas in regions II, it relaxes in the form of damped oscillations. In regions III, there are neuronal oscillations. Panel (f) has two regions II in the region where there are three fixed points: the region II on the left, at small $\langle n \rangle$, corresponds to the high activity state, whereas the region II on the right, at intermediate $\langle n \rangle$, corresponds to the low activity state. In these regions, the other stable point is in region I. In the right column, the solid lines correspond to $\mathrm{Re}\{\lambda_\pm\} = 0$, and the dashed lines correspond to $\mathrm{Im}\{\lambda_\pm\} = 0$. The parameters are the same as in Fig. C.1. Additionally, $\sigma^2 = 10$.

that in all models the region of oscillations is absent when the fixed point corresponds to complete activation of the network, $\rho \approx 1$ (also it only appears at $\alpha < 1$). That is why the region of network oscillations (colored in the figure) shrinks accordingly with the curve's slope of $\rho(\langle n \rangle)$ (panel on the left). Note that in this case the region of oscillations shrinks as g_e increases and oscillations can not appear at sufficiently small $\langle n \rangle$, in contrast with the F-model, but in agreement with the model studied in Chapter 4. However, in this case, the phase diagram appears to have a vertical line of symmetry (when there is only one fixed point at all $\langle n \rangle$), a feature that one can not find in Fig. 4.2, because, for instance, the region of oscillations is bounded by a saddle-node bifurcation, and a Hopf bifurcation, whereas in Figs. C.4(b) and C.4(d), the boundary of the region of oscillations corresponds uniquely to a Hopf bifurcation (as in the F-model). The phase diagrams of Fig. C.4 may give the hint that when the saddle-node bifurcation appears (in Fig. C.4(e)), the region of oscillations disappears. Actually, it is not the case. Our numerical analysis shows that the saddle-node bifurcation emerges at $g_e \gtrsim 0.753$, whereas the region of oscillations disappears at $g_e \lesssim 0.755$ (keeping constant all other parameters). Thus, there is a narrow region of parameters at which we can find both bifurcations in the phase diagram. Nevertheless, it is still qualitatively different from the phase diagram in Fig. 4.2, because the region of oscillations continues to be bounded only by the Hopf bifurcation. Based on the concept of symmetry breaking [181, 232], we expect that the Hopf bifurcation corresponds to a second-order phase transition, whereas the saddle-node bifurcation should be a first-order phase transition (with similar properties as those studied in Chapter 5).

Figure C.5 displays representative oscillations that we can find in this $\langle n \rangle$-model. One can notice that these oscillations are more similar to the oscillations in the random network (recall, for instance, Fig. 4.5(b)), than the oscillations in the F-model (see Fig. C.2).

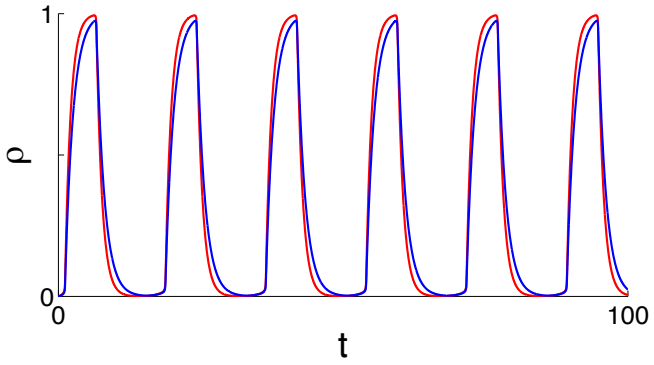

Figure C.5: Neuronal activity oscillations in the $\langle n \rangle$-model. The red line corresponds to excitatory activity, and the blue line corresponds to inhibitory activity. Parameters: $(\langle n \rangle, \alpha) = (22.5, 0.7)$, and the variance of noise $\sigma^2 = 10$. Other parameters are the same as in Fig. C.1. Time t is in units of μ_e^{-1}.

In this appendix, we presented two simple models, the F-model based on the model introduced in [101], and the $\langle n \rangle$-model based on the model discussed in Chapters 3, 4, and

5. The difference was the network structure: instead of a random network, we considered a fully connected network. It is very interesting to observe that the network structure plays a crucial role on the dynamics of its units. Moreover, the dynamics within the F-model differs from the $\langle n \rangle$-model in many aspects (how the region of oscillations depends on g_e, for instance), though the stimulation does not seem so different. However, the same does not happen between the same models, when the network is random, given that the dynamics is fairly similar [101, 102]. Unfortunately, we do not have an explanation for this fact. We can only stress how profoundly the structure can influence on the dynamics based on these results. One should note that the topologies are actually strikingly different, because these topologies are the extreme cases regarding the clustering coefficient. In the case of an undirected network, the clustering coefficient is c/N, which is zero for an infinite random network. In contrast, the clustering coefficient is 1 for a complete graph. The clustering coefficient, as mentioned in Chapter 6, characterizes the occurrence of triangles and other motifs [39]. It means that motifs can be neglected in a random network, but not in a fully connected network, where they may play a very important role in the network dynamics. Note that in our neuronal network there are many different motifs since the network is directed and there are two kinds of nodes (excitatory and inhibitory neurons), making it more difficult to predict how these motifs may influence on the dynamics. The interest of studying networks with high clustering coefficients is motivated by the fact that real neuronal network have large clustering coefficients [23]. On the other hand, taking into account that the mean number of synapses per neuron in the cortex is about 10^4 [1], then one can assume that a complete graph is a good description of a network with about 10^4 neurons in the cortex. It may also give a fair characterization of the dynamics of "super-neurons" observed in neuronal cultures [180] (the "super-neurons" are clusters of neurons that present strong activity correlations; unfortunately, it has not been possible to measure the internal connectivity of these clusters [180]).

Bibliography

[1] E. R. Kandel, J. H. Schwartz, and T. M. Jessell, *Principles of neural science* (McGraw-Hill, New York, 2000).

[2] A. Abbott, Nature **499**, 272 (2013).

[3] C. Bielza and P. Larrañaga, "Machine Learning and Neuroscience," University Seminar (2009).

[4] M. M. Shanechi, R. C. Hu, and Z. M. Williams, Nat. Commun. **5** (2014).

[5] M. Frampton, *Embodiments of Will: Anatomical and Physiological Theories of Voluntary Animal Motion from Greek Antiquity to the Latin Middle Ages, 400 BC-AD 1300* (VDM Verlag, Saarbrucken, 2008).

[6] O. Sporns, G. Tononi, and R. Kötter, PLoS Comput. Biol. **1**, e42 (2005).

[7] E. T. Bullmore and D. S. Bassett, Annu. Rev. Clin. Psycho. **7**, 113 (2011).

[8] L. R. Varshney, B. L. Chen, E. Paniagua, D. H. Hall, and D. B. Chklovskii, PLoS Comput. Biol. **7**, e1001066 (2011).

[9] S. Martinez-Conde and S. L. Macknik, Sci. Am. Mind **25**, 6 (2014).

[10] L. Lapicque, J. Physiol. Pathol. Gen. **9**, 620 (1907).

[11] N. Brunel and M. C. Van Rossum, Biol. Cybern. **97**, 337 (2007).

[12] W. S. McCulloch and W. Pitts, B. Math. Biol. **5**, 115 (1943).

[13] D. O. Hebb, *The organization of behavior* (Wiley, New York, 1949).

[14] A. L. Hodgkin and A. F. Huxley, J. Physiol. **117**, 500 (1952).

[15] M. Perc, Phys. Rev. E **76**, 066203 (2007).

[16] H. Yu, J. Wang, J. Du, B. Deng, X. Wei, and C. Liu, Chaos **23**, 013128 (2013).

[17] R. A. Stefanescu, R. Shivakeshavan, and S. S. Talathi, Seizure **21**, 748 (2012).

[18] H. R. Wilson and J. D. Cowan, Biophys. J. **12**, 1 (1972).

[19] H. R. Wilson and J. D. Cowan, Kybernetik **13**, 55 (1973).

[20] R. Albert and A.-L. Barabási, Rev. Mod. Phys. **74**, 47 (2002).

[21] S. N. Dorogovtsev and J. F. F. Mendes, Adv. Phys. **51**, 1079 (2002).

[22] M. E. J. Newman, SIAM Rev. **45**, 167 (2003).

[23] O. Sporns, D. R. Chialvo, M. Kaiser, and C. C. Hilgetag, Trends Cogn. Sci. **8**, 418 (2004).

[24] E. Bullmore and O. Sporns, Nat. Rev. Neurosci. **10**, 186 (2009).

[25] R. J. Morgan and I. Soltesz, Proc. Natl. Acad. Sci. U.S.A. **105**, 6179 (2008).

[26] P. Bonifazi, M. Goldin, M. A. Picardo, I. Jorquera, A. Cattani, G. Bianconi, A. Represa, Y. Ben-Ari, and R. Cossart, Science **326**, 1419 (2009).

[27] G. Zamora-López, C. Zhou, and J. Kurths, Front. Neuroinform. **4** (2010).

[28] M. P. van den Heuvel and O. Sporns, J. Neurosci. **31**, 15775 (2011).

[29] M. P. van den Heuvel, R. S. Kahn, J. Goñi, and O. Sporns, Proc. Natl. Acad. Sci. U.S.A. **109**, 11372 (2012).

[30] S. Zhou and R. J. Mondragón, IEEE Commun. Lett., **8**, 180 (2004).

[31] V. Colizza, A. Flammini, M. A. Serrano, and A. Vespignani, Nat. Phys. **2**, 110 (2006).

[32] V. B. Mountcastle, A. L. Berman, and P. W. Davies, Am. J. Physiol. **183**, 646 (1955).

[33] D. H. Hubel and T. N. Wiesel, J. Physiol. **160**, 106 (1962).

[34] V. B. Mountcastle, Cereb. Cortex **13**, 2 (2003).

[35] H. S. Meyer, V. C. Wimmer, M. Oberlaender, C. P. de Kock, B. Sakmann, and M. Helmstaedter, Cereb. Cortex **20**, 2277 (2010).

[36] T. A. Jarrell, Y. Wang, A. E. Bloniarz, C. A. Brittin, M. Xu, J. N. Thomson, D. G. Albertson, D. H. Hall, and S. W. Emmons, Science **337**, 437 (2012).

[37] R. Segev, M. Benveniste, Y. Shapira, and E. Ben-Jacob, Phys. Rev. Lett. **90**, 168101 (2003).

[38] E. M. Izhikevich and G. M. Edelman, Proc. Natl. Acad. Sci. U.S.A. **105**, 3593 (2008).

[39] S. N. Dorogovtsev, A. V. Goltsev, and J. F. F. Mendes, Rev. Mod. Phys. **80**, 1275 (2008).

[40] P. Fries, Trends Cogn. Sci. **9**, 474 (2005).

[41] G. Buzsaki, *Rhythms of the Brain*, 1st ed. (Oxford University Press, USA, 2006).

[42] T. J. Sejnowski and O. Paulsen, J. Neurosci. **26**, 1673 (2006).

[43] E. Düzel, W. D. Penny, and N. Burgess, Curr. Opin. Neurobiol. **20**, 143 (2010).

[44] A.-L. Giraud and D. Poeppel, Nat. Rev. Neurosci. **15**, 511 (2012).

[45] G. Buzsáki and A. Draguhn, Science **304**, 1926 (2004).

[46] F. Moss, L. M. Ward, and W. G. Sannita, Clin. Neurophysiol. **115**, 267 (2004).

[47] L. Gammaitoni, P. Hänggi, P. Jung, and F. Marchesoni, Rev. Mod. Phys. **70**, 223 (1998).

[48] G. B. Ermentrout, R. F. Galn, and N. N. Urban, Trends Neurosci. **31**, 428 (2008).

[49] A. Faisal, L. Selen, and D. M. Wolpert, Nat. Rev. Neurosci. **9**, 292 (2008).

[50] M. D. McDonnell and L. M. Ward, Nat. Rev. Neurosci. **12**, 415 (2011).

[51] B. J. Gluckman, T. I. Netoff, E. J. Neel, W. L. Ditto, M. L. Spano, and S. J. Schiff, Phys. Rev. Lett. **77**, 4098 (1996).

[52] J. K. Douglass, L. Wilkens, E. Pantazelou, and F. Moss, Nature **365**, 337 (1993).

[53] K. Wiesenfeld and F. Moss, Nature (London) **373**, 33 (1995).

[54] J. E. Levin and J. P. Miller, Nature **380**, 165 (1996).

[55] D. F. Russell, L. A. Wilkens, and F. Moss, Nature **402**, 291 (1999).

[56] W. C. Stacey and D. M. Durand, J. Neurophysiol. **83**, 1394 (2000).

[57] W. C. Stacey and D. M. Durand, J. Neurophysiol. **86**, 1104 (2001).

[58] I. Hidaka, D. Nozaki, and Y. Yamamoto, Phys. Rev. Lett. **85**, 3740 (2000).

[59] E. Simonotto, M. Riani, C. Seife, M. Roberts, J. Twitty, and F. Moss, Phys. Rev. Lett. **78**, 1186 (1997).

[60] T. Mori and S. Kai, Phys. Rev. Lett. **88**, 218101 (2002).

[61] K. Kitajo, D. Nozaki, L. M. Ward, and Y. Yamamoto, Phys. Rev. Lett. **90**, 218103 (2003).

[62] L. Ward, Contemp. Phys. **50**, 563 (2009).

[63] L. M. Ward, S. E. MacLean, and A. Kirschner, PLoS ONE **5**, e14371 (2010).

[64] T. Sasaki, R. Kimura, M. Tsukamoto, N. Matsuki, and Y. Ikegaya, J. Physiol. **574**, 195 (2006).

[65] D. R. Chialvo, Nat. Phys. **2**, 301 (2006).

[66] D. R. Chialvo, Nat. Phys. **6**, 744 (2010).

[67] J. A. Kelso, Am. J. Physiol. - Reg. I. **246**, R1000 (1984).

[68] H. Haken, J. A. S. Kelso, and H. Bunz, Biol. Cybern. **51**, 347 (1985).

[69] J. Kelso, J. Scholz, and G. Schöner, Phys. Lett. A **118**, 279 (1986).

[70] J. Scholz, J. Kelso, and G. Schöner, Phys. Lett. A **123**, 390 (1987).

[71] J. Kelso, G. Schöner, J. Scholz, and H. Haken, Phys. Scripta **35**, 79 (1987).

[72] J. Kelso, Front. Hum. Neurosci. **4**, 23 (2010).

[73] F. Baldissera, P. Cavallari, and P. Civaschi, Neurosci. Lett. **34**, 95 (1982).

[74] S. L. Bressler and J. Kelso, Trends Cogn. Sci. **5**, 26 (2001).

[75] J.-P. Eckmann, O. Feinerman, L. Gruendlinger, E. Moses, J. Soriano, and T. Tlusty, Phys. Rep. **449**, 54 (2007).

[76] J. M. Beggs and D. Plenz, J. Neurosci. **23**, 11167 (2003).

[77] D. Plenz and T. C. Thiagarajan, Trends Neurosci. **30**, 101 (2007).

[78] T. L. Ribeiro, M. Copelli, F. Caixeta, H. Belchior, D. R. Chialvo, M. A. Nicolelis, and S. Ribeiro, PloS ONE **5**, e14129 (2010).

[79] D. Steyn-Ross and M. Steyn-Ross, *Modeling Phase Transitions in the Brain* (Springer, New York, 2010).

[80] X.-J. Wang, Physiol. Rev. **90**, 1195 (2010).

[81] J. O'Keefe and M. L. Recce, Hippocampus **3**, 317 (1993).

[82] S. Raghavachari, M. J. Kahana, D. S. Rizzuto, J. B. Caplan, M. P. Kirschen, B. Bourgeois, J. R. Madsen, and J. E. Lisman, J. Neurosci. **21**, 3175 (2001).

[83] A. K. Engel, P. Fries, and W. Singer, Nat. Rev. Neurosci. **2**, 704 (2001).

[84] W. Singer and C. M. Gray, Annu. Rev. Neurosci. **18**, 555 (1995).

[85] V. N. Murthy and E. E. Fetz, J. Neurophysiol. **76**, 3949 (1996).

[86] T. J. Kaper, M. A. Kramer, and H. G. Rotstein, Chaos **23**, 046001 (2013).

[87] J. Jeong, J. Clin. Neurophysiol. **115**, 1490 (2004).

[88] D. Terman, J. Rubin, A. Yew, and C. Wilson, J. Neurosci. **22**, 2963 (2002).

[89] K. M. Spencer, P. G. Nestor, R. Perlmutter, M. A. Niznikiewicz, M. C. Klump, M. Frumin, M. E. Shenton, and R. W. McCarley, Proc. Natl. Acad. Sci. U.S.A. **101**, 17288 (2004).

[90] M. Steriade, D. A. McCormick, and T. J. Sejnowski, Science **262**, 679 (1993).

[91] A. A. Leão, J. Neurophysiol. **7**, 359 (1944).

[92] F. Lopes da Silva, W. Blanes, S. N. Kalitzin, J. Parra, P. Suffczynski, and D. N. Velis, Epilepsia **44**, 72 (2003).

[93] J. Jackson, *Selected Writings* (Hodder & Stoughton, London, 1931).

[94] O. N. Markand, Semin. Neurol. **23**, 7 (2003).

[95] I. Timofeev and M. Steriade, Neuroscience **123**, 299 (2004).

[96] R. Q. Quiroga, H. Garcia, and A. Rabinowicz, Electromyo. Clin. Neur. **42**, 323 (2002).

[97] Y.-C. Lai, I. Osorio, M. A. F. Harrison, and M. G. Frei, Phys. Rev. E **65**, 031921 (2002).

[98] F. Lopes da Silva and G. F. Harding, Epilepsy Res. **97**, 278 (2011).

[99] I. Soltesz and K. Staley, *Computational neuroscience in epilepsy* (Academic Press, London, 2011).

[100] M. Scheffer, J. Bascompte, W. A. Brock, V. Brovkin, S. R. Carpenter, V. Dakos, H. Held, E. H. Van Nes, M. Rietkerk, and G. Sugihara, Nature **461**, 53 (2009).

[101] A. V. Goltsev, F. V. de Abreu, S. N. Dorogovtsev, and J. F. F. Mendes, Phys. Rev. E **81**, 061921 (2010).

[102] K.-E. Lee, M. A. Lopes, J. F. F. Mendes, and A. V. Goltsev, Phys. Rev. E **89**, 012701 (2014).

[103] Z. F. Mainen and T. J. Sejnowski, Science **268**, 1503 (1995).

[104] E. Schneidman, B. Freedman, and I. Segev, Neural Comput. **10**, 1679 (1998).

[105] W. Adey, Intern. J. Neurosci. **3**, 271 (1972).

[106] H. Markram, J. Lübke, M. Frotscher, and B. Sakmann, Science **275**, 213 (1997).

[107] L. F. Abbott and S. B. Nelson, Nat. Neurosci. **3**, 1178 (2000).

[108] R. Malinow and R. C. Malenka, Annu. Rev. Neurosci. **25**, 103 (2002).

[109] G. Mongillo, O. Barak, and M. Tsodyks, Science **319**, 1543 (2008).

[110] M. A. Lopes, A. V. Goltsev, and J. F. F. Mendes, Int. J. Comp. Syst. Sci. **1**, 158 (2011).

[111] K.-E. Lee, A. V. Goltsev, M. A. Lopes, and J. F. F. Mendes, AIP Conf. Proc. **1510**, 195 (2012).

[112] A. V. Goltsev, M. A. Lopes, K.-E. Lee, and J. F. F. Mendes, AIP Conf. Proc. **1510**, 28 (2012).

[113] M. A. Lopes, A. V. Goltsev, K.-E. Lee, and J. F. F. Mendes, AIP Conf. Proc. **1510**, 202 (2012).

[114] D. Holstein, A. Goltsev, and J. Mendes, Phys. Rev. E **87**, 032717 (2013).

[115] E. M. Izhikevich, IEEE Trans. Neural Netw. **14**, 1569 (2003).

[116] S. H. Strogatz, *Nonlinear Dynamics And Chaos: With Applications To Physics, Biology, Chemistry, And Engineering* (Perseus Books Group, New York, 1994).

[117] W. G. Lennox, *Epilepsy and related disorders*, Vol. 2 (Little, Brown, Boston, 1960).

[118] L. Abbott and P. Dayan, *Theoretical Neuroscience: Computational and Mathematical Modeling of Neural Systems* (MIT Press, Cambridge, USA, 2001).

[119] L. Pickard, "Rat hippocampal neuron in culture," `https://www.ipmc.cnrs.fr/~duprat/neurophysiology/neuron.htm` (1999).

[120] D. C. Gadsby, Nat. Rev. Mol. Cell Bio. **10**, 344 (2009).

[121] E. M. Izhikevich, *Dynamical systems in neuroscience* (MIT press, Cambridge, USA, 2006).

[122] F. C. Hoppensteadt and E. M. Izhikevich, *Weakly connected neural networks* (Springer-Verlag, New York, 1997).

[123] E. M. Izhikevich, IEEE Trans. Neural Netw. **15**, 1063 (2004).

[124] B. W. Connors and M. J. Gutnick, Trends Neurosci. **13**, 99 (1990).

[125] J. R. Gibson, M. Beierlein, and B. W. Connors, Nature **402**, 75 (1999).

[126] B. Pesaran, S. Musallam, and R. Andersen, Curr. Biol. **16**, R77 (2006).

[127] K. Chung, J. Wallace, S.-Y. Kim, S. Kalyanasundaram, A. S. Andalman, T. J. Davidson, J. J. Mirzabekov, K. A. Zalocusky, J. Mattis, A. K. Denisin, *et al.*, Nature (2013).

[128] R. Baxter, *Exactly Solved Models in Statistical Mechanics* (Academic, San Diego, 1982).

[129] D. J. Amit and N. Brunel, Cereb. Cortex **7**, 237 (1997).

[130] N. Brunel and V. Hakim, Neural Comput. **11**, 1621 (1999).

[131] N. Brunel, J. Comput. Neurosci. **8**, 183 (2000).

[132] S. Ostojic, N. Brunel, and V. Hakim, J. Comput. Neurosci. **26**, 369 (2009).

[133] E. Ledoux and N. Brunel, Front. Comput. Neurosci. **5** (2011).

[134] B. Lindner, B. Doiron, and A. Longtin, Phys. Rev. E **72**, 061919 (2005).

[135] N. Brunel and V. Hakim, Chaos **18**, 015113 (2008).

[136] D. Millman, S. Mihalas, A. Kirkwood, and E. Niebur, Nat. Phys. **6**, 801 (2010).

[137] I. Breskin, J. Soriano, E. Moses, and T. Tlusty, Phys. Rev. Lett. **97**, 188102 (2006).

[138] J. Soriano, M. Rodriguez Martinez, T. Tlusty, and E. Moses, Proc. Natl. Acad. Sci. U.S.A. **105**, 13758 (2008).

[139] G. J. Baxter, S. N. Dorogovtsev, A. V. Goltsev, and J. F. F. Mendes, Phys. Rev. E **82**, 011103 (2010).

[140] J. V. Neumann, *Theory of Self-Reproducing Automata*, edited by A. W. Burks (University of Illinois Press, Champaign, 1966).

[141] B. Kriener, T. Tetzlaff, A. Aertsen, M. Diesmann, and S. Rotter, Neural Comput. **20**, 2185 (2008).

[142] S. Boccaletti, V. Latora, Y. Moreno, M. Chavez, and D.-U. Hwang, Phys. Rep. **424**, 175 (2006).

[143] A. Arenas, A. Diaz-Guilera, J. Kurths, Y. Moreno, and C. Zhou, Phys. Rep. **469**, 93 (2008).

[144] M. Benayoun, J. D. Cowan, W. van Drongelen, and E. Wallace, PLoS Comput. Biol. **6**, e1000846 (2010).

[145] E. Wallace, M. Benayoun, W. van Drongelen, and J. D. Cowan, PLoS ONE **6**, e14804 (2011).

[146] J. A. White, J. T. Rubinstein, and A. R. Kay, Trends Neurosci. **23**, 131 (2000).

[147] B. Lindner, J. Garcıa-Ojalvo, A. Neiman, and L. Schimansky-Geier, Phys. Rep. **392**, 321 (2004).

[148] Y. M. Blanter and M. Büttiker, Phys. Rep. **336**, 1 (2000).

[149] M. Steriade, Neuroscience **101**, 243 (2000).

[150] B.-Q. Mao, F. Hamzei-Sichani, D. Aronov, R. C. Froemke, and R. Yuste, Neuron **32**, 883 (2001).

[151] A. Mazzoni, S. Panzeri, N. K. Logothetis, and N. Brunel, PLoS Comput. Biol. **4**, e1000239 (2008).

[152] D. Randall, W. Burggren, and K. French, *Eckert animal physiology: Mechanisms and Addaptations* (W. H. Freeman, New York, 1997).

[153] Y. Shu, A. Hasenstaub, and D. A. McCormick, Nature **423**, 288 (2003).

[154] B. Haider, A. Duque, A. R. Hasenstaub, and D. A. McCormick, J. Neurosci. **26**, 4535 (2006).

[155] C. van Vreeswijk and H. Sompolinsky, Science **274**, 1724 (1996).

[156] S. El Boustani and A. Destexhe, Neural Comput. **21**, 46 (2009).

[157] P. Heil, Curr. Opin. Neurobiol. **14**, 461 (2004).

[158] H. A. Swadlow, Cereb. Cortex **13**, 25 (2003).

[159] S. Fujisawa, N. Matsuki, and Y. Ikegaya, J. Physiol. **561**, 123 (2004).

[160] M. L. Molineux, F. R. Fernandez, W. H. Mehaffey, and R. W. Turner, J. Neurosci. **25**, 10863 (2005).

[161] R. Pastor-Satorras and A. Vespignani, Phys. Rev. Lett. **86**, 3200 (2001).

[162] R. Pastor-Satorras and A. Vespignani, Phys. Rev. E **63**, 066117 (2001).

[163] M. Catanzaro, M. Boguñá, and R. Pastor-Satorras, Phys. Rev. E **71**, 056104 (2005).

[164] B. Ermentrout and T.-W. Ko, Phil. Trans. R. Soc. A **367**, 1097 (2009).

[165] Y. A. Kuznetsov, *Elements of Applied Bifurcation Theory* (Springer, New York, 1998).

[166] K. F. Ahrens and W. J. Freeman, Brain Res. **911**, 193 (2001).

[167] A. Babloyantz and A. Destexhe, Proc. Natl. Acad. Sci. U.S.A. **83**, 3513 (1986).

[168] D. Contreras, A. Destexhe, T. J. Sejnowski, and M. Steriade, Science **274**, 771 (1996).

[169] A. Bragin, G. Jandó, Z. Nádasdy, J. Hetke, K. Wise, and G. Buzsáki, J. Neurosci. **15**, 47 (1995).

[170] J. G. Orlandi, J. Soriano, E. Alvarez-Lacalle, S. Teller, and J. Casademunt, Nat. Phys. **9**, 582 (2013).

[171] N. Friedman, S. Ito, B. A. Brinkman, M. Shimono, R. L. DeVille, K. A. Dahmen, J. M. Beggs, and T. C. Butler, Phys. Rev. Lett. **108**, 208102 (2012).

[172] A. Clauset, C. R. Shalizi, and M. E. Newman, SIAM Rev. **51**, 661 (2009).

[173] A. Clauset, "Power-law distributions in empirical data," `http://tuvalu.santafe.edu/~aaronc/powerlaws/` (2009).

[174] J. P. Sethna, K. Dahmen, S. Kartha, J. A. Krumhansl, B. W. Roberts, and J. D. Shore, Phys. Rev. Lett. **70**, 3347 (1993).

[175] J. P. Sethna, K. A. Dahmen, and C. R. Myers, Nature **410**, 242 (2001).

[176] A. V. Goltsev, S. N. Dorogovtsev, and J. Mendes, Phys. Rev. E **73**, 056101 (2006).

[177] S. N. Dorogovtsev, A. V. Goltsev, and J. F. F. Mendes, Phys. Rev. Lett. **96**, 040601 (2006).

[178] G. Baxter, S. Dorogovtsev, A. Goltsev, and J. Mendes, Phys. Rev. Lett. **109**, 248701 (2012).

[179] W. L. Shew, H. Yang, S. Yu, R. Roy, and D. Plenz, J. Neurosci. **31**, 55 (2011).

[180] J. Soriano and E. Moses, (private communication).

[181] H. E. Stanley, *Introduction to Phase Transitions and Critical Phenomena* (Oxford University Press, London, 1987).

[182] D. Stauffer and A. Aharony, *Introduction to Percolation Theory* (Taylor and Francis, London, 2003).

[183] K. Binder, Ferroelectrics **73**, 43 (1987).

[184] C. W. Gardiner, *Handbook of Stochastic Methods : For Physics, Chemistry and the Natural Sciences* (Springer, Berlin, 2002).

[185] C. Bedard, H. Kroeger, and A. Destexhe, Phys. Rev. Lett. **97**, 118102 (2006).

[186] P. Bak, *How Nature Works* (Oxford University Press, Oxford, UK, 1997).

[187] J. Rinzel and G. B. Ermentrout (MIT Press, Cambridge, USA, 1989) Chap. Analysis of neural excitability and oscillations, pp. 135–169.

[188] E. M. Izhikevich, Int. J. Bif. and Chaos **10**, 1171 (2000).

[189] M. Steriade and D. Contreras, J. Neurosci. **15**, 623 (1995).

[190] G. Buzsáki, Brain Res. **398**, 242 (1986).

[191] H. Gang, T. Ditzinger, C. Z. Ning, and H. Haken, Phys. Rev. Lett. **71**, 807 (1993).

[192] W. Rappel and S. H. Strogatz, Phys. Rev. E **50**, 3249 (1994).

[193] K. Wiesenfeld, D. Pierson, E. Pantazelou, C. Dames, and F. Moss, Phys. Rev. Lett. **72**, 2125 (1994).

[194] A. Longtin, Phys. Rev. E **55**, 868 (1997).

[195] P. C. Matthews and S. H. Strogatz, Phys. Rev. Lett. **65**, 1701 (1990).

[196] K. Krischer, M. Eiswirth, and G. Ertl, J. Chem. Phys. **96**, 9161 (1992).

[197] L. H. Tweel, Doc. Ophthalmol. **18**, 287 (1964).

[198] R. Hari and R. Salmelin, Trends Neurosci. **20**, 44 (1997).

[199] L. Lehtelä, R. Salmelin, and R. Hari, Neurosci. Lett. **222**, 111 (1997).

[200] W. M. Siebert, *Circuits, Signals, and Systems*, Vol. 2 (MIT press, Cambridge, USA, 1986).

[201] J. Csicsvari, B. Jamieson, K. D. Wise, and G. Buzsáki, Neuron **37**, 311 (2003).

[202] R. Benzi, G. Parisi, A. Sutera, and A. Vulpiani, Tellus **34**, 10 (1982).

[203] J. J. Collins, C. C. Chow, and T. T. Imhoff, Nature **376**, 236 (1995).

[204] M. D. McDonnell, N. G. Stocks, and D. Abbott, Phys. Rev. E **75**, 061105 (2007).

[205] D. R. Chialvo, A. Longtin, and J. Müller-Gerking, Phys. Rev. E **55**, 1798 (1997).

[206] Q. Wang, M. Perc, Z. Duan, and G. Chen, Chaos **19**, 023112 (2009).

[207] Y. Gong, M. Wang, Z. Hou, and H. Xin, Chem. Phys. Chem. **6**, 1042 (2005).

[208] M. Ozer, M. Perc, and M. Uzuntarla, Phys. Lett. A **373**, 964 (2009).

[209] M. Yoshida, H. Hayashi, K. Tateno, and S. Ishizuka, Neural Networks **15**, 1171 (2002).

[210] N. Kashtan and U. Alon, Proc. Natl. Acad. Sci. U.S.A. **102**, 13773 (2005).

[211] J. A. Feldman and D. H. Ballard, Cognitive Sci. **6**, 205 (1982).

[212] J. I. Gold and M. N. Shadlen, Nature **404**, 390 (2000).

[213] M. A. Lopes, K.-E. Lee, A. V. Goltsev, and J. F. F. Mendes, Phys. Rev. E **90**, 052709 (2014).

[214] J. A. Cardin, M. Carlén, K. Meletis, U. Knoblich, F. Zhang, K. Deisseroth, L.-H. Tsai, and C. I. Moore, Nature **459**, 663 (2009).

[215] A. Litwin-Kumar and B. Doiron, Nat. Neurosci. **15**, 1498 (2012).

[216] M. D. McDonnell and L. M. Ward, PloS ONE **9**, e88254 (2014).

[217] B. A. Carlson, P. B. Crilly, and J. Rutledge, *Communication Systems* (McGraw-Hill, New York, 2001).

[218] A. Dyachenko and V. E. Zakharov, J. Exp. Theor. Phys. Lett. **81**, 255 (2005).

[219] A. Calini and C. Schober, Phys. Lett. A **298**, 335 (2002).

[220] J. G. Milton, Epilepsy Behav. **18**, 33 (2010).

[221] R. S. Fisher and A. L. Velasco, Nat. Rev. Neurol. **10**, 261 (2014).

[222] B. Schelter, J. Timmer, and A. Schulze-Bonhage, *Seizure prediction in epilepsy: from basic mechanisms to clinical applications* (John Wiley & Sons, Weinheim, 2008).

[223] M. J. Feigenbaum, Physica D **7**, 16 (1983).

[224] L. Abbott, J. Varela, K. Sen, and S. Nelson, Science **275**, 221 (1997).

[225] H. Markram, Y. Wang, and M. Tsodyks, Proc. Natl. Acad. Sci. U.S.A. **95**, 5323 (1998).

[226] M. Lynch, Physiol. Rev. **84**, 87 (2004).

[227] M. Ito, Annu. Rev. Neurosci. **12**, 85 (1989).

[228] G. A. Gottwald and I. Melbourne, Physica D **212**, 100 (2005).

[229] G. A. Gottwald and I. Melbourne, SIAM J. Appl. Dyn. Syst. **8**, 129 (2009).

[230] C. A. Skarda and W. J. Freeman, Behav. Brain Sci. **10**, 161 (1987).

[231] C. A. Del Negro, C. G. Wilson, R. J. Butera, H. Rigatto, and J. C. Smith, Biophys. J. **82**, 206 (2002).

[232] R. V. Solé, S. C. Manrubia, B. Luque, J. Delgado, and J. Bascompte, Complexity **1**, 13 (1996).

[233] V. B. Mountcastle, Brain **120**, 701 (1997).

[234] J. M. Yeomans, *Statistical mechanics of phase transitions* (Oxford University Press, Oxford, 1992).

[235] P. W. Anderson *et al.*, Science **177**, 393 (1972).

[236] R. D. Fields, Nature **501**, 25 (2013).

[237] R. Carron, A. Chaillet, A. Filipchuk, W. Pasillas-Lépine, and C. Hammond, Front. Syst. Neurosci. **7** (2013).

[238] M. Abramowitz and I. A. Stegun, *Handbook of mathematical functions: with formulas, graphs, and mathematical tables* (Courier Dover Publications, Washington, D.C., 1970).